SHARP INTERFACE MODELS FOR
SOLID STATE DEWETTING
AND THEIR APPLICATIONS

ZHAO QUAN

NATIONAL UNIVERSITY OF SINGAPORE

2017

SHARP INTERFACE MODELS FOR
SOLID STATE DEWETTING
AND THEIR APPLICATIONS

ZHAO QUAN

(B.Sc., University of Science and Technology of China)

A THESIS SUBMITTED
FOR THE DEGREE OF DOCTOR OF PHILOSOPHY
DEPARTMENT OF MATHEMATICS
NATIONAL UNIVERSITY OF SINGAPORE
2017

Supervisors:

Professor Bao Weizhu, Main Supervisor

Professor Ren Weiqing, Co-Supervisor

Examiners:

Associate Professor Chu Delin

Professor Wang Xiaoping, Hong Kong University of Science and Technology

Associate Professor Wang Li Lian, Nanyang Technological University

DECLARATION

I hereby declare that the thesis is my original work and it has
been written by me in its entirety. I have duly
acknowledged all the sources of information which
have been used in the thesis.

This thesis has also not been submitted for any degree
in any university previously.
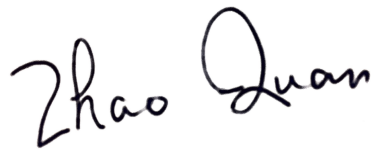
Zhao Quan

ZHAO QUAN

September 7, 2018

Acknowledgements

It is my great honor here to thank those who made this thesis possible.

First and foremost, I would like to express my sincere gratitude to my main supervisor Prof. Weizhu Bao, for his general support for my Ph.D study and related research. His patient guidance and continuous encouragement are indispensable for me to finish such an interesting project, and his advices about life and career will be a great fortune in my future. Besides, I would like to thank my co-supervisor Prof. Weiqing Ren for his insightful comments and encouragement.

My sincere thanks also go to my collaborators Prof. David J. Srolovitz, Prof. Wei Jiang and Dr. Yan Wang for their contribution to the work. Specially, many thanks to Prof. Wei Jiang and Dr. Yan Wang for the fruitful discussions and suggestions on this topic, as well as for reading the draft. It is my fortune to join this research team, in which I have learned a lot during the cooperation.

I thank my former colleagues, fellow graduates in our group, and all my friends in my real life. I would also like to thank NUS for awarding me the Research Scholarship during my Ph.D candidature, and for the financial assistance during the conference leaves.

Last but not least, thank my family for supporting me spiritually throughout writing this thesis and my life in general.

<div align="right">

Zhao Quan

August 2017

</div>

i

Contents

Summary

Solid-state dewetting is a ubiquitous physical phenomenon occurring in the solid-solid-vapor system, describing the agglomeration of solid thin films on the substrate. The thin films supported by the substrate are typically unstable and could exhibit complex morphological evolutions, including hole formulation, edge retraction, rim pinch-off and so on, while still remaining the state of solid. The capillary instability is the driving force of this process and makes the thin film moving towards its equilibrium by decreasing the total surface energy. Surface diffusion flow and contact line migration have been recognised as the two main kinetic features for solid-state dewetting.

The aim of this thesis is to develop mathematical models, propose efficient and accurate numerical methods for simulating the solid-state dewetting both in two dimensions and three dimensions. Moreover, extensive numerical simulation results are presented to validate the convergence of the numerical schemes, show consistent morphological evolutions observed in physics experiments, and demonstrate the accuracy of the models.

Firstly, by using a Cahn-Hoffman $\boldsymbol{\xi}$-vector formulation, we propose a sharp-interface approach for solving solid-state dewetting problems in two dimensions. Based on the thermodynamic variation and smooth vector-field perturbation method,

we rigorously derive a sharp-interface model with weakly anisotropic surface energies, and this model describes the interface evolution which occurs through surface diffusion flow and contact line migration. What is more, a parametric finite element method in terms of the $\boldsymbol{\xi}$-vector formulation is proposed for numerically solving the sharp-interface model. By performing numerical simulations, we examine several specific evolution processes for solid-state dewetting of thin films, e.g., the evolution of small islands, pinch-off of large islands and power-law retraction dynamics of semi-infinite step films, and these simulation results are consistent with experimental observations. Furthermore, we also include the strong surface energy anisotropy into the sharp-interface model and design its corresponding numerical scheme via the $\boldsymbol{\xi}$-vector formulation.

Secondly, we extend our works from 2D to 3D. We present a three-dimensional sharp interface approach for modelling the solid-state dewetting of thin films. The film/vapor interface in this approach is treated as an open surface, i.e., two-dimensional manifold with a plane curve boundary attached to the rigid flat substrate (x-y-plane). Based on the energy variational method, the equilibrium shape that minimizes the total surface energy has been derived rigorously by a mathematical description of the chemical potential together with the anisotropic Young-Dupre equation. Besides, we have also proposed the kinetic sharp-interface model for simulating the evolution of solid-state thin films via a Cahn-Hoffman ξ-vector formulation. The governing equations belong to geometric evolution partial differential equations of fourth-order, and are described by surface diffusion flow and contact line migration. By adding a small surface diffusion regularization for the contact line migration, we could apply the parametric finite element methods to solve both the surface evolution and plane curve evolution.

Finally, the sharp interface model is extended to the cases when the surface energy is strongly anisotropic and when the substrate is curved. Besides, we study capillarity-driven evolution of a solid toroidal island on a flat rigid substrate under the axis-symmetry. We apply the Onsager's variational principle to derive a

simple, reduced-order model and obtain an analytical expression for the rate of island shrinking and validate this prediction by numerical simulations based on a full, sharp-interface model.

List of Tables

List of Figures

List of Symbols and Abbreviations

2D	two dimensions
3D	three dimensions
$\mathbb{R}^d$	d dimensional Euclidean space
PFEM	parametric finite element method
Ω_0	atomic volume
D_s	surface diffusivity
ν	the number of diffusing atoms per unit area
$k_B T_e$	thermal energy
γ_0	unit scale of film/vapor interfacial energy density
L	length scale
γ_{FS}	film/substrate interfacial energy density
γ_{VS}	vapor/substrate interfacial energy density
σ	a dimensionless parameter equals to $\frac{\gamma_{VS} - \gamma_{FS}}{\gamma_0}$
ϵ	small perturbation parameter
δ	small regularization parameter
t	time
s	arc length of the film/vapor interface
ρ	a variable for parameterizing the film/vapor interface

S	surface
S_{sub}	substrate
$\mathbf{n}$	outer unit normal vector
$\mathbf{n}_{\Gamma}$	outer unit normal vector of Γ on substrate
$\mathbf{c}_{\Gamma}$	unit co-normal vector on boundary Γ
$\mathbf{c}_{\Gamma}^{\gamma}$	anisotropic co-normal vector
$\mathbf{n}_{sub}$	unit normal vector of the substrate
κ	curvature of curve
$\mathcal{H}$	mean curvature
$\mathcal{K}$	Gaussian curvature
$M_x(\phi)$	rotational matrix along x axis with angle ϕ under right hand rule
$M_y(\phi)$	rotational matrix along y axis with angle ϕ under right hand rule
$M_z(\phi)$	rotational matrix along z axis with angle ϕ under right hand rule
S^2	the surface of unit sphere
$\mathbf{X}(\cdot, t)$	local parametrization of the film/vapor interface
$\mathbf{X}_{\Gamma}(\cdot, t)$	local parametrization of the contact line
W	total interfacial (surface) energy
W_{FV}	film/vapor interfacial energy
W_{FS}	film/substrate interfacial energy
W_{VS}	vapor/substrate interfacial energy
W_{int}	interfacial energy
W_{sub}	substrate energy
$\gamma(\mathbf{n})$	surface energy density
$\gamma(\theta, \phi)$	surface energy density in spherical coordinates
$\hat{\gamma}(\mathbf{n})$	homogeneous extension of γ
$\boldsymbol{\xi}$	Cahn-Hoffman vector

H_γ	Hessian matrix of $\hat{\gamma}$
T_ε	geometric transformation
$\mathbf{V}$	variation vector field
$\dot{\phi}(\Omega; \mathbf{V})$	material derivative
$\phi'(\Omega; \mathbf{V})$	shape derivative
$dF(\Omega; \mathbf{V})$	first variation in direction $\mathbf{V}$
$\psi(t)$	Mesh-distribution function
$\mathcal{T}_\mathbf{x} S$	tangent space to surface S at point $\mathbf{x}$
$\mathcal{N}_\mathbf{x} S$	normal space to surface S at point $\mathbf{x}$
$\mathcal{F}$	Frank shape
$\mathcal{W}$	Wulff shape
$\perp$	rotating vector by 90 degrees in the clockwise direction
∇_s	surface gradient operator
Δ_s	Laplace-Beltrami operator
$\times$	cross product

Introduction

1.1 Interface/surface Dynamics

1.1.1 Physics background

Interfacial problems are typical in material science for fluid or solid systems and have been widely studied in different aspects. A drop of water on a leaf or a soap bubble tend to form near-spherical shape, as the sphere has the smallest surface area to volume ratio. This phenomenon, know as surface tension, results form the cohesive forces among the liquid molecules. More precisely, molecules inside the liquid are pulling equally in every direction by their neighbouring liquid molecules. However, the molecules that wander to the surface will lose part of their cohesive interactions from outside. Therefore, these molecules are pulled inwards and the force the liquids to adjust their shapes such that the number of molecules on the surface must be minimized. The minimization of the number of molecules on the surface results in a minimization of the surface area, thus giving the spherical shape.

Several effects of the surface tension can be observed with the ordinary water in our daily life, such as the beading of rain water on a leaf, the water dripping from a tap. Although surface tension occurs on solid surface as well, yet few corresponding effects of surface tension in solids has been observed in daily life. The is due to that

the mechanism for solid surface is much more complicated than that of the fluid interface. Different mechanisms are competing among each other to determine the shape evolution for solid surface. In micro and nano-scale, surface tension could be the dominant dynamics for solid surface.

Surface tension of a liquid, usually represented by γ, can be viewed as a force per unit length or energy per unit area. The system is trying to find a state such that the surface energy is minimized.

1.1.2 Interfacial energy density

Unlike liquid or amorphous solids, the interface energy for many materials could be various for different crystallographic orientations, and this anisotropy in the surface energy could lead faceting for crystals. Therefore, for anisotropic materials, as most theories start with, the surface energy density, denoted by γ, is assumed to be dependent on the direction $\mathbf{n}$, the oriented normal of the interface. More precisely, the interfacial energy density can be expressed as a function defined on the surface of a unit sphere denoted by S^2:

$$\gamma(\mathbf{n}) : S^2 \to \mathbb{R}, \tag{1.1.1}$$

where $\mathbf{n}$ is the unit normal vector of the interface. Although there are cases when the interface energy density depends on the temperature, position, curvature [61, 104,106] and so on, for simplicity, here we only restrict to the case when the interface energy density is dependent on the orientation.

When $\gamma(\mathbf{n})$ is smooth, many theories indicate that the derivatives of $\gamma(\mathbf{n})$ play an important role in studying the dynamics and equilibrium problems for the crystals evolutions. However, calculating the derivative with respect to $\mathbf{n}$ restricts us on the surface of a unit sphere, which could cause a lot of troubles. For convenience and further discussion, we usually extend the domain of γ from S^2 to the whole $\mathbb{R}^3$ homogeneously [34] in the following

$$\hat{\gamma}(\mathbf{p}) = |\mathbf{p}|\gamma(\frac{\mathbf{p}}{|\mathbf{p}|}), \quad \forall \mathbf{p} \in \mathbb{R}^3 \backslash \{\mathbf{0}\}. \tag{1.1.2}$$

Under this extension, $\hat{\gamma}$ satisfies the following equation

$$\hat{\gamma}(\lambda\mathbf{p}) = |\lambda|\hat{\gamma}(\mathbf{p}), \quad \forall\lambda \neq 0, \mathbf{p} \in \mathbb{R}^3\backslash\{\mathbf{0}\}. \tag{1.1.3}$$

Moreover, if $\hat{\gamma}(\mathbf{p}) \in C^2(\mathbb{R}^3)$, we have

$$\nabla\hat{\gamma}(\mathbf{p}) \cdot \mathbf{p} = \hat{\gamma}(\mathbf{p}), \qquad \nabla\hat{\gamma}(\lambda\mathbf{p}) = \text{sign}(\lambda)\nabla\hat{\gamma}(\mathbf{p}),$$

$$H_\gamma(\mathbf{p})\mathbf{p} \cdot \mathbf{q} = 0, \qquad H_\gamma(\lambda\mathbf{p}) = \frac{1}{|\lambda|}H_\gamma(\mathbf{p}), \quad \forall\mathbf{p}, \mathbf{q} \in \mathbb{R}^3\backslash\{\mathbf{0}\}, \lambda \neq 0. \tag{1.1.4}$$

Here $\nabla\hat{\gamma}$ denotes the gradient of $\hat{\gamma}$ and H_γ represents the Hessian of $\hat{\gamma}$. It is easy to show that the matrix H_γ is symmetric and has a zero eigenvalue: $H_\gamma(\mathbf{p})\mathbf{p} = \mathbf{0}$. Here are some examples of some choices of the anisotropy:

- Isotropic surface energy

$$\gamma(\mathbf{n}) = |\mathbf{n}| = 1. \tag{1.1.5}$$

- Cubic surface energy

$$\gamma(\mathbf{n}) = 1 + a[n_1^4 + n_2^4 + n_3^4]. \tag{1.1.6}$$

- Ellipsoidal surface energy

$$\gamma(\mathbf{n}) = \sqrt{a_1^2 n_1^2 + a_2^2 n_2^2 + a_3^2 n_3^2}. \tag{1.1.7}$$

- Facet/cusp surface energy

$$\gamma(\mathbf{n}) = |n_1| + |n_2| + |n_3|. \tag{1.1.8}$$

The simplest case is the isotropic case when $\gamma(\mathbf{n})$ is a constant. Some other anisotropies are given such as the cubic crystalline surface energy (Eq. (1.1.6)) and ellipsoidal surface energy (Eq. (1.1.7)). In application of materials science, the surface energy is usually piecewise smooth and has some "cusped" points, where it is not differentiable [61, 89]. A typical example for this type anisotropy is given in Eq. (1.1.6). We can regularize the energy as following to ensure the smoothness.

$$\gamma(\mathbf{n}) = \sqrt{\varepsilon^2 + (1 - \varepsilon^2)n_1^2} + \sqrt{\varepsilon^2 + (1 - \varepsilon^2)n_2^2} + \sqrt{\varepsilon^2 + (1 - \varepsilon^2)n_3^2}. \tag{1.1.9}$$

The classification of anisotropies can be different due to different criteria. In mathematics, we usually classify the anisotropies into two categories by checking whether the following inequality is satisfied:

$$\mathrm{H}_\gamma(\mathbf{p})\mathbf{q} \cdot \mathbf{q} \geq \lambda_0, \quad \forall \mathbf{q} \cdot \mathbf{p} = \mathbf{0}, \quad \mathbf{q}, \mathbf{p} \in \mathrm{S}^2. \tag{1.1.10}$$

Here λ_0 is a positive constant to be found. If the anisotropy satisfies Eq. (1.1.10), we call it weak anisotropy. Otherwise, we call it strong anisotropy. Eq. (1.1.10), also called convexity condition, is crucial to the stability of the Wulff shape [122], well-posedness of the surface diffusion flow [67] and numerical analysis [34]. In materials science, some people may classify the facet anisotropy with cusps as strong anisotropy [71]. The classification criteria could be better understood in two dimensions where the anisotropy is given as $\gamma(\theta)$. Here θ satisfies $\mathbf{n} = (-\sin\theta, \cos\theta)^T$, $\boldsymbol{\tau} = (\cos\theta, \sin\theta)^T$, we can easily obtain that

$$\mathrm{H}_\gamma(\mathbf{n}) = (\gamma(\theta) + \gamma''(\theta)) \begin{pmatrix} n_2^2 & -n_1 n_2 \\ -n_1 n_2 & n_1^2 \end{pmatrix}. \tag{1.1.11}$$

Thus we have $\mathrm{H}_\gamma(\mathbf{n})\boldsymbol{\tau} \cdot \boldsymbol{\tau} = \gamma(\theta) + \gamma''(\theta)$. This indicates that Eq. (1.1.10) is related to the surface stiffness $\gamma(\theta) + \gamma''(\theta)$. In three dimensions, $\mathrm{H}_\gamma(\mathbf{n})\boldsymbol{\tau} \cdot \boldsymbol{\tau}$ can be regarded as the surface stiffness in the $\boldsymbol{\tau}$ direction.

Usually the anisotropy function $\gamma(\mathbf{n})$ can be geometrically represented by the radial plot of γ, and we call it $\gamma-$plot. The shape can be expressed as

$$F = \left\{ \mathbf{x} \in \mathbb{R}^3 : |\mathbf{x}| \leq \gamma(\frac{\mathbf{x}}{|\mathbf{x}|}) \right\}. \tag{1.1.12}$$

1.1.3 Cahn-Hoffman $\boldsymbol{\xi}-$vector

Cahn and Hoffman developed the theory of Cahn-Hoffman $\boldsymbol{\xi}$-vector [27, 65] to describe the surface energies density instead of using the traditional scalar function γ or γ-plot. It is mathematically defined as

$$\boldsymbol{\xi}(\mathbf{n}) = \nabla(r\gamma) = \nabla\hat{\gamma}(\mathbf{n}), \text{ with } \boldsymbol{\xi}_j(\mathbf{n}) = \frac{\partial\hat{\gamma}}{\partial \mathrm{p}_j}(\mathbf{n}) \text{ where } j = 1, 2, 3. \tag{1.1.13}$$

If the surface energy density is given in terms of the spherical coordinates, $\gamma(\theta, \phi)$, with $0 \leq \theta \leq \pi$ and $0 \leq \phi \leq 2\pi$, under the homogeneous extenstion, we have

$$\hat{\gamma}(\mathbf{p}) = |\mathbf{p}|\gamma\Big(\tan^{-1}\Big(\frac{\sqrt{p_1^2 + p_2^2}}{p_3}\Big), \tan^{-1}\Big(\frac{p_2}{p_1}\Big)\Big). \tag{1.1.14}$$

Thus the Cahn-Hoffman $\boldsymbol{\xi}-$vector can be written as

$$\boldsymbol{\xi}(\mathbf{n}) = \nabla\hat{\gamma}(\mathbf{n}) = \gamma\mathbf{n} + \gamma_\theta\hat{\boldsymbol{\theta}} + \frac{1}{\sin\theta}\gamma_\phi\hat{\boldsymbol{\phi}}, \tag{1.1.15}$$

where in this expressions,

$$\mathbf{n} = (\sin\theta\cos\phi, \sin\theta\sin\phi, \cos\theta)^T, \tag{1.1.16a}$$

$$\hat{\boldsymbol{\theta}} = (\cos\theta\cos\phi, \cos\theta\sin\phi, -\sin\theta)^T, \tag{1.1.16b}$$

$$\hat{\boldsymbol{\phi}} = (-\sin\phi, \cos\phi, 0)^T. \tag{1.1.16c}$$

This vector consists of the normal component and tangential component, with each part representing the tendency of minimizing the surface energies by contraction or rotation respectively [65].

1.1.4 Surface energy and evolution

Given the surface energy density $\gamma(\mathbf{n})$, the total surface energy is a integration over the interface S,

$$W = \iint_S \gamma(\mathbf{n}) \, dS. \tag{1.1.17}$$

In polycrystalline material, the grain boundary migrations are driven by curvature, where a grain boundary move with a velocity that is proportional to its mean curvature [108]. This motion is called mean curvature flow and can be regarded as the L^2 gradient flow of the surface energy. Under the mean curvature flow, the surface with isotropic surface energy will evolve into a spherical shape and shrink inward uniformly.

Another important kinetic for surface evolution is surface diffusion flow [86], which can be regarded as the H^{-1} gradient flow of the surface energy. This geometric flow forces the surface to reduce the surface energy while fixing the enclosed volume as a constant.

1.2 Solid State Dewetting
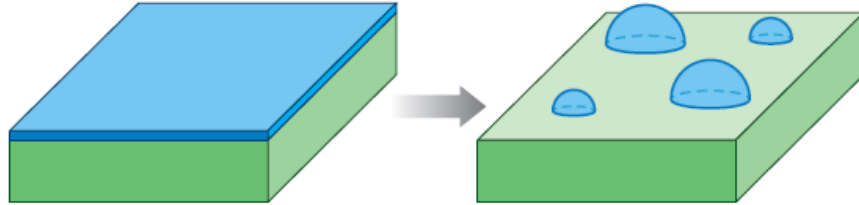
Figure 1.1: Solid thin films dewet to from isolated islands, the image is taken from [117].

1.2.1 Physical experiments and applications

Solid thin film on the substrate is typically unstable and can dewet or agglomerate to form isolated islands (see Fig. 1.1) when heated to sufficiently high temperature, but well below the material's melting point [117]. During this process, the thin film remains in the solid state, thus it is called solid-state dewetting. Driven by capillarity, solid-state dewetting is a process moving towards the equilibrium by minimizing the total surface energy.

In recent physical experiments, some morphological features were observed in the intermediate state of solid-state dewetting. These features include edge retraction, rim growth, hole formation and growth and so on.

For solid-state dewetting, materials from the triple line (where the film, vapor and substrate meet) and corner will be transported to the flat area. This mass transport leads to the formation of rim and valley at edges. See Fig. 1.2(g), as the edge retracts, the rim grows and the depth of the valley increases. For small patches, the valley finally disappears. However, when the size of the patches is large enough, the valley will reach the substrate before they merge and form hole (see Fig. 1.2(e),(f))or edge pinch-off. Moreover, the finger instability can be observed
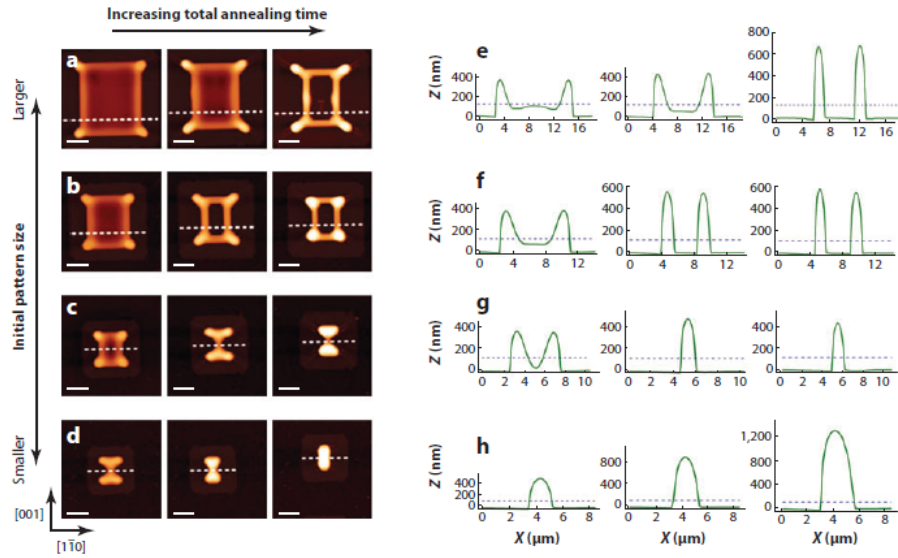
Figure 1.2: Dewetting of Ni with different initial sizes. (e)-(h) shows the corresponding height profile of the single thin film. The image is taken from [128].

during the edge retraction [33, 50, 68, 69, 77]. The thin film produces protruding fingers at the edge by forming rims with different heights and triple lines at different positions, see Fig. 1.3. Anisotropy can greatly influence the morphologies evolution
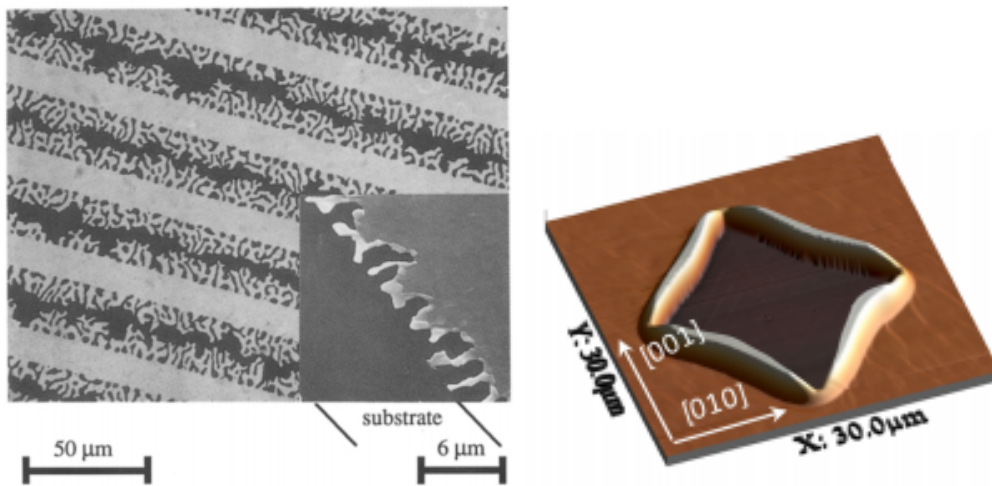
Figure 1.3: The left image taken from [68] shows the finger instability during dewetting. The right image taken from [70] shows the corner instability.

of thin film by producing the faceting geometry. When there exist surfaces parallel

to the substrate, and the orientations of these surfaces do not take a minimum for the surface energy density, the thin film may develop a wave along the flat surface during the edge retraction. This morphological evolution is called the faceting instability. Corner instability is another morphological characteristic for solid-state dewetting. Anisotropic thin films can dewet to form polygonal shaped holes, and these holes can grow anisotropically with increasing annealing time. Physical experiments demonstrate that corners retract faster than the centre of the edges, thus causing dendritic or star-shaped holes [2, 139].
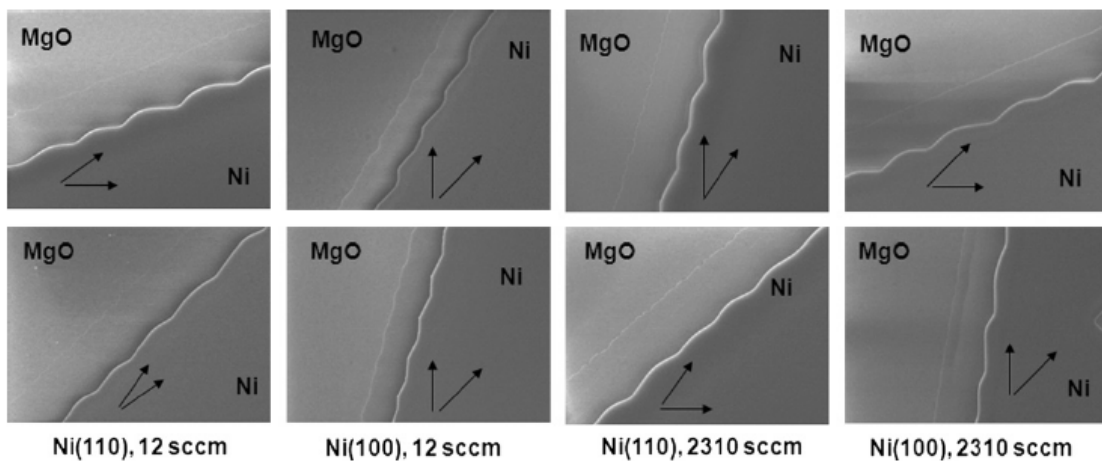
Figure 1.4: Faceting instability for long retracting edges. This image is taken from [130].

In summary, the morphologies evolution of thin film could be affected by many parameters.

- Thin film geometry: experiments by Ye and Thompson [128, 129] has shown the geometry of the thin film, including the size, orientation, location of holes and so on, could dramatically influence the shape evolution (see Fig. 1.5 for an example).

- Substrate topology: the morphological evolution of the thin film could be greatly influenced by the topology of the substrate [53, 83, 90, 112]. It shows that ordered topologically substrate produces ordered dewetting structures.
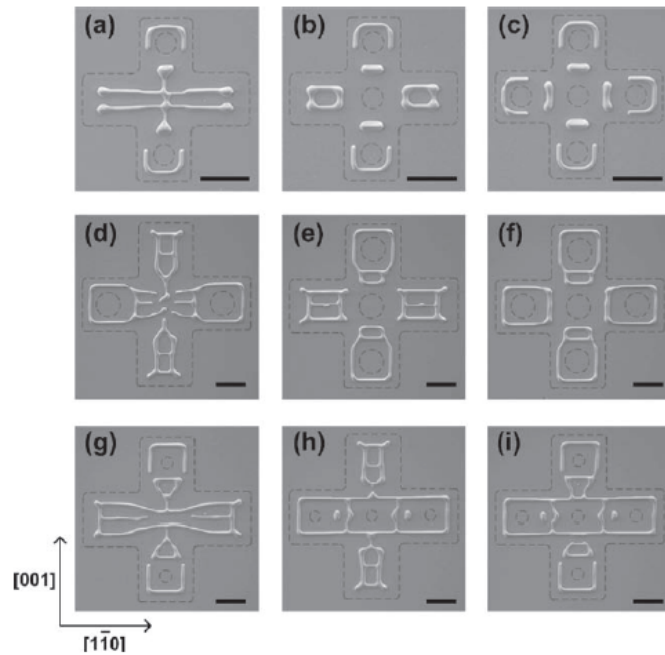
Figure 1.5: Dewetting of cross patches with pre-patterned internal circular holes. The initial size of the patches and the size and location of holes are different. This image is taken from [129].

- Anisotropic surface energies: the anisotropy of the surface energies produces faceting geometry for the thin film and also influences the morphological evolution of the thin film [127–130].

- Some other parameters such as the temperature, or outer environment and so on.

Solid thin films are fundamental components of the microelectronic and optoelectronic devices. The morphological evolution of the small thin film could be a great issue and should be prevented in order to keep the reliability of the device. Thus many research has been carried out to characterize and suppress dewetting in this microsystem. However, the recent understanding of solid-state dewetting makes it possible to provide positive influence. For example, it can be purposely induced to produce catalysts for growth of carbon nanotubes and semiconductor nanowires.

The wide applications of solid-state dewetting make it urgent to have a better understanding of the kinetic patterns and features of solid-state dewetting.

1.2.2 Interfacial energies and surface diffusion

Figure 1.6: A schematical illustration of a solid thin film on a flat rigid substrate in three dimensions.

Fig. 1.6 is a schematic illustration of a solid thin film on a flat rigid substrate in three dimensions. The total surface energy of the solid-state dewetting, can be expressed in the following

$$W = \iint_{S_{FV}} \gamma_{FV} \, dS_{FV} + \underbrace{\iint_{S_{FS}} \gamma_{FS} \, dS_{FS} + \iint_{S_{VS}} \gamma_{VS} \, dS_{VS}}_{\text{Substrate energy}}. \tag{1.2.1}$$

In these expressions, S_{FV}, S_{FS} and S_{VS} represent the film/vapor, film/substrate and and vapor/substrate interfaces. Here γ with the subscripts denote the corresponding surface energy density respectively. The total surface energy includes the film/vapor interface energies and substrate energies. Assume γ_{FS}, γ_{VS} are constants, while $\gamma_{FV} = \gamma(\mathbf{n})$, choose a bounded domain with dimensions $L_x \times L_y$ on the substrate,

then the total surface energy of the bounded system is given as

$$
\begin{aligned}
W &= \iint_{S_{FV}} \gamma_{FV} \, dS_{FV} + \iint_{S_{FS}} \gamma_{FS} \, dS_{FS} + \iint_{S_{VS}} \gamma_{VS} \, dS_{VS} \\
&= \iint_{S} \gamma(\mathbf{n}) \, dS + A(\Gamma)\gamma_{FS} + (L_x L_y - A(\Gamma))\gamma_{VS} \\
&= \iint_{S} \gamma(\mathbf{n}) \, dS + (\gamma_{FS} - \gamma_{VS})A(\Gamma) + L_x L_y \gamma_{VS}.
\end{aligned}
\tag{1.2.2}
$$

Here Γ is the contact line and $A(\Gamma)$ represents the area enclosed by Γ on the substrate. Since the term $L_x L_y \gamma_{VS}$ is fixed as a constant, thus we can always omit it and simplify the total energy as

$$
W = \iint_{S} \gamma(\mathbf{n}) \, dS + (\gamma_{FS} - \gamma_{VS})A(\Gamma).
\tag{1.2.3}
$$

Unlike liquid dewetting, surface diffusion is the dominant mass transport and plays the essential role in determining the shape evolution of solid thin films compared to other types of transport process: viscous flow, evaporation/condensation, and volume diffusion. The surface normal velocity governed by surface diffusion for isotropic materials ($\gamma = \gamma_0$ is a constant) can be mathematically described by Mullins [86] in the following

$$
v_n = B\nabla_s^2 \mathcal{H}, \quad \text{with} \quad B = \frac{D_s \gamma \Omega^2 \nu}{K_B T_e}.
\tag{1.2.4}
$$

Here D_s is the surface diffusivity, $k_B T_e$ is the thermal energy, Ω_0 represents the atomic volume, ν is the surface concentration of mobile atoms, $\mathcal{H}$ is the mean curvature of the surface. ∇_s is the surface gradient operator. In his derivation, the chemical potential is given as

$$
\mu = \Omega_0 \mathcal{H}.
\tag{1.2.5}
$$

Then by the Fick's first law, the flux of the surface atoms is given by

$$
J = -\frac{D_s \nu}{K_B T_e}\nabla_s \mu.
\tag{1.2.6}
$$

The normal velocity of the surface is given by multiplication of Ω_0 and the surface divergence of $-J$ [4],

$$
v_n = -\Omega_0 \nabla_s \cdot J = \frac{D_s \gamma \Omega^2 \nu}{K_B T_e}\nabla_s^2 \mathcal{H}.
\tag{1.2.7}
$$

The surface diffusion flow, governed by fourth order geometric equations, was analytically investigated for the existence in two dimensions [47,54,93]. They showed the local existence, regularity and uniqueness of the solution for an initial smooth curve and global existence for small perturbation of circles. Moreover, Escher et.al [48] extended the theories to the three-dimensional hypersurfaces.

One of the fundamental properties for surface diffusion flow is the conservation of the volume enclosed by the closed curves or surfaces. Besides, the arc length of the closed curves or area of the closed surfaces is decreasing under the surface diffusion flow. Actually, motion by surface diffusion can be regarded as the H^{-1} gradient flow for the energy functional [29]. Eq. (1.2.4) can be extended to the anisotropic case by replacing the mean curvature $\mathcal{H}$ with weighted mean curvature $\mathcal{H}_\gamma$ [115], which is defined as

$$\mathcal{H}_\gamma = \nabla_s \cdot \boldsymbol{\xi}, \tag{1.2.8}$$

with $\boldsymbol{\xi}$ denoting the Cahn-Hoffman vector.

1.2.3   Contact line migration

In solid-state dewetting, the intersection of the thin film, vapor and substrate produces contact line, see Fig. 1.6. Thus the migration for the contact line becomes an additional kinetic feature for solid-state dewetting, in addition to the surface diffusion flow.

When two immiscible fluids are placed on a solid substrate, the intersection of the two fluid phases with the substrate forms a contact line. The moving contact line problems for fluid mechanics have been widely studied in recent years [7, 37, 96–98, 100–103, 119]. In polycrystalline materials, similar problems have also been discussed and studied in grain boundary systems for the migration of triple lines or junctions [32, 55, 56, 82, 95, 118, 134].

For solid-state dewetting with isotropic surface energy, the equilibrium config-uration for the static contact line is the same as that in fluid mechanics or grain
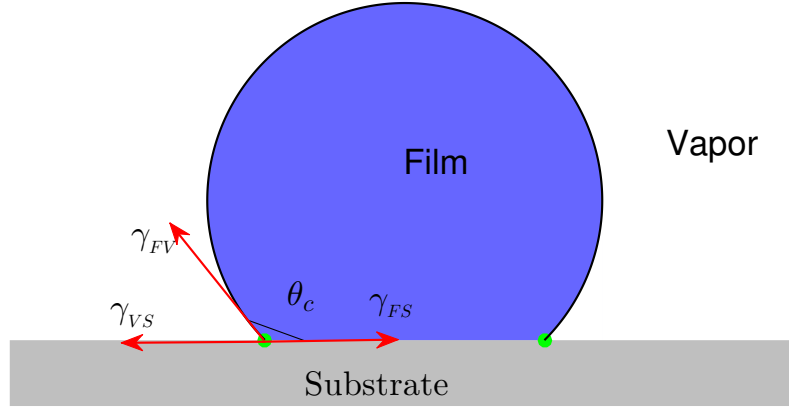
Figure 1.7: The cross-section profile of the equilibrium shape of a solid-thin film on a substrate.

boundaries, where the equilibrium contact angle (see Fig. 1.7) is described by the Young-Dupree equation [131]

$$\gamma_{VS} = \gamma_{FS} + \gamma_{FV} \cos \theta_c. \tag{1.2.9}$$

Here θ_c is the static contact angle on the contact line. The static contact line condition (Eq. (1.2.9)) has been widely adopted as the boundary condition for the dynamic sharp interface model [41, 111, 125]. The static contact line condition can be extended to the anisotropic case in two dimensions [9, 120]

$$\gamma_{VS} = \gamma_{FS} + \gamma(\theta_c) \cos \theta_c - \gamma'(\theta_c) \sin \theta_c, \tag{1.2.10}$$

where $\gamma_{FV} = \gamma(\theta)$ with θ representing the angle made by the normal vector of the interface with respect to the $+y$ direction. Similar static boundary conditions for the contact line have also been proposed for phase field model [46, 66].

When the static contact line condition is coupled as the boundary condition for the dynamic model, the contact angle is assumed to be fixed at its equilibrium value during the evolution. This assumption is reasonable when the thin film approaches the equilibrium shape. However, experimental and atomistic simulations for fluid

mechanics and grain boundary migrations [55, 56, 82, 95, 100, 102, 118] demonstrate that the contact angle need not be in equilibrium. This deviation from the equilibrium angle could be explained by considering the atomic structure of the contact line itself. A finite mobility of the contact line implies this deviation, while infinite mobility implies that the contact angle is always at its equilibrium value. Thus, instead of treating the static contact line condition as a boundary condition, the contact line mobility was introduced recently with a relaxation kinetic (see Eq. (1.4.2b) and Eq. (1.4.2c))for the contact point positions in two dimensions [67, 120]. Some other treatments for the motion of the contact line have been presented by Dornel *et al.* [40] and Klinger *et al.* [72, 73].

1.3 Equilibrium shapes

The equilibrium shape of solid-state dewetting is the minimization of the total surface energy while fixing the total volume of the thin film. The problem is mathematically expressed in the following

$$\min_{\Omega} \left(\iint_S \gamma(\mathbf{n}) \, dS + (\gamma_{FS} - \gamma_{VS}) A(\Gamma) \right) \quad \text{s.t.} \quad |\Omega| = \text{const.} \tag{1.3.1}$$

Here Ω is the region enclosed by the film/vapor interface and substrate. If the thin film is free standing and isolated, then the contribution to the total surface energy is only the film/vapor surface energy. In other words, S is a closed surface, and the minimization problem can be reduced to

$$\min_{\Omega} \left(\iint_S \gamma(\mathbf{n}) \, dS \right) \quad \text{s.t.} \quad |\Omega| = \text{const.} \tag{1.3.2}$$

1.3.1 Wulff construction

After Gibbs first proposed the equilibrium problem Eq. (1.3.2), Wulff presented a theory, known as Gibbs-Wulff theorem, for the equilibrium shape without proof in 1901 [126]. In the theory, he stated that the distance from the centre of the crystal shape to the face is proportional to the surface energy density of that face. Later,
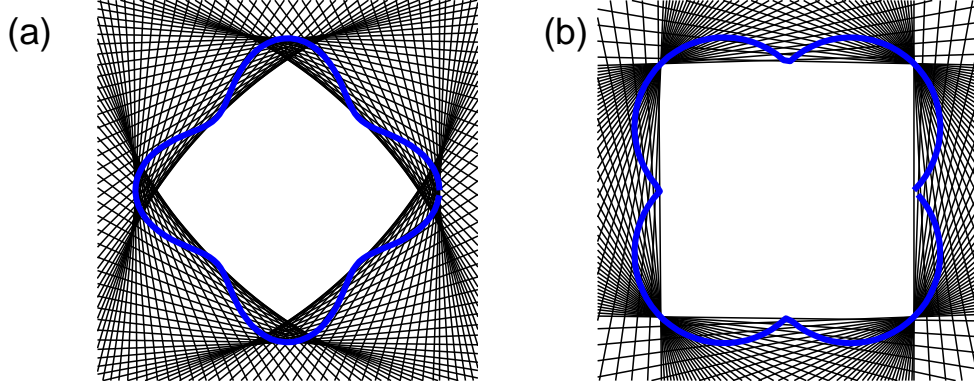
Figure 1.8: The Wulff construction for two-dimensional examples, where (a) $\gamma(\mathbf{n}) = 1 + 0.2(n_1^4 + n_2^4 - 6n_1^2 n_2^2)$, (b) $\gamma(\mathbf{n}) = |n_1| + |n_2|$. The blue line represents the γ-plot and all the black lines represent the lines that perpendicular to $\mathbf{n}$.

subsequent proofs of this theorem have been presented in many works [26, 38, 61, 62, 75, 81].

The equilibrium shape of the crystal can be geometrically constructed based on the γ-plot, and the finally obtained shape is called Wulff shape denoted by $\mathcal{W}$. The procedure can be stated as following four steps:

1. Carry out the polar plot of $\gamma(\mathbf{n})$ and obtain the γ-plot.

2. For each direction $\mathbf{n}$, draw a plane perpendicular to $\mathbf{n}$ with distance to the origin equaling to $\gamma(\mathbf{n})$.

3. The plane draw from the step 2 divides the space into two regions, and the region which is far from the origin is discarded.

4. When this has been done in all directions, the remaining convex region is called the Wulff shape.

Fig. 1.8, is a schematic illustration of the Wulff construction in two dimensions for

two anisotropies. In Fig. 1.8(b), $\gamma(\mathbf{n})$ is chosen as cusp/facet surface energy density $\gamma(\mathbf{n}) = |n_1| + |n_2|$. As a consequence, the corresponding Wulff shape consists of sharp corners and flat edges. Here $\gamma(\mathbf{n})$ is not differentiable where n_1, n_2 are changing their signs, which demonstrates that Wulff construction does not require the continuity and smoothness of $\gamma(\mathbf{n})$. Moreover, as can be seen from Fig. 1.8(a), the equilibrium shape obtained via Wulff construction has some missing orientations on the corners. This indicates that Wulff construction can be interpreted as a convexification of the γ-plot by removing all the unstable orientations. Herring presented a geometric criteria for occurrence of the missing orientation in the Wulff shape via Herring sphere construction [61], see Fig. 1.9. The construction is based on the γ-plot and can be stated as following:

1. Carry out the polar plot of $\gamma(\mathbf{n})$ and obtain the γ-plot.

2. For any orientation $\mathbf{n}$, construct a sphere that is tangent to the γ-plot at $\gamma(\mathbf{n})$ and passing through the origin.

3. If the sphere is totally inside the γ-plot, then orientation $\mathbf{n}$ appears on the equilibrium shape. Otherwise it is missing on the equilibrium shape.

(a)   Herring's tangent circle construction   (b) $1/\gamma$ -plot and tangent lines
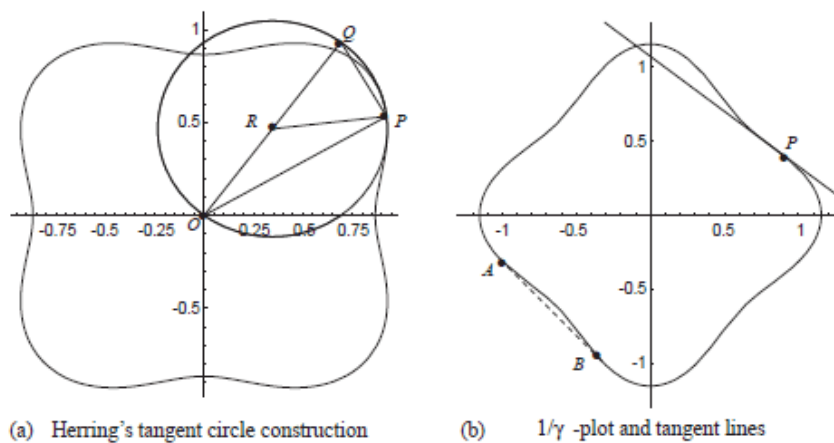
Figure 1.9: (a) A schematic illustration of Herring sphere construction. (b) $1/\gamma$-plot. Both figures are taken from [105].

If the tangent sphere is totally inside the γ-plot, it is equivalent to that the plane inverted from the sphere is totally outside the $1/\gamma-$plot. Thus the non-convexity of the $1/\gamma$-plot can also be used to test the occurrence of the missing orientation [105].

The Wulff shape and the Frank shape ($1/\gamma$-plot) can be mathematically expressed as

$$\mathcal{W} = \{\mathbf{x} \in \mathbb{R}^3 : \mathbf{x} \cdot \mathbf{n} \leq \gamma(\mathbf{n}), \quad \forall \mathbf{n} \in S^2\}. \tag{1.3.3a}$$

$$\mathcal{F} = \{\mathbf{x} \in \mathbb{R}^3 : \gamma(\frac{\mathbf{x}}{|\mathbf{x}|}) \leq 1)\}. \tag{1.3.3b}$$

As the magnitude of the normal component of $\boldsymbol{\xi}$ equals $\gamma(\mathbf{n})$ (see Eq. (3.3.6)), in view of the construction procedure of the Wulff shape, it is easy to know $\boldsymbol{\xi}$-plot shares similar geometry to the Wulff shape [65, 89]. Precisely speaking, the $\boldsymbol{\xi}$-plot is the mathematical representation of the boundary of the Wulff shape when no missing orientation occurs on the Wulff shape. On the other hand, when certain orientations are missing on the Wulff shape, the corresponding $\boldsymbol{\xi}$-plot will have ears and needed to be truncated in order to obtain the equilibrium shape. As depicted in Fig. 1.11, it shows the γ-plot, $1/\gamma$-plot and $\boldsymbol{\xi}$-plot for the cubic surface energy with different choices of the degree of anisotropy. When $a = 0.3$, the corresponding $1/\gamma$-plot is convex and the $\boldsymbol{\xi}$-plot is directly the boundary of the Wulff shape. When $a = 1.0$, the anisotropy becomes strong, $1/\gamma$-plot is no longer convex and the $\boldsymbol{\xi}$-plot forms some ears. We can summarise above results in Table. 1.1,

1.3.2   Winterbottom construction

Thin films are not always free standing and can be attached to a substrate. The Wulff construction is not able to obtain the equilibrium shape which minimizes the total surface energy in this case since the additional substrate energy should be included, see Eq. (1.3.1). Based on the thermodynamic approach, Winterbottom [123] derived that the equilibrium shape of problem defined in Eq. (1.3.1) is directly
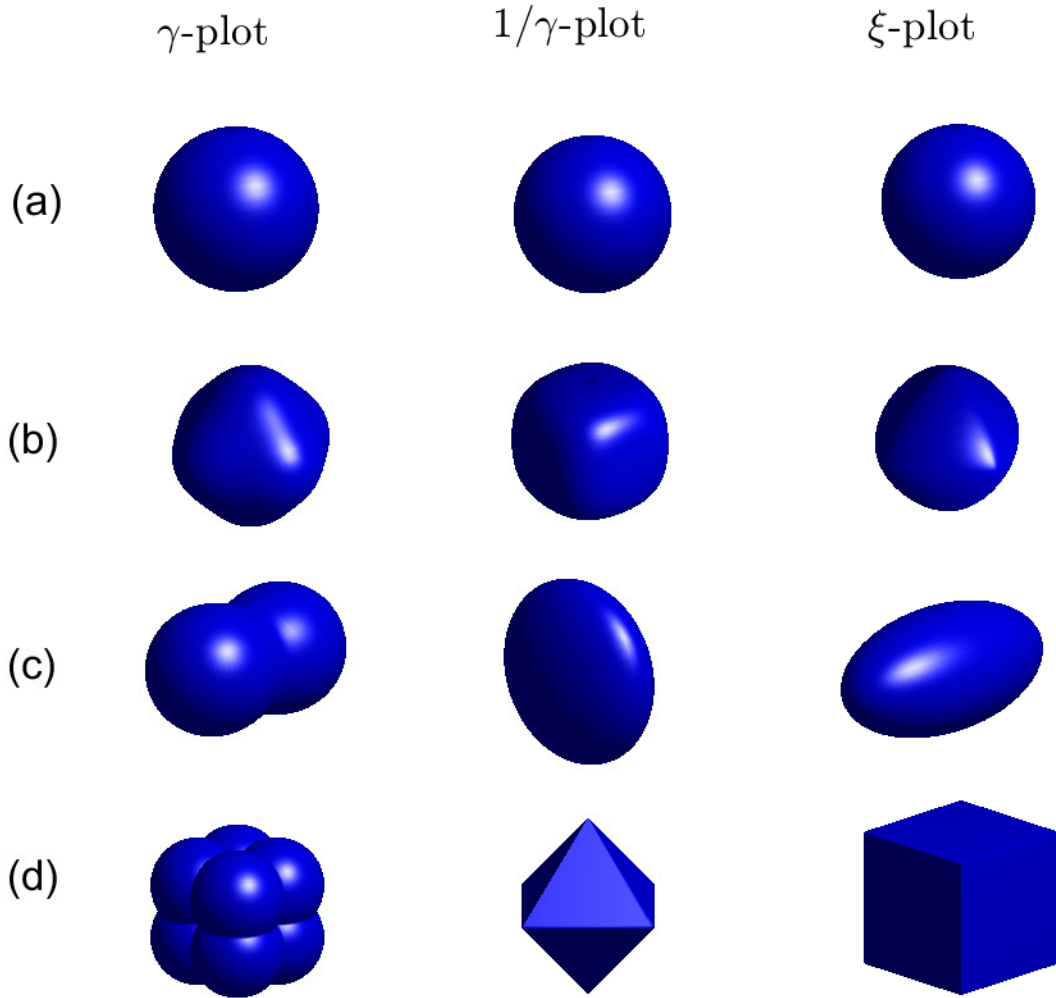
Figure 1.10: γ-plot, $1/\gamma$-plot and $\boldsymbol{\xi}$-plot for different anisotropies. (a) Isotropic surface energy $\gamma(\mathbf{n}) = 1$; (b) cubic anisotropic surface energy defined as $\gamma(\mathbf{n}) = 1 + a(n_1^4 + n_2^4 + n_3^4)$ with $a = 0.3$; (c) ellipsoidal surface energy $\gamma(\mathbf{n}) = \sqrt{a_1 n_1^2 + a_2 n_2^2 + a_3 n_3^2}$ with $a_1 = 4, a_2 = a_3 = 1$; (d) facet/cusp surface energy defined as $\gamma(\mathbf{n}) = |n_1| + |n_2| + |n_3|$ with smooth regularization in Eq. (1.1.9).

Table 1.1: Some distinguished properties between the strong anisotropy and weak anisotropy for $\gamma(\mathbf{n})$

$\gamma(\mathbf{n})$	Weak anisotorpy	Strong anisotropy
$\mathcal{W}$(Wulff shape)	no missing orientation	missing orientation exists
$\mathcal{F}(1/\gamma\text{-plot})$	convex	not convex
$\boldsymbol{\xi}$-plot	no ears	forming ears
Math criteria	$(\mathrm{H}_\gamma(\mathbf{n})\boldsymbol{\tau})\cdot\boldsymbol{\tau} > 0$	$(\mathrm{H}_\gamma(\mathbf{n})\boldsymbol{\tau})\cdot\boldsymbol{\tau} < 0$, for some $\boldsymbol{\tau}$
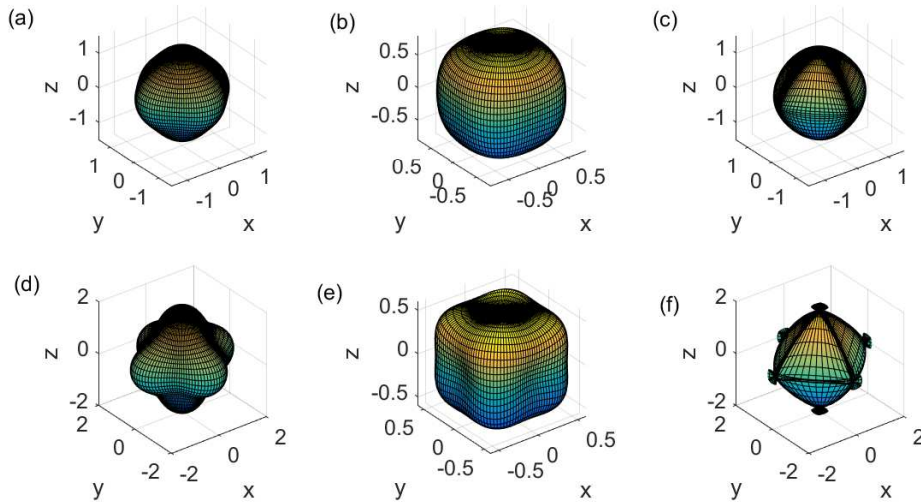
Figure 1.11: The γ-plot, $1/\gamma$-plot and $\boldsymbol{\xi}$-plot are shown in column 1,2,3 respectively. The first row is for weak anisotropy: $\gamma(\mathbf{n}) = 1 + 0.3(n_1^4 + n_2^4 + n_3^4)$ and the second row is for strong anisotropy: $\gamma(\mathbf{n}) = 1 + (n_1^4 + n_2^4 + n_3^4)$.
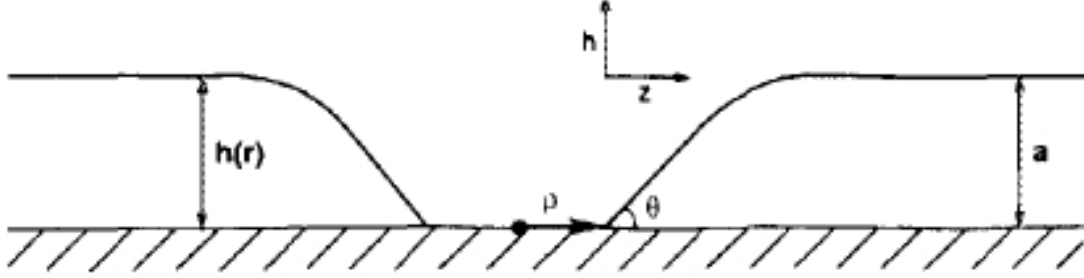
Figure 1.12: A schematic illustration of a cylindrically symmetric thin film with a hole of radius ρ on a substrate, the image is taken from [111].

the Wulff shape of a general surface tension γ^*, which is defined as

$$\gamma^*(\mathbf{n}) = \begin{cases} \gamma(\mathbf{n}), & \mathbf{n} \quad \text{corresponds to the film/vapor interface,} \\ \gamma_{FS} - \gamma_{VS}, & \text{otherwise.} \end{cases} \tag{1.3.4}$$

Thus the equilibrium shape for problem Eq. (1.3.1) can be obtained by cutting the Wulff shape of $\gamma(\mathbf{n})$ with the plane $z = \gamma_{VS} - \gamma_{FS}$.

1.4   Models and computational methods

The first sharp interface model for solid-state dewetting was proposed by Srolovitz and Safran [111] to investigate the hole growth under the assumption of isotropic surface energy and cylindrical symmetry. See Fig. 1.12, if the thin film profile is represented by $(r, h(r))$, in the small slop limit $(\frac{\partial h}{\partial r} \ll 1)$, the surface diffusion equation will reduce to

$$\frac{\partial h}{\partial t} = -\frac{B}{r}\frac{\partial}{\partial r}\Big[r\frac{\partial}{\partial r}\big[\frac{1}{r}\frac{\partial}{\partial r}(r\frac{\partial h}{\partial r})\big]\Big], \qquad r > \rho, \ t > 0, \tag{1.4.1}$$

with $B = \frac{D_s \nu \gamma_{FV} \Omega_0^2}{k_B T_e}$. For the contact points, the following boundary conditions were included

$$h(\rho, t) = -a, \tag{1.4.2a}$$

$$\frac{\partial h}{\partial r}(\rho, t) = \tan \theta_c, \tag{1.4.2b}$$

$$\frac{\partial^3 h}{\partial r^3}(\rho, t) + \frac{1}{\rho}\frac{\partial^2 h}{\partial t^2}(\rho, t) - \frac{1}{\rho^2}\frac{\partial h}{\partial r}(\rho, t) = 0, \tag{1.4.2c}$$

$$\lim_{r \to \infty} h(r, 0) = 0. \tag{1.4.2d}$$

The boundary conditions Eq. (1.4.2a) and Eq. (1.4.2d) come directly from the coordinate system. Eq. (1.4.2b) expresses the equilibrium contact angle at the boundary while Eq. (1.4.2c) implies there is no source or sink for matter at the contact point. Based on this model, they showed that large holes can migrates such that the edge retraction distance can be scaled by $t^{1/4}$ while small holes will shrink.

This model was then generalized to both the two-dimensional case [125] and three-dimensional case with cylindrical symmetry [42] in Lagrangian representation. Numerical results in [125] demonstrated that semi-infinite thin film undergoes a periodic mass shedding. Moreover, the authors showed numerically and analytically that the edge retraction distance could be scaled by $t^{2/5}$ at a later time for the semi-infinite film.

However, these models all start from the initial assumption that the surface energy is isotropic, thus the influence of the crystalline anisotropy on the morphological evolution for solid-state dewetting could be ignored. Besides, physical experiments [2, 127, 130, 139] have demonstrated that surface energy anisotropy could greatly influence the kinetics of solid-state dewetting, such as the faceting instability and corner instability. To include this crystalline anisotropy, recently some new models have been proposed, including the discrete model by Dornel [40], a kinetic Monte Carlo method [43, 92, 92] and the crystalline method [70, 138]. Some other models have been presented to study kinetics of hole growth [2, 139]. While the drawback of these approaches is that the evolution does not account for the full

anisotropic free energy of the system or do not represent a completely mathematical description.
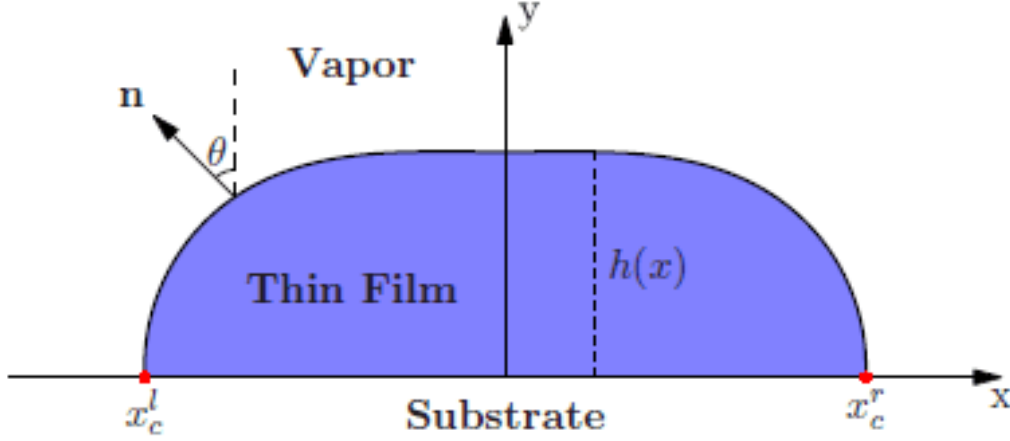
Figure 1.13: A schematic illustration of a solid thin film on a flat rigid substrate in two dimensions, this image is taken from [120].

More recently, based on thermodynamic variation, Wang et al. [120] derived rigorously a continuum sharp interface model for simulating the solid-state dewetting with weakly anisotropic surface energies. In their model, see Fig. 1.13, they assume the moving film/vapor interface is given by an open curve $\mathbf{X}(x(s,t), y(s,t))$, where s is the arc lenght and t is time. Then the dimensionless sharp interface model with weakly anisotropic surface energies in two dimensions can be described as

$$\frac{\partial \mathbf{X}}{\partial t} = \frac{\partial^2}{\partial s^2}\Big[\big(\gamma(\theta) + \gamma''(\theta)\big)\kappa\Big]\mathbf{n}. \tag{1.4.3}$$

They also proposed the following boundary conditions

$$y(x_c^l, t) = y(x_c^r, t) = 0, \tag{1.4.4a}$$

$$\frac{dx_c^l}{dt} = \eta(\gamma(\theta_d^l)\cos\theta_d^l - \gamma'(\theta_d^l)\sin\theta_d^l - \sigma), \tag{1.4.4b}$$

$$\frac{dx_c^r}{dt} = -\eta(\gamma(\theta_d^r)\cos\theta_d^r - \gamma'(\theta_d^r)\sin\theta_d^r - \sigma), \tag{1.4.4c}$$

$$\frac{\partial\mu}{\partial s}(x_c^l, t) = \frac{\partial\mu}{\partial s}(x_c^r, t) = 0. \tag{1.4.4d}$$

They introduced the relaxation kinetics Eqs. (1.4.4b),(1.4.4c) for the contact point position to replace the static contact angle equation Eq. (1.4.2b). The governing equations of the models belong to a new type of 4th-order geometric evolution partial differential equations about open curve interface tracking problems, which include anisotropic surface diffusion flow and contact line migration. With Willmore energy regularization, this model was then generallized to the strongly anisotropic case [67]. Besides, a new zero-curvature boundary condition was included to ensure the energy dissipation and wellposedness for the new 6th-order PDEs.

There is a long history in the numerical simulations of moving interfacial problems, and different numerical methods have been proposed in the literature for simulating the evolution of a closed curve/surface under mean curvature flow, surface diffusion flow, Willmore flow and so on. Some theories on the stable finite element method based on the graph representation of the surface [5, 34–36] were well developed, and corresponding error analysis was derived. However, the condition that the evolution surface can be explicitly parameterized on some base domain in $\mathbb{R}^n$ is so harsh to satisfy in most cases. Numerical methods that could be applied to more general curves/surfaces became more popular, such as the marker-particle methods [63, 78, 79], and the parametric finite element methods [6, 58, 94]. Among these methods, the main issue is that mesh quality during the curve/surface evolution could not be preserved and can deteriorate to make the scheme unstable; thus these algorithms need some kinds of mesh regularizations or re-meshing to maintain the mesh quality. Recently, this mesh issue has been well overcome by J.W. Barrett et al. [16, 17, 19, 20] with a new novel parametric finite element method, which has very good properties with respect to the distribution of the mesh points. Precisely, this scheme introduced a particular tangential motion for the mesh points such that these mesh points automatically moved tangentially over the surface and maintained good mesh properties. Therefore the discrete scheme can be performed without any mesh regularization. More recently, this scheme has been extended for simulating the grain boundary motion and application of thermal grooving and sintering [24, 134].

For solid-state dewetting, i.e., the evolution of an open curve/surface under surface diffusion flow and contact line migration, based on the previous mathematical models and numerical simulations, different numerical algorithms have been developed in the literature [8, 9, 40, 42, 67, 120, 125]. Generally these numerical methods can be classified into two main categories: interface-tracking methods and interface-capturing methods.

In the interface tracking methods, the moving interface is simulated by the sharp interface model. Numerically, it is explicitly represented by the computational mesh, and the mesh is updated when the interface evolves. The marker-particle methods [42, 125] were firstly presented for solving the sharp interface model of solid-state dewetting problems. This method is an explicit finite difference scheme, thus posing a very severe restriction on the numerical stability. Besides, at each time step, this algorithm requires re-meshing to redistribute the mesh points for the numerical stability. In consideration of these factors, the marker-particle method is tedious to perform and time-consuming, and the extension to the three dimensions is awkward. In [8], the authors recently have presented a parametric semi-implicit mixed finite element method for solving the sharp interface models, which they rigorously derived from the variation of the energy functionals. The numerical scheme they proposed is based on the automatically mesh-distributing scheme in [16], thus inheriting the good properties for mesh distribution. Their scheme can be applied to the case when the surface energy is weakly anisotropic and strongly anisotropic. Their ample numerical simulations and reports of some interesting theories on the two-dimensional solid-state dewetting demonstrate the parametric finite element method is powerful for the simulation of this problem.

The interface-capturing methods include the level set method and phase field method. They are based on an implicit representation of the surface by using the auxiliary function (level set function for level set method and phase function for phase field method) over a global domain, such that surface is implicitly captured via the zero contour of the auxiliary function. The interface-capturing methods to

compute the surface diffusion have been studied in the literature for level set methods [31,74,107] and phase field methods [13–15,25,124]. However, in the solid-state dewetting problem, in addition to the surface diffusion, the main difficulty for these interface-capturing methods lies in how to deal with the complex boundary conditions which result from the contact line migration. To our knowledge, the level set approach for solids-state dewetting problem is still a big challenge due to the complicated boundary conditions. On the other hand, Jiang *et al.* [66] first proposed a phase field model for simulating the solid-state dewetting with isotropic surface energy. The model includes the Cahn-Hilliard equation with degenerate mobility and nonlinear boundary conditions along the substrate. By making use of discrete cosine transforms (DCT) and discrete sine transforms (DST), they also proposed a highly efficient, stabilized, semi-implicit algorithm for solving the model. The numerical simulations obtained via this phase field approach showed qualitatively excellent agreement with physical experiments. The extended model for weakly anisotropic surface energy has been recently presented in [46] together with a matched asymptotic analysis for the sharp interface limit.

For comparisons between the interface-tracking and interface-capturing methods, each one has its own advantages and disadvantages. The interface-tracking methods via the sharp-interface model can always give the correct physics about surface diffusion together with contact line migration for the solid-state dewetting, and it is computationally efficient since it is one dimension less in space compared to the phase field model. But it is very tedious and troublesome to handle topological changes, e.g., pinch-off events. On the other hand, the interface-capturing methods via the phase field model can in general handle automatically topological changes and complicated geometries, but the sharp-interface limits of these phase field models are still unclear [76], and efficient and accurate simulations for surface diffusion and solid-state dewetting problems by using these models are still not well developed.

1.5   Scope of this thesis

Solid-state dewetting problems have been extensively studied with different models and numerical methods. However, there are still some limitations for these approaches. Firstly, the sharp interface model in two dimensions has been rigorously derived and an efficient parametric finite element method has been proposed to solve it. However, their models are not easy to be extended to the full three dimensions. Secondly, the extension of the parametric finite element method to three dimensions is not straightforward. This motives us to focus the following issues in this thesis,

- In chapter 2, we study the solid-state dewetting via thermodynamic variation in two dimensions as a start. The equilibrium shape and its linear stability has been well analysed. The sharp interface model with anisotropic surface energies is derived based on the thermodynamic variation via Cahn-Hoffman vector formulation. Efficient and stable numerical scheme is designed to solve the fourth-order geometric curve evolution equations.

- In chapter 3, based on the velocity speed method and shape derivatives, we derive the fully three-dimensional sharp interface model for solid-state dewetting with anisotropic surface energy and rigid flat substrate. The model includes the anisotropic surface diffusion flow and contact line migrations.

- In chapter 4, we present parametric finite element methods for solving the sharp the sharp interface model in both isotropic and anisotropic case. Extensive numerical results are presented to show the convergence of the numerical methods, the morphological characteristics for thin film during solid-state dewetting, and so on.

- In chapter 5, we extend our sharp interface model to the cases when the anisotropy is strong and and when the substrate is curved. Besides, the migration laws for the toroidal thin film on a flat substrate have been investigated and a reduced model will be obtained via Onsager's principle for describing

the migration.

The main works of this thesis are based on the papers [10, 11, 135, 136].

Chapter 2

Modeling and Simulation in Two Dimensions

The solid-state dewetting problems in two dimensions have been well studied recently [8, 9, 67, 120] via the sharp interface models. In these works, the authors presented the chemical potential in the form of a multiplication of the surface stiffness and the curve curvature, that is

$$\mu = (\gamma(\theta) + \gamma''(\theta))\kappa\,\Omega_0, \tag{2.0.1}$$

where $\gamma(\theta) + \gamma''(\theta)$ is the surface stiffness, κ is the curvature, Ω_0 is the atomic volume. Based on the expression, a generalized Winterbottom construction was proposed for the anisotropic particles on substrates via the variational approach, and conditions for the stable equilibrium were presented [9]. The theory was then numerically validated by solving these sharp interface models with the parametric finite element method [8]. Moreover, many physical phenomena of the solid-state dewetting have been investigated, such as the Rayleigh instability and power law retraction. However, the extensions of this mathematical representation for the chemical potential as well as the numerical methods to three dimensions are tedious although a similar representation is presented by Herring [60] for the three-dimensional Gibbs-Thompson

equation in local coordinates

$$\mu = \left[(\gamma + \frac{\partial^2 \gamma}{\partial n_x^2})\kappa_x + (\gamma + \frac{\partial^2 \gamma}{\partial n_y^2})\kappa_y\right]\Omega_0, \tag{2.0.2}$$

where κ_x, κ_y are the two principle curvatures, n_x, n_y are the two corresponding angles in the two principle directions.

Therefore in this chapter, based on the Cahn-Hoffman $\boldsymbol{\xi}$-vector, we will present a new approach to studying the solid-state dewetting in two dimensions, and this approach is easily generalised to the three-dimensional case. In addition, we will consider the equilibrium problems via the variational approach and predicate the equilibrium shape as well as its stability conditions. Based on this variation we can derive the dynamic, sharp interface model via the form of the Cahn-Hoffman $\boldsymbol{\xi}$-vector formulation. This model includes the surface diffusion flow and relaxed contact angle conditions for describing the motion of the interface curve and migrations of the contact points, respectively. Moreover, a variational formulation of the model is proposed, and then a new parametric finite element method is applied to solve it. The strongly anisotropic surface energy will also be considered via the Willmore energy regularization. Extensive numerical results will be shown afterwards.

2.1 Interfacial energy and thermodynamic variation

As illustrated in Fig. 2.1, in two dimensions, we consider that an open curve $\Gamma = \mathbf{X}(x(s),\ y(s))$, parameterized by the arc length s, which separates the vapor and the thin film, attaches on a flat rigid substrate ($x-$axis) with two contact points x_c^r and x_c^l. Here $\mathbf{n}$ is the unit normal vector that points to the vapor phase and $\boldsymbol{\tau}$ is the unit tangential vector. The total interfacial energy of the system can be written as

$$W(\Gamma) = \int_{\Gamma_{FV}} \gamma_{FV}\ d\Gamma_{FV} + \int_{\Gamma_{FS}} \gamma_{FS}\ d\Gamma_{FS} + \int_{\Gamma_{VS}} \gamma_{VS} d\Gamma_{VS}. \tag{2.1.1}$$
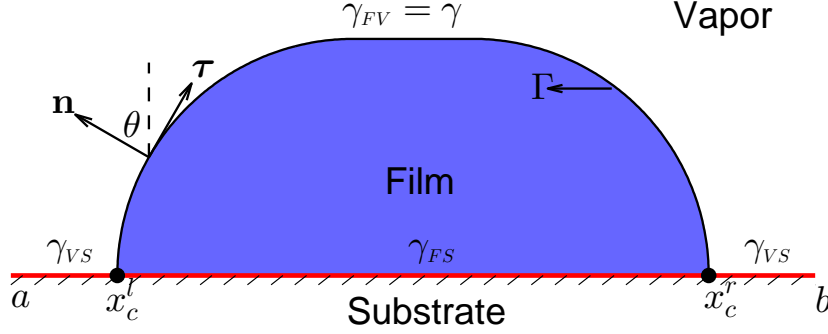
Figure 2.1: A schematic illustration of solid thin film on a rigid, flat substrate (x-axis) in two dimensions with two contact points x_c^l and x_c^r.

Here, $\Gamma_{FV} := \Gamma, \Gamma_{FS}$ and Γ_{VS} represent the film/vapor, film/substrate and vapor/substrate interface, respectively, and $\gamma_{FV}, \gamma_{FS}, \gamma_{VS}$ represent their corresponding surface energy densities (surface energy per unit length). For solid-state dewetting problems, we often assume that γ_{FS}, γ_{VS} are two constants, while $\gamma_{FV} = \gamma(\mathbf{n}) \in C^2(S^1)$ depends on the orientation of the film/vapor interface. By dropping off a constant part, the total interfacial energy can be simplified as the following form (still labeled as $W(\Gamma)$):

$$W(\Gamma) = \int_\Gamma \gamma(\mathbf{n}) \, ds - (\gamma_{VS} - \gamma_{FS})(x_c^r - x_c^l), \qquad (2.1.2)$$

where the first term refers to the film/vapor interfacial energy part, and the second term represents the substrate energy part. In the following, we will introduce a smooth vector-field perturbation method to obtain the first variation of the above energy functional with respect to the open curve Γ.

First, we introduce an independent parameter $\rho \in I = [0, 1]$ to parameterize a family of perturbed curves $\{\Gamma^\epsilon\}_{\epsilon \in [0, \epsilon_0]}$, where the parameter ϵ controls the amplitude of the perturbation and ϵ_0 is the maximum perturbation amplitude, i.e.,

$$\Gamma^\epsilon = \mathbf{X}(\rho, \epsilon) : [0, 1] \times [0, \epsilon_0] \to \mathbb{R}^2, \qquad (2.1.3)$$

and $\Gamma := \Gamma^0 = \mathbf{X}(\rho, 0)$. In order to calculate the variation of a shape functional, we

introduce a smooth perturbation vector-field as follows:

$$\mathbf{V}(\rho, \epsilon) = \frac{\partial \mathbf{X}(\rho, \epsilon)}{\partial \epsilon}, \quad \forall \epsilon \in [0, \epsilon_0], \tag{2.1.4}$$

and each point on the curve Γ is continuously deformed by the above equation defined by the perturbation vector-field $\mathbf{V}$. Note that if the vector-field $\mathbf{V}$ is smooth enough, the family of perturbed curves $\{\Gamma^\epsilon\}$ preserve the regularity of the original curve Γ: if Γ is of class C^k-curves, for any $\epsilon \in [0, \epsilon_0]$, Γ^ϵ is also of class C^k-curves.

Then, assume that given an arbitrary shape functional $F(\Gamma)$, we can define its first variation with respect to any smooth perturbation vector-field V as

$$\delta F(\Gamma; \mathbf{V}) = \lim_{\epsilon \to 0} \frac{F(\Gamma^\epsilon) - F(\Gamma)}{\epsilon}. \tag{2.1.5}$$

Lemma 2.1.1. *Assume that $\Gamma = \mathbf{X}(s) \in C^2([0, L]) \times C^2([0, L])$ is an open smooth curve with its two endpoints locating at $s = 0$ and $s = L$, where $s := s(\rho), \rho \in [0, 1]$ represents the arc length of the curve. If the shape functional $F(\Gamma) = \int_\Gamma \gamma(\mathbf{n}) \, ds$, then its first variation can be written as:*

$$\delta F(\Gamma; \mathbf{V}) = -\int_\Gamma [(\partial_s \boldsymbol{\xi})^\perp \cdot \mathbf{n}] (\mathbf{V}_0 \cdot \mathbf{n}) \, ds + \left[\boldsymbol{\xi}^\perp \cdot \mathbf{V}_0 \right] \Big|_{s=0}^{s=L}, \tag{2.1.6}$$

where $\perp$ represents the clockwise rotation of a vector by 90 degrees, $\boldsymbol{\xi} = \boldsymbol{\xi}(\mathbf{n})$ is the Cahn-Hoffman vector and the deformation velocity is denoted as $\mathbf{V}_0 = \mathbf{V}(\rho, 0)$, and $\mathbf{V}_0 \cdot \mathbf{n}$ represents the deformation velocity along the outer normal direction of the interface.

Proof. We first extend the definition domain of the surface energy density function $\gamma(\mathbf{n})$ from unit vectors $\mathbf{n}$ to arbitrary non-zero vectors $\mathbf{p}$ as below

$$\hat{\gamma}(\mathbf{p}) = |\mathbf{p}| \gamma(\frac{\mathbf{p}}{|\mathbf{p}|}), \quad \forall \mathbf{p} \in \mathbb{R}^2 \backslash \{\mathbf{0}\}, \tag{2.1.7}$$

where $\hat{\gamma}(\mathbf{p})$ extends γ as a homogeneous function of the first degree.

The perturbed curve is labeled as $\Gamma^\epsilon := \mathbf{X}(\rho, \epsilon)$. By using the identity $\partial_\rho s = |\partial_\rho \mathbf{X}|$, we can have the following expression

$$F(\Gamma^\epsilon) = \int_0^1 \gamma(\mathbf{n}^\epsilon) |\partial_\rho \mathbf{X}(\rho, \epsilon)| \, d\rho. \tag{2.1.8}$$

Note that the following expressions hold:

$$\boldsymbol{\tau}^\epsilon = \frac{\partial_\rho \mathbf{X}(\rho, \epsilon)}{\partial_\rho s(\rho, \epsilon)}, \qquad \mathbf{n}^\epsilon = -(\boldsymbol{\tau}^\epsilon)^\perp = -\frac{[\partial_\rho \mathbf{X}(\rho, \epsilon)]^\perp}{|\partial_\rho \mathbf{X}(\rho, \epsilon)|},$$

$$\nabla \hat{\gamma}(\mathbf{p}) \cdot \mathbf{p} = \hat{\gamma}(\mathbf{p}), \qquad \mathbf{V}_0 = \mathbf{V}(\rho, 0) = \partial_\epsilon \mathbf{X}(\rho, \epsilon)\Big|_{\epsilon=0}. \tag{2.1.9}$$

Denote $\mathbf{X} = \mathbf{X}(\rho, 0)$, then we can take the Taylor expansion for the following terms at $\epsilon = 0$,

$$|\partial_\rho \mathbf{X}(\rho, \epsilon)| = |\partial_\rho \mathbf{X}| + \frac{\partial_\rho \mathbf{X} \cdot \partial_\rho \mathbf{V}_0}{|\partial_\rho \mathbf{X}|}\epsilon + O(\epsilon^2), \tag{2.1.10a}$$

$$\mathbf{n}^\epsilon = \mathbf{n} + \Big[\frac{\partial_\rho \mathbf{X} \cdot \partial_\rho \mathbf{V}_0}{|\partial_\rho \mathbf{X}|^3}(\partial_\rho \mathbf{X})^\perp - \frac{(\partial_\rho \mathbf{V}_0)^\perp}{|\partial_\rho \mathbf{X}|}\Big]\epsilon + O(\epsilon^2), \tag{2.1.10b}$$

$$\gamma(\mathbf{n}^\epsilon) = \gamma(\mathbf{n}) + \nabla \hat{\gamma}(\mathbf{n}) \cdot \Big[\frac{\partial_\rho \mathbf{X} \cdot \partial_\rho \mathbf{V}_0}{|\partial_\rho \mathbf{X}|^3}(\partial_\rho \mathbf{X})^\perp - \frac{(\partial_\rho \mathbf{V}_0)^\perp}{|\partial_\rho \mathbf{X}|}\Big]\epsilon + O(\epsilon^2). \tag{2.1.10c}$$

The first variation of the shape functional can be written as

$$\delta F(\Gamma; \mathbf{V}) = \lim_{\epsilon \to 0} \frac{F(\Gamma^\epsilon) - F(\Gamma)}{\epsilon} = \int_0^1 \lim_{\epsilon \to 0} \frac{1}{\epsilon}\Big[\gamma(\mathbf{n}^\epsilon)|\partial_\rho \mathbf{X}(\rho, \epsilon)| - \gamma(\mathbf{n})|\partial_\rho \mathbf{X}(\rho, 0)|\Big]\, d\rho.$$

By substituting Eqs. (2.1.10a) - (2.1.10c) into the above equation, and using the identity $\nabla \hat{\gamma}(\mathbf{n}) \cdot \mathbf{n} = \gamma(\mathbf{n})$, we can obtain

$$\begin{aligned}
\delta F(\Gamma; \mathbf{V}) &= \int_0^1 \nabla \hat{\gamma}(\mathbf{n}) \cdot \Big[\frac{\partial_\rho \mathbf{X} \cdot \partial_\rho \mathbf{V}_0}{|\partial_\rho \mathbf{X}|^3}(\partial_\rho \mathbf{X})^\perp - \frac{(\partial_\rho \mathbf{V}_0)^\perp}{|\partial_\rho \mathbf{X}|}\Big]|\partial_\rho \mathbf{X}|\, d\rho \\
&\quad + \int_0^1 \gamma(\mathbf{n})\frac{\partial_\rho \mathbf{X} \cdot \partial_\rho \mathbf{V}_0}{|\partial_\rho \mathbf{X}|}\, d\rho \\
&= -\int_0^1 \nabla \hat{\gamma}(\mathbf{n}) \cdot (\partial_\rho \mathbf{V}_0)^\perp\, d\rho = \int_0^1 \nabla \hat{\gamma}(\mathbf{n})^\perp \cdot \partial_\rho \mathbf{V}_0\, d\rho. \tag{2.1.11}
\end{aligned}$$

By using integration by parts, and Cahn-Hoffman vector $\boldsymbol{\xi} = \nabla \hat{\gamma}(\mathbf{n})$, we can obtain

$$\begin{aligned}
\delta F(\Gamma; \mathbf{V}) &= -\int_0^1 (\partial_\rho \boldsymbol{\xi})^\perp \cdot \mathbf{V}_0\, d\rho + \Big[\boldsymbol{\xi}^\perp \cdot \mathbf{V}_0\Big]\Big|_{\rho=0}^{\rho=1} \\
&= -\int_\Gamma (\partial_s \boldsymbol{\xi})^\perp \cdot \mathbf{V}_0\, ds + \Big[\boldsymbol{\xi}^\perp \cdot \mathbf{V}_0\Big]\Big|_{s=0}^{s=L}. \tag{2.1.12}
\end{aligned}$$

Making use of the expressions: $\partial_s \boldsymbol{\xi} \parallel \boldsymbol{\tau}$ and $(\partial_s \boldsymbol{\xi})^\perp \parallel \mathbf{n}$, we can immediately obtain the conclusion from the above Eq. (2.1.12). $\qquad \square$

By using the above Lemma. 2.1.1, we can easily obtain the following theorem about the first variation of the free energy functional (2.1.2):

Theorem 2.1.1. *The first variation of the free energy functional* (2.1.2) *used in solid-state dewetting problems with respect to any smooth deformation field* $\mathbf{V}$ *can be written as:*

$$\delta W(\Gamma; \mathbf{V}) = -\int_{\Gamma} [(\partial_s \boldsymbol{\xi})^{\perp} \cdot \mathbf{n}] \, (\mathbf{V}_0 \cdot \mathbf{n}) \, ds + \left[\left(\xi_2 - (\gamma_{VS} - \gamma_{FS}) \right) (\mathbf{V}_0 \cdot \mathbf{e}_1) \right] \Big|_{s=0}^{s=L}, \quad (2.1.13)$$

where $\boldsymbol{\xi} = (\xi_1, \xi_2)$, $\mathbf{e}_1 = (1, 0)$ *represents the unit vector along the x-coordinate (or the substrate line), and* $(\mathbf{V}_0 \cdot \mathbf{e}_1) \Big|_{s=0}^{s=L}$ *represents the deformation velocity along the substrate line at two contact points.*

Proof. For solid-state dewetting problems, as shown in Fig. 2.1, the contact points must move along the substrate. Under the assumption that the substrate is flat, the velocity field $\mathbf{V}(\rho, 0)$ at the two contact points (i.e., the two endpoints of the curve Γ) must satisfy the constraints: $\mathbf{V}_0(s = 0) \parallel \mathbf{e}_1$ and $\mathbf{V}_0(s = L) \parallel \mathbf{e}_1$.

By using the above Eq. (2.1.6), and $\boldsymbol{\xi}^{\perp} = (\xi_2, -\xi_1)$, we can obtain

$$
\begin{aligned}
\delta W(\Gamma; \mathbf{V}) &= -\int_{\Gamma} [(\partial_s \boldsymbol{\xi})^{\perp} \cdot \mathbf{n}] \, (\mathbf{V}_0 \cdot \mathbf{n}) \, ds + \left[(\boldsymbol{\xi}^{\perp} \cdot \mathbf{e}_1) \, (\mathbf{V}_0 \cdot \mathbf{e}_1) \right] \Big|_{s=0}^{s=L} \\
&\quad - \left[(\gamma_{VS} - \gamma_{FS}) \, (\mathbf{V}_0 \cdot \mathbf{e}_1) \right] \Big|_{s=0}^{s=L}, \\
&= -\int_{\Gamma} [(\partial_s \boldsymbol{\xi})^{\perp} \cdot \mathbf{n}] \, (\mathbf{V}_0 \cdot \mathbf{n}) \, ds + \left[\left(\xi_2 - (\gamma_{VS} - \gamma_{FS}) \right) (\mathbf{V}_0 \cdot \mathbf{e}_1) \right] \Big|_{s=0}^{s=L}.
\end{aligned}
$$

$\square$

2.2 Equilibrium and its stability condition

Physical systems tend to move towards their equilibriums in the direction of decreasing the total energy. This principle can be mathematically formulated via the thermodynamic variation. The equilibrium shape equation can be obtained via the first variation of the energy functional. The second variation of the energy is often used to study the stability. So in this section, we will consider the equilibrium shape of solid-state dewetting via the thermodynamic variation approach.

2.2.1   Equilibrium shapes

The solid-state dewetting equilibrium problem can be written as a minimization of the total surface energy subject to the constraint of constant volume:

$$\min_{\Omega} W := \int_{\Gamma} \gamma(\mathbf{n}) ds - \sigma(x_c^r - x_c^l) \quad s.t. \quad |\Omega| = \text{const.} \tag{2.2.1}$$

We first give a lemma about the first variation of area of the enclosed region Ω.

Lemma 2.2.1. *Suppose* $\Gamma = \mathbf{X}(s) = (x(s), y(s)) \in C^1([0, L]) \times C^1([0, L])$ *is an open curve with two endpoints attached to the $x-$axis. Let A denote the total area enclosed by Γ and the x-axis, then we have*

$$A(\Gamma) = \int_{\Gamma} y \partial_s x \, ds, \qquad dA(\Gamma; \mathbf{V}) = \int_{\Gamma} \mathbf{V}_0 \cdot \mathbf{n} \, ds. \tag{2.2.2}$$

Proof. The enclosed area can be obtain based on the divergence theorem

$$A(\Gamma) = \frac{1}{2} \int_{\Gamma} \mathbf{X} \cdot \mathbf{n} \, ds. \tag{2.2.3}$$

The unit normal vector can be expressed as $\mathbf{n} = (-\partial_s y, \partial_s x)$. Besides, noting that $y(0) = y(L) = 0$, then integrating by part, we can obtain

$$
\begin{aligned}
A(\Gamma) &= \frac{1}{2} \int_{\Gamma} (y \partial_s x - x \partial_s y) \, ds \\
&= \frac{1}{2} \int_{\Gamma} y \partial_s x \, ds + \frac{1}{2} \int_{\Gamma} \partial_s x y \, ds - (xy)_{s=0}^{s=L} = \int_{\Gamma} y \partial_s x \, ds.
\end{aligned} \tag{2.2.4}
$$

Now based on the perturbation defined in Eq. (2.1.3) and the corresponding parametrization of Γ^ε on $[0, 1]$, we have

$$
\begin{aligned}
dA(\Gamma; \mathbf{V}) &= \lim_{\varepsilon \to 0} \frac{A(\Gamma^\varepsilon) - A(\Gamma)}{\varepsilon} = \int_0^1 \lim_{\varepsilon \to 0} \frac{1}{\varepsilon} [y(\rho, \varepsilon) \partial_\rho \mathbf{x}(\rho, \varepsilon) - y(\rho, 0) \partial_\rho x(\rho, 0)] \, d\rho \\
&= \int_0^1 V_y \partial_\rho x \, d\rho - \int_0^1 V_x \partial_\rho y \, d\rho + y V_x \Big|_{\rho=0}^{\rho=1} = \int_{\Gamma} \mathbf{V}_0 \cdot \mathbf{n} \, ds.
\end{aligned} \tag{2.2.5}
$$

This directly gives the first variation of enclosed area.   □

The equilibrium shape is obtained when the first variation of the total surface energy vanishes, thus we have the following lemma from [9]:

Definition 2.2.1 (Equilibrium shapes [9])**.** *If an open curve* $\Gamma_e = (x(s), y(s)) \in C^2([0, L]) \times C^2([0, L])$, *where L is the arc length of Γ_e, satisfies $dW(\Gamma_e; \mathbf{V}) \equiv 0$, where $\mathbf{V}$ is a smooth vector field satisfying $\int_{\Gamma_e} \mathbf{n} \cdot \mathbf{V}_0 \, ds \equiv 0$, then it is the equilibrium shape of solid-state dewetting problem* (2.2.1)*.*

Based on the definition of equilibrium shape of solid state dewetting problem [9], we have

Lemma 2.2.2. *Assume there is a curve satisfies $\Gamma_e = (x(s), y(s)) \in C^2[0, L]$, where L is the arc length of Γ_e. Then if Γ_e is an equilibrium shape of solid state dewetting problem* (2.2.1) *if and only if the following two conditions are satisfied:*

$$-\partial_s(\boldsymbol{\xi})^{\perp} \cdot \mathbf{n} = C, \quad \forall s \in [0, L], \tag{2.2.6}$$

$$\xi_2\Big|_{s=0} - \sigma = 0, \quad \xi_2\Big|_{s=L} - \sigma = 0. \tag{2.2.7}$$

Here the constant C is determined by the total volume of the thin film.

Proof. The procedure of the proof for this lemma is similar to the proof in [9], so we omit it. $\square$

The above lemma is expressed in the form of the Cahn-Hoffman $\boldsymbol{\xi}$- vector, which is the same as the lemma given in [9]. Eq. (2.2.6) could be written in a different expression

$$\nabla_s \cdot \boldsymbol{\xi} = (\partial_s \boldsymbol{\xi}) \cdot \boldsymbol{\tau} = C, \quad \forall s \in [0, L], \tag{2.2.8}$$

which can be extended to the three-dimensional case directly, see Chapter 3. Eq. (2.2.7) can be regarded as the anisotropic Young equation. If the interfacial energy is isotropic, we obain that $\boldsymbol{\xi} = \mathbf{n}$, and on the boundary (two contact points), Eq. (2.2.7) collapses to $\cos \theta_c = \sigma$ with θ_c denoting the contact angle.

2.2.2 Stability condition

In absence of the substrate, the equilibrium shape that minimise the energy functional $\int_{\Gamma} \gamma(\mathbf{n}) \, ds$ while preserving the total volume is given by Wulff shape [126].

When $\gamma(\mathbf{n}) = 1$, this problem reduces to the well-known isopermetric problem. The stability of the corresponding equilibrium shape: sphere has been proved [12, 121] based on the second variational approach. The stability of Wulff shape for general anisotropy has been widely studied [87, 122]. The result can be concluded as : if the anisotropy satisfies the convexity assumption, that is

$$\mathrm{H}_\gamma(\mathbf{p})\mathbf{q} \cdot \mathbf{q} \geq \lambda_0|\mathbf{q}|, \quad \forall \mathbf{q} \in \mathrm{S}^1, \mathbf{p} \cdot \mathbf{q} = 0, \tag{2.2.9}$$

where λ_0 is a positive constant, then only closed, orientated, stable critical points of the energy functional is Wulff shape, up to scaling and translation. However, when the convexity condition is not satisfied, we knew that ears appear in the Wulff envelope ($\boldsymbol{\xi}$-plot) as some orientations are missing on the Wulff shape. The Wulff envelope truncated by a flat substrate line could produce multiple equilibrium shapes [67]. On the other hand, the condition for the stable equilibrium is that its second variation of the energy functional is non-negative for all variations that preserving the area. So in this section, we perform the second variation of the energy functional and derive the stability conditions of the equilibrium shape for solid-state dewetting. For simplicity, and avoiding using the Jacobia operator for a vector varaition field, we assume the perturbation is expressed in one parameter, that is

$$\mathbf{X}(\rho, \varepsilon) = \mathbf{X}(\rho, 0) + \varepsilon \mathbf{X}^1(\rho). \tag{2.2.10}$$

Thus we have $V_0 = \mathbf{X}^1(\rho)$, and we can define the second variation

$$d^2 F(\Gamma; \mathbf{V}) = \frac{d^2 F(\Gamma^\varepsilon)}{d\varepsilon^2}\bigg|_{\varepsilon=0}. \tag{2.2.11}$$

We have the following lemma for the second variation.

Lemma 2.2.3. *Suppose* $\Gamma = \mathbf{X}(s) \in C^2([0, L]) \times C^2([0, L])$ *is an open curve where* $s(0 \leq s \leq L)$ *is the arc length and assume the perturbation is given by.* (2.2.10). *Let* $F(\Gamma) = \int_\Gamma \gamma(\mathbf{n}) ds$, *then we have*

$$d^2 F(\Gamma; \mathbf{V}) = \int_\Gamma \mathrm{H}_\gamma(\mathbf{n}) \boldsymbol{\tau} \cdot \boldsymbol{\tau} (\partial_s \mathbf{V}_0 \cdot \mathbf{n})^2 \, ds, \tag{2.2.12}$$

where $\boldsymbol{\tau}$ *is the unit tangential vector.*

Proof. Here we can write the second variation as

$$d^2 F(\Gamma; \mathbf{V}) = \frac{d^2}{d\varepsilon^2}\bigg|_{\varepsilon=0} \int_0^1 \gamma(\mathbf{n}^\varepsilon)|\partial_\rho \mathbf{X}(\rho, \varepsilon)| \, d\rho. \tag{2.2.13}$$

Expand $\Gamma(\mathbf{n}^\varepsilon)$ and $|\partial_\rho \mathbf{X}(\rho, \varepsilon)|$ up to second order under the perturbation defined in Eq. (2.2.10), we obtain (see Appendix. A for detailed derivation),

$$\frac{|\partial_\rho \mathbf{X}(\rho, \varepsilon)|}{|\partial_\rho \mathbf{X}|} = 1 + (\boldsymbol{\tau} \cdot \partial_s \mathbf{V}_0)\varepsilon + \frac{1}{2}\big(\partial_s \mathbf{V}_0 \cdot \partial_s \mathbf{V}_0 - (\boldsymbol{\tau} \cdot \partial_s \mathbf{V}_0)^2\big)\varepsilon^2 + O(\varepsilon^3), \tag{2.2.14a}$$

$$\begin{aligned}
\gamma(\mathbf{n}^\varepsilon) = \gamma(\mathbf{n}) &+ \Big[-\gamma(\mathbf{n})(\boldsymbol{\tau} \cdot \partial_s \mathbf{V}_0) - \nabla\hat\gamma(\mathbf{n}) \cdot (\partial_s \mathbf{V}_0)^\perp\Big]\varepsilon \\
&+ \frac{1}{2}\Big[2\nabla\hat\gamma(\mathbf{n}) \cdot (\partial_s \mathbf{V}_0 \cdot \boldsymbol{\tau})(\partial_s \mathbf{V}_0)^\perp - \gamma(\mathbf{n})(\partial_s \mathbf{V}_0 \cdot \partial_s \mathbf{V}_0) \\
&+ 3\gamma(\mathbf{n})(\boldsymbol{\tau} \cdot \partial_s \mathbf{V}_0)^2 + H_\gamma(\mathbf{n})(\partial_s \mathbf{V}_0)^\perp \cdot (\partial_s \mathbf{V}_0)^\perp\Big]\varepsilon^2 + O(\varepsilon^3).
\end{aligned} \tag{2.2.14b}$$

Extracting all $O(\varepsilon)$ terms of $\gamma(\mathbf{n}^\varepsilon)|\partial_\rho \mathbf{X}(\rho, \varepsilon)|$, we get

$$\begin{aligned}
\frac{d^2}{d\varepsilon^2}&\Big(\gamma(\mathbf{n}^\varepsilon)|\partial_\rho \mathbf{X}(\rho, \varepsilon)|\Big)\bigg|_{\varepsilon=0} \\
&= -2|\partial_\rho \mathbf{X}|\Big[\gamma(\mathbf{n})(\boldsymbol{\tau} \cdot \partial_s \mathbf{V}_0) + \nabla\hat\gamma(\mathbf{n}) \cdot (\partial_s \mathbf{V}_0)^\perp\Big](\boldsymbol{\tau} \cdot \partial_s \mathbf{V}_0) \\
&\quad + |\partial_\rho \mathbf{X}|\gamma(\mathbf{n})\Big[\partial_s \mathbf{V}_0 \cdot \partial_\rho \mathbf{V}_0 - (\boldsymbol{\tau} \cdot \partial_s \mathbf{V}_0)^2\Big] \\
&\quad + |\partial_\rho \mathbf{X}|\Big[2\nabla\hat\gamma(\mathbf{n}) \cdot (\partial_s \mathbf{V}_0 \cdot \boldsymbol{\tau})(\partial_s \mathbf{V}_0)^\perp - \gamma(\mathbf{n})(\partial_s \mathbf{V}_0 \cdot \partial_s \mathbf{V}_0) \\
&\quad + 3\gamma(\mathbf{n})(\boldsymbol{\tau} \cdot \partial_s \mathbf{V}_0)^2 + H_\gamma(\mathbf{n})(\partial_s \mathbf{V}_0)^\perp \cdot (\partial_s \mathbf{V}_0)^\perp\Big] \\
&= H_\gamma(\mathbf{n})(\partial_s \mathbf{V}_0)^\perp \cdot (\partial_s \mathbf{V}_0)^\perp|\partial_\rho \mathbf{X}|.
\end{aligned} \tag{2.2.15}$$

The last equality of above equations is due to a simple reduction. Thus we can directly obtain that

$$\begin{aligned}
d^2 F(\Gamma; \mathbf{V}) &= \int_0^1 H_\gamma(\mathbf{n})(\partial_s \mathbf{V}_0)^\perp \cdot (\partial_s \mathbf{V}_0)^\perp|\partial_\rho \mathbf{X}| \, d\rho \\
&= \int_\Gamma H_\gamma(\mathbf{n})(\partial_s \mathbf{V}_0)^\perp \cdot (\partial_s \mathbf{V}_0)^\perp \, ds.
\end{aligned} \tag{2.2.16}$$

Express $(\partial_s \mathbf{V}_0)^\perp$ into the linear combination of normal and tangential parts

$$\begin{aligned}
(\partial_s \mathbf{V}_0)^\perp &= [(\partial_s \mathbf{V}_0)^\perp \cdot \mathbf{n}]\mathbf{n} + [(\partial_s \mathbf{V}_0)^\perp \cdot \boldsymbol{\tau}]\boldsymbol{\tau} \\
&= [\partial_s \mathbf{V}_0 \cdot \boldsymbol{\tau}]\mathbf{n} - [\partial_s \mathbf{V}_0 \cdot \mathbf{n}]\boldsymbol{\tau}.
\end{aligned} \tag{2.2.17}$$

Note that $H_\gamma(\mathbf{n})\mathbf{n} = \mathbf{0}$, we obtain

$$d^2 F(\Gamma; \mathbf{V}) = \int_\Gamma H_\gamma(\mathbf{n})\boldsymbol{\tau} \cdot \boldsymbol{\tau}(\partial_s \mathbf{V}_0 \cdot \mathbf{n})^2 \, ds. \tag{2.2.18}$$

$\square$

According to lemma. 2.2.3, we know that the second variation under the perturbation Eq. (2.2.10) is given directly as

$$d^2 W(\Gamma; \mathbf{V}) \;=\; \int_\Gamma \mathrm{H}_\gamma(\mathbf{n}) \boldsymbol{\tau} \cdot \boldsymbol{\tau} (\partial_s \mathrm{V}_0 \cdot \mathbf{n})^2 \, \mathrm{ds}. \tag{2.2.19}$$

Thus the stability condition for an equilibrium shape is given by

$$\mathrm{H}_\gamma(\mathbf{n}) \boldsymbol{\tau} \cdot \boldsymbol{\tau} > 0. \tag{2.2.20}$$

The same stability condition for an equilibrium shape has been derived in [9] with the surface stiffness $\gamma(\theta) + \gamma''(\theta) > 0$. Here the condition is presented in a different form. These two forms are equivalent. Based on this stability condition, the author proposed a generalized Winterbottom construction to include all the possible multiple equilibrium shapes for strongly anisotropic case.

2.3 The sharp interface model

In this section, based on thermodynamic variation, the sharp interface model will be developed. The mass conservation and energy dissipation for the dynamic model will be shown afterwards.

By using the above Theorem 2.1, the first variation of the total energy functional (2.1.2) with respect to the interface Γ and two contact points x_c^l and x_c^r can be written as:

$$\frac{\delta W}{\delta \Gamma} = -(\partial_s \boldsymbol{\xi})^\perp \cdot \mathbf{n}, \quad \frac{\delta W}{\delta x_c^l} = -\Big(\xi_2|_{s=0} - (\gamma_{VS} - \gamma_{FS}) \Big), \quad \frac{\delta W}{\delta x_c^r} = \xi_2|_{s=L} - (\gamma_{VS} - \gamma_{FS}). \tag{2.3.1}$$

From the Gibbs-Thomson relation [86, 113], the chemical potential μ of the system is defined as

$$\mu = \Omega_0 \frac{\delta W}{\delta \Gamma}, \tag{2.3.2}$$

where Ω_0 represents the atomic volume of the thin film material. The normal velocity of the interface curve Γ, labeled as v_n, is expressed by the following surface diffusion flow [27, 86]:

$$\mathbf{j} = -\frac{D_s \nu}{k_B T_e} \nabla_s \mu, \qquad v_n = -\Omega_0 (\nabla_s \cdot \mathbf{j}) = \frac{D_s \nu \Omega_0}{k_B T_e} \partial_{ss} \mu, \qquad (2.3.3)$$

where $\mathbf{j}$ is the mass flux along the interface, ∇_s is the surface gradient operator, D_s is the surface diffusivity, ν is the number of diffusing atoms per unit length, and $k_B T_e$ is the thermal energy. Furthermore, the motion of the two contact points are given by the energy gradient flow, which is determined by the time-dependent Ginzburg-Landau kinetic equations [120], i.e.,

$$\frac{dx_c^l(t)}{dt} = -\eta \frac{\delta W}{\delta x_c^l}, \qquad \frac{dx_c^r(t)}{dt} = -\eta \frac{\delta W}{\delta x_c^r}, \qquad (2.3.4)$$

with $\eta \in (0, +\infty)$ representing the finite contact point mobility. For the physical explanation behind this approach, please refer to the recent paper [?].

2.3.1   The dimensionless equations

We choose the characteristic length scale and characteristic surface energy scale as h_0 and γ_0 respectively, the time scale as $\frac{h_0^4}{B\gamma_0}$ with $B = \frac{D_s \nu \Omega_0^2}{k_B T_e}$, and the contact line mobility is scaled by $\frac{B}{h_0^3}$. Then, we can obtain a dimensionless sharp-interface model again [8, 120] for solid-state dewetting via a $\boldsymbol{\xi}$-vector formulation, which can be written as follows (for simplicity, we still use the same notations for the variables):

$$\partial_t \mathbf{X} = \partial_{ss} \mu \, \mathbf{n}, \qquad 0 < s < L(t), \qquad t > 0, \qquad (2.3.5)$$

$$\mu = -(\partial_s \boldsymbol{\xi})^{\perp} \cdot \mathbf{n}, \qquad \boldsymbol{\xi} = \nabla \hat{\gamma}(\mathbf{p})\Big|_{\mathbf{p}=\mathbf{n}}; \qquad (2.3.6)$$

where $\Gamma := \Gamma(t) = \mathbf{X}(s,t) = (x(s,t), y(s,t))$ represents the moving film/vapor interface, s is the arc length or distance along the interface, t is the time, $\mathbf{n} = (-\partial_s y, \partial_s x)$ is the interface outer unit normal vector, $\mu := \mu(s,t)$ is the chemical potential, $\boldsymbol{\xi} = (\xi_1, \xi_2)$ is the dimensionless Cahn-Hoffman vector (scaled by γ_0) and

$L := L(t)$ represents the total length of the moving interface. The initial condition is given as

$$\mathbf{X}(s,0) := \mathbf{X}_0(s) = (x(s,0), y(s,0)) = (x_0(s), y_0(s)),\ 0 \le s \le L_0 := L(0),\ (2.3.7)$$

satisfying $y_0(0) = y_0(L_0) = 0$ and $x_0(0) < x_0(L_0)$, and the boundary conditions are:

(i) contact point condition

$$y(0,t) = 0, \qquad y(L,t) = 0, \qquad t \ge 0; \tag{2.3.8}$$

(ii) relaxed contact angle condition

$$\frac{dx_c^l}{dt} = \eta(\xi_2|_{s=0} - \sigma), \qquad \frac{dx_c^r}{dt} = -\eta(\xi_2|_{s=L} - \sigma), \qquad t \ge 0; \tag{2.3.9}$$

where the dimensionless material constant $\sigma = \frac{\gamma_{VS} - \gamma_{FS}}{\gamma_0}$, and γ_0 is the dimensionless unit of surface energy density.

(iii) zero-mass flux condition

$$\partial_s \mu(0,t) = 0, \qquad \partial_s \mu(L,t) = 0, \qquad t \ge 0. \tag{2.3.10}$$

For the above boundary conditions, condition (i) ensures that the contact points always move along the substrate, condition (ii) allows for the relaxation of the contact angle, and condition (iii) ensures that the total area/mass of the thin film is conserved, implying that there is no mass flux at the contact points. We note here that the above governing equations (2.3.5)-(2.3.6) are mathematically well-posed when the surface energy is isotropic or weakly anisotropic; if the surface energy is strongly anisotropic, the above equations will become anti-diffusion type, and they are ill-posed. In the strongly anisotropic case, we need to regularize these equations by adding some high-order terms, and we will discuss this case later.

2.3.2 Mass conservation and energy dissipation

In this section, we show that the mass is conserved and total energy is decreasing under the dynamics of the above sharp-interface model.

Proposition 2.3.1 (Mass conservation and energy dissiaption). *Let $\Gamma(t) = \mathbf{X}(s,t)$ be the exact solution of Eqs. (2.3.5), (2.3.6) coupled with the boundary conditions (2.3.8)-(2.3.10), and the initial curve is given by $\Gamma(0) = (x_0(s), y_0(s))$. Then the total mass of the thin film is conserved during the evolution, i.e.,*

$$A(t) \equiv A(0) = \int_{\Gamma(0)} y_0(s)\partial_s x_0(s)\, ds, \qquad t \geq 0. \tag{2.3.11}$$

and the total energy of the thin film is decreasing during the evolution, i.e.,

$$W(t) \leq W(t_1) \leq W(0) = \int_{\Gamma(0)} \gamma(\mathbf{n})\, ds - (x_c^r(0) - x_c^l(0))\sigma, \qquad t \geq t_1 \geq 0. \tag{2.3.12}$$

Proof. From Eq. (2.2.2), by directly calculating the time derivative of $A(t)$ and using lemma 2.2.1, we can obtain the following expression

$$\frac{d}{dt}A(t) = \int_{\Gamma(t)} \mathbf{X}_t \cdot \mathbf{n}\, ds = \int_{\Gamma(t)} \mu_{ss}\, ds = 0. \tag{2.3.13}$$

The last equality follows from the zero-mass flux boundary condition, and it indicates that the mass is conserved.

To obtain the time derivative of $W(t)$, we can make use of the Eq. (2.1.13), but replace the perturbation parameter by the time t, then we get:

$$\frac{d}{dt}W(t) = -\int_{\Gamma}(\partial_s \boldsymbol{\xi})^{\perp} \cdot \mathbf{X}_t ds + (\xi_2|_{s=L(t)} - \sigma)\frac{dx_c^r}{dt} - (\xi_2|_{s=0} - \sigma)\frac{dx_c^l}{dt}. \tag{2.3.14}$$

Now use (2.3.5) and (2.3.6) and the contact line moving boundary conditions (2.3.9), also note that $\partial_s \boldsymbol{\xi} \cdot \mathbf{n} = 0$, we have

$$\begin{aligned}
\frac{d}{dt}W(t) &= \int_{\Gamma(t)} \mu\partial_{ss}\mu\, ds - \frac{1}{\eta}\Big[\Big(\frac{dx_c^l}{dt}\Big)^2 + \Big(\frac{dx_c^r}{dt}\Big)^2\Big] \\
&= -\int_{\Gamma(t)}(\partial_s \mu)^2\, ds - \frac{1}{\eta}\Big[\Big(\frac{dx_c^l}{dt}\Big)^2 + \Big(\frac{dx_c^r}{dt}\Big)^2\Big] \leq 0. \tag{2.3.15}
\end{aligned}$$

The last inequality immediately implies the energy dissipation. $\qquad\square$

2.4   A parametric finite element method (PFEM)

In this section, motivated by the *parametric finite element method (PFEM)* recently used for solving a class of geometric partial differential equations (e.g., [6,8,16,17,36]), we propose a parametric finite element numerical scheme for solving the above proposed sharp-interface mathematical model, i.e., Eqs. (2.3.5)-(2.3.6) coupled with the boundary conditions Eqs. (2.3.8)-(2.3.10).

2.4.1   Variational formulation

Following the previous notions, we assume that $\Gamma(t)$ is a family of open evolution curves in the plane which intersect with the substrate line (x-axis) at the two contact points, then we can parameterize the curves as

$$\Gamma(t) = \mathbf{X}(\rho, t) : I \times [0, T] \to \mathbb{R}^2, \tag{2.4.1}$$

where $t \in [0, T]$ represents the time, the time-independent spatial variable $\rho \in I$, and I denotes a fixed reference spatial domain. For simplicity, we choose it as $I := [0, 1]$.

In order to briefly present its variational formulation of the sharp-interface model, we introduce the following L^2 inner product which depends on the evolution curve $\Gamma(t)$ as

$$\left\langle u, v \right\rangle_\Gamma := \int_I u(\rho) \cdot v(\rho) |\partial_\rho \mathbf{X}(\rho, t)| \, d\rho, \tag{2.4.2}$$

where $u, v \in L^2(I)$ are any scalar (or vector) functions. In addition, here we always assume that $\partial_\rho s(\rho, t) = |\partial_\rho \mathbf{X}(\rho, t)| \in L^\infty(I)$. On the other hand, when the interface curve $\Gamma(t)$ evolves, the x-coordinates of two contact points at which $\Gamma(t)$ intersects with the x-axis will evolve according to the relaxed contact angle condition Eq. (2.3.9), and therefore, we can define the following Dirichlet-type functional space of the solutions for the proposed sharp-interface model as

$$H^1_{a,b}(I) = \{u \in H^1(I) : u(0) = a, u(1) = b\}, \tag{2.4.3}$$

where a and b are two preassigned constants which are related to x-coordinates (or y-coordinates) of the two contact points at a fixed time, respectively. For simplicity, we denote $H_0^1(I) := H_{0,0}^1(I)$.

Now, we can define the variational formulation of the above sharp-interface model for simulating the solid-state dewetting of thin films: given an initial curve $\Gamma(0) = \mathbf{X}(\rho, 0) = \mathbf{X}_0(s)$ with $s = L_0\rho$ for $\rho \in I$ (defined in Eq. (2.3.7)), for any time $t \in (0, T]$, find the evolution curves $\Gamma(t) = \mathbf{X}(\rho, t) \in H_{a,b}^1(I) \times H_0^1(I)$ with the x-coordinate positions of moving contact points $a = x_c^l(t) \leq x_c^r(t) = b$, the chemical potential $\mu(\rho, t) \in H^1(I)$ such that

$$\left\langle \partial_t \mathbf{X}, \ \varphi \mathbf{n} \right\rangle_\Gamma + \left\langle \partial_s \mu, \ \partial_s \varphi \right\rangle_\Gamma = 0, \quad \forall \, \varphi \in H^1(I), \tag{2.4.4}$$

$$\left\langle \mu \mathbf{n}, \ \boldsymbol{\omega} \right\rangle_\Gamma - \left\langle \boldsymbol{\xi}^\perp, \ \partial_s \boldsymbol{\omega} \right\rangle_\Gamma = 0, \quad \forall \, \boldsymbol{\omega} \in H_0^1(I) \times H_0^1(I), \tag{2.4.5}$$

coupled with that the positions of the moving contact points, i.e., $x_c^l(t)$ and $x_c^r(t)$, are updated by the relaxed contact angle boundary condition, i.e., Eq. (2.3.9). Here, the Cahn-Hoffman $\boldsymbol{\xi}$-vector is determined from the surface energy density $\gamma(\mathbf{n})$ and the curve orientation $\mathbf{n}$, i.e., $\boldsymbol{\xi} = \nabla \hat{\gamma}(\mathbf{p}) \Big|_{\mathbf{p}=\mathbf{n}}$. It is noted that Eq. (2.4.4) is obtained by reformulating Eq. (2.3.5) as $\partial_t \mathbf{X} \cdot \mathbf{n} = \partial_{ss} \mu$, then multiplying a scalar test function φ on the both sides and integrating over the interface curve $\Gamma(t)$, and finally using the integration by parts and the zero-mass flux boundary condition (2.3.10). Similarly, Eq. (2.4.5) can be obtained by reformulating Eq. (2.3.6) as $\mu \, \mathbf{n} = -\partial_s \boldsymbol{\xi}^\perp$ because $\partial_s \boldsymbol{\xi}^\perp \parallel \mathbf{n}$, multiplying a vector- valued test function $\boldsymbol{\omega}$ on its both sides, and the integration by parts.

2.4.2 Fully-discrete scheme

A uniform partition of I is given as: $\rho \in I = [0, 1] = \bigcup_{j=1}^N I_j = \bigcup_{j=1}^N [\rho_{j-1}, \rho_j]$, where N denotes the number of divided small intervals, and $\rho_j = jh$ denotes the interval nodes with the uniform interval length $h = 1/N$. In addition, we subdivide the time interval as $0 = t_0 < t_1 < \ldots < t_{M-1} < t_M = T$ with $\tau_m = t_{m+1} - t_m$.

Define the finite dimensional spaces to approximate $H^1(I)$ and $H^1_{a,b}(I)$ as

$$V^h := \{u \in C(I): \ u\mid_{I_j} \in P_1, \quad \forall\, j = 1, 2, \dots, N\} \subseteq H^1(I), \tag{2.4.6}$$

$$\mathcal{V}^h_{a,b} := \{u \in V^h: \ u(0) = a, \ u(1) = b\} \subseteq H^1_{a,b}(I), \tag{2.4.7}$$

where a and b are two given constants, P_1 denotes the polynomial with degrees at most 1. And again, for simplicity, we denote $\mathcal{V}^h_0 = \mathcal{V}^h_{0,0}$.

Since we use the P_1 (linear) elements to approximate the moving curves, the numerical solutions for the moving interfaces are polygonal curves. If we introduce that, $\mathbf{h}^m_j := \mathbf{X}^m(\rho_j) - \mathbf{X}^m(\rho_{j-1})$, is a straight line (or a vector) which connects with the marker points $\mathbf{X}^m(\rho_j)$ and $\mathbf{X}^m(\rho_{j-1})$, where $j = 1 \to N$, then we can denote the evolution curve at time $t = t_m$ as: $\mathbf{X}^m = \bigcup_{j=1}^N \mathbf{h}^m_j$, and its tangential, normal vector of the numerical solution Γ^m are step functions with possible discontinuities or jumps at nodes ρ_j. For two piecewise continuous scalar or vector functions u and v defined on the interval I, with possible jumps at the nodes $\{\rho_j\}_{j=1}^{N-1}$, we can define the mass lumped inner product $\langle \cdot, \cdot \rangle^h_{\Gamma^m}$ over Γ^m as

$$\langle u, \ v \rangle^h_{\Gamma^m} := \frac{1}{2} \sum_{j=1}^N \left| \mathbf{X}^m(\rho_j) - \mathbf{X}^m(\rho_{j-1}) \right| \left[(u \cdot v)(\rho_j^-) + (u \cdot v)(\rho_{j-1}^+) \right], \tag{2.4.8}$$

where $u(\rho_j^\pm) = \lim_{\rho \to \rho_j^\pm} u(\rho)$. The unit tangential vector can be computed as $\boldsymbol{\tau}^m_j = \boldsymbol{\tau}^m\mid_{I_j} = \frac{\mathbf{h}^m_j}{|\mathbf{h}^m_j|}$, and the normal vector can be numerically computed as $\mathbf{n}^m = -(\boldsymbol{\tau}^m)^\perp$.

Let $\Gamma^m := \mathbf{X}^m$, $\mathbf{n}^m$ and μ^m be the numerical approximations of the moving curve $\Gamma(t_m) := \mathbf{X}(\cdot, t_m)$, the normal vector $\mathbf{n}$ and the chemical potential μ at time t_m, respectively. For simplicity, we denote $\mathbf{X}^m(\rho_j) = (x^m_j, y^m_j)$. Take $\Gamma^0 = \mathbf{X}^0 \in \mathcal{V}^h_{x_0(0), x_0(L_0)} \times \mathcal{V}^h_0$ such that $\mathbf{X}^0(\rho_j) = \mathbf{X}_0(s^0_j)$ with $s^0_j = jL_0/N = L_0\rho_j$ for $j = 0, 1, \dots, N$, then a semi-implicit *parametric finite element method (PFEM)* for the variational problem (2.4.4)-(2.4.5) can be given as: for $m \geq 0$, find $\Gamma^{m+1} = \mathbf{X}^{m+1} \in \mathcal{V}^h_{a,b} \times \mathcal{V}^h_0$ with the x-coordinate positions of the moving contact points $a := x^l_c(t_{m+1}) \leq b := x^r_c(t_{m+1})$ and $\mu^{m+1} \in V^h$ such that

$$\left\langle \frac{\mathbf{X}^{m+1} - \mathbf{X}^m}{\tau_m}, \ \varphi_h \mathbf{n}^m \right\rangle^h_{\Gamma^m} + \left\langle \partial_s \mu^{m+1}, \ \partial_s \varphi_h \right\rangle^h_{\Gamma^m} = 0, \quad \forall\, \varphi_h \in V^h, \tag{2.4.9a}$$

$$\left\langle \mu^{m+1} \mathbf{n}^m, \ \boldsymbol{\omega_h} \right\rangle^h_{\Gamma^m} - \left\langle (\boldsymbol{\xi}^{m+\frac{1}{2}})^\perp, \ \partial_s \boldsymbol{\omega_h} \right\rangle^h_{\Gamma^m} = 0, \quad \forall\, \boldsymbol{\omega_h} \in \mathcal{V}^h_0 \times \mathcal{V}^h_0, \tag{2.4.9b}$$

where the x-coordinates of the two contact point positions $x_c^l(t_{m+1})$ and $x_c^r(t_{m+1})$ are updated via the relaxed contact angle condition Eq. (2.3.9) by using the forward Euler numerical approximation,

$$\frac{x_c^l(t_{m+1}) - x_c^l(t_m)}{\tau_m} = \eta \Big[\xi_2^m\Big|_{\rho=0} - \sigma\Big], \quad \frac{x_c^r(t_{m+1}) - x_c^r(t_m)}{\tau_m} = -\eta \Big[\xi_2^m\Big|_{\rho=1} - \sigma\Big]. \quad (2.4.10)$$

According to the specific form of the surface energy density, we can define the numerical approximation term $\boldsymbol{\xi}^{m+\frac{1}{2}}$ in the above scheme as follows: If the surface energy density is expressed as the form of $\gamma(\mathbf{n})$, the numerical approximation term $\boldsymbol{\xi}^{m+\frac{1}{2}}$ can be defined as:

$$\boldsymbol{\xi}^{m+\frac{1}{2}} = \gamma(\mathbf{n}^m)\mathbf{n}^{m+1} + (\boldsymbol{\xi}^m \cdot \boldsymbol{\tau}^m)\boldsymbol{\tau}^{m+1}, \quad (2.4.11)$$

where $\mathbf{n}^{m+1}$ and $\boldsymbol{\tau}^{m+1}$ are numerically approximated by $-(\partial_s \mathbf{X}^{m+1})^\perp$ and $\partial_s \mathbf{X}^{m+1}$ respectively. The main idea comes from that the Cahn-Hoffman vector can be decomposed as: $\boldsymbol{\xi} = \gamma(\mathbf{n})\mathbf{n} + (\boldsymbol{\xi} \cdot \boldsymbol{\tau})\boldsymbol{\tau}$, where $\boldsymbol{\xi} \cdot \mathbf{n} = \gamma(\mathbf{n})$, and then we use the semi-implicit discretization. Furthermore, in some literatures, the surface energy density function $\gamma(\mathbf{n})$ can be chosen as a special form, e.g., Riemannian metric form [19, 36]

$$\gamma(\mathbf{n}) = \sum_{k=1}^{K} \sqrt{G_k \mathbf{n} \cdot \mathbf{n}}, \qquad \boldsymbol{\xi}(\mathbf{n}) = \sum_{k=1}^{K} \Big[\sqrt{G_k \mathbf{n} \cdot \mathbf{n}}\Big]^{-1} G_k \mathbf{n}, \quad (2.4.12)$$

where G_k, $k = 1, \cdots, K$, is a symmetric positive definite matrix. In this special case, the numerical approximation term $\boldsymbol{\xi}^{m+\frac{1}{2}}$ can be defined as:

$$\boldsymbol{\xi}^{m+\frac{1}{2}} = \sum_{k=1}^{K} \Big[\sqrt{G_k \mathbf{n}^m \cdot \mathbf{n}^m}\Big]^{-1} G_k \mathbf{n}^{m+1}. \quad (2.4.13)$$

On the other hand, in two dimensions, the surface energy density function $\gamma(\mathbf{n})$ can be equivalently expressed as the form of $\gamma(\theta)$, where $\mathbf{n} = (-\sin\theta, \cos\theta)$, $\theta \in [-\pi, \pi]$ represents the local orientation (i.e., the angle between the interface outer normal $\mathbf{n}$ and y-axis), and by simple calculations we can evaluate the linear approximation $\boldsymbol{\xi}^{m+\frac{1}{2}}$ in Eq. (2.4.9b) to the Cahn-Hoffman vector as

$$\boldsymbol{\xi}^{m+\frac{1}{2}} = \gamma(\theta^m)\mathbf{n}^{m+1} - \gamma'(\theta^m)\boldsymbol{\tau}^{m+1}, \quad (2.4.14)$$

where the value of the orientation angle θ is explicitly calculated at time $t = t^m$, and we have used $\boldsymbol{\xi} \cdot \boldsymbol{\tau} = -\gamma'(\theta)$ in Eq. (2.4.11).

For the above semi-implicit parametric finite element scheme, we have the following theorem:

Theorem 2.4.1 (Well-posedness for the PFEM scheme). *The above discrete variational problem Eqs.* (2.4.9a)-(2.4.9b) *admits a unique solution (i.e., well-posed).*

Proof. Note that the two moving contact points is first updated explicitly according to the relaxed boundary condition, and therefore, the boundary conditions of the variables for the above discrete variational problem can be regarded as the Dirichlet type. Proving that the resulted linear system has a unique solution is equivalent to proving that the corresponding homogeneous linear system has zero solutions, i.e., the system can be reduced to: find $\{\mathbf{X}^{m+1}, \mu^{m+1}\} \in \{\mathcal{V}_0^h \times \mathcal{V}_0^h, V^h\}$ such that

$$\left\langle \mathbf{X}^{m+1}, \; \varphi_h \mathbf{n}^m \right\rangle_{\Gamma^m}^h + \left\langle \partial_s \mu^{m+1}, \; \partial_s \varphi_h \right\rangle_{\Gamma^m}^h = 0, \quad \forall \, \varphi_h \in V^h, \tag{2.4.15a}$$

$$\left\langle \mu^{m+1} \mathbf{n}^m, \; \boldsymbol{\omega_h} \right\rangle_{\Gamma^m}^h - \left\langle (\boldsymbol{\xi}^{m+\frac{1}{2}})^\perp, \; \partial_s \boldsymbol{\omega_h} \right\rangle_{\Gamma^m}^h = 0, \quad \forall \, \boldsymbol{\omega}_h \in \mathcal{V}_0^h \times \mathcal{V}_0^h, \tag{2.4.15b}$$

with $\boldsymbol{\xi}^{m+\frac{1}{2}} = \gamma(\theta^m)(-\partial_s \mathbf{X}^{m+1})^\perp - \gamma'(\theta^m)\partial_s \mathbf{X}^{m+1}$ defined in Eq. (2.4.14). Now if we set $\varphi_h = \mu^{m+1}, \boldsymbol{\omega}_h = \mathbf{X}^{m+1}$ and by noting that $(\partial_s \mathbf{X}^{m+1})^\perp \cdot \partial_s \mathbf{X}^{m+1} = 0$, we can obtain

$$\left\langle \partial_s \mu^{m+1}, \; \partial_s \mu^{m+1} \right\rangle_{\Gamma^m}^h + \left\langle \gamma(\theta^m)\partial_s \mathbf{X}^{m+1}, \; \partial_s \mathbf{X}^{m+1} \right\rangle_{\Gamma^m}^h = 0. \tag{2.4.16}$$

Because the surface energy density $\gamma(\theta)$ is always non-negative, the above equation directly tells us that $\mathbf{X}^{m+1} = \mathbf{0}$, $\mu^{m+1} = \mathbf{0}$. Therefore, the corresponding homogeneous linear system only has zero solutions, which indicates the discrete scheme has a unique solution. $\qquad \square$

Note that in the above proof, we assume that the surface energy density is of the $\gamma(\theta)$ form; if it is written as the $\gamma(\mathbf{n})$ form, the proof is the same. On the other hand, if the surface energy density is specially chosen as the Riemannian metric form, the proof can be found in [19].

The above proposed PFEM scheme via the Cahn-Hoffman $\boldsymbol{\xi}$ has many advantages over the PFEM scheme previously proposed by us in [8]: (a) first, in the present PFEM, we only need to solve a linear algebra system which includes the unknown variables $\{\mathbf{X}^{m+1}, \mu^{m+1}\}$, while it includes $\{\mathbf{X}^{m+1}, \mu^{m+1}, \kappa^{m+1}\}$ in the previous one; (b) second, the present PFEM is well-posed and can work for any form of the surface energy density function, while the previous one only works for the $\gamma(\theta)$ form and can be proved to be well-posed only in the isotropic surface energy case; (c) third, the present scheme only needs to deal with the first derivative of $\gamma(\theta)$, while the previous needs to compute its second derivative. In addition, we note here that in practical simulations, when the surface energy anisotropy becomes stronger and stronger, the interface curve will form sharper and sharper corners. Under these circumstances, we need to redistribute mesh points at evenly spaced arc lengths, and a kind of mesh redistribution algorithm which can conserves the total area can be found in the reference [6].

For any form of $\gamma(\mathbf{n})$, how to prove that the above fully-discrete scheme Eqs. (2.4.9a)-(2.4.9b) preserves the discrete energy-dissipation property seems difficult. But in some special forms, for example, if $\gamma(\mathbf{n})$ is chosen as the Riemannian metric form with $K = 1$, i.e., Eq.(2.4.12), Barrett *et al.* [19] can prove a stronger conclusion that the scheme is unconditionally energy-stable (i.e., energy-dissipative regardless of how to choose τ_m and h) for closed evolution curves with periodical boundary conditions. Some more generalized PFEM schemes which can ensure the stability and are applicable for all types of anisotropy have been discussed and developed in the reference [36]. The main idea behind these schemes is to explicitly evaluate the nonlinear term $\boldsymbol{\xi}$ by adding a stabilized term to Eq. (2.4.15b) on the right hand side. The fully-discrete stabilized PFEM scheme for solving the sharp-interface model can be written as: for $m \geq 0$, find $\Gamma^{m+1} = \mathbf{X}^{m+1} \in \mathcal{V}_{a,b}^h \times \mathcal{V}_0^h$ with the x-coordinate positions of the moving contact points $a := x_c^l(t_{m+1}) \leq b := x_c^r(t_{m+1})$ and $\mu^{m+1} \in V^h$

such that

$$\left\langle \frac{\mathbf{X}^{m+1} - \mathbf{X}^m}{\tau_m}, \; \varphi_h \mathbf{n}^m \right\rangle_{\Gamma^m}^h + \left\langle \partial_s \mu^{m+1}, \; \partial_s \varphi_h \right\rangle_{\Gamma^m}^h = 0, \quad \forall \, \varphi_h \in V^h, \qquad (2.4.17a)$$

$$\left\langle \mu^{m+1} \mathbf{n}^m, \; \boldsymbol{\omega_h} \right\rangle_{\Gamma^m}^h - \left\langle (\boldsymbol{\xi}^m)^\perp, \; \partial_s \boldsymbol{\omega_h} \right\rangle_{\Gamma^m}^h$$
$$- \lambda \left\langle \gamma(\mathbf{n}^m) \, \partial_s (\mathbf{X}^{m+1} - \mathbf{X}^m), \; \partial_s \boldsymbol{\omega_h} \right\rangle_{\Gamma^m}^h = 0, \quad \forall \, \boldsymbol{\omega_h} \in \mathcal{V}_0^h \times \mathcal{V}_0^h,$$
$$(2.4.17b)$$

where the two contact point positions $x_c^l(t_{m+1})$ and $x_c^r(t_{m+1})$ are first determined by Eq. (2.4.10) via forward Euler scheme. Here, λ is a stabilized parameter (often chosen as a positive constant). This stabilized PFEM is also a good candidate numerical method for solving our proposed model. But, since the stabilized term may influence the accuracy of the scheme, especially when the stabilized parameter λ is chosen to be large to control the stability, so in real simulations this scheme is not our first option compared to the former PFEM scheme, i.e., Eqs. (2.4.9a)-(2.4.9b).

2.5 Numerical results

Based on the mathematical model and numerical methods presented above, we will test the convergence order of our PFEM Eqs. (2.4.9a),(2.4.9b) and (2.4.10). For comparison, the convergence order of PFEM for closed curve (periodical boundary conditions) will also be presented. In addition, we will present the numerical simulation results in this section from simulating solid-state dewetting in several different thin-film geometries with several kinds of anisotropic surface energy in 2D. For simplicity, we set the initial thin film thickness to unity in the following simulations. The contact line mobility η determines the relaxation rate of the dynamical contact angle to the equilibrium contact angle, and in principle, it is a material parameter and should be determined either from physical experiments or microscopic (e.g., molecular dynamical) simulations. Here we will always choose the contact line mobility as $\eta = 100$ in numerical simulations, and the detailed discussion about

its influence to solid-state dewetting evolution process can be found in the reference [120]. The first type of anisotropic surface energy density we will investigate is the k-fold smooth crystalline surface energy, which is usually defined as the $\gamma(\theta)$ form

$$\gamma(\theta) = 1 + \beta\cos(k\theta), \quad \theta \in [-\pi, \pi], \tag{2.5.1}$$

where $\beta \geq 0$ controls the degree of the anisotropy, k is the order of the rotational symmetry (usually taken as $k = 2, 3, 4, 6$ for crystalline materials). For this surface energy, when $\beta = 0$, it is isotropic; when $0 < \beta < \frac{1}{k^2-1}$, it is weakly anisotropic; and when $\beta > \frac{1}{k^2-1}$, it is strongly anisotropic.

Another type of surface energy density we will focus on is of the Riemannian metric form defined in Eq. (2.4.12), i.e.,

$$\gamma(\mathbf{n}) = \sum_{k=1}^{K} \sqrt{G_k \mathbf{n} \cdot \mathbf{n}}, \quad G_k = R(-\phi_k)D(\delta_k)R(\phi_k), \quad k = 1, \cdots, K, \tag{2.5.2}$$

where the matrices D and R are defined as

$$D(\delta) = \begin{pmatrix} 1 & 0 \\ 0 & \delta^2 \end{pmatrix}, \qquad R(\phi) = \begin{pmatrix} \cos\phi & \sin\phi \\ -\sin\phi & \cos\phi \end{pmatrix}. \tag{2.5.3}$$

Here, the matrix D is positive definite, and the regularization parameter δ can be viewed as a kind of smooth regularization for this type of surface energy anisotropy (i.e., used for smoothing sharp corners which will appear in equilibrium shapes). When δ decrease from a small positive number to zero, its corresponding equilibrium shape will exhibit sharper and sharper corners.

2.5.1 Convergence test

Firstly we apply our PFEM on the closed curve evolution and open curve evolution (solid-state dewetting problem) under surface diffusion both in isotropic and weakly anisotropic cases. The uniform time step is used during the numerical simulation.

For closed curve evolution, including the isotropic (shown in Table 2.1) and anisotropic (shown in Table 2.2) cases, the initial shape of thin film is chosen as a closed tube, i.e., a rectangle of length 4 and width 1 added by two semi-circles with radii of 0.5 to its left and right sides, and the parameters $h_0 = (8 + \pi)/120$ and $\tau_0 = 0.01$; for an open curve evolution, including the isotropic (shown in Table 2.3) and anisotropic (shown in Table 2.4) cases, the initial shape of thin film is chosen as a rectangle island of length 5 and thickness 1, and $h_0 = 0.05$ and $\tau_0 = 0.005$. In order to compute the convergence order at any fixed time, we can define the following numerical approximation solution in any time interval as

$$\mathbf{X}_{h,\tau}(\rho_j, t) = \frac{t - t_{m-1}}{\tau}\mathbf{X}^m(\rho_j) + \frac{t_m - t}{\tau}\mathbf{X}^{m-1}(\rho_j), \ j = 0, 1, \ldots, N, t \in [t_{m-1}, t_m], \ (2.5.4)$$

where h and τ denote the uniform grid size and time step that we used in the numerical simulations. The numerical error $e_{h,\tau}(t)$ in the L^∞ norm can be defined as

$$e_{h,\tau}(t) = \| \mathbf{X}_{h,\tau} - \mathbf{X}_{\frac{h}{2}, \frac{\tau}{4}} \|_{L^\infty} = \max_{0 \le j \le N} \min_{\rho \in [0,1]} |\mathbf{X}_{h,\tau}(\rho_j, t) - \mathbf{X}_{\frac{h}{2}, \frac{\tau}{4}}(\rho, t)|, \qquad (2.5.5)$$

where the curve $\mathbf{X}_{\frac{h}{2}, \frac{\tau}{4}}(\rho, t)$ belongs to the piecewise linear finite element vector spaces and at the interval nodes $\rho = \rho_j$, its values are equal to the values of numerical solutions $\mathbf{X}_{\frac{h}{2}, \frac{\tau}{4}}(\rho_j, t)$.

We compute the convergence rate of the scheme at three different times $t = 0.5, t = 2.0, t = 5.0$. The results are shown in Table. 2.1-2.4. From the table, we can clearly observe that for closed curve evolution under surface diffusion, the convergence order is second order when the surface energy is isotropic. However, the anisotropic surface energy can decrease the convergence order to around 1.7 (Table. 2.2). This deterioration may be caused by the linearization of $\boldsymbol{\xi}$ ($\boldsymbol{\xi}^{m+\frac{1}{2}} = \gamma(\theta^m)(-\partial_s\mathbf{X}^{m+1})^\perp - \gamma'(\theta^m)\partial_s\mathbf{X}^{m+1})$). For the open curves, the convergence order further reduce to first order both for the isotropic and anisotropic cases. This deterioration may be due to that the forward Euler scheme was applied to discretize the relaxed contact angle boundary condition, ie Eq. (2.3.9).

Compared to the traditional explicit finite difference method (e.g., marker-particle methods) for computing the fourth-order geometric evolution PDEs [42, 120, 125],

Table 2.1: Convergence rates in the L^∞ norm for a closed curve evolution under the isotropic surface diffusion flow, that is the surface energy density $\gamma = 1$

$e_{h,\tau}(t)$	$h = h_0$ $\tau = \tau_0$	$h_0/2$ $\tau_0/2^2$	$h_0/2^2$ $\tau_0/2^4$	$h_0/2^3$ $\tau_0/2^6$	$h_0/2^4$ $\tau_0/2^8$
$e_{h,\tau}(t = 0.5)$	4.58E-3	1.09E-3	2.63E-4	6.40E-5	1.58E-5
order	–	2.07	2.05	2.04	2.02
$e_{h,\tau}(t = 2.0)$	3.61E-3	9.43E-4	2.45E-4	6.31E-5	1.61E-5
order	–	1.94	1.95	1.96	1.97
$e_{h,\tau}(t = 5.0)$	3.63E-3	9.47E-4	2.46E-4	6.33E-5	1.62E-5
order	–	1.94	1.95	1.96	1.97

Table 2.2: Convergence rates in the L^∞ norm for a closed curve evolution under the anisotropic surface diffusion flow, where $\gamma(\theta) = 1 + 0.05\cos(4\theta)$

$e_{h,\tau}(t)$	$h = h_0$ $\tau = \tau_0$	$h_0/2$ $\tau_0/2^2$	$h_0/2^2$ $\tau_0/2^4$	$h_0/2^3$ $\tau_0/2^6$	$h_0/2^4$ $\tau_0/2^8$
$e_{h,\tau}(t = 0.5)$	1.24E-2	2.25E-3	6.71E-4	2.48E-4	7.10E-5
order	–	2.46	1.74	1.44	1.80
$e_{h,\tau}(t = 2.0)$	4.86E-3	1.44E-3	4.57E-4	1.37E-4	3.71E-5
order	–	1.76	1.66	1.74	1.89
$e_{h,\tau}(t = 5.0)$	4.88E-3	1.44E-3	4.58E-4	1.37E-5	3.74E-5
order	–	1.76	1.66	1.74	1.89

Table 2.3: Convergence rates in the L^∞ norm for an open curve evolution under the isotropic surface diffusion flow (solid-state dewetting with isotropic surface energy), where $\gamma(\theta) = 1$, $\sigma = \cos(5\pi/6)$.

$e_{h,\tau}(t)$	$h = h_0$ $\tau = \tau_0$	$h_0/2$ $\tau_0/2^2$	$h_0/2^2$ $\tau_0/2^4$	$h_0/2^3$ $\tau_0/2^6$
$e_{h,\tau}(t = 0.5)$	2.59E-2	1.32E-2	6.52E-3	3.29E-3
order	–	0.97	1.01	0.99
$e_{h,\tau}(t = 2.0)$	2.39E-2	1.22E-2	6.10E-3	3.07E-3
order	–	0.97	1.00	0.99
$e_{h,\tau}(t = 5.0)$	1.91E-2	9.67E-3	4.84E-3	2.43E-3
order	–	0.98	1.00	0.99

Table 2.4: Convergence rates in the L^∞ norm for an open curve evolution under the anisotropic surface diffusion flow (solid-state dewetting with anisotropic surface energy), where $\gamma(\theta) = 1 + 0.05\cos(4\theta)$, $\sigma = \cos(5\pi/6)$.

$e_{h,\tau}(t)$	$h = h_0$ $\tau = \tau_0$	$h_0/2$ $\tau_0/2^2$	$h_0/2^2$ $\tau_0/2^4$	$h_0/2^3$ $\tau_0/2^6$
$e_{h,\tau}(t = 0.5)$	2.82E-2	1.41E-2	6.88E-3	3.44E-3
order	–	0.99	1.04	1.00
$e_{h,\tau}(t = 2.0)$	2.71E-2	1.37E-2	6.78E-3	3.40E-3
order	–	0.98	1.02	0.99
$e_{h,\tau}(t = 5.0)$	2.32E-2	1.12E-3	5.80E-3	2.92E-3
order	–	1.00	1.00	0.99

which imposes the extremely strong stability restriction on the time step, i.e., $\tau \sim \mathcal{O}(h^4)$, the proposed semi-implicit PFEM can greatly alleviate the stability restriction and our numerical experiments indicate that the time step only needs to be chosen as $\tau \sim \mathcal{O}(h^2)$ to maintain the numerical stability. Of course, rigorous numerical analysis for these observations including convergence rates and stability condition of PFEM is very important and challenging, while its mathematical study is ongoing.

2.5.2 Small islands
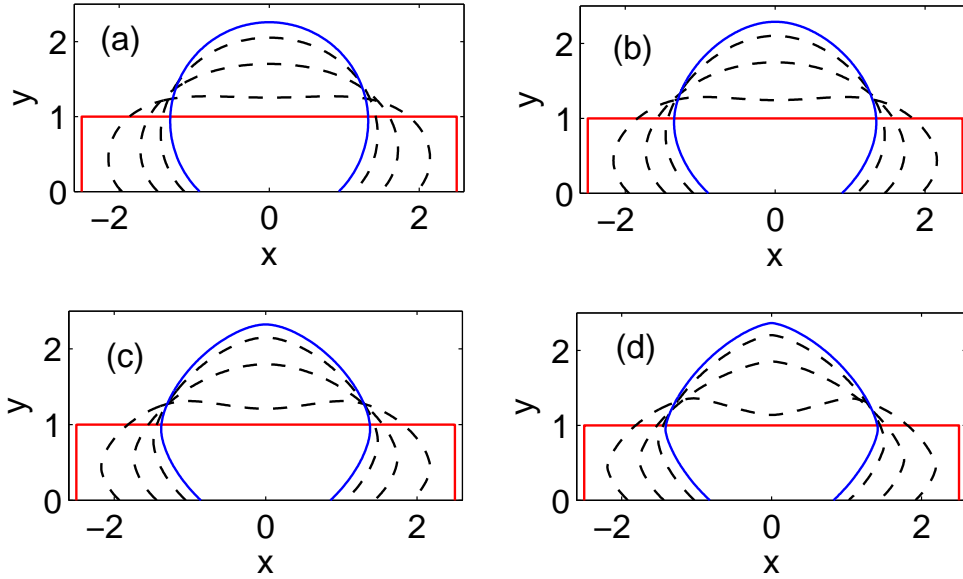
Figure 2.2: Several steps in the evolution of small, initial rectangle islands (shown in red) towards their equilibrium shapes (shown in blue) for different degrees of the anisotropy β with the crystalline symmetry order $k = 4$, where the parameters are chosen as $\sigma = \cos\frac{3\pi}{4}$, and the degree of the anisotropy: (a) $\beta = 0$, (b) $\beta = 0.02$, (c) $\beta = 0.04$, (d) $\beta = 0.06$.

We start with the numerical examples for the 4-fold anisotropy under four different degrees β. As depicted in Fig. 2.2, it shows the evolution process of an initially
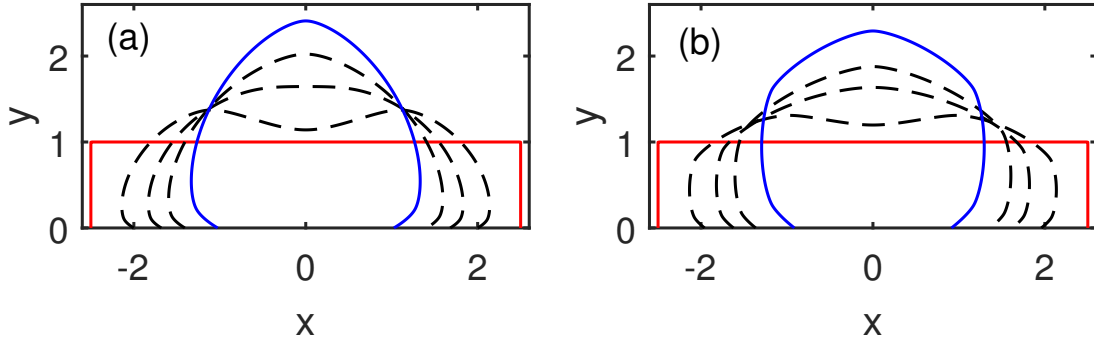
Figure 2.3: Several steps in the evolution of small initial rectangle islands (shown in red) towards their equilibrium shapes (shown in blue), where the parameters are chosen as $\sigma = \cos\frac{3\pi}{4}$, (a) $k = 3, \beta = 0.1$; (b) $k = 6, \beta = 0.022$.
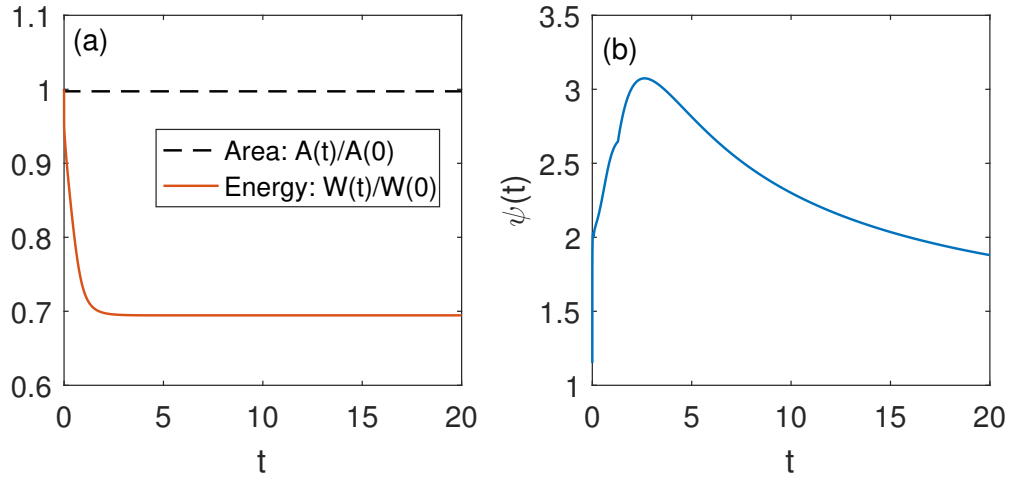
Figure 2.4: (a) The temporal evolution of the normalized total free energy and the normalized total area/mass; (b) the temporal evolution of the mesh distribution function $\psi(t)$. The computational parameters are chosen as the same as Fig. 2.2(c).

rectangular thin film (in red solid lines) towards its equilibrium shapes (in blue solid lines). The initial rectangular island film is chosen as the length 5 and height 1. From Fig. 2.2(a) to Fig. 2.2(d), the material constants are all chosen $\sigma = \cos(\frac{3\pi}{4})$, while the degree of the anisotropy β increases gradually from $\beta = 0$ to $\beta = 0.06$. The number of the grid points is chosen as $N = 400$, and the time step is chosen as a fixed value $\tau = 2 \times 10^{-4}$. As can be seen clearly in Fig. 2.2, the equilibrium shapes (in blue solid lines) gradually change from a circular arc to an anisotropic shape with increasingly sharper and sharper corners, and the number of "facets" in the equilibrium shape also exhibits the 4-fold geometric symmetry. Moreover, we also test the numerical examples by choosing different symmetry orders k, and observe that the k-fold symmetry appears in the equilibrium shape (as shown in Fig. 2.3).

Fig. 2.4(a) shows the temporal evolution of the normalized free energy $W(t)/W(0)$ and the normalized area/mass $A(t)/A(0)$ defined in the previous section. As clearly shown in Fig. 2.4(a), the horizontal black dash line implies that our PFEM has a very good property which ensures that the total area/mass of the thin film conserves, and the monotonically decreasing red solid line implies the energy dissipation property during the whole evolution process. We also investigate the mesh quality by defining the mesh distribution function $\psi(t)$ as

$$\psi(t_m) = \frac{\max_{1 \leq j \leq N} |\mathbf{h}_j^m|}{\min_{1 \leq j \leq N} |\mathbf{h}_j^m|}, \quad \text{where } \Gamma^m = \cup_{j=1}^N \mathbf{h}_j^m. \tag{2.5.6}$$

Fig. 2.4(b) shows the temporal evolution of the mesh distribution function $\psi(t)$. As shown in the figure, we can clearly observe that the distribution function first quickly increases from 1 to about 3 and then gradually decreases to a value around 2, and its value is always not big during the evolution. We find that the mesh quality is always preserved well during the simulation when the surface energy anisotropy is not very strong (i.e., β is not very big). Some theoretic analysis for the mesh-distribution property in the isotropic surface energy case can be found in the reference [16], and an intuitive explanation is because Eq. (2.4.9a) allows the tangential velocity of mesh points which does not change the shape of the interface curve, while this tangential velocity tends to distribute the mesh points uniformly according to

the arc length due to Eq. (2.4.9b).
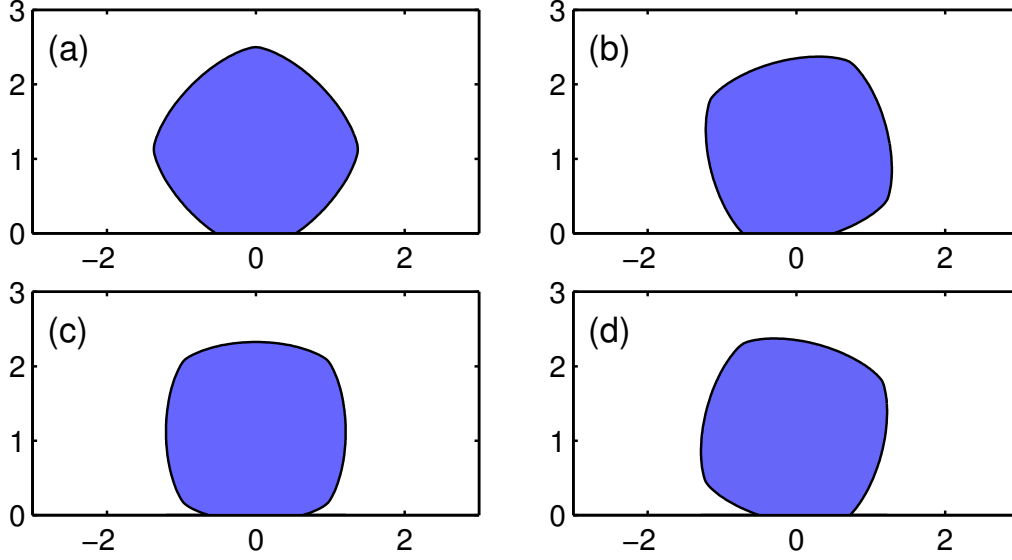
Figure 2.5: Equilibrium island morphologies for a small, initially rectangular island film under several different crystalline rotations ϕ (phase shifts):(a) $\phi = 0$; (b) $\phi = \pi/6$; (c) $\phi = \pi/4$; (d) $\phi = \pi/3$. The other computational parameters are chosen as: $k = 4, \beta = 0.06, \sigma = \cos(5\pi/6)$.

To observe rotation effects of the crystalline axis of the island relative to the substrate normal, we also performed numerical simulations of the evolution of small islands with different phase shifts ϕ for the weakly anisotropic cases under the computational parameters: $k = 4, \beta = 0.06, \sigma = \cos(5\pi/6)$. As shown in Fig. 2.5, the asymmetry of the equilibrium shapes is clearly observed, which can be explained as breaking the symmetry of the surface energy anisotropy (defined in Eq. (2.5.1)) with respect to the substrate normal.

Under the above type of surface energy defined in Eq. (2.5.2), we perform numerical simulations for investigating the kinetic evolution of solid-state dewetting. Fig. 2.6 shows the kinetic evolution of a small initial rectangular island (in red) towards its equilibrium shape (in blue), where the material constant is chosen as $\sigma = \cos\frac{3\pi}{4}$, and the parameters that control the surface energy anisotropy are chosen as: (a) $K = 2, \phi_1 = 0, \phi_2 = \frac{\pi}{2}, \delta_1 = \delta_2 = 0.1$, and (b) $K = 3, \phi_1 = 0, \phi_2 = \frac{\pi}{3}, \phi_3 =$
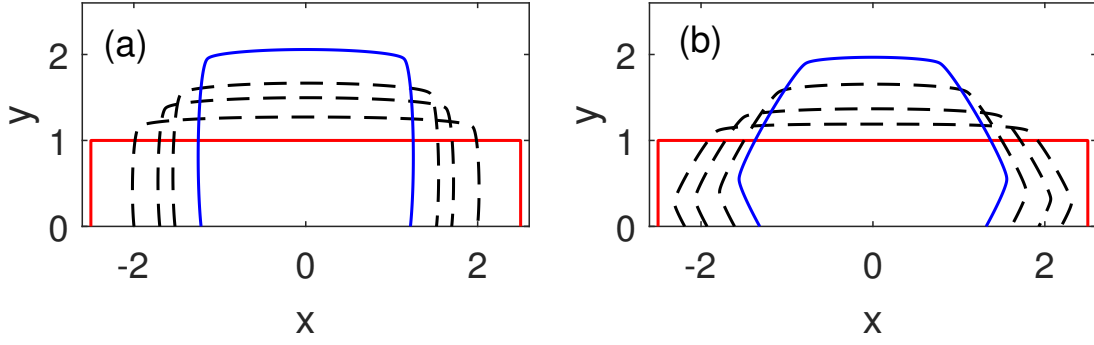
Figure 2.6: Several steps in the evolution of small, initially rectangular island (shown in red) towards their equilibrium shapes (shown in blue) where the anisotropy is given by Eq. (2.5.2), $\sigma = \frac{3\pi}{4}$ with (a) $L = 1, \phi_0 = 0, \phi_1 = \frac{\pi}{2}, \delta_0 = \delta_1 = 0.1$ (b) $L = 2, \phi_0 = 0, \phi_1 = \frac{\pi}{3}, \phi_2 = \frac{2\pi}{3}, \delta_0 = \delta_1 = \delta_2 = 0.1$.
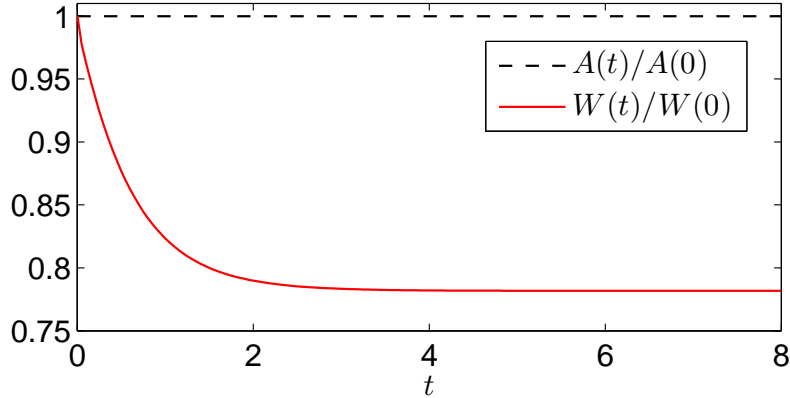
Figure 2.7: The temporal evolution of the normalized free energy and normalized mass, where the anisotropy is given by Eq. (2.5.2). The computational parameters are chosen as same as Fig. 2.6(a).
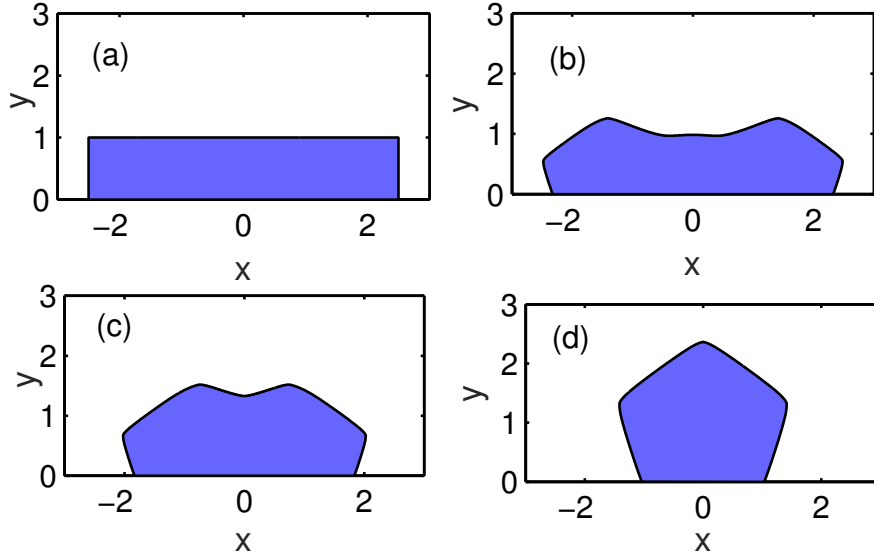
Figure 2.8: Several snapshots in the evolution of a small, initially rectangular island film towards its equilibrium shape:(a) $t = 0$; (b) $t = 0.1$; (c) $t = 0.6$; (d) $t = 7.5$. The anisotropy is chosen $\gamma(\theta) = 1 + 0.19|\cos(\frac{5}{2}\theta)|$ with smooth regularization parameter $\delta = 0.1$. The computational parameter is chosen as $\sigma = \cos(3\pi/4), \lambda = 20$.

$\frac{2\pi}{3}, \delta_1 = \delta_2 = \delta_3 = 0.1$. As clearly shown in Fig. 2.6, it can be observed that the evolution shape for this type of anisotropy seems to be more "faceting" than the smooth k-fold anisotropy, and the equilibrium shape for Fig. 2.6(a) is a truncation of a square while it is a truncation of a hexagon for Fig. 2.6(b), which implies that the parameter K plays the same role in determining the symmetry as it does in the smooth k-fold anisotropy. The small regularization parameter δ is here used to smoothen sharp corners which connect with two different facets.

Fig. 2.7 shows the temporal evolution of the normalized free energy $W(t)/W(0)$ and normalized mass $A(t)/A(0)$. It clearly indicates that our discrete scheme has the same good properties of maintaining mass conservation and energy dissipation under this cusps surface energy density.

The last type of surface energy anisotropy we consider in this section is defined

as [**?**],

$$\gamma(\theta) = 1 + \beta \left| \cos \frac{k\theta}{2} \right|, \tag{2.5.7}$$

and this type of surface energy is not smooth at the points where the function $\cos \frac{k\theta}{2}$ changes its sign. A smooth regularization technique can be done as follows because the proposed PFEM needs $\gamma(\theta) \in C^1[-\pi, \pi]$,

$$\gamma(\theta) = 1 + \beta \sqrt{\delta^2 + \cos^2 \frac{k\theta}{2}}, \tag{2.5.8}$$

where β controls the degree of anisotropy. During our practical simulations, we find that in this case when β becomes very large (but still in the weakly anisotropic regime, i.e., $\gamma(\theta) + \gamma''(\theta) > 0$), the PFEM scheme (2.4.9a)-(2.4.10) does not work better than the stabilized PFEM scheme (2.4.17a)-(2.4.17b) in the sense that we use the same number of grid points. So here, we use the stabilized PFEM scheme (2.4.17a)-(2.4.17b) for simulating solid-state dewetting with this special type of anisotropy. As shown in Fig. 2.8, the interface curve evolves from a small rectangular island to its equilibrium shape (a regular k-polygon truncated by a flat substrate). Here, the computational parameter about this type of anisotropy is chosen as $\beta = 0.19$, $k = 5$, $\delta = 0.1$ and the stabilized parameter is chosen as $\lambda = 20$.

2.5.3 Large islands

As widely discussed in the papers [8, 40, 66, 120], when the aspect ratios of thin island films are larger than a critical value, the large islands will pinch-off to form small separated islands.

In order to obtain a qualitative comparison with other numerical methods, we choose the same computational parameters as in the paper [8, 120]. The numerical computation is set up as follows: the initial thin film is chosen as a very large thin island with length $L = 60$ and height $h = 1$. The anisotropy is given as 4-fold anisotropic surface energy density with $\beta = 0.06$ and the material constant is given by $\sigma = \cos 5\pi/6$.
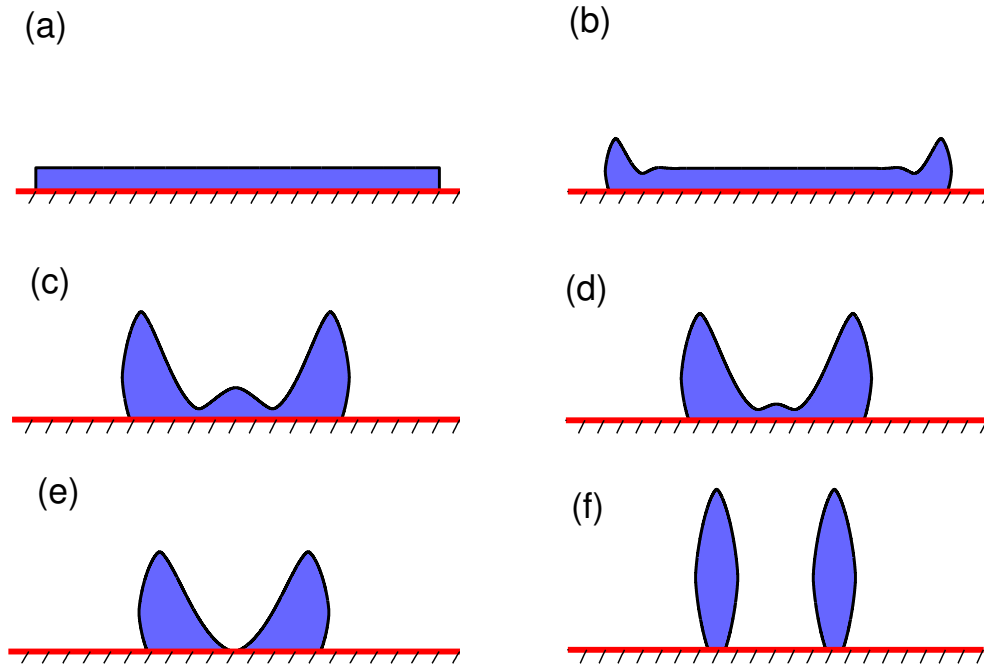
Figure 2.9: Several snapshots in the evolution of a long, thin island film (aspect ratio of 60) with k-fold anisotropic surface energy ($k = 4, \beta = 0.06, \phi = 0$) and the material parameter $\sigma = \cos(5\pi/6)$. (a) $t = 0$; (b) $t = 10$; (c) $t = 240$; (d) $t = 320$; (e) $t = 371$; (f) $t = 711$. Note the difference in vertical and horizontal scales.
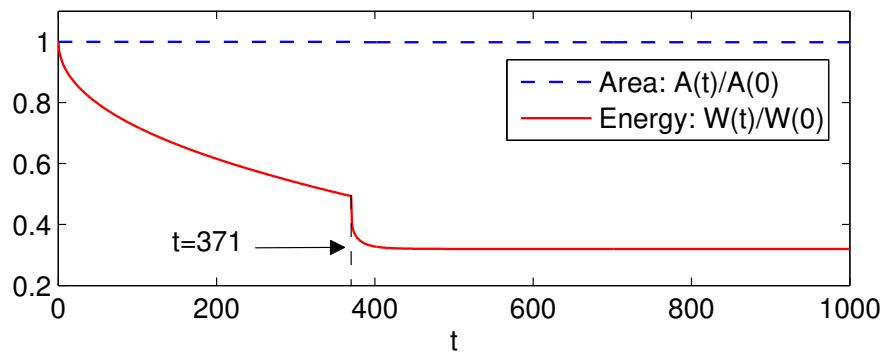
Figure 2.10: The corresponding temporal evolution in Fig. 2.9 for the normalized total free energy and the normalized area (mass).
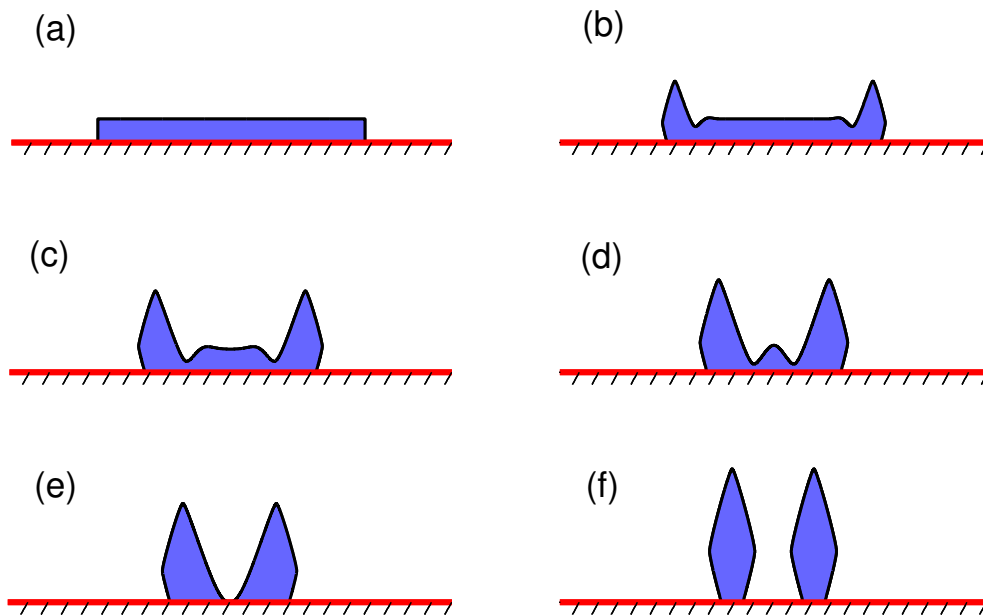
Figure 2.11: Several snapshots in the evolution of a long, thin island film (aspect ratio of 40) for surface energy defined in (2.5.2), with $L = 1, \phi_0 = \pi/4, \phi_1 = 3\pi/4, \delta_0 = \delta_1 = 0.1$. The material parameter is choen as $\sigma = \cos(5\pi/6)$: (a) $t = 0$; (b) $t = 10$; (c) $t = 50$; (d) $t = 100$; (e) $t = 140$; (f) $t = 400$. Note the difference in vertical and horizontal scales.

Fig. 2.9 depicts the temporal geometric evolution of this initially rectangular island during the solid-state dewetting. As can be seen in the figure, solid-state dewetting very quickly leads to the formation of ridges at the island edges followed by two valleys. As time evolves, the ridges and valleys become increasingly exaggerated, then the two valleys merge near the island center. At the time $t = 371$, the valley at the center of the island hits the substrate, leading to a pinch-off event that separates the initial island into a pair of islands. Finally, the two separated islands continue to evolve until they reach their equilibrium shapes. The corresponding evolution of the normalized total free energy and normalized total area (mass) are shown in Fig. 2.10. An interesting phenomenon here is that the total energy undergoes a sharp drop at $t = 371$, the moment when the pinch-off event occurs.

The pinch-off time $t = 371$ we obtained by using our PFEM for this particular example is very close to the result $t = 374$ by using marker-particle methods in [**?**]. But under the same computational resource, the computational time by using PFEM for this example is about two hours, while it is about two weeks by using marker-particle methods [120]. Besides, the obtained pinch-off time is exactly the same as the result by using another PFEM method recently proposed in [8] which does not use $\boldsymbol{\xi}$-vector and has more unknown variables in its variational form, and it validates the accuracy of the new PFEM from one side. Note here that once the interface curve hits the substrate somewhere in the simulation, it means that a pinch-off event has happened and a new contact point is generated, then after the pinch-off, we compute each part of the pinch-off curve separately.

The pinch-off event is not limited to the smooth k-fold anisotropy, and it can also be observed for other types of surface energy, e.g., Eq. (2.5.2). Fig. 2.11 shows the geometric evolution of a large, initially rectangular island with aspect ratio of 40. The material constant σ is chosen as the same as Fig. 2.9. The parameters which control the surface energy anisotropy are chosen as $K = 2, \phi_1 = \pi/4, \phi_2 = 3\pi/4, \delta_1 = \delta_2 = 0.1$. As shown in the figure, we can clearly observe that the thin film quickly forms valleys and ridges at its edges and then the pinch-off event happens

at about the time $t = 140$. Subsequently, the thin film breaks up into two small thin island pieces which finally evolve into their corresponding equilibrium shapes. This evolution process shares a similar geometric evolution with the smooth k-fold anisotropy.

2.5.4 Semi-infinite films

For the retraction of a semi-infinite step film, a lot of earlier studies have shown that the retraction distance $R(t)$ of a semi-infinite step film as a function of time satisfies a power-law relation [66,70,111,125], i.e., $R(t) \sim t^\alpha$. But most of the above studies focused on the isotropic surface energy case [66, 110, 125] or some specific forms of surface energy anisotropy [120, 138, 139]. For any form of surface energy anisotropy, does the power law exponent α depend on the type of surface energy anisotropy? this is still a question. Here, we want to investigate this power-law relation by performing ample numerical simulations on semi-infinite thin step films with the surface energy anisotropy defined in Eq. (2.5.2). As illustrated in Fig. 2.12 and Fig. 2.13, we simulate the retraction evolution process of a semi-infinite step film in two different cases. In both cases, the material constant is chosen as $\sigma = \cos \frac{5\pi}{6}$, while the anisotropies are chosen as two different parameters: for Case A, $\gamma(\mathbf{n})$ is chosen as the form of Eq. (2.5.2) with the parameters $(\phi_1, \phi_2) = (0, \frac{\pi}{2}), \delta_1 = \delta_2 = 0.1$; for Case B, $\gamma(\mathbf{n})$ is chosen as the form of Eq. (2.5.2) with the parameters $(\phi_1, \phi_2) = (\frac{\pi}{4}, \frac{3\pi}{4}), \delta_1 = \delta_2 = 0.1$. The surface energy density in Case B can be viewed as the rotation of $\frac{\pi}{4}$ for Case A.

As is clearly shown in Fig. 2.12, a ridge quickly forms at the retracting edge but no valley appears behind the ridge, and the whole semi-infinite step film gradually moves towards the right direction along the substrate. As time evolves, the ridge becomes higher and higher, but because no valley forms, the pinch-off will never happen. This can be explained as because the surface energy density attains its minimum at the orientations $\mathbf{n} = (0, 1), (1, 0), (-1, 0)$, and the step film quickly

evolves to its "quasi-equilibrium" shape, i.e., preferring its minimum energy orientations, and the oblique direction is not the most favorable energy directions, so valleys never form for this kind of surface energy. On the other hand, if we use another kind of surface energy (e.g. taking a 45 degrees rotation to the minimal energy orientations), as shown in Fig. 2.13, a valley will quickly form behind the ridge, and as time evolves, the valley sinks with time and eventually touches with the substrate, then the pinch-off will happen. It should be noted that, for isotropic surface energy, a lot of research works have shown that valleys always form ahead of retracting ridges and can eventually lead to the pinch-off phenomena [40, 66, 125]. However, for anisotropic surface energy, the situation is totally different, and valleys may appear or be absent at retracting edges according to different surface energies (shown in Fig. 2.12). This observation is consistent with experimental studies for single crystal thin films, and the formation of valleys ahead of the ridges can be observed or not observed in real experiments with different set-ups [138, 139].

,
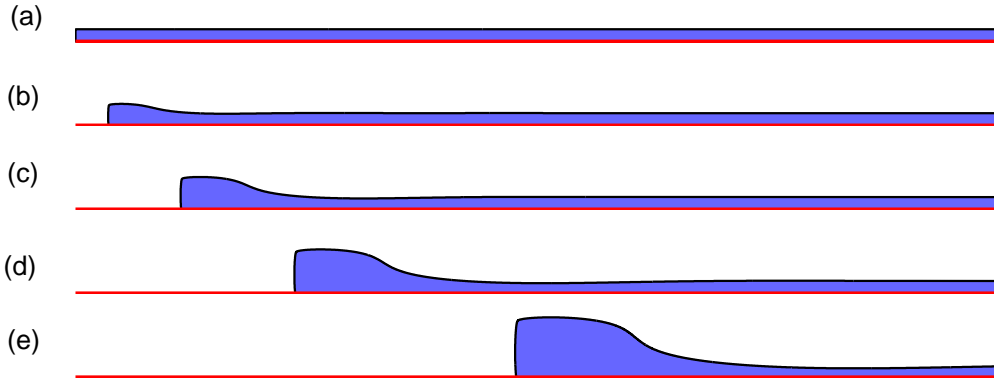
Figure 2.12: The evolution of semi infinite long film with parameter chosen as: $\sigma = \cos(\frac{5\pi}{6})$, γ is chosen as Eq. (2.5.2) with $L = 2$; $\phi = (0, \frac{\pi}{2}), \delta_1 = \delta_2 = 0.1$, where (a) $t = 0$; (b) $t = 10$; (c) $t = 100$; (d) $t = 500$; (e) $t = 2500$.

Figs. 2.14 and ig. 2.15 depict the log-log plots of the retraction distance $R(t)$ versus time t under different material constants σ, and the surface energy is chosen as the form of Eq. (2.5.2) with different controlled parameters: (a) $(\phi_1, \phi_2) =$
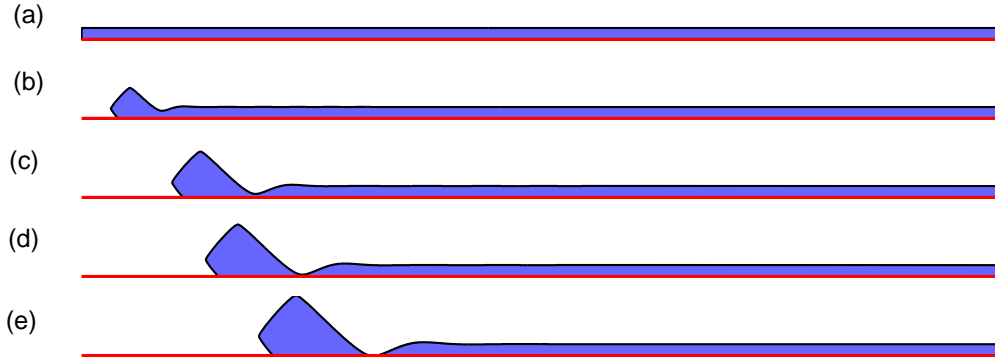
Figure 2.13: The evolution of semi infinite long film with parameter chosen as: $\sigma = \cos(\frac{5\pi}{6})$, γ is chosen as Eq. (2.5.2) with $L = 2$; $\phi = (\frac{\pi}{4}, \frac{3\pi}{4})$, $\delta_1 = \delta_2 = 0.1$, where (a) $t = 0$; (b) $t = 10$; (c) $t = 100$; (d) $t = 200$; (e) $t = 445$.
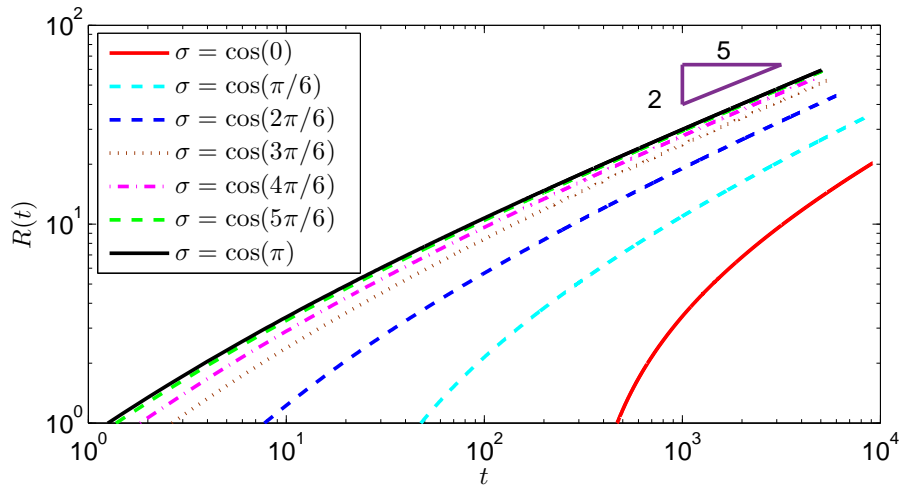
Figure 2.14: The retraction distance versus time t of a semi-infinite step film with the form of surface energy anisotropy defined in Eq. (2.5.2) under different material constants σ, where : $(\phi_1, \phi_2) = (0, \frac{\pi}{2})$, $\delta_1 = \delta_2 = 0.1$,.
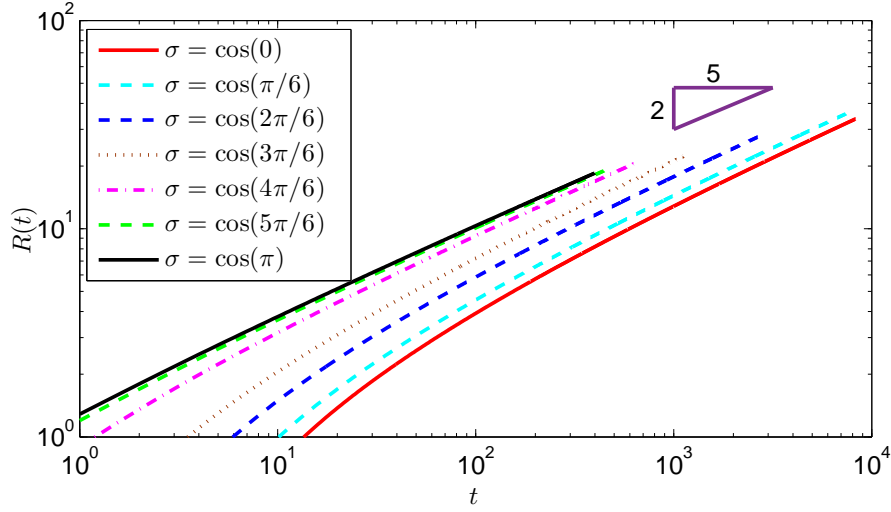
Figure 2.15: The retraction distance till the pinch off happening versus time t of a semi-infinite step film with the form of surface energy anisotropy defined in Eq. (2.5.2) under different material constants σ , where $(\phi_1, \phi_2) = (\frac{\pi}{4}, \frac{3\pi}{4}), \delta_1 = \delta_2 = 0.1$.

$(0, \frac{\pi}{2}), \delta_1 = \delta_2 = 0.1$; (b) $(\phi_1, \phi_2) = (\frac{\pi}{4}, \frac{3\pi}{4}), \delta_1 = \delta_2 = 0.1$. The numerical results clearly show that the retraction distance $R(t)$ can be well described by a power-law relation, and the power-law exponent $\alpha \approx 2/5$ is insensitive to the material constant and surface energy anisotropy.

2.6 Extension to strongly anisotropic case

Sharp corners would appear in the equilibrium shape when the surface stiffness $H_\gamma(\mathbf{n})\boldsymbol{\tau} \cdot \boldsymbol{\tau} = \gamma(\theta) + \gamma''(\theta) < 0$ for some orientations θ, i.e., the strongly anisotropic case. In this case, the sharp-interface governing equations (2.3.5)-(2.3.6) becomes ill-posed. These governing equations can be regularized by adding regularization terms such that the regularized sharp-interface model is well-posed. In this section, we regularize the total interfacial energy $W(\Gamma)$ defined in Eq. (2.1.2) by adding the well-known Willmore energy [57, 80], which is defined as

$$W_r = \frac{\delta^2}{2} \int_\Gamma \kappa^2 \, ds, \tag{2.6.1}$$

where κ is curvature of the curve and δ is a small regularization parameter. With this regularization, the dimensionless total energy can be written as follows

$$W_{reg}^{\delta} = W + W_r = \int_{\Gamma} \left(\gamma(\mathbf{n}) + \frac{\delta^2}{2} \kappa^2 \right) ds - \sigma(x_c^r - x_c^l). \tag{2.6.2}$$

2.6.1 The regularized energy and thermodynamic variation

In order to perform the first variation of the total surface energy defined in Eq. (2.6.2), we need the following lemma.

Lemma 2.6.1. *Suppose* $\Gamma = \mathbf{X}(s) \in C^4([0,L]) \times C^4([0,L])$ *is an open curve where* $s(0 \leq s \leq L)$ *is the arc length. Consider a perturbation for* Γ *with* $\mathbf{V}(\rho, \varepsilon)$ *representing the smooth variational vector field defined in Eq. (2.1.4). Let* $F(\Gamma) = \int_{\Gamma} \kappa^2 \, ds$, *then we have*

$$\begin{aligned} dF(\Gamma; \mathbf{V}) &= -\int_{\Gamma} (\kappa^3 + 2\partial_{ss}\kappa)(\mathbf{n} \cdot \mathbf{V}_0) ds \\ &\quad - \left(2\kappa \, \mathbf{n} \cdot \partial_s \mathbf{V}_0 - 2\partial_s \kappa \, (\mathbf{n} \cdot \mathbf{V}_0) + \kappa^2 (\boldsymbol{\tau} \cdot \mathbf{V}_0) \right) \Big|_{s=0}^{s=L}. \end{aligned} \tag{2.6.3}$$

Proof. If we define $\theta^{\varepsilon} = \theta(\rho, \varepsilon) = \arctan \frac{\partial_{\rho} y(\rho, \varepsilon)}{\partial_{\rho} x(\rho, \varepsilon)}$, then κ can be expressed as

$$\kappa^{\varepsilon} = -\partial_{s^{\varepsilon}} \theta^{\varepsilon} = -\frac{\partial_{\rho} \theta^{\varepsilon}}{|\partial_{\rho} \mathbf{X}(\rho, \varepsilon)|}. \tag{2.6.4}$$

From the parameterization defined in Eq. (**??**), $F(\Gamma^{\varepsilon})$ is given by

$$F(\Gamma^{\varepsilon}) = \int_0^1 (\kappa^{\varepsilon})^2 |\partial_{\rho} \mathbf{X}(\rho, \varepsilon)| \, d\rho. \tag{2.6.5}$$

By taking derivative of $F(\Gamma^{\varepsilon})$ with respect to ε and noting the independence between ε and ρ, based on Eq. (2.6.4), we have

$$\begin{aligned} \frac{d}{d\varepsilon} F(\Gamma^{\varepsilon}) &= \int_0^1 2\kappa^{\varepsilon} \partial_{\varepsilon} \kappa^{\varepsilon} |\partial_{\rho} \mathbf{X}(\rho, \varepsilon)| \, d\rho + \int_0^1 (\kappa^{\varepsilon})^2 \partial_{\varepsilon} |\partial_{\rho} \mathbf{X}(\rho, \varepsilon)| \, d\rho \\ &= -2 \int_0^1 \kappa^{\varepsilon} \partial_{\varepsilon} \partial_{\rho} \theta^{\varepsilon} \, d\rho - 2 \int_0^1 \kappa \partial_{\rho} \theta^{\varepsilon} \partial_{\varepsilon} \frac{1}{|\partial_{\rho} \mathbf{X}(\rho, \varepsilon)|} |\partial_{\rho} \mathbf{X}(\rho, \varepsilon)| \, d\rho \\ &\quad + \int_0^1 \kappa^2 \partial_{\varepsilon} |\partial_{\rho} \mathbf{X}(\rho, \varepsilon)| \, d\rho \\ &= I + II + III. \end{aligned} \tag{2.6.6}$$

Note that the expansion of θ^ε and $\frac{1}{|\partial_\rho \mathbf{X}(\rho,\varepsilon)|}$ at $\varepsilon = 0$ give us

$$\theta^\varepsilon = \theta - \frac{\partial_\rho \mathbf{X}^\perp \cdot \partial_\rho \mathbf{V}_0}{|\partial_\rho \mathbf{X}|^2}\varepsilon + O(\varepsilon^2) = \theta + \theta'\varepsilon + O(\varepsilon^2). \tag{2.6.7a}$$

$$\frac{1}{|\partial_\rho \mathbf{X}(\rho,\varepsilon)|} = \frac{1}{|\partial_\rho \mathbf{X}|} - \frac{\partial_\rho \mathbf{X} \cdot \partial_\rho \mathbf{V}_0}{|\partial_\rho \mathbf{X}|^3}\varepsilon + O(\varepsilon^2). \tag{2.6.7b}$$

Using above expansion and Eq. (2.1.10a), and for the three parts I, taking value at $\varepsilon = 0$ and then integration by parts, we have

$$
\begin{aligned}
I\Big|_{\varepsilon=0} &= \int_0^1 2\kappa(-\partial_\rho \theta')\, d\rho = -\Big(2\kappa\theta'\Big)\Big|_{\rho=0}^{\rho=1} - \int_0^1 2\partial_\rho \kappa \Big(\frac{\partial_\rho \mathbf{X}^\perp \cdot \partial_\rho \mathbf{V}_0}{|\partial_\rho \mathbf{X}|^2}\Big)\, d\rho \\
&= -\Big(2\kappa\theta'\Big)\Big|_{\rho=0}^{\rho=1} - \int_0^1 2\partial_\rho \kappa \Big(\frac{\partial_\rho \mathbf{X}^\perp \cdot \partial_\rho \mathbf{V}_0}{|\partial_\rho \mathbf{X}|^2}\Big)\, d\rho \\
&= -\Big(2\kappa\theta'\Big)\Big|_{\rho=0}^{\rho=1} - \Big(\frac{2\partial_\rho \kappa \partial_\rho \mathbf{X}^\perp \cdot \mathbf{V}_0}{|\partial_\rho \mathbf{X}|^2}\Big)\Big|_{\rho=0}^{\rho=1} + \int_0^1 \partial_\rho \Big(\frac{2\partial_\rho \kappa \partial_\rho \mathbf{X}^\perp}{|\partial_\rho \mathbf{X}|^2}\Big) \cdot \mathbf{V}_0 \, d\rho \\
&= -\Big(2\kappa\theta'\Big)\Big|_{\rho=0}^{\rho=1} - \Big(\frac{2\partial_\rho \kappa \partial_\rho \mathbf{X}^\perp \cdot \mathbf{V}_0}{|\partial_\rho \mathbf{X}|^2}\Big)\Big|_{\rho=0}^{\rho=1} + \int_\Gamma (2\partial_{ss}\kappa\partial_s \mathbf{X}^\perp + 2\partial_s\kappa\partial_{ss}\mathbf{X}^\perp) \cdot \mathbf{V}_0 \, ds \\
&= \Big(-2\kappa\theta' + 2\partial_s\kappa\, \mathbf{n}\cdot \mathbf{V}_0\Big)\Big|_{s=0}^{s=L} - 2\int_\Gamma (\partial_{ss}\kappa \mathbf{n} + \partial_s\kappa\kappa\boldsymbol{\tau}) \cdot \mathbf{V}_0 \, ds. \tag{2.6.8}
\end{aligned}
$$

$$
\begin{aligned}
II\Big|_{\varepsilon=0} &= \int_0^1 2\kappa\partial_\rho\theta \frac{\partial_\rho \mathbf{X} \cdot \partial_\rho \mathbf{V}_0}{|\partial_\rho \mathbf{X}|^2}\, d\rho = 2\Big(\kappa\partial_\rho\theta\frac{\partial_\rho \mathbf{X} \cdot \mathbf{V}_0}{|\partial_\rho \mathbf{X}|^2}\Big)\Big|_{\rho=0}^{\rho=1} - \int_0^1 2\partial_\rho \Big(\kappa\partial_\rho\theta\frac{\partial_\rho \mathbf{X}}{|\partial_\rho \mathbf{X}|^2}\Big)\mathbf{V}_0 \, d\rho \\
&= 2\Big(\kappa\partial_\rho\theta\frac{\partial_\rho \mathbf{X} \cdot \mathbf{V}_0}{|\partial_\rho \mathbf{X}|^2}\Big)\Big|_{\rho=0}^{\rho=1} + \int_\Gamma 2\partial_s(\kappa^2\partial_s \mathbf{X}) \cdot \mathbf{V}_0 \, ds \\
&= 2\Big(\kappa\partial_\rho\theta\frac{\partial_\rho \mathbf{X} \cdot \mathbf{V}_0}{|\partial_\rho \mathbf{X}|^2}\Big)\Big|_{\rho=0}^{\rho=1} + \int_\Gamma (4\kappa\partial_s\kappa\partial_s \mathbf{X} + 2\kappa^2\partial_{ss}\mathbf{X}) \cdot \mathbf{V}_0 \, ds \\
&= -2\Big(\kappa^2\boldsymbol{\tau}\cdot \mathbf{V}_0\Big)\Big|_{s=0}^{s=L} + 2\int_\Gamma (2\kappa\partial_s\kappa\boldsymbol{\tau} - \kappa^3\mathbf{n}) \cdot \mathbf{V}_0 \, ds. \tag{2.6.9}
\end{aligned}
$$

$$
\begin{aligned}
III\Big|_{\varepsilon=0} &= \int_0^1 \kappa^2\frac{\partial_\rho \mathbf{X} \cdot \partial_\rho \mathbf{V}_0}{|\partial_\rho \mathbf{X}|}\, d\rho = \Big(\kappa^2\frac{\partial_\rho \mathbf{X} \cdot \mathbf{V}_0}{|\partial_\rho \mathbf{X}|}\Big)_{\rho=0}^{\rho=1} - \int_0^1 \partial_\rho \Big(\kappa^2\frac{\partial_\rho \mathbf{X}}{|\partial_\rho \mathbf{X}|}\Big)\mathbf{V}_0 \, d\rho \\
&= \Big(\kappa^2\frac{\partial_\rho \mathbf{X} \cdot \mathbf{V}_0}{|\partial_\rho \mathbf{X}|}\Big)\Big|_{\rho=0}^{\rho=1} - \int_\Gamma \partial_s\Big(\kappa^2\partial_s \mathbf{X}\Big) \cdot \mathbf{V}_0 \, ds \\
&= \Big(\kappa^2\frac{\partial_\rho \mathbf{X} \cdot \mathbf{V}_0}{|\partial_\rho \mathbf{X}|}\Big)\Big|_{\rho=0}^{\rho=1} - \int_\Gamma (2\kappa\partial_s\kappa\partial_s \mathbf{X} + \kappa^2\partial_{ss}\mathbf{X}) \cdot \mathbf{V}_0 \, ds \\
&= \Big(\kappa^2\boldsymbol{\tau}\cdot \mathbf{V}_0\Big)\Big|_{s=0}^{s=L} - \int_\Gamma (2\kappa\partial_s\kappa\boldsymbol{\tau} - \kappa^3\mathbf{n}) \cdot \mathbf{V}_0 \, ds. \tag{2.6.10}
\end{aligned}
$$

Summarising them together, so we obtain

$$
\begin{aligned}
dF(\Gamma; \mathbf{V}_0) &= (I + II + III)\Big|_{\varepsilon=0} \\
&= -\int_\Gamma (\kappa^3 + 2\partial_{ss}\kappa)\,\mathbf{n}\cdot\mathbf{V}_0\,ds - \Big(2\kappa\theta'\Big)\Big|_{s=0}^{s=L} + \Big((2\partial_s\kappa\mathbf{n} - \kappa^2\boldsymbol{\tau})\cdot\mathbf{V}_0\Big)\Big|_{s=0}^{s=L}.
\end{aligned}
$$

Note that θ' is defined as

$$
\theta' = -\frac{\partial_\rho\mathbf{X}^\perp\cdot\partial_\rho\mathbf{V}_0}{|\partial_\rho\mathbf{X}|^2} = \mathbf{n}\cdot\partial_s\mathbf{V}_0, \tag{2.6.11}
$$

thus we have

$$
\begin{aligned}
dF(\Gamma; \mathbf{V}_0) &= -\int_\Gamma (\kappa^3 + 2\partial_{ss}\kappa)\,(\mathbf{n}\cdot\mathbf{V}_0\,)ds \\
&\quad - \Big(2\kappa\,\mathbf{n}\cdot\partial_s\mathbf{V}_0 - 2\partial_s\kappa\,(\mathbf{n}\cdot\mathbf{V}_0) + \kappa^2\,(\boldsymbol{\tau}\cdot\mathbf{V}_0)\Big)\Big|_{s=0}^{s=L}. \tag{2.6.12}
\end{aligned}
$$

$\square$

Proposition 2.6.1. *Suppose* $\Gamma = \mathbf{X}(s) \in C^4([0, L]) \times C^4([0, L])$ *is a closed curve where* $s(0 \le s \le L)$ *is the arc length. Let* $F(\Gamma) = \int_\Gamma \kappa^2\,ds$, *then we have*

$$
dF(\Gamma; \mathbf{V}) = -\int_\Gamma (\kappa^3 + 2\partial_{ss}\kappa)\,\mathbf{n}\cdot\mathbf{V}_0\,ds. \tag{2.6.13}
$$

Proof. The proof is similar to that of the lemma 2.6.1, but integration by parts will not give us any boundary terms due to the periodic boundary conditions. $\square$

2.6.2 The regularized model

Now, based on the energy form Eq. (2.6.2), from the lemma. 2.6.1, the first variation of the regularized term is given by

$$
\begin{aligned}
dW_r(\Gamma; \mathbf{V}) &= -\delta^2\int_\Gamma (\frac{\kappa^3}{2} + \partial_{ss}\kappa)\,\mathbf{n}\cdot\mathbf{V}_0\,ds \\
&\quad + \delta^2\Big(\kappa\,\mathbf{n}\cdot\partial_s\mathbf{V}_0 - \partial_s\kappa\,(\mathbf{n}\cdot\mathbf{V}_0) + \frac{\kappa^2}{2}\,\boldsymbol{\tau}\cdot\mathbf{V}_0\Big)\Big|_{s=0}^{s=L}. \tag{2.6.14}
\end{aligned}
$$

The boundary term $-\Big(2\kappa\mathbf{n}\cdot\partial_s\mathbf{V}_0\Big)\Big|_{s=0}^{s=L}$ inspires us to include the zero curvature boundary conditions into the model to ensure the energy decay for any arbitrary ε. In addition, the variation vector field is assume to satisfy $(V_x, V_y) = \mathbf{V}_0 \mathbin{/\mkern-5mu/} \mathbf{x}^+$ on

the boundary. Combined with the Eq. (3.2.11), the first variation of the strongly anisotropic surface energy is given by

$$
\begin{aligned}
dW_{reg}^{\delta}(\Gamma; \mathbf{V}) &= \Big[V_x(\xi_2 - \sigma + \delta^2 n_1 \partial_s \kappa) \Big]\Big|_{s=L} - \Big[V_x(\xi_2 - \sigma + \delta^2 n_1 \partial_s \kappa) \Big]\Big|_{s=0} \\
&\quad - \int_{\Gamma} \Big(\partial_s \boldsymbol{\xi}^{\perp} + \delta^2 (\frac{\kappa^3}{2} + \partial_{ss}\kappa)\mathbf{n} \Big) \cdot \mathbf{V}_0 \; ds.
\end{aligned} \tag{2.6.15}
$$

Thus we obtain the first variation of the strongly anisotropic surface energy with respect to the curve Γ and the two contact points are given as follows

$$
\frac{\delta W_{reg}^{\delta}}{\delta \Gamma} = -[\partial_s \boldsymbol{\xi}]^{\perp} \cdot \mathbf{n} - \delta^2 (\frac{\kappa^3}{2} + \partial_{ss}\kappa), \tag{2.6.16}
$$

$$
\frac{\delta W_{reg}^{\delta}}{\delta x_c^l} = -\Big[\xi_2 - \sigma + \delta^2 n_1 \partial_s \kappa \Big]\Big|_{s=0}, \tag{2.6.17}
$$

$$
\frac{\delta W_{reg}^{\delta}}{\delta x_c^r} = \Big[\xi_2 - \sigma + \delta^2 n_1 \partial_s \kappa \Big]\Big|_{s=L}. \tag{2.6.18}
$$

Similar to the weakly anisotropic case and by using the same dimensionless scale units, we can obtain a dimensionless sharp-interface model again [8, 67] for solid-state dewetting of thin films with strongly anisotropic surface energy via a $\boldsymbol{\xi}$-vector formulation, which can be written as follows (for simplicity, we still use the same notations for the variables):

$$
\partial_t \mathbf{X} = \partial_{ss}\mu \; \mathbf{n}, \qquad 0 < s < L(t), \qquad t > 0, \tag{2.6.19}
$$

$$
\mu = -[\partial_s \boldsymbol{\xi}]^{\perp} \cdot \mathbf{n} - \delta^2 \Big(\frac{\kappa^3}{2} + \partial_{ss}\kappa \Big), \quad \kappa = -(\partial_{ss}\mathbf{X}) \cdot \mathbf{n}, \tag{2.6.20}
$$

where $\Gamma := \Gamma(t) = \mathbf{X}(s,t) = (x(s,t), y(s,t))$ represents the moving film/vapor interface, s is the arc length or distance along the interface, t is the time, $\mathbf{n} = (n_1, n_2) = (-\partial_s y, \partial_s x)$ is the interface outer unit normal vector, $\mu := \mu(s,t)$ is the chemical potential, $\boldsymbol{\xi} = (\xi_1, \xi_2)$ is the Cahn-Hoffman vector and $L := L(t)$ represents the total length of the moving interface, ε is a small regularization parameter. The initial condition is given as

$$
\mathbf{X}(s,0) := \mathbf{X}_0(s) = (x(s,0), y(s,0)) = (x_0(s), y_0(s)), 0 \le s \le L_0 := L(0), \tag{2.6.21}
$$

satisfying $y_0(0) = y_0(L_0) = 0$ and $x_0(0) < x_0(L_0)$, and the boundary conditions are:

(i) contact point condition:

$$y(0,t) = 0, \qquad y(L,t) = 0, \qquad t \geq 0, \tag{2.6.22}$$

(ii) relaxed (or dissipative) contact angle condition:

$$\frac{dx_c^l}{dt} = \eta \left[\xi_2 - \sigma_0 + \delta^2 \partial_s \kappa n_1 \right]\Big|_{s=0}, \qquad \frac{dx_c^r}{dt} = -\eta \left[\xi_2 - \sigma_0 + \delta^2 \partial_s \kappa n_1 \right]\Big|_{s=L}, \tag{2.6.23}$$

(iii) zero-mass flux condition:

$$\partial_s \mu(0,t) = 0, \qquad \partial_s \mu(L,t) = 0, \qquad t \geq 0, \tag{2.6.24}$$

(iv) zero-curvature condition

$$\kappa(0,t) = 0, \qquad \kappa(L,t) = 0, \qquad t \geq 0. \tag{2.6.25}$$

In the following we will show that the total mass of the thin film is always conserved during the evolution, and the total free energy of the system decreases monotonically at all times.

Proposition 2.6.2 (Mass conservation and energy dissipation). *Let $\Gamma(t) = \mathbf{X}(s,t)$ be the exact solution of the Eqs. (2.6.19)-(2.6.20) coupled with boundary conditions Eqs. (2.6.22)-(2.6.25). Given the initial curve $\Gamma(0) = (x_0(s), y_0(s))$, then the total mass of the thin film is conserved during the evolution, i.e.,*

$$A(t) \equiv A(0) = \int_{\Gamma(0)} y_0(s) \partial_s x_0(s)\, ds, \qquad t \geq 0, \tag{2.6.26}$$

and the total energy of the thin film is decreasing during the evolution, i.e.,

$$W_{reg}^{\delta}(t) \leq W_{reg}^{\delta}(t_1) \leq W_{reg}^{\delta}(0) = \int_{\Gamma(0)} \left(\gamma(\theta) + \delta^2 \frac{\kappa^2}{2} \right) ds - (x_c^r(0) - x_c^l(0))\sigma,$$
$$t \geq t_1 \geq 0. \tag{2.6.27}$$

Proof. The proof for the mass conservation is the same as that for the weak case. For the energy, based on the variation form in Eq. (2.6.15), we have:

$$\begin{aligned} \frac{d}{dt} W_{reg}^{\delta} &= -\int_{\Gamma} \left[\partial_s \boldsymbol{\xi}^{\perp} + \delta^2 \left(\frac{\kappa^3}{2} + \partial_{ss}\kappa \right) \mathbf{n} \right] \cdot \mathbf{X}_t\, ds \\ &+ \frac{dx_c^r}{dt} \left[\xi_2 - \sigma + \delta^2 \partial_s \kappa n_1 \right]\Big|_{s=L} - \frac{dx_c^l}{dt} \left[\xi_2 - \sigma + \delta^2 \partial_s \kappa n_1 \right]\Big|_{s=0}. \end{aligned} \tag{2.6.28}$$

Using the Eq. (2.6.19), Eq. (2.6.20) and the contact line moving boundary conditions, we have:

$$
\begin{aligned}
\frac{d}{dt} W_{reg}^{\delta} &= \int_{\Gamma(t)} \mu \mu_{ss} \, ds - \frac{1}{\eta} \Big[(\frac{dx_c^l}{dt})^2 + (\frac{dx_c^r}{dt})^2 \Big] \\
&= -\int_{\Gamma(t)} (\mu_s)^2 \, ds - \frac{1}{\eta} \Big[(\frac{dx_c^l}{dt})^2 + (\frac{dx_c^r}{dt})^2 \Big] \le 0.
\end{aligned}
\tag{2.6.29}
$$

Note the last identity follows from the zero mass flux boundary condition. □

2.6.3 A discretization by PFEM

In order to obtain the variational formulation for equations (2.6.19),(2.6.20) with the boundary conditions (2.6.22)-(2.6.25), we need to introduce a new vector $\mathbf{I}$. Here we assume $\mathbf{I}$ is parallel to $\mathbf{n}$, thus we are able to rewrite the equations in the following form

$$
\partial_t \mathbf{X} \cdot \mathbf{n} = \partial_{ss} \mu, \qquad \mu \, \mathbf{n} = -[\partial_s \boldsymbol{\xi}]^{\perp} - \delta^2 \mathbf{I},
\tag{2.6.30}
$$

$$
\mathbf{I} \cdot \mathbf{n} = (\frac{1}{2}\kappa^3 + \partial_{ss}\kappa), \qquad \kappa \, \mathbf{n} = -\partial_{ss}\mathbf{X}.
\tag{2.6.31}
$$

By using the integration by parts, the weak formulation for solid-state dewetting problems with strongly anisotropic surface energy can be stated as the following variational problem: given the initial curve $\Gamma(0) = \mathbf{X}(\rho, 0), \rho \in I$, for every time $t \in (0, T]$, find the evolution curves $\Gamma(t) = \mathbf{X}(\rho, t) \in H_{a,b}^1(I) \times H_0^1(I)$ with the x-coordinate positions of moving contact points $a = x_c^l(t) \le x_c^r(t) = b$, the chemical potential $\mu(\rho, t) \in H^1(I)$, $\mathbf{I}(\rho, t) \in H^1(I) \times H^1(I)$ and the curvature $\kappa(\rho, t) \in H_0^1(I)$ such that

$$
\big\langle \partial_t \mathbf{X}, \, \varphi \mathbf{n} \big\rangle_\Gamma + \big\langle \partial_s \mu, \, \partial_s \varphi \big\rangle_\Gamma = 0, \quad \forall \, \varphi \in H^1(I),
\tag{2.6.32a}
$$

$$
\big\langle \mu \mathbf{n}, \, \boldsymbol{\omega}_1 \big\rangle_\Gamma - \big\langle \boldsymbol{\xi}^{\perp}, \, \partial_s \boldsymbol{\omega}_1 \big\rangle_\Gamma - \delta^2 \big\langle \mathbf{I}, \, \boldsymbol{\omega}_1 \big\rangle_\Gamma + (\boldsymbol{\xi}^{\perp} \cdot \boldsymbol{\omega}_1)|_{s=0}^{s=L(t)} = 0,
$$

$$
\forall \boldsymbol{\omega}_1 \in (H^1(I))^2,
\tag{2.6.32b}
$$

$$
\big\langle \mathbf{I}, \, \mathbf{n}\phi \big\rangle_\Gamma - \frac{1}{2}\big\langle \kappa^3, \, \phi \big\rangle_\Gamma + \big\langle \partial_s \kappa, \, \partial_s \phi \big\rangle_\Gamma = 0, \quad \forall \phi \in H_0^1(I),
\tag{2.6.32c}
$$

$$
\big\langle \kappa \mathbf{n}, \, \boldsymbol{\omega_2} \big\rangle_\Gamma - \big\langle \partial_s \mathbf{X}, \, \partial_s \boldsymbol{\omega_2} \big\rangle_\Gamma = 0, \quad \forall \boldsymbol{\omega_2} \in (H_0^1(I))^2.
\tag{2.6.32d}
$$

After temporal and spatial discretization, the full-discrete finite element scheme for the variational formulation (2.6.32a)-(2.6.32d) then can be described as: given the curve $\Gamma^m = \mathbf{X}^m$ $(m = 0, 1, \ldots, M-1)$, for the next time level t_{m+1}, find the numerical solution for evolution curves $\Gamma^{m+1} = \mathbf{X}^{m+1} \in \mathcal{V}_{a,b}^h \times \mathcal{V}_0^h$ with the x-coordinate positions of moving contact points $a = x_c^l(t_{m+1}) \le x_c^r(t_{m+1}) = b$, the numerical solution for $\mathbf{I}^{m+1} \in V^h \times V^h$, chemical potential $\mu^{m+1} \in V^h$ and the numerical solution for curvature $\kappa^{m+1} \in \mathcal{V}_0^h$ such that:

$$\left\langle \frac{\mathbf{X}^{m+1} - \mathbf{X}^m}{\tau_m}, \ \varphi_h \mathbf{n}^m \right\rangle_{\Gamma^m}^h + \left\langle \partial_s \mu^{m+1}, \ \partial_s \varphi_h \right\rangle_{\Gamma^m}^h = 0, \quad \forall \, \varphi_h \in V^h, \tag{2.6.33a}$$

$$\left\langle \mu^{m+1} \mathbf{n}^m - \delta^2 \mathbf{I}^{m+1}, \ \boldsymbol{\omega}_{1h} \right\rangle_{\Gamma^m}^h - \left\langle (\boldsymbol{\xi}^{m+\frac{1}{2}})^{\perp}, \ \partial_s \boldsymbol{\omega}_{1h} \right\rangle_{\Gamma^m}^h = -(\boldsymbol{\xi}^m)^{\perp} \cdot \boldsymbol{\omega}_{1h} \Big|_{\rho=0}^{\rho=1},$$
$$\forall \boldsymbol{\omega}_{1h} \in (V^h)^2, \tag{2.6.33b}$$

$$\left\langle \mathbf{I}^{m+1}, \ \mathbf{n}^m \phi_h \right\rangle_{\Gamma^m}^h - \frac{1}{2} \left\langle (\kappa^m)^2 \kappa^{m+1}, \ \phi_h \right\rangle_{\Gamma^m}^h + \left\langle \partial_s \kappa^{m+1}, \ \partial_s \phi_h \right\rangle_{\Gamma^m}^h = 0,$$
$$\forall \phi_h \in \mathcal{V}_0^h, \tag{2.6.33c}$$

$$\left\langle \kappa^{m+1} \mathbf{n}^m, \ \boldsymbol{\omega}_{2h} \right\rangle_{\Gamma^m}^h - \left\langle \partial_s \mathbf{X}^{m+1}, \ \partial_s \boldsymbol{\omega}_{2h} \right\rangle_{\Gamma^m}^h = 0, \quad \forall \boldsymbol{\omega}_{2h} \in (\mathcal{V}_0^h)^2. \tag{2.6.33d}$$

Here $x_c^l(t_{m+1})$ and $x_c^r(t_{m+1})$ are updated from Eqs. (2.6.23) by Euler forward scheme.

2.6.4 Numerical results

In the following, we will present some numerical convergence tests of our fully discrete scheme (2.6.33a),(2.6.33b),(2.6.33c),(2.6.33d). Similar to the weak anisotropy, we perform our numerical scheme on both closed curve evolution and open curve evolution (solid-state dewetting). For closed curve evolution, shown in Table. 2.5, the initial shape of thin film is chosen as a closed tube, i.e., a rectangle of length 4 and width 1 added by two semi-circles with radii of 0.5 to its left and right sides, and the parameters are chosen as $h_0 = (8+\pi)/120$ and $\tau_0 = 0.005$; for an open curve evolution, shown in Table 2.4, the initial shape of thin film is chosen as a rectangle island of length 5 and thickness 1, and $h_0 = 0.1$ and $\tau_0 = 0.0005 = 0.05h_0^2$. Table. 2.5 shows the convergence rate in the L^∞ norm for a closed curve evolution under the strongly anisotropic surface diffusion flow, where $\gamma(\theta) = 1 + 0.1\cos(4\theta), \delta = 0.1$. It clearly shows that the convergence order is around second order, while for open

curves, the convergence order decrease to first order. Same as the isotropic/weakly anisotropic case, the decrease of the convergence order may due to the application of the forward Euler scheme on the relaxed contact angle conditions.

Table 2.5: Convergence rates in the L^∞ norm for a closed curve evolution under the anisotropic surface diffusion flow, where $\gamma(\theta) = 1 + 0.1\cos(4\theta), \delta = 0.1$.

$e_{h,\tau}(t)$	$h = h_0$ $\tau = \tau_0$	$h_0/2$ $\tau_0/2^2$	$h_0/2^2$ $\tau_0/2^4$	$h_0/2^3$ $\tau_0/2^6$
$e_{h,\tau}(t=0.5)$	1.54E-3	6.22E-4	1.57E-4	3.80E-5
order	–	1.31	1.98	2.07
$e_{h,\tau}(t=2.0)$	7.66E-4	2.21E-4	5.51E-4	1.30E-5
order	–	1.79	2.01	2.06
$e_{h,\tau}(t=5.0)$	7.52E-4	2.10E-4	5.32E-4	1.30E-5
order	–	1.84	1.98	2.03

Table 2.6: Convergence rates in the L^∞ norm for an open curve evolution under the strongly anisotropic surface diffusion flow (solid-state dewetting with isotropic surface energy), where $\gamma(\theta) = 1 + 0.1\cos(4\theta), \delta = 0.1, \sigma = \cos(5\pi/6)$.

$e_{h,\tau}(t)$	$h = h_0$ $\tau = \tau_0$	$h_0/2$ $\tau_0/2^2$	$h_0/2^2$ $\tau_0/2^4$	$h_0/2^3$ $\tau_0/2^6$
$e_{h,\tau}(t=0.5)$	3.25E-2	1.60E-2	8.14E-3	4.16E-3
order	–	1.02	0.98	0.97
$e_{h,\tau}(t=2.0)$	2.67E-2	1.41E-2	7.23E-3	3.70E-3
order	–	0.92	0.97	0.97
$e_{h,\tau}(t=5.0)$	2.33E-2	1.18E-3	6.02E-3	3.05E-3
order	–	0.98	0.98	0.98
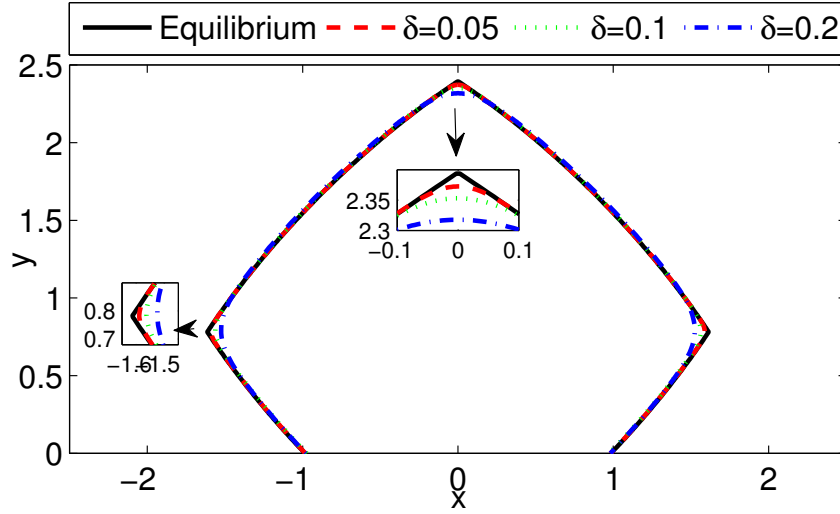
Figure 2.16: Comparison of the numerical equilibrium shapes of thin island film with its theoretical equilibrium shape for several values of regularization parameter δ, where the solid black lines represent the theoretical equilibrium and colored lines represent the numerical equilibriums, and $\gamma(\theta) = 1 + 0.2\cos(4\theta), \sigma = \cos(2\pi/3)$.

Fig. 2.16 plots the numerical equilibrium shapes for $\delta = 0.2, 0.1, 0.05$ as well as the theoretical equilibrium shape (show in solid blue line) under the parameter $\sigma = \cos(2\pi/3), \gamma(\theta) = 1 + 0.2\cos(4\theta)$. The numerical equilibrium shapes converge to the theoretical equilibrium shape when the regularization parameter ϵ approaches zero. As illustrated in Fig. 2.17, we also compute the equilibrium shape for a small, initially rectangular island film with different strongly anisotropic smooth k-fold surface energy under the parameters $\sigma = \cos(3\pi/4), \delta = 0.1$. Fig. 2.17(a)-(b) depict the effect of increasing the degree of anisotropy from $\beta = 0.1$ to $\beta = 0.3$ for 4-fold crystalline symmetry, and we can see that the equilibrium shape becomes more and more faceting. The effect of increasing the rotational symmetry, which is reflected from increasing the parameter k, can be observed from Fig. 2.17(c) ($k = 3, \beta = 0.3$) to Fig. 2.17(d) ($k = 6, \beta = 0.1$).

The numerical example for strongly anisotropic case is set up as follows. The initial thin film is chosen as a rectangular island with width $L = 5$ and height
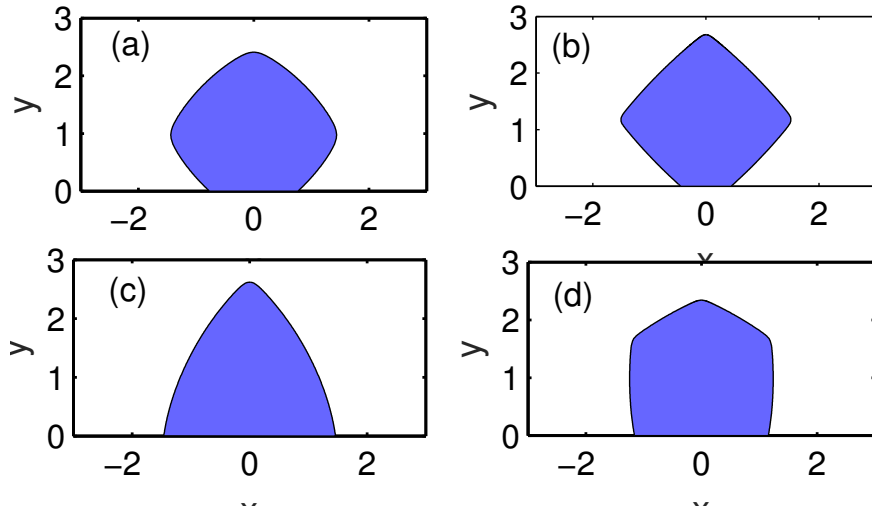
Figure 2.17: Equilibrium island morphologies for a small, initially rectangular island under several different crystalline fold of symmetry k and degree of anisotropy β respectively. (a) $k = 4, \beta = 0.1$; (b) $k = 4, \beta = 0.3$; (c) $k = 3, \beta = 0.3$; (d) $k = 6, \beta = 0.1$. The other computational parameters are chosen as, $\phi = 0, \sigma = \cos(3\pi/4), \delta = 0.1$.
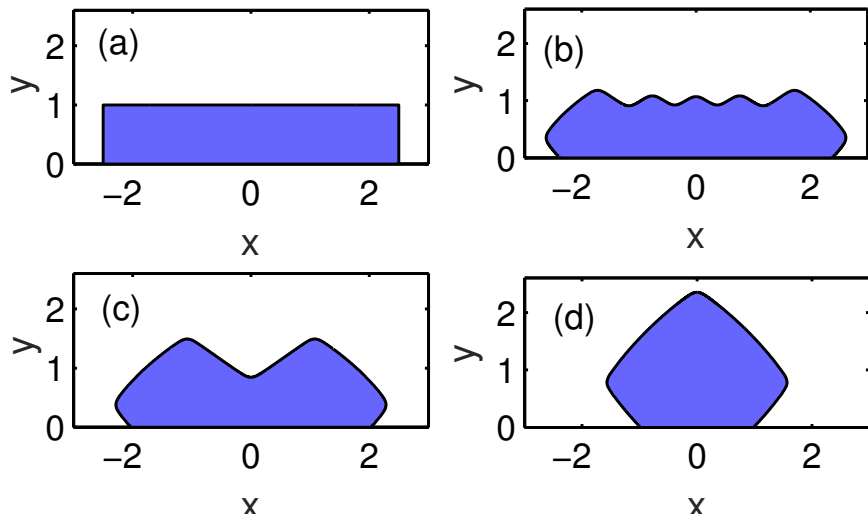
Figure 2.18: Several snapshots in the geometric evolution of a small initially rectangular island to the equilibrium shape (blue line). (a) $t = 0$, (b) $t = 0.02$, (c) $t = 0.04$, (d) $t = 10.32$, where $\gamma(\theta) = 1 + 0.2\cos(4\theta)$, $\sigma = \cos(2\pi/3), \delta = 0.1$.
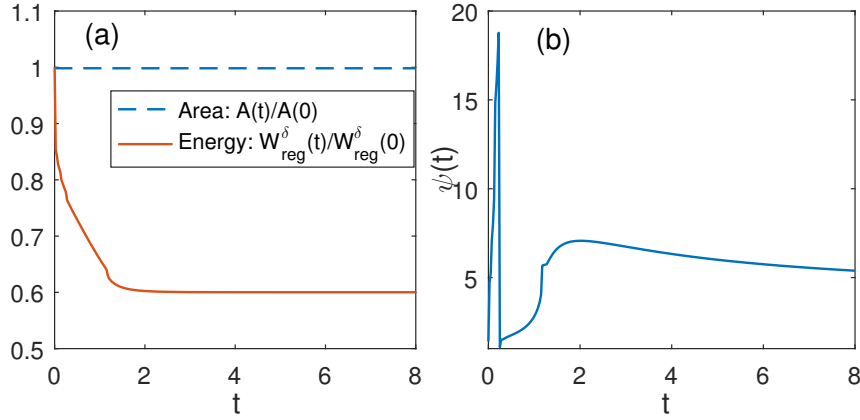
Figure 2.19: (a) The temporal evolution of the normalized free energy and normalized area, (b) the temporal evolution of the mesh distribution function $\psi(t)$, where $\gamma(\theta) = 1 + 0.2 \cos(4\theta), \sigma = \cos \frac{2\pi}{3}, \delta = 0.1$.

$h = 1$. The anisotropic surface energy is given by the 4-fold crystalline surface energy defined in Eq. (2.5.1) with $\beta = 0.2$. The computational parameters are chosen as $\sigma = \cos(2\pi/3), \delta = 0.1$. As depicted in Fig. 2.18, it shows the kinetic evolution process of an initial rectangle island film towards its equilibrium shape. We can observe that wavy structure first appears during the evolution (Fig. 2.18(b)), and eventually the island film evolves into an almost "faceting" shape with three regularized rounded corners (Fig. 2.18(d)).

The corresponding temporal evolution of the free energy and area are shown in Fig. 2.19. From the figure, we can observe that the area conservation and energy dissipation are well satisfied for the discrete numerical solutions. Moreover, Fig. 2.19(b) shows the value of mesh distribution function during the evolution. The mesh distribution function is cut from the top at value 20 because of the artificial re-mesh during the evolution when ψ is bigger than 20. We find that when the surface energy is strongly anisotropic, the mesh could be deteriorated in a very short time from the initial. Thus this re-mesh is essential and necessary to enable the stability of the scheme. Luckily, it is only needed in the earlier stage of the evolution and the mesh can be well preserved in the later time.

A Sharp Interface Model in Three Dimensions
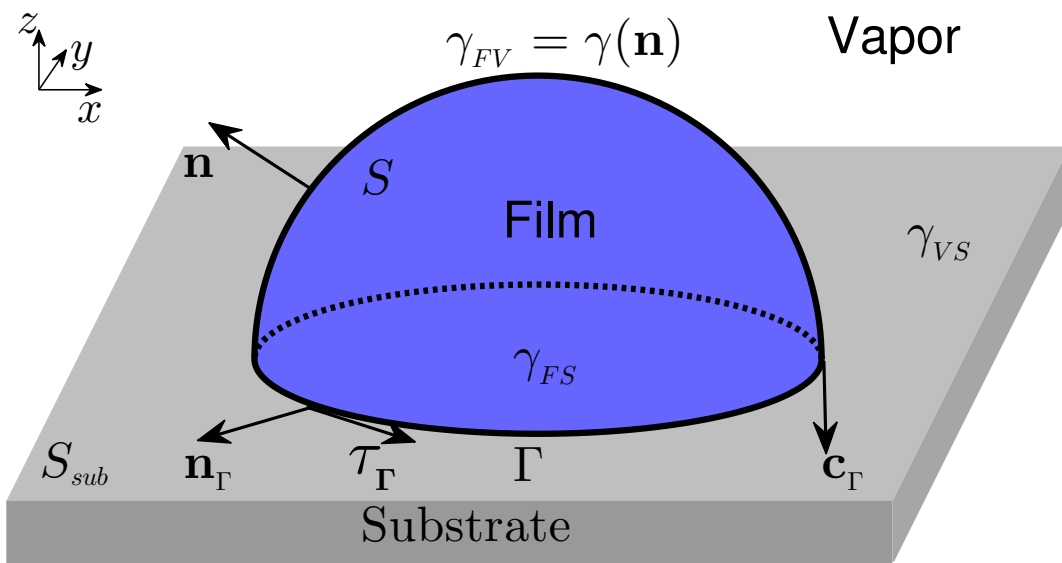
Figure 3.1: A schematic illustration of solid-state dewetting on a rigid flat substrate in three dimensions.

As depicted in Figure. 3.1, a solid thin film (colored in blue) lies on a flat rigid

substrate (colored in gray). The moving film/vapor interface is geometrically described by a two-dimensional open manifold S with boundary Γ, where Γ is a closed plane curve attached to the flat substrate S_{sub}. The unit vector $\mathbf{n}$ represents the normal direction of S and points towards the vapour while $\mathbf{n}_\Gamma$, $\boldsymbol{\tau}_\Gamma$ and $\mathbf{c}_\Gamma$ are three unit vectors defined along the boundary Γ. Exactly, $\mathbf{n}_\Gamma$ is the outer unit normal vector of the plane curve Γ on the substrate S_{sub}. $\boldsymbol{\tau}_\Gamma$ is the unit tangent vector of Γ on the substrate S_{sub} and pointing in the counter-clockwise direction when viewed from the $+z$ axis. The unit vector $\mathbf{c}_\Gamma$, called the co-normal vector, is normal to Γ, tangent to S and pointing outwards, see Fig. 3.1. In other words, for $\mathbf{x} \in S$, if we denote $\mathcal{T}_\mathbf{x} S$ and $\mathcal{N}_\mathbf{x} S$ as the tangent and normal space to S respectively, then the following expressions hold,

$$
\begin{aligned}
&\mathbf{n}(\mathbf{x}) \in \mathcal{N}_\mathbf{x} S, \quad \forall \mathbf{x} \in S, \\
&\mathbf{c}_\Gamma(\mathbf{x}) \in \mathcal{T}_\mathbf{x} S, \quad \mathbf{c}_\Gamma(\mathbf{x}) \perp \boldsymbol{\tau}_\Gamma, \quad \forall \mathbf{x} \in \Gamma, \\
&\mathbf{n}_\Gamma(\mathbf{x}) \perp \boldsymbol{\tau}_\Gamma, \quad \mathbf{n}_\Gamma(\mathbf{x}) /\!\!/ S_{sub}, \quad \forall \mathbf{x} \in \Gamma.
\end{aligned}
\tag{3.0.1}
$$

Now from Eq. (1.2.3), the total surface energy of the system can be written as

$$
W = W_{int} + W_{sub} = \iint_S \gamma(\mathbf{n}) \, dS + (\gamma_{FS} - \gamma_{VS}) A(\Gamma).
\tag{3.0.2}
$$

Here in these expressions, γ_{FV}, γ_{FS} and γ_{VS} represent the energy densities of the film/vapor, film/substrate and vapor/substrate respectively. $A(\Gamma)$ denotes the area enclosed by the the plane curve Γ on the substrate. We assume that γ_{FS} and γ_{VS} are constants, while $\gamma_{FV} = \gamma(\mathbf{n})$ is dependent on the orientation of the film/vapor interface. The total surface energy is composed of two parts, the interfacial energy of film/vapor interface denoted by W_{int}, and the substrate energy denoted by W_{sub}.

The derivation of the three-dimensional sharp interface model seems quite straightforward by simply repeating the procedure in chapter 2 as long as we are given the energy equation. However, performing the thermodynamic variation of the surface integral W_{int} is not as easy as we think. In short, there are two major difficulties in calculating the first variation. Firstly, if S is a closed surface, then the perturbation of the surface in the tangential direction would contribute nothing to the first

variation. Thus only the perturbation in the normal direction will be considered and the variation of some geometric objects such as the normal vector, the mean curvature can be directly obtained [34]. However, when it comes to the solid-state dewetting problem, the infinitesimal perturbation of the surface in the tangential direction could be essential to the first variation of the surface energy. More precisely, the interface S is open and the tangent deformation on the boundary of S plays an important role in investigating the contact line migration along the substrate [9,67]. Secondly, unlike 2D, calculating the variation via the parameterization of the surface could be too tedious to perform in three dimensions. Therefore in this chapter, we are engaged in the derivation of the three-dimensional sharp interface model. We will develop the sharp interface model rigorously with the help of speed method and shape derivatives from shape sensitivity analysis [109]. This approach avoids the parameterization of the surface on a fixed reference domain and is able to deal with perturbation in arbitrary direction [39, 64, 109].

3.1 Shape differential calculus

We start by introducing some basic knowledge about surface calculus and differential geometry. For more related knowledge, please refer to the [45, 109].

3.1.1 Hypersurface

Definition 3.1.1 (C^k-hypersurface)**.** $S \subset \mathbb{R}^3$ *is called a* $C^k-hypersurface$, *where* $k \in \mathbb{N} \cup \{\infty\}$, *if for each point* $\mathbf{x}_0 \in S$, *there exists an open set* $U \subset \mathbb{R}^3$ *containing* $\mathbf{x}_0$ *and a function* $\phi \in C^k(U)$, *such that*

$$U \cap S = \{\mathbf{x} \in U \mid \phi(\mathbf{x}) = 0\}, \qquad \nabla\phi(\mathbf{x}) \neq 0, \ \forall \mathbf{x} \in U \cap S. \tag{3.1.1}$$

In view of the definition of hypersurface, we know that the normal vector of S at point $\mathbf{x}$ can be locally computed as $\frac{\nabla\phi(\mathbf{x})}{|\nabla\phi(\mathbf{x})|}$ or $-\frac{\nabla\phi(\mathbf{x})}{|\nabla\phi(\mathbf{x})|}$.

Definition 3.1.2. *A function $f \in C^2(S)$ is defined on a C^2-hypersurface S with $S \subset \mathbb{R}^3$. If $\mathbf{n}$ is the unit normal vector of S, and $\bar{f}$ is an arbitrary extension of f in the neighbourhood of S in $\mathbb{R}^3$, the surface gradient of f on S is defined as*

$$\nabla_{_S} f = \nabla \bar{f} - (\nabla \bar{f} \cdot \mathbf{n})\mathbf{n}. \tag{3.1.2}$$

It is easy to prove that $\nabla_{_S} f$ is independent of the extension of f and only reliable on the value of f on S. We can write $\nabla_{_S}$ as a vector operator

$$\nabla_{_S} = (\underline{D}_1, \underline{D}_2, \underline{D}_3), \tag{3.1.3}$$

then the surface divergence of function $\mathbf{g} = (g_1, g_2, g_3) \in [C^1(S)]^3$ is given by

$$\nabla_{_S} \cdot \mathbf{g} = \sum_{i=1}^{3} \underline{D}_i g_i. \tag{3.1.4}$$

Moreover, the Laplace-Beltrami operator can be expressed as

$$\Delta_{_S} f = \nabla_{_S} \cdot \nabla_{_S} f = \sum_{i=1}^{3} \underline{D}_i \underline{D}_i f. \tag{3.1.5}$$

Here $\nabla_{_S} f$ comes from the gradient of $\bar{f}$ by subtracting the normal components. Thus we know that $\nabla_{_S} f(\mathbf{x}) \in \mathcal{T}_{\mathbf{x}} S$, $\forall \mathbf{x} \in S$. We can also define the following matrix $\mathbf{H}$ such that the its element is taken as

$$\mathbf{H}_{ij} = \underline{D}_i \, n_j. \tag{3.1.6}$$

This matrix is called the extended Weingarten map with a zero eigenvalue in normal direction and two other eigenvalues given by the two principle curvatures of S. The mean curvature is the trace of the matrix

$$\mathcal{H} = \sum_{i=1}^{3} \mathbf{H}_{ii} = \nabla_{_S} \cdot \mathbf{n}. \tag{3.1.7}$$

If we denote κ_1 and κ_2 as the two principle curvatures, by noting the eigenvalues of $\mathbf{H}$, we have that

$$\text{trace}(\mathbf{H^2}) = \kappa_1^2 + \kappa_2^2 = \mathcal{H}^2 - 2\mathcal{K}, \tag{3.1.8}$$

with $\mathcal{K}$ representing the Gaussian curvature.

The formula for integration by parts on surface S reads as

Theorem 3.1.1 ([45], p.297, Thm. 2.10). *Assume S is a hypersurface in $\mathbb{R}^3$ with smooth boundary Γ, $f \in H^1(S)$, then we have*

$$\iint_S \nabla_s f \, dS = \iint_S f \mathcal{H} \mathbf{n} \, dS + \int_\Gamma f \mathbf{c}_\Gamma \, d\Gamma, \tag{3.1.9}$$

where $\mathbf{n}$ and $\mathbf{c}_\Gamma$ are the normal vector and co-normal vector respectively. $\mathcal{H}$ is the mean curvature.

The following proposition can be directly obtained from above theorem.

Proposition 3.1.1. *Let S be a hypersurface in $\mathbb{R}^3$ with smooth boundary Γ, and f and g belong to $H^1(S)$, we have*

$$\iint_S \nabla_s f g \, dS = -\iint_S f \nabla_s g \, dS + \iint_S f g \mathcal{H} \mathbf{n} \, dS + \int_\Gamma f g \mathbf{c}_\Gamma \, d\Gamma, \tag{3.1.10}$$

by using the fact that $\nabla_s(fg) = \nabla_s f \, g + f \nabla_s g$.

3.1.2   Parameterized hypersurface

Definition 3.1.3 (Parametrized C^k-surface). *We call $S \in \mathbb{R}^3$ is a parameterized C^k-surface, where $k \in \mathbb{N} \cup \infty$, if for every $\mathbf{x} \in S$, there exists an open set $V \in \mathbb{R}^3$ with $\mathbf{x} \in V$, an open connected set $U \in \mathbb{R}^2$ and a map $\mathbf{X} : U \to V \cap S$ such that $\mathbf{X} \in C^k(U, \mathbb{R}^3)$ and $\mathbf{X}$ is bijective with $\mathrm{rank}(\nabla \mathbf{X}) = 2$ on U. Then the map $\mathbf{X}$ is called a local parameterization of S.*

We have the following lemma for the relationship between the parameterized surface and hypersurface.

Lemma 3.1.1 (Lemma 2.2 in [45]). *Assume S is a C^k-hypersurface in $\mathbb{R}^3$. Then for every $\mathbf{x} \in S$, there exist an open set $V \in \mathbb{R}^3$ with $\mathbf{x} \in V$ and a parameterized C^k-surface $\mathbf{X} : U \to V \cap S$ such that $\mathbf{X}$ is a bijective map from U to $V \cap S$. On the other hand, if $\mathbf{X} : U \to V \cap S$ is a parameterized C^k-surface, then there is an open set $\hat{U} \subset U$ such that $\mathbf{X}(\hat{U})$ is a C^k-hypersurface.*

Let $\mathbf{X} \in C^4(U, \mathbb{R}^3)$ be a local parametrization of S, and $(u_1, u_2) \in U$, the first fundamental form can be given by

$$G(u, v) = (g_{ij})_{i,j=1,2}, \text{ with } g_{ij} = \frac{\partial \mathbf{X}}{\partial u_i} \cdot \frac{\partial \mathbf{X}}{\partial u_j}. \tag{3.1.11}$$

Let $g = \det(G)$. Besides, the inversion of matrix G is denote by

$$G^{-1} = (g^{ij})_{i,j=1,2}. \tag{3.1.12}$$

Now given a function $f : S \to \mathbb{R}$ defined S, let $F(u_1, u_2) = f(\mathbf{X}(u_1, u_2))$, the surface gradient of f can be expressed in terms of the parameters as

$$\nabla_s f = \sum_{i,j=1}^{2} g^{ij} \frac{\partial F}{\partial u_i} \cdot \frac{\partial \mathbf{X}}{\partial u_j}. \tag{3.1.13}$$

Moreover, we have

$$\Delta_s f = \frac{1}{g} \sum_{i,j=1}^{2} \frac{\partial}{\partial u_j} \left(g^{ij} \sqrt{g} \frac{\partial F}{\partial u_i} \right). \tag{3.1.14}$$

3.1.3   Shape derivatives

To carry out the first variation of the integral on a manifold, we need to introduce a family of perturbations. Consider a domain $D \in \mathbb{R}^3$ with the boundary ∂D which is piecewise C^k for a given integer $k \geq 0$, we can define the transformation as

$$T_\varepsilon : \bar{D} \to \bar{D}, \qquad \varepsilon \in [0, \varepsilon_0), \tag{3.1.15}$$

where T_ε is a one-to-one map. Here we assume that T_ε and T_ε^{-1} belong to $C^k(\bar{D}, \bar{D})$ for all $\varepsilon \in [0, \varepsilon_0)$, also T_ε belongs to $C^k([0, \varepsilon_0))$ for all $\mathbf{x} \in \bar{D}$, where $k \in \mathbb{N} \cup \{\infty\}$. Now under this transformation, a bounded domain Ω or surface S in $\bar{D}$ will be changed to

$$\Omega_\varepsilon = T_\varepsilon(\Omega), \qquad S_\varepsilon = T_\varepsilon(S), \tag{3.1.16}$$

with $S_0 = S, \Omega_0 = \Omega$.

Let $\mathbf{x}(\mathbf{X}, \varepsilon) = T_\varepsilon(\mathbf{X})$, the speed vector field $\mathbf{V}(\mathbf{x}, \varepsilon)$ at point $\mathbf{x}$ is defined as

$$\mathbf{V}(\mathbf{x}, \varepsilon) = \frac{\partial \mathbf{x}}{\partial \varepsilon}(T_\varepsilon^{-1}(\mathbf{x}), \varepsilon). \tag{3.1.17}$$

Now we consider the following ODEs:

$$\frac{d}{d\varepsilon}\mathbf{x}(\mathbf{X}, \varepsilon) = V(\mathbf{x}(\mathbf{X}, \varepsilon), \varepsilon),$$
$$\mathbf{x}(\mathbf{X}, 0) = \mathbf{X}, \tag{3.1.18}$$

with $\mathbf{X} \in D$. The existence of the one-to-one map has been shown by Theorem 2.16 in [109]. In other words, as long as the vector field $\mathbf{V}$ satisfy $\mathbf{V} \in C(C^k(\bar{D}, \bar{D}); [0, \varepsilon_0))$, then it uniquely determines the transformations T_ε. Thus the transformation T_ε and the $\mathbf{V}$ are uniquely determined by each other. In the following, when the vector field $\mathbf{V}$ is introduced, we use $T_\varepsilon(\mathbf{V})$ to denote the corresponding transformation. For simplicity, we also assume $\mathbf{V}_0 = \mathbf{V}(\mathbf{X}, 0)$.

We have the following lemma for the transformation $T_\varepsilon(\mathbf{V})$.

Lemma 3.1.2 (Lemma. 2.44, Lemma 2.49 in [109]). *Assume $D \in \mathbb{R}^3$ is a bounded domain, and $\mathbf{V} \in C(C^k(\bar{D}, \bar{D}); [0, \varepsilon_0))$ is the given vector field with $k \geq 1$, such that $\mathbf{V} \cdot \mathbf{n} = 0$ a.e on ∂D. Furthermore, it is assumed that $\mathbf{V} = 0$ at any singular point of ∂D. If DT_ε is the Jacobian matrix of the transformation T_ε, that is*

$$DT_\varepsilon = \left(\frac{\partial T_{\varepsilon,i}(\mathbf{V})}{\partial X_j})(\mathbf{X})\right)_{i,j=1,2,3}. \tag{3.1.19}$$

Define $\zeta(\mathbf{x}, \varepsilon)$ and $\omega(\mathbf{x}, \varepsilon)$ as follows

$$\zeta(\mathbf{X}, \varepsilon) = \det(\mathrm{DT}_\varepsilon), \tag{3.1.20a}$$
$$\omega(\mathbf{X}, \varepsilon) = \zeta(\mathbf{X}, \varepsilon)||DT_\varepsilon^{-T}\mathbf{n}||, \tag{3.1.20b}$$

then we have

$$\frac{\partial\zeta(\mathbf{X}, \varepsilon)}{\partial\varepsilon}\bigg|_{\varepsilon=0} = \nabla \cdot \mathbf{V}_0, \tag{3.1.21a}$$
$$\frac{\partial\omega(\mathbf{X}, \varepsilon)}{\partial\varepsilon}\bigg|_{\varepsilon=0} = \nabla_s \cdot \mathbf{V}_0. \tag{3.1.21b}$$

Functions $\zeta(\mathbf{X}, \varepsilon)$ and $\omega(\mathbf{X}, \varepsilon)$ will be useful in performing the change of variables of the domain and surface integrals.

We can define the first variation of the shape functionals as follows.

Definition 3.1.4 (First variation). *Let $J(\Omega)$ be a shape functional, and Ω is a bounded domain in $\bar{D}$, the first variation of the functional $J(\Omega)$ at Ω in the direction of the vector field $\mathbf{V} \in C(C^k(\bar{D}, \bar{D}); [0, \varepsilon_0))$ is given as a limit:*

$$dJ(\Omega; \mathbf{V}) = \lim_{\varepsilon \to 0} \frac{J(\Omega_\varepsilon) - J(\Omega)}{\varepsilon}. \tag{3.1.22}$$

Similarly, let $J(S)$ be a shape functional, the first variation of the functional $J(S)$ at S in the direction of the vector field $\mathbf{V}$ is given as a limit:

$$dJ(S; \mathbf{V}) = \lim_{\varepsilon \to 0} \frac{J(S_\varepsilon) - J(S)}{\varepsilon}. \tag{3.1.23}$$

Definition 3.1.5 (Material derivative, [109], Def.2.71, Def.2.74). *The material derivative $\dot{\varphi}(\Omega; \mathbf{V})$ of φ on Ω in the direction $\mathbf{V}$ is given as*

$$\dot{\varphi}(\Omega; \mathbf{V}) = \lim_{\varepsilon \to 0} \frac{\varphi(\Omega_\varepsilon) \circ T_\varepsilon(V) - \varphi}{\varepsilon}. \tag{3.1.24}$$

Similarly, the material derivative $\dot{\varphi}(S; \mathbf{V})$ of φ on S in the direction $\mathbf{V}$ is given as

$$\dot{\varphi}(S; \mathbf{V}) = \lim_{\varepsilon \to 0} \frac{\varphi(S_\varepsilon) \circ T_\varepsilon(V) - \varphi}{\varepsilon}. \tag{3.1.25}$$

The above material derivative is the derivative with respect to the moving coordinate systems. On the other hand, we can define the shape derivative of φ in the following by subtracting the term $(\nabla\varphi) \cdot \mathbf{V}_0$, which represents the derivative with respect to the stationary coordinates.

Definition 3.1.6. *[Shape derivative on domain, [109], Def.2.85] The shape derivative $\varphi'(\Omega; \mathbf{V})$ of φ on Ω in the direction $\mathbf{V}$ is given as*

$$\varphi'(\Omega; \mathbf{V}) = \dot{\varphi}(\Omega; \mathbf{V}) - \nabla\varphi(\Omega) \cdot \mathbf{V}_0. \tag{3.1.26}$$

As can been seen, if φ is independent of Ω, we can obtain $\varphi'(\Omega; \mathbf{V}) = 0$. We have the following lemma for the first variation of the domain integrals.

Lemma 3.1.3. *Let Ω be a domain in $\bar{D}$ and its boundary $\partial\Omega$ is smooth enough, $y(\Omega) \in L^1(\Omega)$ is a function such that the material derivative $\dot{y}(\Omega; \mathbf{V})$ exists or exists in the weak sense and $\dot{y}(\Omega; \mathbf{V}) \in L^1(\Omega)$, let $J(\Omega) = \iiint_\Omega y(\Omega) \, dx$, then we have*

$$dJ(\Omega; \mathbf{V}) = \iiint_\Omega \dot{y}(\Omega; \mathbf{V}) \, dX + \iiint_\Omega y(\Omega) \nabla \cdot \mathbf{V}_0 \, dX. \tag{3.1.27}$$

Furthermore, if the shape derivative $y'(\Omega; \mathbf{V})$ exists and $\nabla y(\Omega) \cdot \mathbf{V}_0 \in L^1(\Omega)$, we then have

$$dJ(\Omega; \mathbf{V}) = \iiint_\Omega y'(\Omega; \mathbf{V}) \, dX + \iint_{\partial\Omega} y(\Omega)\mathbf{V}_0 \cdot \mathbf{n} \, dS, \tag{3.1.28}$$

where we use dX, dx as integration on domain $\Omega, \Omega_\varepsilon$, respectively.

Proof. For the shape functional $J(\Omega_\varepsilon) = \iiint_{\Omega_\varepsilon} y(\Omega_\varepsilon) \, dx$, using the change of variables $\mathbf{x} = T_\varepsilon(\mathbf{V})(\mathbf{X})$ for $J(\Omega_\varepsilon)$, we have

$$J(\Omega_\varepsilon) = \iiint_\Omega y(\Omega_\varepsilon) \circ T_\varepsilon(\mathbf{V})\zeta(\mathbf{X}, \varepsilon) \, dX. \tag{3.1.29}$$

By noting the fact that $\zeta(\mathbf{X}, 0) = 1$, we obtain the following equations,

$$
\begin{aligned}
dJ(\Omega; \mathbf{V}) &= \lim_{\varepsilon \to 0} \frac{J(\Omega_\varepsilon) - J(\Omega)}{\varepsilon} \\
&= \iiint_\Omega \lim_{\varepsilon \to 0} \big[\frac{y(\Omega_\varepsilon) \circ T_\varepsilon(\mathbf{V})\zeta(\mathbf{X}, \varepsilon) - y(\Omega) \circ T_0(\mathbf{V})\zeta(\mathbf{X}, 0)}{\varepsilon}\big] \, dX \\
&= \iiint_\Omega \big[\dot{y}(\Omega; \mathbf{V})\zeta(\mathbf{X}, 0) + y(\Omega)\frac{\partial \zeta(\mathbf{X}, \varepsilon)}{\partial \varepsilon}\Big|_{\varepsilon=0}\big] \, dX. \tag{3.1.30}
\end{aligned}
$$

In view of lemma. 3.1.2, the above equations can be changed to

$$dJ(\Omega; \mathbf{V}) = \iiint_\Omega \dot{y}(\Omega; \mathbf{V}) \, dX + \iiint_\Omega y(\Omega)\nabla \cdot \mathbf{V}_0 \, dX. \tag{3.1.31}$$

Using the equation $y(\Omega)\nabla \cdot \mathbf{V}_0 + (\nabla y(\Omega)) \cdot \mathbf{V}_0 = \nabla \cdot (y(\Omega) \mathbf{V}_0)$, we obtain

$$dJ(\Omega; \mathbf{V}) = \iiint_\Omega [\dot{y}(\Omega; \mathbf{V}) - \nabla y(\Omega) \cdot \mathbf{V}_0] \, dX + \iiint_\Omega \nabla \cdot (y(\Omega) \mathbf{V}_0) \, dX. \tag{3.1.32}$$

Now by the definition of shape derivative on the domain Ω (Definition. 3.1.6), and also applying stokes formula for the second term, we finally get

$$dJ(\Omega; \mathbf{V}) = \iiint_\Omega y'(\Omega; \mathbf{V}) \, dX + \iint_{\partial\Omega} y(\Omega)\mathbf{V}_0 \cdot \mathbf{n} \, dS \tag{3.1.33}$$

$\square$

Different to the shape derivative on the domain, the shape derivative on the surface is defined in the following,

Definition 3.1.7. *[Shape derivative, [109], Def.2.88] The shape derivative $\psi'(S; \mathbf{V})$ of ψ on S in the direction $\mathbf{V}$ is given as*

$$\psi'(S; \mathbf{V}) = \dot{\psi}(S; \mathbf{V}) - \nabla_s \psi(S) \cdot \mathbf{V}_0. \tag{3.1.34}$$

Now let us consider the shape functional $J(S_\varepsilon) = \iint_{S_\varepsilon} \varphi(S_\varepsilon) \, dS_\varepsilon$, we have the following lemma.

Lemma 3.1.4. *Let S be a two-dimensional manifold in $\bar{D}$ with smooth boundary Γ, $\varphi(S) \in L^1(S)$ is a function such that the material derivative $\dot{\varphi}(S; \mathbf{V})$ exists or exists in the weak sense and $\dot{\varphi}(S; \mathbf{V}) \in L^1(S)$, let $J(S) = \iint_S \varphi(S) \, dS$, we then have*

$$dJ(S; \mathbf{V}) = \iint_S \dot{\varphi}(S; \mathbf{V}) \, dS + \iint_S \varphi(S) \nabla_s \cdot \mathbf{V}_0 \, dS. \tag{3.1.35}$$

Furthermore, if the shape derivative $\varphi'(S; \mathbf{V})$ exists and $\nabla_s \varphi \cdot \mathbf{V}_0 \in L^1(S)$, we have

$$dJ(S; \mathbf{V}) = \iint_S \varphi'(S; \mathbf{V}) \, dS + \iint_S \varphi(S) \mathcal{H} \mathbf{V}_0 \cdot \mathbf{n} \, dS + \int_\Gamma \varphi(S) \mathbf{V}_0 \cdot \mathbf{c}_\Gamma \, d\Gamma. \tag{3.1.36}$$

Proof. For the shape functional $J(S)$ under the varition vector field $\mathbf{V}$, we have

$$J(S_\varepsilon) = \iint_S (\varphi \circ T_\varepsilon(V)) \omega(\mathbf{X}, \varepsilon) \, dS, \tag{3.1.37}$$

where $\omega(\mathbf{X}, \varepsilon)$ is defined in Lemma. 3.1.2. By using the fact that $\omega(\mathbf{X}, 0) = 1$ and Lemma. 3.1.2, we obtain the following equations

$$
\begin{aligned}
dJ(S; \mathbf{V}) &= \lim_{\varepsilon \to 0} \frac{J(S_\varepsilon) - J(S)}{\varepsilon} \\
&= \iint_S \lim_{\varepsilon \to 0} \left[\frac{\varphi(S_\varepsilon) \circ T_\varepsilon(V) \omega(\mathbf{X}, \varepsilon) - \varphi \circ T_0(V) \omega(\mathbf{X}, 0)}{\varepsilon} \right] dS \\
&= \iint_S \dot{\varphi}(S; \mathbf{V}) \omega(\mathbf{X}, 0) \, dS + \iint_S \varphi(S) \frac{\partial \omega(\mathbf{X}, \varepsilon)}{\partial \varepsilon} \bigg|_{\varepsilon=0} dS \\
&= \iint_S \dot{\varphi}(S; \mathbf{V}) \, dS + \iint_S \varphi(S) \nabla_s \cdot \mathbf{V}_0 \, dS. \tag{3.1.38}
\end{aligned}
$$

For the second term, using Eq. (3.1.10) and integration by parts, also noting the

definition of the shape derivative on S, we obtain directly

$$
\begin{aligned}
dJ(S;\mathbf{V}) &= \iint_S \dot{\varphi}(S;\mathbf{V}_0)\, dS - \iint_S \nabla_s \varphi(S)\cdot\mathbf{V}_0\, dS + \iint_S \varphi(S)\mathbf{V}_0\cdot n\mathcal{H}\, dS \\
&\quad + \int_\Gamma \varphi(S)\mathbf{V}_0\cdot\mathbf{c}_\Gamma\, d\Gamma \\
&= \iint_S \varphi'(S;\mathbf{V})\, dS + \iint_S \varphi(S)\mathcal{H}\mathbf{V}_0\cdot\mathbf{n}\, dS \\
&\quad + \int_\Gamma \varphi(S)\mathbf{V}_0\cdot\mathbf{c}_\Gamma\, d\Gamma.
\end{aligned}
\tag{3.1.39}
$$

$\square$

Moreover, we have the following theorem based on above lemma.

Theorem 3.1.2. *Assume $S \in \bar{D}$ is a two dimensional manifold with smooth boundary Γ, let $J(S) = \iint_S \varphi(S)\ dS$ with $\varphi(S) \in H^1(S)$, $\mathbf{V}$ is the variation vector field such that $\mathbf{V} \in C(C^k(\bar{D},\bar{D}); [0,\varepsilon_0))$, if the shape derivative $\varphi'(S;\mathbf{V})$ exist and $\varphi'(S;\mathbf{V}) \in L^1(S)$, then we have*

$$
dJ(S;\mathbf{V}) = \iint_S \varphi'(S;\mathbf{V})\, dS + \iint_S \varphi(S)\mathcal{H}\mathbf{V}_0\cdot\mathbf{n}\, dS + \int_\Gamma \varphi(S)\mathbf{V}_0\cdot\mathbf{c}_\Gamma\, d\Gamma. \tag{3.1.40}
$$

Furthermore, if $y(\Omega)$ is a function defined on Ω such that $y(\Omega)\big|_S = \varphi(S)$, we have

$$
dJ(S;\mathbf{V}) = \iint_S y'(\Omega,\mathbf{V})\big|_S\, dS + \iint_S \big[\partial_{\mathbf{n}} y + y\mathcal{H}\big]\mathbf{V}_0\cdot\mathbf{n}\, dS + \int_\Gamma y\mathbf{V}_0\cdot\mathbf{c}_\Gamma\, d\Gamma. \tag{3.1.41}
$$

Proof. The proof of this theorem is straightforward by noting the definition of shape derivatives on Ω and S with above lemma. $\square$

Given a arbitrary function defined on S, the shape derivative is not easy to calculate. Luckily, with the help of the signed distance function, the shape derivative of the normal vector and the mean curvature can be obtained. Consider a closed domain $\Omega \in \mathbb{R}^3$ with its smooth boundary $\partial\Omega$, the signed distance function is given as

$$
b(\mathbf{x}) = \begin{cases} \mathrm{dist}(\mathbf{x},\partial\Omega), & \forall \mathbf{x} \in \mathbb{R}^3/\Omega, \\ 0, & \forall \mathbf{x} \in \partial\Omega, \\ -\mathrm{dist}(\mathbf{x},\partial\Omega), & \forall \mathbf{x} \in \Omega. \end{cases}
\tag{3.1.42}
$$

Here $\text{dist}(\mathbf{x}, \partial\Omega) = \inf_{\mathbf{y} \in \partial\Omega} ||\mathbf{x} - \mathbf{y}||$. The signed distance function has significant relationships with the normal vector and mean curvature of the surface $\partial\Omega$. Precisely, we can extend the normal vector $\mathbf{n}$ and mean curvature $\mathcal{H}$ in a tubular neighbourhood in the following

$$\mathbf{n}(\mathbf{x}) = \nabla b(\mathbf{x})\Big|_{\partial\Omega}, \qquad \mathcal{H}(\mathbf{x}) = \Delta b(\mathbf{x})\Big|_{\partial\Omega}. \tag{3.1.43}$$

Lemma 3.1.5 ([64]). *Assume that $\Omega \in \mathbb{R}^3$ is a closed domain with smooth boundary $\partial\Omega$, $S \subset \partial\Omega$ is an open two-dimensional manifold, then the shape derivative of the unit normal vector $\mathbf{n}$ and the mean curvature $\mathcal{H}$ of S in the direction of velocity $\mathbf{V}$ are given as*

$$\mathbf{n}' = \mathbf{n}'(\Omega; \mathbf{V})\Big|_S = -\nabla_S(\mathbf{V}_0 \cdot \mathbf{n}), \qquad \mathcal{H}' = \mathcal{H}'(\Omega; \mathbf{V})\Big|_S = -\Delta_S(\mathbf{V}_0 \cdot \mathbf{n}). \tag{3.1.44}$$

3.2 Thermodynamic variation

In this section, we will calculate the thermodynamic variation of the surface energy defined in Eq. (3.0.2) for solid-state dewetting. By applying Eq. (3.1.41) and making use of the shape derivatives of the unit normal vector, we have the following lemma.

Lemma 3.2.1. *Assume $S \in \bar{D}$ is a two dimensional manifold of class C^2 with smooth boundary Γ. Let $\mathbf{n}$ be the unit normal vector of S, and $\mathbf{V}$ be the variation vector field such that $\mathbf{V} \in C(C^k(\bar{D}, \bar{D}); [0, \epsilon_0))$. If $J(S) = \int_S \gamma(\mathbf{n})\, dS$ with $\gamma \in C^1(S^2)$, then the first variation of $J(S)$ is given by*

$$\delta J(S; \mathbf{V}) = \int_S (\nabla_s \cdot \boldsymbol{\xi})\,(\mathbf{V}_0 \cdot \mathbf{n})\, dS + \int_\Gamma (\mathbf{c}_\Gamma^\gamma \cdot \mathbf{V}_0)\, d\Gamma. \tag{3.2.1}$$

Here $\boldsymbol{\xi} := \boldsymbol{\xi}(\mathbf{n})$ is defined previously as the Cahn-Hoffman vector, and $\mathbf{V}_0 \cdot \mathbf{n}$ represents the deformation velocity along the outer normal direction of the interface S. We define a new vector $\mathbf{c}_\Gamma^\gamma := (\boldsymbol{\xi} \cdot \mathbf{n})\,\mathbf{c}_\Gamma - (\boldsymbol{\xi} \cdot \mathbf{c}_\Gamma)\,\mathbf{n}$ with $\mathbf{c}_\Gamma$ representing the unit co-normal vector defined.

Proof. We firstly assume $\hat{\gamma}$ is a homogeneous extension of γ,

$$\hat{\gamma}(\mathbf{p}) = |\mathbf{p}|\gamma(\frac{\mathbf{p}}{|\mathbf{p}|}), \quad \forall \mathbf{p} \in \mathbb{R}^2\backslash\{\mathbf{0}\}, \tag{3.2.2}$$

where the definition domain of the function $\gamma(\mathbf{n})$ changes from unit vectors $\mathbf{n}$ to arbitrary non-zero vectors $\mathbf{p} \in \mathbb{R}^3$.

We next consider a domain Ω such that $S \subset \partial\Omega$. Then based on the signed distance function defined in (3.1.42), we can regard $\nabla b(x)$ as an extension of the normal vector $\mathbf{n}$ in the neighbourhood of S. Thus we can rewrite

$$J(S) = \int_S \hat{\gamma}\Big(\nabla b(\mathbf{x})\Big)\Big|_S \, dS = \int_S y(\Omega)\Big|_S \, dS, \tag{3.2.3}$$

with $y(\Omega) = \hat{\gamma}\Big(\nabla b(\mathbf{x})\Big)$. Using the chain rule for shape derivatives and definition of $\boldsymbol{\xi}$, we know the following expression holds,

$$y'(\Omega; \mathbf{V})\Big|_S = \nabla\hat{\gamma}\Big(\nabla b(\mathbf{x})\Big) \cdot \mathbf{n}'(\Omega; \mathbf{V})\Big|_S = -\boldsymbol{\xi} \cdot \nabla_s(\mathbf{V}_0 \cdot \mathbf{n}). \tag{3.2.4}$$

Moreover, By noting the fact $|\nabla b(\mathbf{x})| = 1$, we obtain

$$\partial_{\mathbf{n}}y\Big|_S = \boldsymbol{\xi} \cdot \Big(\big[D(\nabla b(\mathbf{x}))\big]\nabla b(\mathbf{x})\Big)\Big|_S = 0. \tag{3.2.5}$$

In view of Eq. (3.1.41) and combined Eq. (3.2.4), (3.2.5), we immediately have

$$\begin{aligned}
\delta J(S; \mathbf{V}) &= -\int_S \boldsymbol{\xi} \cdot \nabla_s(\mathbf{V}_0 \cdot \mathbf{n}) \, dS + \int_S \gamma(\mathbf{n})(\mathbf{V}_0 \cdot \mathbf{n})\mathcal{H} \, dS + \int_\Gamma \gamma(\mathbf{n})(\mathbf{V}_0 \cdot \mathbf{c}_\Gamma) \, d\Gamma \\
&= I + II + III.
\end{aligned} \tag{3.2.6}$$

For the first term, integration by parts gives us

$$I = \int_S (\nabla_s \cdot \boldsymbol{\xi})(\mathbf{V}_0 \cdot \mathbf{n}) \, dS - \int_S (\boldsymbol{\xi} \cdot \mathbf{n})(\mathbf{n} \cdot \mathbf{V}_0)\mathcal{H} \, dS - \int_\Gamma (\boldsymbol{\xi} \cdot \mathbf{c}_\Gamma)(\mathbf{n} \cdot \mathbf{V}_0) \, d\Gamma. \tag{3.2.7}$$

Based on the definition of Cahn-Hoffman vector, we have $\gamma(\mathbf{n}) = \boldsymbol{\xi} \cdot \mathbf{n}$. Thus we can rewrite

$$II = \int_S (\boldsymbol{\xi} \cdot \mathbf{n})(\mathbf{V}_0 \cdot \mathbf{n})\mathcal{H} \, dS. \tag{3.2.8}$$

$$III = \int_\Gamma (\boldsymbol{\xi} \cdot \mathbf{n})(\mathbf{V}_0 \cdot \mathbf{c}_\Gamma) \, d\Gamma. \tag{3.2.9}$$

Now combined the three terms together, we immediately have

$$
\begin{aligned}
\delta J(S; \mathbf{V}) &= \int_S (\nabla_s \cdot \boldsymbol{\xi}) \, (\mathbf{V}_0 \cdot \mathbf{n}) \, dS + \int_\Gamma \left[(\boldsymbol{\xi} \cdot \mathbf{n}) \, \mathbf{c}_\Gamma - (\boldsymbol{\xi} \cdot \mathbf{c}_\Gamma) \, \mathbf{n} \right] \cdot \mathbf{V}_0 \, d\Gamma \\
&= \int_S (\nabla_s \cdot \boldsymbol{\xi}) \, (\mathbf{V}_0 \cdot \mathbf{n}) \, dS + \int_\Gamma \mathbf{c}_\Gamma^\gamma \cdot \mathbf{V}_0 \, d\Gamma,
\end{aligned}
\tag{3.2.10}
$$

with $\mathbf{c}_\Gamma^\gamma = (\boldsymbol{\xi} \cdot \mathbf{n}) \, \mathbf{c}_\Gamma - (\boldsymbol{\xi} \cdot \mathbf{c}_\Gamma) \, \mathbf{n}$. $\qquad\square$

By using above lemma, we can easily obtain the first variation of the energy functional for solid-state dewetting.

Theorem 3.2.1. *The first variation of the energy functional* (3.0.2) *used in solid-state dewetting problems with respect to the smooth vector field* $\mathbf{V}$ *can be written as:*

$$
\delta W(S; \mathbf{V}) = \int_S (\nabla_s \cdot \boldsymbol{\xi}) \, (\mathbf{V}_0 \cdot \mathbf{n}) \, dS + \int_\Gamma (\mathbf{c}_\Gamma^\gamma \cdot \mathbf{n}_\Gamma + \gamma_{FS} - \gamma_{VS})(\mathbf{n}_\Gamma \cdot \mathbf{V}_0) \, d\Gamma. \tag{3.2.11}
$$

Proof. The total free energy consists of two parts. For the film/vapor interface energy, by using lemma. 3.1.4, we have

$$
\delta W_{\text{int}}(S; \mathbf{V}) = \int_S (\nabla_s \cdot \boldsymbol{\xi}) \, \mathbf{V}_0 \cdot \mathbf{n} \, dS + \int_\Gamma \mathbf{c}_\Gamma^\gamma \cdot \mathbf{V}_0 \, d\Gamma. \tag{3.2.12}
$$

Here $\mathbf{c}_\Gamma^\gamma$ is a linear combination of $\mathbf{c}_\Gamma$ and $\mathbf{n}$, thus we have

$$
\mathbf{c}_\Gamma \perp \boldsymbol{\tau}_\Gamma, \quad \mathbf{n} \perp \boldsymbol{\tau}_\Gamma \quad \Rightarrow \quad \mathbf{c}_\Gamma^\gamma \perp \boldsymbol{\tau}_\Gamma. \tag{3.2.13}
$$

For solid-state dewetting, see in Fig. 3.1, we require the contact line to move along the substrate, namely

$$
T_\epsilon \Gamma \subset S_{\text{sub}}, \qquad \mathbf{V}(\epsilon, \mathbf{x}) \mathbin{/\mkern-5mu/} S_{\text{sub}}, \qquad \forall \mathbf{x} \in \Gamma, \ \epsilon \in [0, \epsilon_0). \tag{3.2.14}
$$

We denote P_{sub} as the projection of vector onto the substrate. By noting Eq. (3.2.13), we have $P_{\text{sub}} \mathbf{c}_\Gamma^\gamma = k \mathbf{n}_\Gamma$ with k representing the scalar projection. Then we can rewrite

$$
\begin{aligned}
\mathbf{c}_\Gamma^\gamma \cdot \mathbf{V}_0 &= (P_{\text{sub}} \mathbf{c}_\Gamma^\gamma + (I - P_{\text{sub}}) \mathbf{c}_\Gamma^\gamma) \cdot \mathbf{V}_0 \\
&= P_{\text{sub}} \mathbf{c}_\Gamma^\gamma \cdot \mathbf{V}_0 = k \mathbf{n}_\Gamma \cdot \mathbf{V}_0 = (c_\Gamma^\gamma \cdot \mathbf{n}_\Gamma)(\mathbf{n}_\Gamma \cdot \mathbf{V}_0).
\end{aligned}
$$

Thus we can simplify (3.2.10) as

$$\delta W_{\text{int}}(S; \mathbf{V}) = \int_S (\nabla_s \cdot \boldsymbol{\xi})\,(\mathbf{V}_0 \cdot \mathbf{n})\,dS + \int_\Gamma (\mathbf{c}_\Gamma^\gamma \cdot \mathbf{n}_\Gamma)(\mathbf{n}_\Gamma \cdot \mathbf{V}_0)\,d\Gamma. \qquad (3.2.15)$$

For the substrate energy W_{sub}, we can write it as

$$W_{\text{sub}} = (\gamma_{FS} - \gamma_{VS})A(\Gamma) = (\gamma_{FS} - \gamma_{VS})\int_{S_{FS}} dS_{FS}. \qquad (3.2.16)$$

Applying Lemma. 3.1.4, and noting that φ is a constant and S_{FS} is a flat surface ($\mathcal{H} = 0$, $\mathbf{n}_\Gamma$ is the unit co-normal vector of surface S_{FS}), therefore we have

$$\delta W_{\text{sub}}(S; \mathbf{V}) = (\gamma_{FS} - \gamma_{VS})\int_\Gamma \mathbf{V}_0 \cdot \mathbf{n}_\Gamma\,d\Gamma. \qquad (3.2.17)$$

Now combine Eq. (3.2.15) and Eq. (3.2.17), we obtain the first variation of the total surface energy of solid-state dewetting in the direction of the vector filed $\mathbf{V}$

$$\delta W(S; \mathbf{V}) = \int_S (\nabla_s \cdot \boldsymbol{\xi})\,(\mathbf{V}_0 \cdot \mathbf{n})\,dS + \int_\Gamma (\mathbf{c}_\Gamma^\gamma \cdot \mathbf{n}_\Gamma + \gamma_{FS} - \gamma_{VS})(\mathbf{n}_\Gamma \cdot \mathbf{V}_0)\,d\Gamma. \quad (3.2.18)$$

$$\square$$

3.3 Equilibrium

The equilibrium shape for solid-state dewetting problem is obtained by minimizing the total free energy while fixing the total volume of the thin film. The optimization problem can be stated as

$$\min_\Omega \left(W := \int_S \gamma(\mathbf{n})\,dS + (\gamma_{FS} - \gamma_{VS})A(\Gamma) \right) \quad \text{s.t.} \quad |\Omega| = \text{C}, \qquad (3.3.1)$$

where $C > 0$ is a constant denoting the total volume, and Ω represents the domain enclosed by the interface S and substrate S_{sub}.

The Lagrangian for the minimization problem can then be expressed as

$$L(S, \lambda) = \int_S \gamma(\mathbf{n})\,dS + (\gamma_{FS} - \gamma_{VS})A(\Gamma) - \lambda(|\Omega| - C), \qquad (3.3.2)$$

with λ representing the Lagrange multiplier. By noting the lemma. 3.1.3, the first variation of the total volume can be given by simply letting $y = 1$. Thus combined

with Eq. (3.2.11), the first variation of the Lagrangian with resect to a smooth vector field $\mathbf{V}$ can be given as

$$\delta L(S, \lambda; \mathbf{V}) = \int_S (\nabla_s \cdot \boldsymbol{\xi} - \lambda)(\mathbf{V}_0 \cdot \mathbf{n}) \, dS + \int_\Gamma (\mathbf{c}_\Gamma^\gamma \cdot \mathbf{n}_\Gamma + \gamma_{FS} - \gamma_{VS})(\mathbf{n}_\Gamma \cdot \mathbf{V}_0) \, d\Gamma. \quad (3.3.3)$$

Based on above variation, we have the following lemma which give the necessary conditions for the equilibrium shape of solid-state dewetting.

Lemma 3.3.1. *Assume there is a surface S_e with smooth boundary Γ_e. If S_e is the equilibrium shape of the solid-state dewetting problem Eq. (3.3.1), then the following conditions must be satisfied*

$$\nabla_{S_e} \cdot \boldsymbol{\xi} = \lambda, \ \ on \ S_e. \tag{3.3.4a}$$

$$\mathbf{c}_\Gamma^\gamma \cdot \mathbf{n}_\Gamma + \gamma_{FS} - \gamma_{VS} = 0, \ \ on \ \Gamma_e. \tag{3.3.4b}$$

where the constant λ is determined by the total volume.

Proof. If S_e is the equilibrium shape, then Eq. (3.3.3) must vanish at $S = S_e$ for any smooth vector field $\mathbf{V}$. Thus we immediately obtain the two conditions. $\quad\square$
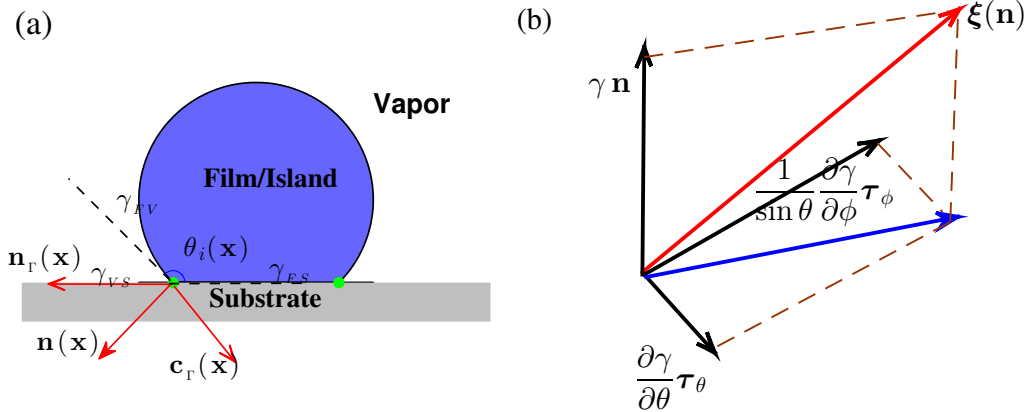
Figure 3.2: (a) The cross-section profile in configuration of the vectors along the contact line Γ. (b) The three components of the Cahn-Hoffman $\boldsymbol{\xi}$-vector.

For isotropic surface energy, Eq. (3.3.4a) will collapse to the condition for constant mean curvature surface. Eq. (3.3.4b) can be regarded as the Young equation

for anisotropic surface energy $\gamma(\mathbf{n})$ in three dimensions. Denote Γ_e as the boundary of S_e, for arbitrary $\mathbf{x} \in \Gamma_e$, let $\theta(x)$ represent the corresponding contact angle at $\mathbf{x}$. For isotropic case, i.e., $\gamma(\mathbf{n}) = \gamma_0$ with a constant γ_0, we have $\boldsymbol{\xi} = \gamma_0 \mathbf{n}$ and $\mathbf{c}_\Gamma^\gamma = \mathbf{c}_\Gamma$. Thus Eq. (3.3.4b) will collapse to

$$\gamma_0 \cos \theta(\mathbf{x}) + \gamma_{FS} - \gamma_{VS} = 0, \quad \forall \mathbf{x} \in \Gamma_e, \tag{3.3.5}$$

which is directly the isotropic Young equation [131]. For the anisotropic case, we can write the surface energy density in terms of the spherical coordinates, i.e., $\gamma_{FV} = \gamma(\theta, \phi)$. Then the Cahn-Hoffman $\boldsymbol{\xi}$-vector can be can be divided into the three components, and written as follows

$$\boldsymbol{\xi}(\mathbf{n}) = \nabla \hat{\gamma}(\mathbf{n}) = \gamma(\theta, \phi)\mathbf{n} + \frac{\partial \gamma(\theta, \phi)}{\partial \theta} \boldsymbol{\tau}_\theta + \frac{1}{\sin \theta} \frac{\partial \gamma(\theta, \phi)}{\partial \phi} \boldsymbol{\tau}_\phi, \tag{3.3.6}$$

where in these expressions,

$$\mathbf{n} = (\sin \theta \cos \phi, \sin \theta \sin \phi, \cos \theta)^T, \tag{3.3.7a}$$

$$\boldsymbol{\tau}_\theta = (\cos \theta \cos \phi, \cos \theta \sin \phi, -\sin \theta)^T, \tag{3.3.7b}$$

$$\boldsymbol{\tau}_\phi = (-\sin \phi, \cos \phi, 0)^T. \tag{3.3.7c}$$

Besides, we have the following expressions hold.

$$\boldsymbol{\xi} \cdot \mathbf{n} = \gamma(\theta, \phi), \qquad \mathbf{c}_\Gamma \cdot \mathbf{n}_\Gamma = \cos \theta(\mathbf{x}). \tag{3.3.8a}$$

$$\boldsymbol{\xi} \cdot \mathbf{c}_\Gamma = \frac{\partial \gamma(\theta, \phi)}{\partial \theta}, \qquad \mathbf{n} \cdot \mathbf{n}_\Gamma = \sin \theta(\mathbf{x}). \tag{3.3.8b}$$

Thus we can rewrite Eq. 3.3.4b into

$$\gamma(\theta, \phi) \cos(\theta(\mathbf{x})) - \frac{\partial \gamma(\theta, \phi)}{\partial \theta} \sin(\theta(\mathbf{x})) + \gamma_{FS} - \gamma_{VS} = 0, \tag{3.3.9}$$

which is consistent with the anisotropic Young equation in two-dimensional case [9, 120].

Since we have $\nabla_S \cdot \mathbf{X} = 2$, if $\mathbf{X}$ is the position vector of S. Thus we know that the equilibrium shape for solid-state dewetting must demonstrate similar geometry to the $\boldsymbol{\xi}$-plot, up to a scaling. Based on the Winterbottom construction [123] and recent

work for solid-state dewetting [9], we can construct the equation for the equilibrium shape. Now firstly we define the domain U_ϕ as

$$U_\phi := \{\theta \Big| \gamma(\theta, \phi) \cos(\theta) - \frac{\partial \gamma(\theta, \phi)}{\partial \theta} \sin(\theta) - \sigma \geq 0, \theta \in [0, \pi]\}. \tag{3.3.10}$$

Based on lemma. 3.3.1, we can construct the equilibrium shape in the parametric form as $S_e(\theta, \phi) := \mathbf{X}(\theta, \phi) = (x(\theta, \phi), y(\theta, \phi), z(\theta, \phi))$,

$$\begin{cases} x(\theta, \phi) = \lambda[\gamma(\theta, \phi) \sin \theta \cos \phi + \frac{\partial \gamma(\theta, \phi)}{\partial \theta} \cos \theta \cos \phi - \frac{1}{\sin \theta} \frac{\partial \gamma(\theta, \phi)}{\partial \phi} \sin \phi], \\ y(\theta, \phi) = \lambda[\gamma(\theta, \phi) \sin \theta \sin \phi + \frac{\partial \gamma(\theta, \phi)}{\partial \theta} \cos \theta \sin \phi + \frac{1}{\sin \theta} \frac{\partial \gamma(\theta, \phi)}{\partial \phi} \cos \phi], \\ z(\theta, \phi) = \lambda[\gamma(\theta, \phi) \cos \theta - \frac{\partial \gamma(\theta, \phi)}{\partial \theta} \sin \theta - \sigma], \end{cases} \tag{3.3.11}$$

where $0 < \phi \leq 2\pi, \theta \in U_\phi$, and λ is the scaling constant determined by the total volume $|\Omega|$.
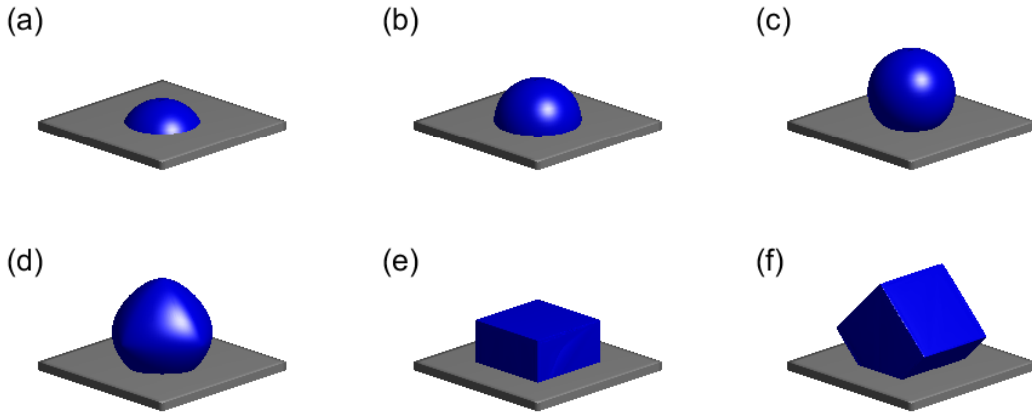
Figure 3.3: The equilibrium shape defined by Eq. (3.3.11), where (a)-(c) is for isotropic surface energy, i.e., $\gamma = 1$, but with $\sigma = \cos(\pi/3)$, $\sigma = \cos(\pi/2)$, $\sigma = \cos(3\pi/4)$ respectively. (d) $\gamma(\mathbf{n}) = 1 + 0.2(n_1^4 + n_2^4 + n_3^4)$, $\sigma = \cos(3\pi/4)$; (e) The surface energy density is given directly by Eq. (1.1.9), $\sigma = \cos(3\pi/4)$, $\epsilon = 0.01$; (f) The surface energy density is given by $\gamma(\boldsymbol{M}_x(\pi/4)\mathbf{n})$ where $\gamma(\mathbf{n})$ is defined by Eq. (1.1.9) and $\boldsymbol{M}_x(\pi/4)$ represents the matrix for rotation by an angle $\pi/4$ about the x-axis in three dimensions, using the right-hand rule, $\sigma = \cos(3\pi/4)$, $\epsilon = 0.01$.

Based on Eq. (3.3.11), the equilibrium shape under different anisotropies, e.g., the cubic anisotropy and regularized facet/cusps anisotropic defined in Eq. (1.1.9), can be easily constructed. Fig. 3.3(a)-(c) shows the equilibrium shape for isotropic surface energy with the material constant σ chosen as $\sigma = \cos(\pi/3), \cos(\pi.2), \cos(3\pi/4)$ respectively. It clearly demonstrates the effects of the material constant σ on the equilibrium shape by influencing the contact angle via (3.3.5). Moreover, we also present the equilibrium shape for the cubic anisotropic surface energy i.e., $\gamma(\mathbf{n}) = 1 + a(n_1^4 + n_2^4 + n_3^4)$ and regularized cusps surface energy defined in Eq. (1.1.9) with the same $\sigma = \cos(3\pi/4)$ in Fig. 3.3(d),(e). The anisotropy for Fig. 3.3(f) is forced an anti-clockwise rotation along the x-axis by 45 degrees under the right hand rule for the cusps surface energy. We can observe the this rotation results in a corresponding rotation of the equilibrium shape.

3.4 The kinetic sharp-interface model and its properties

In this section, we will propose the kinetic sharp-interface model for solid-state dewetting of thin films with anisotropic surface energies.

3.4.1 The model

Based on Eq. (3.2.1), we can obtain the variation of the total surface energy with respect to the film/vapor interface S and the contact line Γ as

$$\frac{\delta W}{\delta S} = \nabla_s \cdot \boldsymbol{\xi}, \qquad \frac{\delta W}{\delta \Gamma} = \mathbf{c}_\Gamma^\gamma \cdot \mathbf{n}_\Gamma + \gamma_{FS} - \gamma_{VS}. \tag{3.4.1}$$

From the Gibbs-Thomson relation [86,113], the chemical potential can be defined as

$$\mu = \Omega_0 \frac{\delta W}{\delta S} = \Omega_0 \nabla_s \cdot \boldsymbol{\xi}, \tag{3.4.2}$$

with Ω_0 representing the atomic volume. The normal velocity of the moving interface is controlled by surface diffusion flow [27, 86], and it can be defined as follows by Fick's laws of diffusion [4]

$$\mathbf{J} = -\frac{D_s\nu}{k_B\,T_e}\nabla_S\,\mu, \qquad v_n = -\Omega_0(\nabla_S\cdot\mathbf{J}) = \frac{D_s\nu\Omega_0}{k_B\,T_e}\nabla_S^2\mu. \qquad (3.4.3)$$

In these expressions, $\mathbf{J}$ is the mass flux, D_s is the surface diffusivity, $k_B\,T_e$ is the thermal energy, ν is the number of diffusing atoms per unit area, ∇_S is the surface gradient. In addition to the surface diffusion which controlled the motion of the moving interface, we still need the boundary condition for the moving contact line. Following the idea in two dimensions [67, 120], we assume that the normal velocity of the contact line Γ is given by the energy gradient flow, which is determined by the time-dependent Ginzburg-Landau kinetic equations

$$v_{n_\Gamma} = -\eta\frac{\delta W}{\delta\Gamma} = -\eta[\mathbf{c}_\Gamma^\gamma\cdot\mathbf{n}_\Gamma + \gamma_{FS} - \gamma_{VS}], \qquad (3.4.4)$$

with $0 < \eta < \infty$ denoting the constant contact line mobility as a reciprocal of a constant friction coefficient.

We choose the characteristic length scale and characteristic surface energy scale as h_0 and γ_0 respectively, the time scale as $\frac{h_0^4}{B\gamma_0}$ with $B = \frac{D_s\nu\Omega_0^2}{k_B\,T_e}$, and the contact line mobility is scaled by $\frac{B}{h_0^3}$. Let $\mathbf{X}(\cdot,t) = (x(\cdot,t),\ y(\cdot,t),\ z(\cdot,t))$ be a local parameterization of the moving film/vapor interface S, then we can obtain the dimensionless sharp interface model for solid-state dewetting of thin film via a $\boldsymbol{\xi}$-vector formulation as

$$\partial_t\mathbf{X} = \Delta_S\mu\,\mathbf{n}, \qquad t > 0, \qquad (3.4.5)$$

$$\mu = \nabla_S\cdot\boldsymbol{\xi}, \qquad \boldsymbol{\xi}(\mathbf{n}) = \nabla\hat{\gamma}(\mathbf{p})\Big|_{\mathbf{p}=\mathbf{n}}, \qquad (3.4.6)$$

where t is the time, $\mathbf{n}$ is the outer unit normal vector of S, and $\boldsymbol{\xi}(\mathbf{n})$ is the Cahn-Hoffman vector (scaled by γ_0). Here for simplicity, we still use the same notations for all the dimensionless variables. Let $\mathbf{X}_\Gamma(\cdot,t) = (x_\Gamma(\cdot,t),\ y_\Gamma(\cdot,t),\ z_\Gamma(\cdot,t))$ represents a parameterization of the contact line Γ. The initial condition is given as S_0 with

boundary Γ_0 such that

$$S_0 := \mathbf{X}(\cdot, 0) = (x_0,\ y_0,\ z_0), \quad \Gamma_0 := \mathbf{X}(\cdot, 0)\Big|_\Gamma. \tag{3.4.7}$$

where $z_0\Big|_\Gamma = z_\Gamma(\cdot, 0) = 0$. The above governing equations are coupled with the following boundary conditions:

(1) contact line condition

$$z_\Gamma(\cdot, t) = 0, \quad t \geq 0; \tag{3.4.8}$$

(2) relaxed contact angle condition

$$\partial_t \mathbf{X}_\Gamma = -\eta\Big(\mathbf{c}_\Gamma^\gamma \cdot \mathbf{n}_\Gamma - \sigma\Big)\mathbf{n}_\Gamma, \qquad t \geq 0; \tag{3.4.9}$$

(3) zero-mass flux condition

$$\Big(\mathbf{c}_\Gamma \cdot \nabla_s\, \mu\Big)\Big|_\Gamma = 0, \qquad t \geq 0; \tag{3.4.10}$$

where η represents the dimensionless contact line mobility and $\mathbf{c}_\Gamma^\gamma$ is the anisotropic co-normal vector defined as $\mathbf{c}_\Gamma^\gamma := (\boldsymbol{\xi} \cdot \mathbf{n})\,\mathbf{c}_\Gamma - (\boldsymbol{\xi} \cdot \mathbf{c}_\Gamma)\,\mathbf{n}$. $\mathbf{c}_\Gamma = (c_\Gamma^1,\ c_\Gamma^2,\ c_\Gamma^3)$ represents the co-normal vector, and $\mathbf{n}_\Gamma = (n_\Gamma^1,\ n_\Gamma^2,\ 0)$ is the outer unit normal vector of Γ on the substrate (cf. Fig. 3.1), and $\sigma = \frac{\gamma_{VS} - \gamma_{FS}}{\gamma_c}$ is a material constant. The contact line condition defined in Eq. (3.4.8) ensures that the moving contact line is always attached on the substrate, which is also implied by Eq. (3.4.9). By noting that Γ is on the substrate (x-y plane), we know that the third component of $\mathbf{n}_\Gamma$ is always zero, i.e., $n_\Gamma^3 = 0$. Thus as long as the initial condition satisfies $z_\Gamma(\cdot, 0) = 0$, we can obtain boundary conditin (i) $z_\Gamma(\cdot, t) = 0, \forall t > 0$ from boundary condition (ii). The last boundary condition (iii) is included such that there is no mass flux along the triple contact line.

3.4.2   Mass conservation and energy dissipation

In the following, we will prove that the proposed sharp interface model for solid-state dewetting satisfies the properties of mass conservation and energy dissipation during time evolution.

Proposition 3.4.1. *Suppose* $\big(\mathbf{X}(\cdot,t),\ \mu(\cdot,t)\big)$ *is the exact solution of the sharp in-terface model for solid-state dewetting: Eqs.* (3.4.5), (3.4.6) *with boundary conditions Eqs.* (3.4.8), (3.4.9) *and* (3.4.10). *Denote* $S(t) := \mathbf{X}(\cdot,t)$ *as the moving interface, then the total volume of the domain* $\Omega(t)$ *enclosed by the interface* $S(t)$ *and the substrate* S_{sub} *is conserved, i.e.,*

$$|\Omega(t)| \equiv |\Omega(0)|, \qquad t \geq 0, \tag{3.4.11}$$

and the total surface energy of the system is decreasing during the evolution, i.e.,

$$W(t) \leq W(t_1) \leq W(0) = \int_{S(0)} \gamma(\mathbf{n})\, dS - \sigma A(\Gamma(0)), \qquad t \geq t_1 \geq 0. \tag{3.4.12}$$

Proof. For simplicity, we use S to denote $S(t)$ in the following. Taking time deriva-tive of the volume or the energy is similar to finding the first variation of the func-tional with respect to the smooth vector field. Now replacing ϵ by the time t, and consequently V_0 can be replaced by $\partial_t \mathbf{X}$. Therefore, by noting lemma. 3.1.3 (set $y = 1$) and Eq. (3.4.5), the time derivative of the total volume is given as

$$\frac{d}{dt} M(t) = \int_{S(t)} \partial_t \mathbf{X} \cdot \mathbf{n}\, dS = \int_{S(t)} \Delta_s \mu\, dS = 0. \tag{3.4.13}$$

The last equality comes from the integration by parts and the boundary condition Eq. (3.4.10). Thus the total volume is conserved.

In order to prove the energy dissipation, we take derivative with respect to t for the total energy. By Eq. (3.2.1), we obtain

$$\frac{d}{dt} W(t) \;=\; \int_{S(t)} (\nabla_s \cdot \boldsymbol{\xi})(\partial_t \mathbf{X} \cdot \mathbf{n})\, dS + \int_{\Gamma(t)} (\mathbf{c}_\Gamma^\gamma \cdot \mathbf{n}_\Gamma - \sigma)(\partial_t \mathbf{X}_\Gamma \cdot \mathbf{n}_\Gamma)\, d\Gamma.$$

Substitute the following three equations

$$\Delta_s \mu = \partial_t \mathbf{X} \cdot \mathbf{n}, \quad \nabla_s \cdot \boldsymbol{\xi} = \mu, \quad \partial_t \mathbf{X}_\Gamma \cdot \mathbf{n}_\Gamma = -\eta(\mathbf{c}_\Gamma^\gamma \cdot \mathbf{n}_\Gamma - \sigma), \tag{3.4.14}$$

and integration by parts, we obtain

$$\begin{aligned}
\frac{d}{dt} W(t) \;&=\; \int_{S(t)} \mu \Delta_S \mu\, dS - \eta \int_{\Gamma(t)} (\mathbf{c}_\Gamma^\gamma \cdot \mathbf{n}_\Gamma - \sigma)^2\, d\Gamma \\
&=\; -\int_{S(t)} (\nabla_s \mu)^2\, dS - \eta \int_{\Gamma(t)} (\mathbf{c}_\Gamma^\gamma \cdot \mathbf{n}_\Gamma - \sigma)^2\, d\Gamma \leq 0, \tag{3.4.15}
\end{aligned}$$

which immediately implies the energy dissipation. $\qquad\square$

The proof of above proposition involves calculating the time derivative of the mass functional or energy functional. It is equivalent to obtaining the first variation with respect to the smooth vector field $\mathbf{V}$ by considering the time t as the perturbation parameter ϵ.

Chapter 4

A PFEM in Three Dimensions

The idea of the parametric finite element method is presented by Dziuk in [44] in a seminar paper, where the author formulated the discrete numerical algorithm by assuming that the new surface S^{m+1} is parameterized over the last step surface S^m instead of on a fixed reference domain. Thus the evolving surfaces can be generated step by step without any parameterisation of the initial surface. In recent years, the parametric finite element methods have been widely used for numerically solving some geometric equations such as the mean curvature flow, surface diffusion flow, Willmore flow and so on [6, 16, 17, 19, 20, 23, 24, 94]. Among these methods, the most considerable works are the parametric finite element methods proposed by J.W. Barrett *et al*. Their methods have a good preservation of the mesh quality by automatically distributing the mesh points along the discrete polygonal surfaces. These methods can be applied to the isotropic case and anisotropic case when the surface energy is given in the form of Riemannian metric.

In this chapter, we will present the parametric finite element method for solving the sharp interface model we derived in the last chapter (Eqs.(3.4.5), (3.4.6) with boundary conditions Eq. (3.4.8)-(3.4.10)). We start with a isotropic case, and then extend it to the anisotropic case when the surface energy density is not limited to the form of Riemannian metric.

Let $\mathbf{X} = (X_1,\ X_2,\ X_3)$ be the point vector of a surface, and $\mathbf{n} = (n_1,\ n_2,\ n_3)$

be the unit normal vector. When the surface energy is isotropic, the Cahn-Hoffman vector can be reduced to $\boldsymbol{\xi}(\mathbf{n}) = \mathbf{n}$. It is obvious to obtain the following expression based on the definition of surface gradient

$$\underline{D}_i X_j = \delta_{ij} - n_i n_j. \tag{4.0.1}$$

By noting the definition of Δ_s, we obtain directly

$$\Delta_s X_j = \sum_{i=1}^{3} \underline{D}_i(-n_i n_j) = -(\nabla_s \cdot \mathbf{n})n_j - \nabla_s n_j \cdot \mathbf{n} = -(\nabla_s \cdot \mathbf{n})n_j. \tag{4.0.2}$$

In view of the above equation, the dimensionless chemical potential μ can then be presented in the following form

$$\Delta_s \mathbf{X} = -(\nabla_s \cdot \mathbf{n})\,\mathbf{n} = -\mu\,\mathbf{n}. \tag{4.0.3}$$

Besides, the anisotropic co-normal vector will simultaneously reduce to the co-normal vector $\mathbf{c}_\Gamma$.

Now let $S(t)$ be the open surface representing the interface between the film and vapor with boundary $\Gamma(t)$. Assume $\mathbf{X}(\cdot, t)$ is a local parameterization of $S(t)$, thus the sharp interface model for the solid-state dewetting with isotropic surface energy in three dimensions can be stated as follows,

$$\partial_t \mathbf{X} = \Delta_s \mu\,\mathbf{n}, \qquad t > 0, \tag{4.0.4}$$

$$\mu = \mathcal{H} = -\Delta_s \mathbf{X} \cdot \mathbf{n}, \tag{4.0.5}$$

with the following boundary conditions on Γ

(1) contact line condition

$$\Gamma \subset S_{sub}, \qquad t \geq 0, \tag{4.0.6}$$

(2) relaxed contact angle condition

$$\partial_t \mathbf{X}_\Gamma = -\eta\Big[\mathbf{c}_\Gamma \cdot \mathbf{n}_\Gamma - \sigma\Big]\mathbf{n}_\Gamma, \qquad t \geq 0; \tag{4.0.7}$$

where $\mathbf{n}_\Gamma = \frac{P_{sub}\mathbf{n}}{|P_{sub}\mathbf{n}|} = \frac{1}{\sqrt{n_1^2 + n_2^2}}(n_1, n_2, 0)$, $\sigma = \frac{\gamma_{VS} - \gamma_{FS}}{\gamma_0}$, P_{sub} is the projection operator that maps a vector onto the tangent space of S_{sub}.

(3) zero-mass flux condition

$$\left.(\mathbf{c}_{\Gamma} \cdot \nabla_s \, \mu)\right|_{\Gamma} = 0, \qquad t \geq 0. \tag{4.0.8}$$

4.1 Variational formulation

We firstly assume that the evolution interface $S(t)$ can be parameterized over a fixed reference domain U such that

$$S(t) = \mathbf{X}(u, v, t) : U \times [0, T] \to \mathbb{R}^3. \tag{4.1.1}$$

Therefore, the boundary Γ is a closed plane curve and can be simultaneously considered as a parameterisation on the boundary of U, i.e.,

$$\Gamma(t) = \mathbf{X}_{\Gamma}(u, v, t) : \partial U \times [0, T] \to \mathbb{R}^3. \tag{4.1.2}$$

The reason we require that the surface $S(t)$ should be parameterized on a reference domain U is to propose the variational formulation. However, in the full-discrete scheme, this assumption is not compulsory as the discrete solutions are not defined on the reference domain.

4.1.1 For surface diffusion flow

Assume α represents a function defined over ∂U, we can define the following functional space for the solution of solid-state dewetting problem as

$$H_{\alpha}^1(U) := \{\varphi \in H^1(U), \ \left.\varphi\right|_{\partial U} \equiv \alpha\}. \tag{4.1.3}$$

Thus $H_0^1(U)$ denotes the functions in $H^1(U)$ with trace being zero.

For any scalar or vector valued functions u, v, the inner product over surface S can be given by

$$\langle u, \ v \rangle_S = \iint_S u \cdot v \, dS. \tag{4.1.4}$$

Now rewrite Eqs. (4.0.4),(4.0.5),

$$\partial_t \mathbf{X} \cdot \mathbf{n} = \Delta_s \mu, \tag{4.1.5a}$$

$$\mu \, \mathbf{n} = -\Delta_s \mathbf{X}. \tag{4.1.5b}$$

By multiplying a test function $\phi \in H^1(S)$ for Eq. (4.1.5a), and integrating by parts from Eq. (3.1.10), we obtain

$$
\begin{aligned}
0 &= \iint_S \partial_t \mathbf{X} \cdot \mathbf{n} \, \phi \, dS - \iint_S \Delta_s \mu \phi \, dS = \iint_S \partial_t \mathbf{X} \cdot \mathbf{n} \, \phi \, dS \\
&\quad + \iint_S \nabla_s \mu \cdot \nabla_s \phi \, dS - \iint_S (\nabla_s \mu \cdot \mathbf{n}) \phi \mathcal{H} \, dS - \int_\Gamma (\nabla_s \mu \cdot \mathbf{c}_\Gamma) \phi \, d\Gamma \\
&= \iint_S \nabla_s \mu \cdot \nabla_s \phi \, dS.
\end{aligned}
\tag{4.1.6}
$$

The last equality holds on because of the zero-mass flux boundary condition (4.0.8) and $\nabla_s \mu \cdot \mathbf{n} = 0$. Similarly, for Eq. (4.1.5b), we multiply a test function $\mathbf{g} \in (H_0^1(S))^3$ with zero values on the boundary, and integration by parts gives us

$$\iint_S \mu \, \mathbf{n} \cdot \mathbf{g} \, dS - \iint_S \nabla_s \mathbf{X} \cdot \nabla_s \mathbf{g} \, dS = 0, \tag{4.1.7}$$

where $\nabla_s \mathbf{X} \cdot \nabla_s \mathbf{g} = \sum_{j=1}^3 \nabla_s X_j \cdot \nabla_s g_j$.

Thus we can obtain the variational formulation for the surface diffusion flow: given the initial surface $S(0) = \mathbf{X}(U, 0)$ with its boundary (contact line) $\Gamma(0)$, we want to find the evolutionary surface $S(t) \in H_\alpha^1(U) \times H_\beta^1(U) \times H_0^1(U)$, $\mu \in H^1(S)$ such that

$$\left\langle \partial_t \mathbf{X} \cdot \mathbf{n}, \ \phi \right\rangle_S + \left\langle \nabla_s \mu, \ \nabla_s \phi \right\rangle_S = 0, \qquad \forall \phi \in H^1(S), \tag{4.1.8}$$

$$\left\langle \mu, \ \mathbf{n} \cdot \mathbf{g} \right\rangle_S - \left\langle \nabla_s \mathbf{X}, \ \nabla_s \mathbf{g} \right\rangle_S = 0, \qquad \forall \mathbf{g} \in (H_0^1(S))^3. \tag{4.1.9}$$

where α, β represents the x, y-coordinates of the moving contact line $\Gamma(t)$. Here the variational formulation is not closed as we still need to determine Γ. In the following we will present the variational formulation for the contact line migration, from which we can obtain $\Gamma(t)$.

4.1.2 For contact line migration

The contact line migration is given by Eq. (4.0.7), which describes the motion of a plane curve on the substrate. To obtain a variational formulation for the contact line migration, we begin by adding a small regularization term

$$\partial_t \mathbf{X}_\Gamma = \varepsilon^2 \partial_{ss} \kappa \mathbf{n}_\Gamma - \eta \Big[\mathbf{c}_\Gamma \cdot \mathbf{n}_\Gamma - \sigma \Big] \mathbf{n}_\Gamma, \qquad t \geq 0. \tag{4.1.10}$$

Here s is the arc length of the plane curve Γ, ε is a small regularization parameter, and κ is the curvature. In addition, for scalar or vector valued functions u, v, we define the L^2 inner product over Γ

$$\langle u, \ v \rangle_\Gamma = \int_\Gamma u \cdot v \, ds. \tag{4.1.11}$$

Then a variational formulation for Eq. (4.1.10) can be stated as following: given the initial plane curve $\Gamma(0) = \mathbf{X}_\Gamma(\partial U, 0)$, for any time $t \in (0, T]$, find the evolution curves $\Gamma(t) = \mathbf{X}_\Gamma(\partial U, t) \in (H^1(\partial U))^3$, $\kappa \in H^1(\Gamma)$ such that

$$\langle \partial_t \mathbf{X}_\Gamma \cdot \mathbf{n}_\Gamma, \ \varphi \rangle_\Gamma + \varepsilon^2 \langle \partial_s \kappa, \ \partial_s \varphi \rangle_\Gamma = -\eta \langle \mathbf{c}_\Gamma \cdot \mathbf{n}_\Gamma - \sigma, \ \varphi \rangle_\Gamma, \quad \forall \varphi \in H^1(\Gamma), \tag{4.1.12a}$$

$$\langle \kappa, \ \mathbf{n}_\Gamma \cdot \boldsymbol{\omega} \rangle_\Gamma - \langle \partial_s \mathbf{X}_\Gamma, \ \partial_s \boldsymbol{\omega} \rangle_\Gamma = 0, \quad \forall \boldsymbol{\omega} \in (H^1(\Gamma))^3, \tag{4.1.12b}$$

with $\Gamma = \Gamma(t)$. Eq. (4.1.12a) is obtain by writing the Eq. (4.1.10) in the form

$$\partial_t \mathbf{X}_\Gamma \ \mathbf{n}_\Gamma = \varepsilon^2 \partial_{ss} \kappa - \eta \Big[\mathbf{c}_\Gamma \cdot \mathbf{n}_\Gamma - \sigma \Big], \tag{4.1.13}$$

then multiplying the test functions φ and integrating by parts with periodic boundary conditions. Similarly, Eq. (4.1.12b) is obtained by presenting the curvature in the form $\kappa \ \mathbf{n} = -\partial_{ss} \mathbf{X}_\Gamma$. The advantage of adding this small surface diffusion flow regularization for the contact line migration is that we can propose a nice variational formulation for the motion of the contact line based on the work by J. W. Barrett [16]. Besides, the fully discrete scheme based on this variational formulation tends to distribute the mesh points uniformly according to the arc length, which is helpful to increase the total mesh quality [8, 16]. In most cases, the initial contact line is given as a closed curve which is only piecewise smooth with some sharp corners. This small surface diffusion regularization can help to round the corner after

several steps evolution, thus avoiding ear formulation. Note here $\mathbf{c}_\Gamma$ in Eq. (4.1.12a) is dependent on the surface $S(t)$.

4.1.3 Mass conservation and energy dissipation

Proposition 4.1.1 (Mass conservation for weak solution). *Let* $(\mathbf{X}(u,v,t),\mu(S,t))$ *be a weak solution for the above variational problem Eq.* (4.1.8),(4.1.9),(4.1.12a) *and* (4.1.12b), *then the total volume enclosed by the surfaece and the substrate is conserved,i.e.,*

$$M(t) \equiv M(0) = \iiint_{\Omega(0)} dX, \qquad t \geq 0. \tag{4.1.14}$$

Proof. It is easy to obtain that

$$\frac{d}{dt}M(t) = -\iint_S \partial_t \mathbf{X} \cdot \mathbf{n} \, dS. \tag{4.1.15}$$

Let $\phi = 1$ in Eq. (4.1.8), we have $\frac{d}{dt}M(t) = 0$. This immediately indicates that the total volume is conserved. $\qquad\square$

Proposition 4.1.2. *Let* $(\mathbf{X}(u,v,t),\mu(S,t))$ *be a weak solution for the above variational problem Eq.* (4.1.8),(4.1.9), (4.1.12a) *and* (4.1.12b). *If we assume that the surface has high regulariaty, that is* $\mathbf{X}(u,v,t) \in C^1(C^2(U),[0,T])$ *and the contact line* $\mathbf{X}_\Gamma(\partial U,t) \in C^1(C^2(\partial U),[0,T])$, *then the total energy of the system is decreasing, i.e.,*

$$W(t) \leq W(t_1) \leq W(0) \equiv \iint_{S(0)} dS - \sigma A(\Gamma(0)), \qquad t \geq t_1 \geq 0. \tag{4.1.16}$$

Proof. Taking derivative of the total energy with respect to the time t, based on Eq. (3.1.38), Eq. (3.2.17), and noting that $\mathbf{V}_0 = \partial_t \mathbf{X}$, we have the following

$$\frac{d}{dt}W(t) = \iint_S \nabla_s \cdot \partial_t \mathbf{X} \, dS - \sigma \int_\Gamma \partial_t \mathbf{X}_\Gamma \cdot \mathbf{n}_\Gamma \, d\Gamma. \tag{4.1.17}$$

Besides, for arbitrary vector $\mathbf{V}$, we have

$$
\begin{aligned}
\nabla_s \mathbf{X} \cdot \nabla_s \mathbf{V} &= \sum_{i=1}^{3}\sum_{j=1}^{3} \underline{D}_j X_i \, \underline{D}_j V_i = \sum_{i=1}^{3}\sum_{j=1}^{3} (\delta_{ij} - n_i n_j) \underline{D}_j V_i \\
&= \sum_{i=1}^{3}\sum_{j=1}^{3} \delta_{ij} \underline{D}_j V_i - \sum_{i=1}^{3}\sum_{j=1}^{3} n_i n_j \underline{D}_j V_i \\
&= \sum_{i=1}^{3} \underline{D}_i V_i - \sum_{i=1}^{3} n_i \mathbf{n} \cdot \nabla_s V_j = \nabla_S \cdot \mathbf{V}.
\end{aligned}
\tag{4.1.18}
$$

Thus we can rewrite Eq. (4.1.17) as

$$
\frac{d}{dt} W(t) = \iint_S \nabla_s \mathbf{X} \cdot \nabla_s (\partial_t \mathbf{X}) \, dS - \sigma \int_\Gamma \partial_t \mathbf{X}_\Gamma \cdot \mathbf{n}_\Gamma \, d\Gamma.
\tag{4.1.19}
$$

As the surface S and the cotact line Γ are parametrized on the reference domain U and ∂U respectively, if the test function is defined on S or Γ, we can also regard it as a parametrization on U or ∂U. Now for fixed δ, there exist a closed domain V belongs to the reference domain U such that the measure $m(U/V) < \delta$, and choose the test function $\mathbf{g}$ in Eq. (4.1.9) such that $\mathbf{g}\big|_V = \partial_t \mathbf{X}\big|_V$, and $\mathbf{g}\big|_{\partial U} = 0$, also let $\varphi = \mu$ in Eq. (4.1.8), we obtain

$$
\begin{aligned}
&\left\langle \nabla_s \mathbf{X}, \ \nabla_s (\partial_t \mathbf{X}) \right\rangle_S \\
&= \left\langle \nabla_s \mathbf{X}, \ \nabla_s (\partial_t \mathbf{X} - \mathbf{g}) \right\rangle_S + \left\langle \nabla_s \mathbf{X}, \ \nabla_s \mathbf{g} \right\rangle_S \\
&= \left\langle \nabla_s \mathbf{X}, \ \nabla_s (\partial_t \mathbf{X} - \mathbf{g}) \right\rangle_S + \left\langle \mu, \mathbf{n} \cdot \mathbf{g} \right\rangle_S \\
&= \left\langle \nabla_s \mathbf{X}, \ \nabla_s (\partial_t \mathbf{X} - \mathbf{g}) \right\rangle_S + \left\langle \mu, \mathbf{n} \cdot \partial_t \mathbf{X} \right\rangle_S + \left\langle \mu, \mathbf{n} \cdot (\mathbf{g} - \partial_t \mathbf{X}) \right\rangle_S \\
&= \left\langle \nabla_s \mathbf{X}, \ \nabla_s (\partial_t \mathbf{X} - \mathbf{g}) \right\rangle_S - \left\langle \nabla_s \mu, \ \nabla_s \mu \right\rangle_S + \left\langle \mu, \mathbf{n} \cdot (\mathbf{g} - \partial_t \mathbf{X}) \right\rangle_S.
\end{aligned}
\tag{4.1.20}
$$

The regularity of the surface ensures that we can perform integration by parts for the first term of above equation,

$$
\left\langle \nabla_s \mathbf{X}, \ \nabla_s (\partial_t \mathbf{X} - \mathbf{g}) \right\rangle_S = \left\langle (\partial_t \mathbf{X} - \mathbf{g}), \ \mathbf{n}\,(\nabla_s \cdot \mathbf{n}) \right\rangle_S + \left\langle (\partial_t \mathbf{X} - \mathbf{g})\big|_\Gamma, \ \mathbf{c}_\Gamma \right\rangle_\Gamma.
\tag{4.1.21}
$$

Thus we obtain that

$$
\begin{aligned}
\frac{d}{dt} W(t) &= \left\langle (\mu + \nabla_s \cdot \mathbf{n}), \ \mathbf{n} \cdot (\mathbf{g} - \partial_t \mathbf{X}) \right\rangle_S \\
&\quad - \left\langle \nabla_s \mu, \ \nabla_s \mu \right\rangle_S + \left\langle \partial_t \mathbf{X}_\Gamma \cdot \mathbf{n}_\Gamma, \ \mathbf{c}_\Gamma \cdot \mathbf{n}_\Gamma - \sigma \right\rangle_\Gamma.
\end{aligned}
\tag{4.1.22}
$$

Now let $\varphi = \mathbf{c}_\Gamma \cdot \mathbf{n}_\Gamma - \sigma$ in Eq. (4.1.12a), we obtain that

$$
\begin{aligned}
\frac{d}{dt} W(t) &= \big\langle (\mu - \nabla_s \cdot \mathbf{n}), \ \mathbf{n} \cdot (\mathbf{g} - \partial_t \mathbf{X}) \big\rangle_S - \varepsilon^2 \big\langle \partial_s \kappa, \ \partial_s (\mathbf{c}_\Gamma \cdot \mathbf{n}_\Gamma) \big\rangle_\Gamma \\
&\quad - \big\langle \nabla_s \mu, \ \nabla_s \mu \big\rangle_S - \eta \big\langle \mathbf{c}_\Gamma \cdot \mathbf{n}_\Gamma - \sigma, \ \mathbf{c}_\Gamma \cdot \mathbf{n}_\Gamma - \sigma \big\rangle_\Gamma.
\end{aligned} \tag{4.1.23}
$$

By the definition of $\mathbf{g}$, the first term can be as small as possible and bounded by $C\delta$. The second term can be bounded by the last term for smaller enough ε. So this indicates that $\frac{d}{dt} W(t) \leq 0$. $\qquad\square$

4.2 Spatial/temporal discretization

Based on the variational formulation Eq. (4.1.8), (4.1.9), (4.1.12a) and (4.1.12b), in this section, we introduce the fully discrete scheme. We first divide the time as

$$
0 = t_1 < t_2 < \ldots < t_M = T, \tag{4.2.1}
$$

with time step $\tau_m = t_{m+1} - t_m$. In the spatial level, let

$$
S^m = \bigcup_{j=1}^N \bar{D}_j^m, \quad \text{where } \{D_j^m\}_{j=1}^N \text{ are mutually disjoint triangle surfaces,} \tag{4.2.2}
$$

be a polygonal surface approximating the evolution surface $S(t_m)$ for $1 \leq m \leq M$. Assume the polygonal surface has K vertices given as $\{\mathbf{q}_k\}_{k=1}^K$. The boundary of the polygonal surface S^m is a polygonal curve Γ^m, which can be expressed as

$$
\Gamma^m = \bigcup_{j=1}^{N_c} \bar{h}_j^m, \quad \{h_j^m\}_{j=1}^{N_c} \text{ are line segments of the curve } \Gamma^m, \tag{4.2.3}
$$

where these line segments are ordered in anti-clockwise direction when viewing from the top. We use the P^1 finite elements, that means the function is linear on every element. Therefore we can define the following finite element spaces on S^m and Γ^m

$$
\mathcal{V}^h(\Gamma^m) := \left\{ \phi \in C(\Gamma^m, \mathbb{R}) : \phi\big|_{h_j^m} \text{ is linear } \forall 1 \leq i \leq N_c \right\} \subset H^1(\Gamma^m). \tag{4.2.4a}
$$

$$
\mathcal{V}^h(S^m) := \left\{ \phi \in C(S^m, \mathbb{R}) : \phi\big|_{D_j^m} \text{ is linear } \forall 1 \leq i \leq N \right\} \subset H^1(S^m). \tag{4.2.4b}
$$

Besides, we can define the finite element space on S^m with zero values on Γ^m

$$\mathcal{V}_0^h(S^m) := \{\phi \in \mathcal{V}^h(S^m), \phi\big|_{h_k^m} = 0, \ \forall 1 \leq k \leq N_c\} \subset H_0^1(S^m). \qquad (4.2.5)$$

Assume $\alpha \in H^1(\Gamma^m)$, we can defined the finite element space on S^m with boundary given by α

$$\mathcal{V}_\alpha^h(S^m) := \{\varphi \in V^h(S^m) : \ \varphi\big|_{\Gamma^m} = \alpha\} \qquad (4.2.6)$$
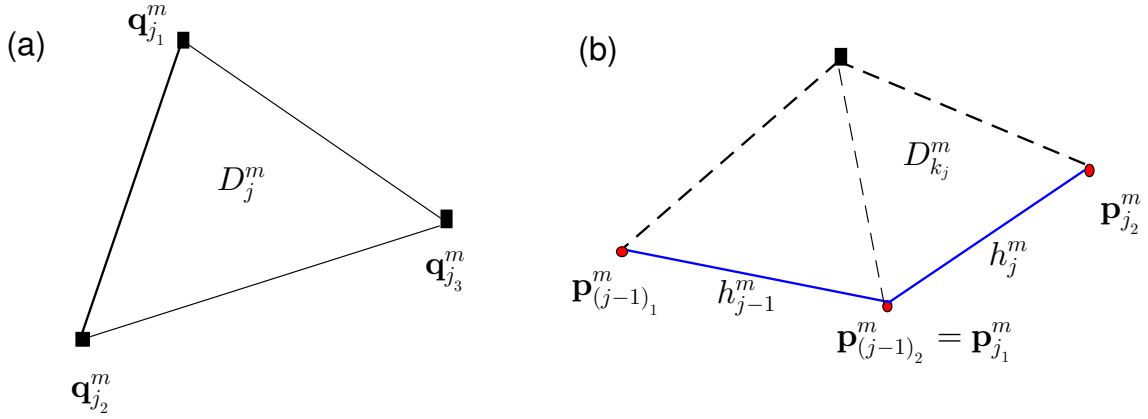
Figure 4.1: Typical triangles in the mesh. (a) A triangle with no edges on the boundary. (b) Two connected triangles with edges on the boundary.

The polygonal surface S^m consists of N triangle surfaces $\{D_j^m\}_{j=1}^N$ in three dimensions, see Fig. 4.1(a). If we assume that $\{\mathbf{q}_{j_1}^m, \mathbf{q}_{j_2}^m, \mathbf{q}_{j_3}^m\}$ are the vertices of the triangles D_j^m and ordered in the anti-clockwise direction viewing from the outside, then we know the normal function $\mathbf{n}^m$ of the surface S^m is a step function with discontinuities on the edges of each triangle. Denote $\mathbf{n}_j^m$ as the normal function on D_j^m, then we have

$$\mathbf{n}_j^m = \mathbf{n}^m\big|_{D_j^m} = \frac{(\mathbf{q}_{j_2}^m - \mathbf{q}_{j_1}^m) \times (\mathbf{q}_{j_3}^m - \mathbf{q}_{j_1}^m)}{|(\mathbf{q}_{j_2}^m - \mathbf{q}_{j_1}^m) \times (\mathbf{q}_{j_3}^m - \mathbf{q}_{j_1}^m)|}, \quad \forall 1 \leq j \leq N. \qquad (4.2.7)$$

In addition, as the boundary of the surface S^m, Γ^h is a plane curve on the substrate (xOy plane), which consists of connected line segments, see Fig. 4.1(b) (colored in blue). Here we assume that $\{\mathbf{p}_{j_1}^m, \mathbf{p}_{j_2}^m\}$ are the two vertices of h_j^m and ordered in the

anti-clockwise direction viewing from the positive z axis direction. Let $\mathbf{n}_{\Gamma^m}$ denote the unit normal vector of Γ^m on the substrate, then it is also a step function with discontinuities on the endpoints of each line segment h_j^m. If $\mathbf{n}_{\Gamma^m,j}$ is the normal function of Γ^m on line segment h_j^m, then

$$\mathbf{n}_{\Gamma^m,j} = \mathbf{n}_{\Gamma^m}\Big|_{h_j^m} = \frac{(\mathbf{p}_{j_2}^m - \mathbf{p}_{j_1}^m) \times \mathbf{z}}{|(\mathbf{p}_{j_2}^m - \mathbf{p}_{j_1}^m) \times \mathbf{z}|}, \quad \forall 1 \le j \le N_c, \tag{4.2.8}$$

where $\mathbf{z}$ is the unit vector along the positive direction of z axis. Now we can define the following mass-lumped norms to approximate the integration on S^m or Γ^m respectively,

$$\langle u, \ v \rangle_{S^m} = \frac{1}{3} \sum_{j=1}^N |D_j^m| \sum_{k=1}^3 u((\mathbf{q}_{j_k}^m)^-) \cdot v((\mathbf{q}_{j_k}^m)^-).$$

$$\langle f, \ g \rangle_{\Gamma^m} = \frac{1}{2} \sum_{j=1}^{N_c} |h_j^m| \sum_{k=1}^2 f((\mathbf{p}_{j_k}^m)^-) \cdot g((\mathbf{p}_{j_k}^m)^-).$$

Here in this expressions, $|D_j^m|, |h_j^m|$ are the area of the triangle of D_j^m and length of h_j^m respectively. u, v are two scalar or vector functions defined on S^m. f, g are two scalar or vector functions defined on Γ^m. Since the integrand could be discontinuous functions, thus we define $u((\mathbf{q}_{j_k}^m)^-)$ as the limit of $u(\mathbf{x})$ when $\mathbf{x}$ approaches towards $\mathbf{q}_{j_k}^m$ from triangles D_j^m, and $f((\mathbf{p}_{j_k}^m)^-)$ as the limit of $f(\mathbf{x})$ when $\mathbf{x}$ approaches towards $\mathbf{p}_{j_k}^m$ from the line segment h_j^m.

Finally we propose the following approximation of the variational formulation Eqs. (4.1.12a),(4.1.12b),(4.1.8) and (4.1.9): assume $S^0 = \bigcup_{j=1}^N \bar{D}_j^0$ is a discretization of the initial surface $S(0)$ with good mesh quality, and $\Gamma^0 = \bigcup_{j=1}^{N_c} \bar{h}_j^0$, for $1 \le m \le M-1$, we want to find $S^{m+1} := \mathbf{X}^{m+1} \in \mathcal{V}_\alpha^h(S^m) \times \mathcal{V}_\beta^h(S^m) \times \mathcal{V}_0^h(S^m), \mu^{m+1} \in \mathcal{V}^h(S^m)$, such that

$$\left\langle \frac{\mathbf{X}^{m+1} - \mathbf{X}^m}{\tau_m} \cdot \mathbf{n}^m, \ \phi_h \right\rangle_{S^m} + \left\langle \nabla_S \mu^{m+1}, \ \nabla_S \phi_h \right\rangle_{S^m} = 0, \quad \forall \phi_h \in \mathcal{V}^h(S^m), \tag{4.2.9a}$$

$$\left\langle \mu^{m+1}, \ \mathbf{n}^m \cdot \mathbf{g}_h \right\rangle_{S^m} - \left\langle \nabla_S \mathbf{X}^{m+1}, \ \nabla_S \mathbf{g}_h \right\rangle_{S^m} = 0, \quad \forall \mathbf{g}_h \in (\mathcal{V}_0^h(S^m))^3, \tag{4.2.9b}$$

where $\alpha, \ \beta$ are the $x, \ y$-coodrintes of the contact line Γ^{m+1}, and Γ^{m+1} can be found by the following approximation: find $\Gamma^{m+1} := \mathbf{X}_{\Gamma^{m+1}} \in (\mathcal{V}^h(\Gamma^m))^3, \kappa^{m+1} \in \mathcal{V}^h(\Gamma^m)$,

such that

$$\left\langle \frac{\mathbf{X}_{\Gamma^{m+1}} - \mathbf{X}_{\Gamma^m}}{\tau_m} \cdot \mathbf{n}_{\Gamma^m}, \ \varphi_h \right\rangle_{\Gamma^m} + \varepsilon^2 \left\langle \partial_s \kappa^{m+1}, \ \partial_s \varphi_h \right\rangle_{\Gamma^m} + \eta \left\langle \mathbf{c}_{\Gamma^m} \cdot \mathbf{n}_{\Gamma^m} - \sigma, \ \varphi_h \right\rangle_{\Gamma^m} = 0,$$

$$\forall \varphi_h \in \mathcal{V}^h(\Gamma^m), \tag{4.2.10a}$$

$$\left\langle \kappa^{m+1}, \ \mathbf{n}_{\Gamma^m} \cdot \boldsymbol{\omega_h} \right\rangle_{\Gamma^m} - \left\langle \partial_s \mathbf{X}_{\Gamma^{m+1}}, \ \partial_s \boldsymbol{\omega_h} \right\rangle_{\Gamma^m} = 0, \quad \forall \boldsymbol{\omega_h} \in (\mathcal{V}^h(\Gamma^m))^3. \tag{4.2.10b}$$

We note that in the above discrete scheme, we use the semi-implicit parametric finite element method instead of the fully implicit parametric finite element method. The integrations are calculated on S^m and Γ^m. Besides, all the nonlinear terms such as $\mathbf{n}^m$ and $\mathbf{n}_\Gamma$ are also valued explicitly. For each time step, we first update the boundary Γ^{m+1} by solving Eqs. (4.2.10a),(4.2.10b). In this scheme, $\mathbf{c}_{\Gamma^m}$ is the unit co-normal vector of the polygonal surface on the boundary, which is a step function on Γ^m. We can numerically value it as

$$\mathbf{c}_{\Gamma^m,j} = \mathbf{c}_{\Gamma^m}\Big|_{h_j^m} = \frac{(\mathbf{p}_{j_2}^m - \mathbf{p}_{j_1}^m) \times \mathbf{n}_{k_j}^m}{|(\mathbf{p}_{j_2}^m - \mathbf{p}_{j_1}^m)|}, \tag{4.2.11}$$

where $\mathbf{p}_{j_1}^m, \mathbf{p}_{j_2}^m$ are the vertices of the line segment h_j^m and ordered in the anti-clock wise direction. $\mathbf{n}_{k_j}^m$ is the unit outer normal vector of the triangle surface $D_{k_j}^m$ which contains the line segment h_j^m. After this, we can obtain S^{m+1} from Eqs. (4.2.16a),(4.2.10b). By considering that S^{m+1} is parametrized on S^m and Γ^{m+1} is parametrized on Γ^m, the term ∇_s and ∂_s operators can be easily calculated, which demonstrates the essential convenience of parametric finite element method. Precisely, consider triangle surface D_j^m with vertices $\{\mathbf{q}_{j_1}^m, \mathbf{q}_{j_2}^m, \mathbf{q}_{j_3}^m\}$ ordered in the anti-clockwise direction from the outside of the surface, then we have

$$\nabla_s B_i(S^m)\Big|_{D_j^m} = \frac{(\mathbf{q}_{j_3}^m - \mathbf{q}_{j_2}^m) \times \mathbf{n}_j^m}{2|D_j^m|}, \tag{4.2.12}$$

where B_i is the nodial basis function at point $\mathbf{q}_{j_i}^m$. Thus for any arbitrary function $\phi \in \mathcal{V}^h(S^m)$, we can derive

$$\nabla_s \phi\Big|_{D_j^m} = \sum_{i=1}^3 \phi(\mathbf{q}_{j_i}^m) \nabla_s B_i. \tag{4.2.13}$$

Similarly, for any arbitrary function $\varphi \in \mathcal{V}^h(\Gamma^m)$, we also have

$$\partial_s \varphi\Big|_{h_j^m} = \frac{\varphi(\mathbf{p}_{j_2}^m) - \varphi(\mathbf{p}_{j_1}^m)}{|h_j^m|}. \tag{4.2.14}$$

The numerical approximation of the geometric operator ∇_s, ∂_s becomes easier, and the discrete numerical approximations turn out to be two linear systems. We have the following theorem for the well-posedness of the scheme.

Theorem 4.2.1. *[Well-posedness of the PFEM scheme] The discrete variational problems, Eqs.* (4.2.16a), (4.2.16b), (4.2.10a) *and* (4.2.10b) *is well-posed.*

Proof. To prove the well-posedness of the PFEM scheme, we need prove the linear system obtained from Eqs. (4.2.16a), (4.2.16b) and the linear system obtained from Eqs. (4.2.10a), (4.2.10b) both has unique solution. It is equivalent to prove the two corresponding homogenous linear systems only have zero solutions. To solve Γ^{m+1}, we prove the following system has zero solution.

$$\left\langle \mathbf{X}_{\Gamma^{m+1}} \cdot \mathbf{n}_{\Gamma^m}, \ \varphi_h \right\rangle_{\Gamma^m} + \tau_m \varepsilon^2 \left\langle \partial_s \kappa^{m+1}, \ \partial_s \varphi_h \right\rangle_{\Gamma^m} = 0, \ \forall \varphi_h \in \mathcal{V}^h(\Gamma^m), \quad (4.2.15a)$$

$$\left\langle \kappa^{m+1}, \ \mathbf{n}_{\Gamma^m} \cdot \boldsymbol{\omega_h} \right\rangle_{\Gamma^m} - \left\langle \partial_s \mathbf{X}_{\Gamma^{m+1}}, \ \partial_s \boldsymbol{\omega_h} \right\rangle_{\Gamma^m} = 0, \ \forall \boldsymbol{\omega_h} \in (\mathcal{V}^h(\Gamma^m))^3. \quad (4.2.15b)$$

By choosing $\boldsymbol{\omega}_h = \mathbf{X}_{\Gamma^{m+1}}, \varphi = \kappa^{m+1}$, it is easy to prove that $\mathbf{X}_{\Gamma^{m+1}} = \mathbf{0}, \kappa^{m+1} = 0$ is the solution, see [16].

For the linear system of Eqs. (4.2.16a), (4.2.16b), the correpsonding homogenous linear system is to find $\mathbf{X}^{m+1} \in (\mathcal{V}_0^h(S^m))^3, \mu \in \mathcal{V}^h(S^m)$

$$\left\langle \mathbf{X}^{m+1} \cdot \mathbf{n}^m, \ \phi_h \right\rangle_{S^m} + \tau_m \left\langle \nabla_s \mu^{m+1}, \ \nabla_s \phi_h \right\rangle_{S^m} = 0, \ \forall \phi_h \in \mathcal{V}^h(S^m), \quad (4.2.16a)$$

$$\left\langle \mu^{m+1}, \ \mathbf{n}^m \cdot \mathbf{g}_h \right\rangle_{S^m} - \left\langle \nabla_s \mathbf{X}^{m+1}, \nabla_s \mathbf{g}_h \right\rangle_{S^m} = 0, \ \forall \mathbf{g}_h \in (\mathcal{V}_0^h(S^m))^3. \quad (4.2.16b)$$

By choosing $\phi = \mu^{m+1}, \mathbf{g}_h = \mathbf{X}^{m+1}$, we can obtain

$$\tau_m \left\langle \nabla_s \mu^{m+1}, \nabla_s \mu^{m+1} \right\rangle_{S^m} + \left\langle \nabla_s \mathbf{X}^{m+1}, \nabla_s \mathbf{X}^{m+1} \right\rangle_{S^m} = 0. \quad (4.2.17)$$

Thus we obtain $\mathbf{X}^{m+1} = \mathbf{0}$ by the zero boundary, and then $\mu^{m+1} = 0$. So we have prove the uniqueness and existence of the two linear systems obtained from the scheme, thus the semi-implicit PFEM scheme is well-posed. $\qquad\square$

To summarise, our parametric finite element method is a combination of the parametric finite element method for closed curve evolution [16] (the contact line

migration by a small surface diffusion regularization) and the parametric finite element method for open surface [20] (interface evolution under surface diffusion flow). The mesh quality can be preserved such that there is no need to do any mesh regularizations during the evolution as long as the initial mesh quality is good enough. The two linear systems obtained from the PFEM scheme can be solved via Spare LU decomposition. The mass matrix under the the mass-lumped norm can be reduced to the simple diagonal matrix, thus the linear systems are easy to be solved even though the mass matrix and stiffness matrix are dependent on the time step.

4.3   Numerical results

In this section, based on the PFEM scheme, we will show some numerical results for the scheme.

4.3.1   Contact line mobility and smooth regularization effect

From the relaxation boundary condition in Eq. (4.0.7), which controls the migration of the contact line, we know that the mobility precisely represents the relaxation rate of the contact angle towards the equilibrium contact angle. The large η will accelerate the relaxation process [120]. Thus the choice of η will have significant influence on the dynamic evolution of the surface, especially the contact angles of the surface. On the other hand, η is a material parameter and could be variant for different materials. Therefore, we will numerically investigate the effect of η on the evolution of the dynamic contact angles firstly. For the polygonal surface, we define the following indicator,

$$\bar{\theta}^m = \frac{1}{N_c} \sum_{j=1}^{N_c} \arccos(\mathbf{c}_{\Gamma^m,j} \cdot \mathbf{n}_{\Gamma^m,j}), \qquad (4.3.1)$$

which is the mean value of all the contact angles on each line segment of Γ^m. Fig. 4.2 shows the temporal evolution of $\bar{\theta}^m$ and the normalized energy $W(t)/W(0)$ under different choices of the mobility. The initial thin film is chosen as a unit cube
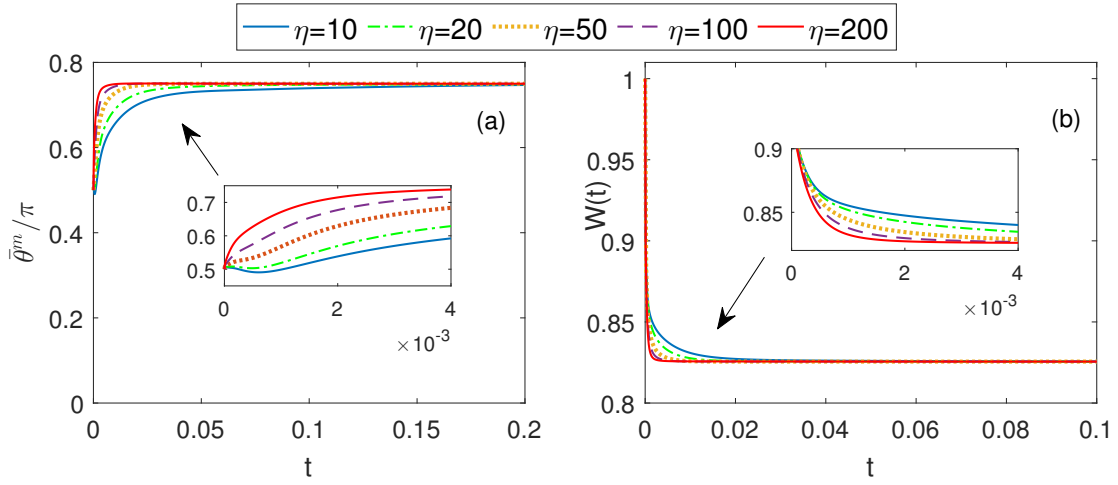
Figure 4.2: (a) The temporal evolution of contact angle $\bar{\theta}^m$ defined in Eq. (4.3.1); (b) the temporal evolution of the normalized energy $W(t)/W(0)$ for different choices of mobility.

on the substrate with material constant $\sigma = \cos(3\pi/4)$. From the figure, we can observe that the larger mobility will accelerate the process of relaxation such that the contact angles evolve faster towards the same equilibrium angle $\frac{3\pi}{4}$. Similarly, as shown in Fig. 4.2(b), the energy decays faster for larger mobility, but finally reaches the same value. This indicates that the equilibrium contact angles as well as the equilibrium shape are independent on the choice of η. So in the following, without special mention, we always assume the mobility is chosen as $\eta = 100$.

As discussed previously, the introduction of the smooth regularization for the contact line migration enables us to apply PFEM to approximate the contact line migration. It is obvious that the smaller regularization parameter ε is desired. However, numerical mesh size, as well as the time step, prevents us from choosing too small ε. Fig. 4.3 shows the geometric comparison of the contact lines for different ε at time $t = 0.02, 0.12, 0.52$. The initial thin film is given by a $(3.2, 3.2, 0.1)$ cuboid with computational parameter chosen as $\eta = 100, \sigma = \cos(5\pi/6)$. From the figure, we can observe that when $\varepsilon \leq 0.01$, the influence of the regularization on the contact line migrations could be almost ignored. Thus, it is always assumed the regularization
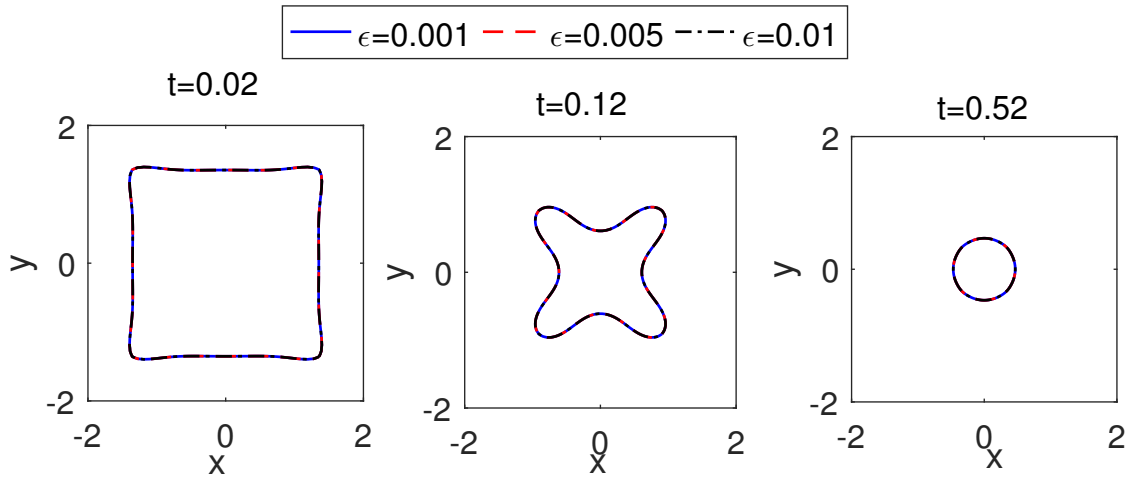
Figure 4.3: Comparison of the dynamic contact lines under different regularization parameter ε. The initial thin film is a cuboid with dimension $(3.2, 3.2, 0.1)$. The computational parameter is chosen as $\eta = 100, \sigma = \cos(5\pi/6)$.

parameter is chosen as $\varepsilon = 0.01$ if there is no special mention. On the other hand, our numerical simulations demonstrate that when ε is too big, this regularization could be regarded as a drag effect and will cause the mesh deterioration.

4.3.2 Convergence test
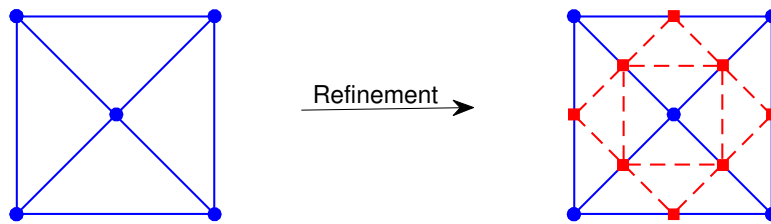
Figure 4.4: A illustration of mesh refinement procedure by dividing each triangle into four small triangles.

For an initial cuboid, we assume each face of the cuboid except the face on the

substrate consists of squares and each square is divided into 4 triangles. Based on this mesh, we can refine it by dividing each right triangle into four small ones, see Fig. 4.4. This mesh refinement procedure can be then repeated to produce the mesh with desirable mesh size. For the initial polygonal mesh, we can define mesh size h as the length of the hypotenuse of the small right triangles. Thus for a mesh obtained via n refinements, one can immediately get $h = \frac{1}{2^n}$.

We firstly want to investigate the convergence of our PFEM for the equilibrium shape. Fig. 4.5 and Fig. 4.6 show the convergence of the cross-section profiles and contact lines respectively. For mesh1, the initial polygonal mesh is obtained after 3 refinements with $h = 0.125$, and the time step is chosen as $\tau_1 = 1.25 \times 10^{-3}$. As mesh2 is a refinement of mesh1 and mesh3 is a refinement of mesh2, thus the time step for them is chosen as $\frac{\tau_1}{4}$ and $\frac{\tau_1}{4^4}$. The two figures clearly demonstrate that the numerical equilibrium shape is convergence towards the theoretical equilibrium shape as the mesh size decreases.
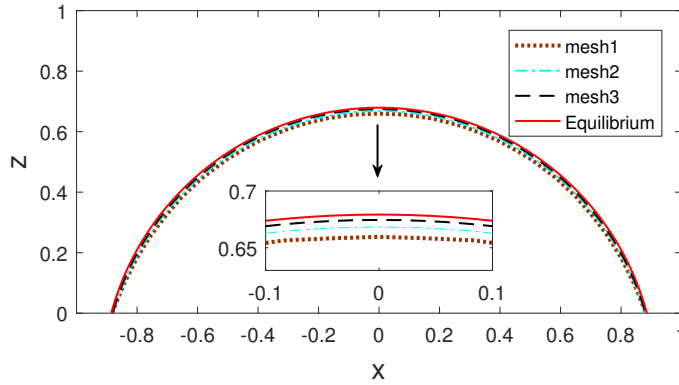
Figure 4.5: Comparison of the cross-section profiles in x-direction of the numerical equilibrium shapes for different meshes with that of the theoretical equilibrium shape. The initial surface is a unit cube on the substrate, $\sigma = \cos(15\pi/36)$.

To our knowledge there is no theory for the convergence order of the PFEM scheme so far, but it is still interesting to investigate the convergence of the scheme. Given the numerical polygonal surface $\mathbf{X}^m$ at discrete time t_m with $0 \leq m \leq M$,
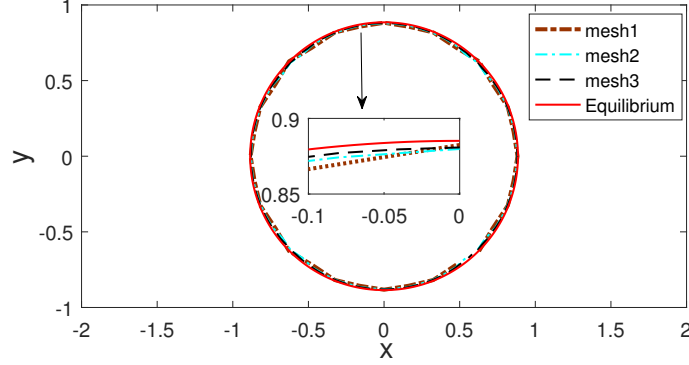
Figure 4.6: Comparison of the numerical contact lines of the equilibrium shapes for different meshes with the contact line of the theoretical equilibrium shape. The initial surface is a unit cube on the substrate, $\sigma = \cos(15\pi/36))$.

we can define the numerical solution at arbitrary time $t_m \leq t < t_{m+1}$ as a linear interpolation

$$\mathbf{X}_{h,\tau}(t) = \frac{t_{m+1} - t}{\tau_m}\mathbf{X}^m + \frac{t - t_m}{\tau_m}\mathbf{X}^{m+1}. \tag{4.3.2}$$

Here h is the mesh size of the $\mathbf{X}^0$, τ is the uniform time step. Since there is no analytical solution for us to compare with our numerical solution, we define the numerical error as following

$$e_{h,\tau}(t) = ||\mathbf{X}_{h,\tau}(t) - \mathbf{X}_{\frac{h}{2},\frac{\tau}{4}}(t)||_{L^\infty} = \max_{1 \leq k \leq K} \min_{1 \leq j \leq N} \text{dist}(\mathbf{q}_k, D_j), \tag{4.3.3}$$

where $\mathbf{q}_j$ is the vertices of $\mathbf{X}_{h,\tau}$, and D_j is the triangle of $\mathbf{X}_{\frac{h}{2},\frac{\tau}{4}}(t)$. dist is the distance function for a vertices to a triangle in three dimensions. In order to test the convergence order, the computation set-up is prepared as following: the initial thin film is chosen as a cuboid with dimension $(1, 2, 1)$. The material constant is fixed with $\sigma = \cos(3\pi/4)$, and $h_0 = 0.5, \tau_0 = 0.005$. We compute the convergence order at three different time $t = 0.02, 0.05, 0.1$.

From Table. 4.1, we can observe the convergence order is around 1. The convergence test for the PFEM applied to mean curvature flow with closed surface has

Table 4.1: Convergence rates in the L^∞ norm for an open surface evolution under the isotropic surface diffusion flow (solid-state dewetting with isotropic surface energy), where the computational parameters are chosen as: $\sigma = \cos(3\pi/4)$. The initial thin film is given as a $(1, 2, 1)$ cuboid.

$e_{h,\tau}(t)$	$h = h_0$ $\tau = \tau_0$	$h_0/2$ $\tau_0/2^2$	$h_0/2^2$ $\tau_0/2^4$	$h_0/2^3$ $\tau_0/2^6$
$e_{h,\tau}(t = 0.02)$	1.13E-1	3.63E-2	1.34E-2	5.90E-2
order	–	1.63	1.43	1.18
$e_{h,\tau}(t = 0.05)$	1.14E-1	4.16E-2	1.72E-2	8.40E-2
order	–	1.45	1.27	1.03
$e_{h,\tau}(t = 0.10)$	1.00E-1	4.23E-2	2.00E-2	1.01E-2
order	–	1.24	1.08	0.99

been reported in [20] and the convergence order is 2. Here the convergence order for our PFEM reduces to 1. The reason may be due to our explicit scheme for the contact line migration.

4.3.3 Small islands

Fig. 4.7 shows several stages of the evolution of a unit cube towards its equilibrium shape. The initial mesh consists of 1280 same right triangles with two legs sharing the same length of $\frac{\sqrt{2}}{2^4}$. The mesh contains 657 vertices with 32 vertices on the boundary. We can observe that the unit cube finally evolves into a spherical geometry with contact angle approximating $\frac{3\pi}{4}$.

Fig. 4.8(a) shows the temporal evolution of the normalized mass and energy, where the computational parameter is chosen the same as Fig. 4.7. As is shown in the figure, the mass conservation and energy dissipation is clearly demonstrated, which indicates the discrete PFEM scheme can grasp these fundamental properties
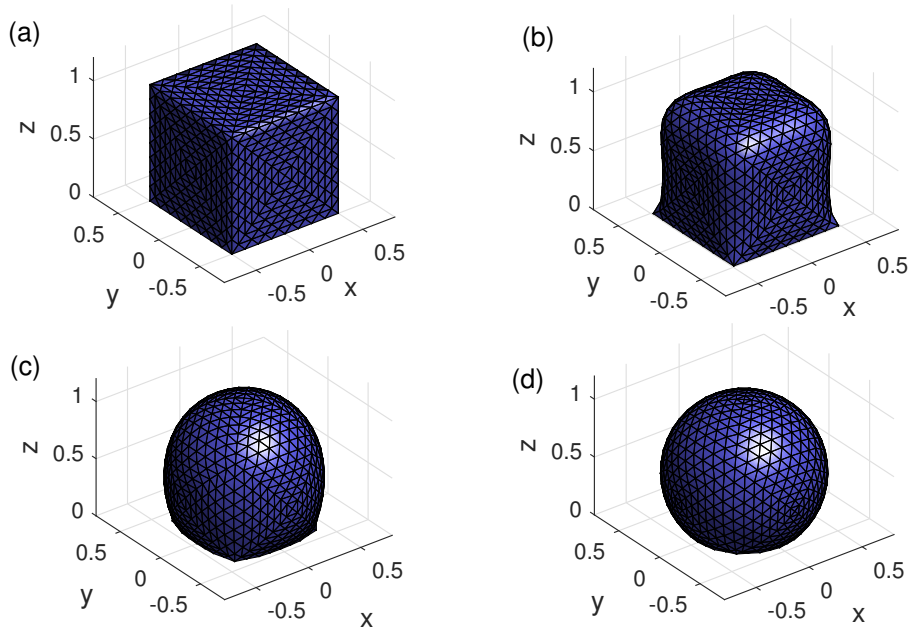
Figure 4.7: Several snapshots in the evolution of a small initially unit cube towards its equilibrium shape with parameter chosen as $\sigma = \cos(3\pi/4)$, (a) $t = 0$; (b) $t = 2e - 4$; (c) $t = 0.02$; (d) $t = 0.2$.
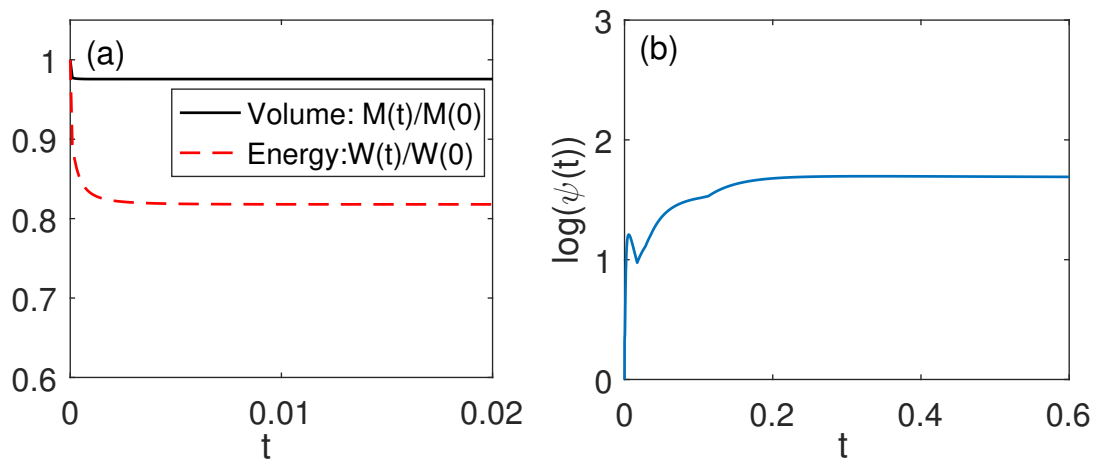
Figure 4.8: (a) The temporal evolution of the normalized total free energy and the normalized volume (mass); (b) the temporal evolution of the logarithm of the mesh distribution function $\psi(t)$. The computational parameter is chosen as same as Fig. 4.2.

of solid-state dewetting. Fig. 4.8(b) depicts the logarithm of the mesh distribution function $\psi(t)$ during the time evolution, where $\psi(t)$ is the indicator of the mesh quality defined as

$$\psi(t_m) = \frac{\max_{j=1}^N |D_j^m|}{\min_{j=1}^N |D_j^m|}. \tag{4.3.4}$$

From the figure, it can be seen that $\ln(\psi(t))$ is bounded and tends to be horizontal as time evolves, which indicates that our PFEM scheme has a good mesh quality preservation. Thus mesh regularization is not needed during the computation.

The influence of the material constant σ on the equilibrium shape has been investigated and the result is shown in Fig. 4.9. It clearly demonstrates that the σ determines the contact angle of the equilibrium shape.
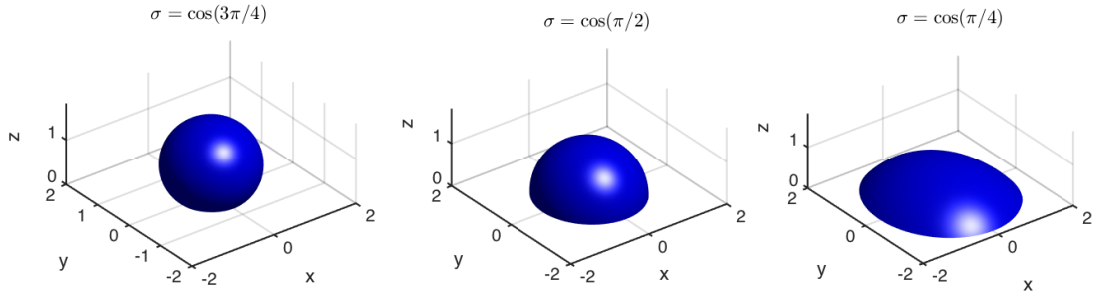
Figure 4.9: The equilibrium shape of an initial unit cube with different material constants σ.

4.3.4 Large islands

If the initial thin film is given by long thin islands, it possibly breaks up into small islands due to the Rayleigh instability [84, 99]. Therefore, we want to investigate the evolution of long islands with dimensions $(1, m, 1)$. We test three examples with $m = 4, 12, 16$, and the material constant is fixed with $\sigma = \cos(3\pi/4)$. As depicted in Fig. 4.10, the thin film with dimension $(1, 4, 1)$ evolves and forms a single island with spherical geometry. When we choose larger m, the thin films break up into 2 small islands or 3 smalls islands, see Fig. 4.11 and Fig. 4.12 respectively.

Figure 4.10: Several snapshots in the evolution of an initial cuboid with dimension $(1, 4, 1)$ towards its equilibrium. (a) $t = 0$; (b) $t = 0.01$; (c) $t = 0.10$; (d) $t = 2.35$. The computational parameter is chosen as $\sigma = \cos(3\pi/4)$.

Figure 4.11: Several snapshots in the evolution of an initial cuboid with dimension $(1, 12, 1)$ until its pinch off. (a) $t = 0$; (b) $t = 0.01$; (c) $t = 0.50$; (d) $t = 1.07$. The computational parameter is chosen as $\sigma = \cos(3\pi/4)$.

Figure 4.12: Several snapshots in the evolution of an initial cuboid with dimension $(1, 16, 1)$ until its pinch off. (a) $t = 0$; (b) $t = 0.20$; (c) $t = 0.75$; (d) $t = 1.14$. The computational parameter is chosen as $\sigma = \cos(3\pi/4)$.

In order to fully understand the geometry evolution for the thin film, we have depicted several snapshots for the contact lines and cross-section profiles for the thin film, see Fig. 4.13. From the figure, we can observe that the thin films pinch off at a point, where both the contact line and cross-section profiles break up.

Then there must exist critical lengths L_1, L_2, such that when $L_1 \leq m \leq L_2$, the long thin film breaks up into 2 small isolated islands, and when $L \geq L_2$, the long thin film breaks up into 3 or more than 3 small isolated islands. Besides, these two critical lengths should be dependent on the the material constant σ. We give the phase diagrams for the numbers of islands formed from the initially $(1, L, 1)$ cuboid islands with material constant σ in Fig. 4.14(a). From the figure, we can observe that for the long islands, the critical length L_1 and L_2 are linear to $\frac{1}{\sin(\arccos \sigma/2)}$. This relation has been observed and reported in two dimensions both for isotropic and weakly anisotropic surface energy [40,120]. Moreover, we also plot the pinch-off time t_p for $(1, L, 1)$ cuboid island for $\sigma = \cos \frac{\pi}{3}, \cos \frac{\pi}{2}, \cos \frac{2\pi}{3}$. From the figure, we can observe, at the beginning, as L increases, the time the thin film pinches off
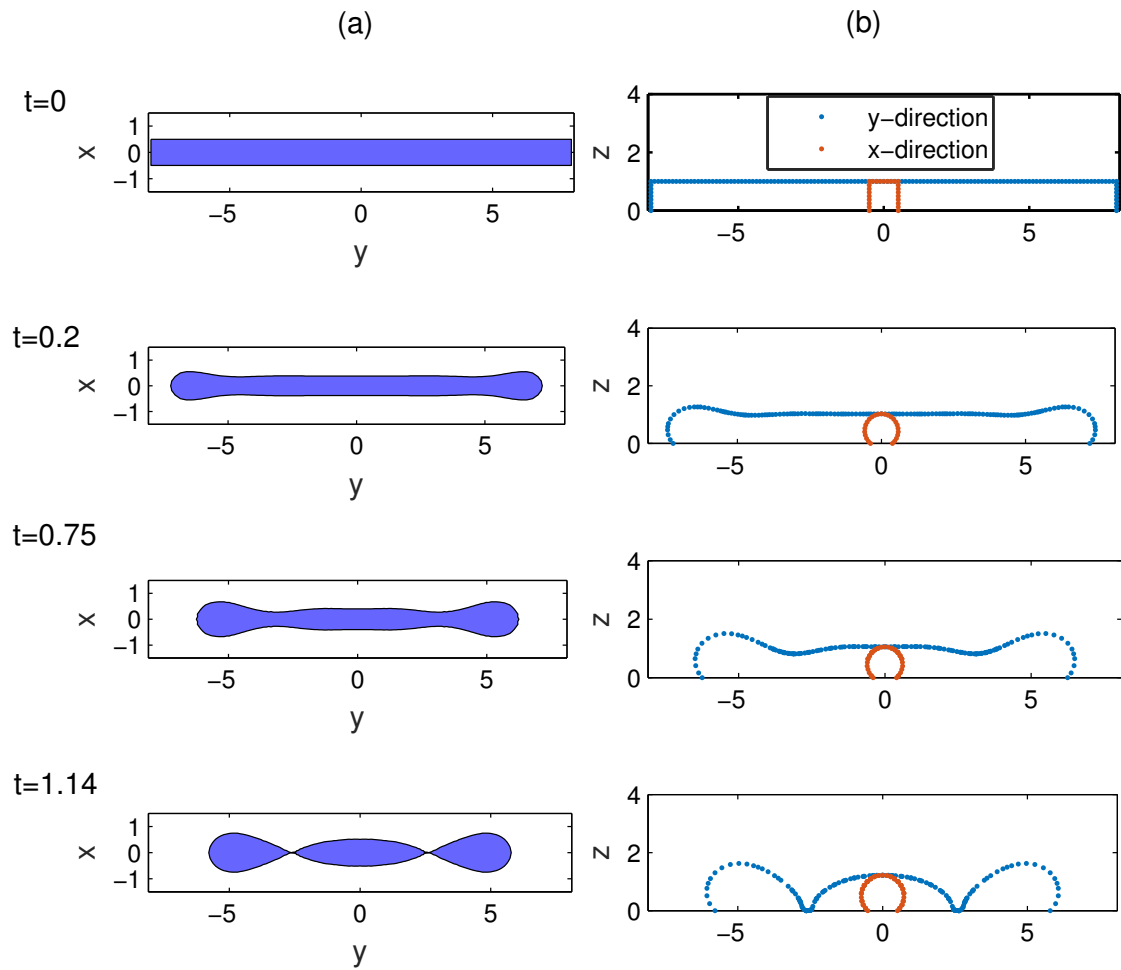
Figure 4.13: Several snapshots in the evolution of the contact lines (shown in column (a)) and the cross-section profile (shown in column (b)) until pinch off. The computational parameter is chosen as $\sigma = \cos(3\pi/4)$.
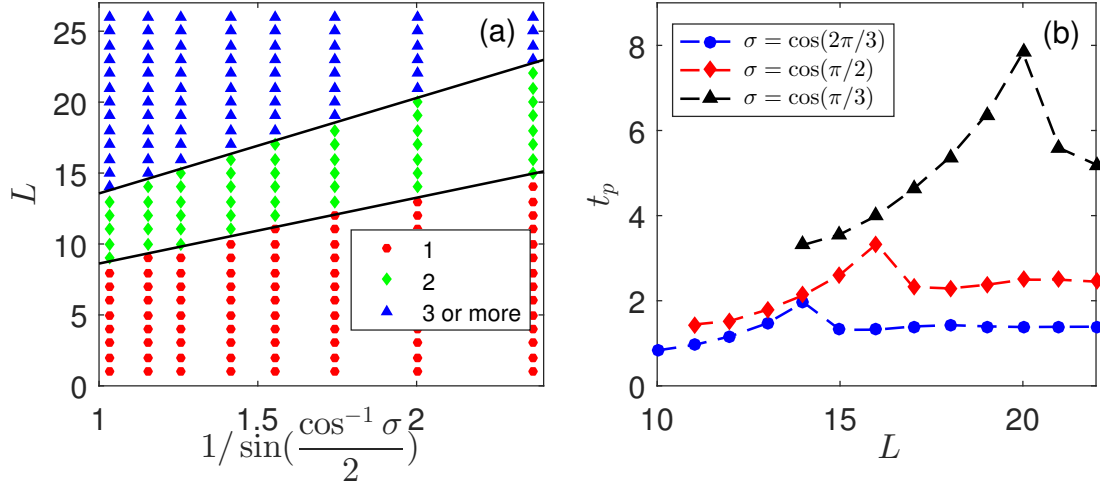
Figure 4.14: (a) Phase diagram for the number of islands formed from the initial $(1, L, 1)$ cuboid with material constant σ. The boundaries are given by our fitting linear curve $L = 3.98 + 4.64x$ and $L = 6.84 + 6.725x$, where $x = \frac{1}{\sin(\frac{\arccos \sigma}{2})}$. (b) The pinch off time t_p for the initial $(1, L, 1)$ cuboid island with three different σ.

increasing quickly as a consequence. However, as L reaches the critical length L_2, the line for pinch-off time drops and then almost stays horizontal.

We consider the morphology evolutions of large thin films with dimensions $(m, m, 1)$. We start by simulating the evolution of an initial square with dimensions $(3.2, 3.2, 0.1)$, and the parameter is chosen as $\sigma = \cos(5\pi/6)$. As shown in Fig. 4.15, the thin film evolves into a single spherical geometry. During the evolution, the corners retract much more slowly than the edges at the beginning, see Fig. 4.16. This phenomenon of corner accumulation has also been observed in experiment [117]. These corners at last catch up with the edges and the contact line moves towards a circular shape. If we enlarge the size of the thin film, as is depicted in Fig. 4.17, the thin film demonstrates the similar corner accumulation at the beginning but finally pinches off and forms hole in the centre, see Fig. 4.18. These two examples have also been numerically simulated in [66] via the phase field approach. Our numerical results are consistent with theirs.
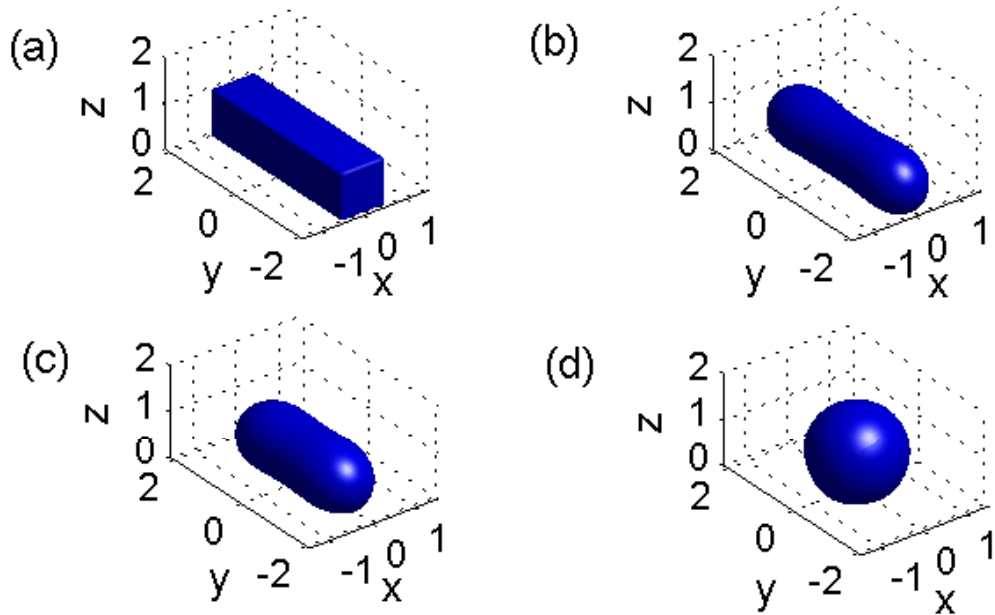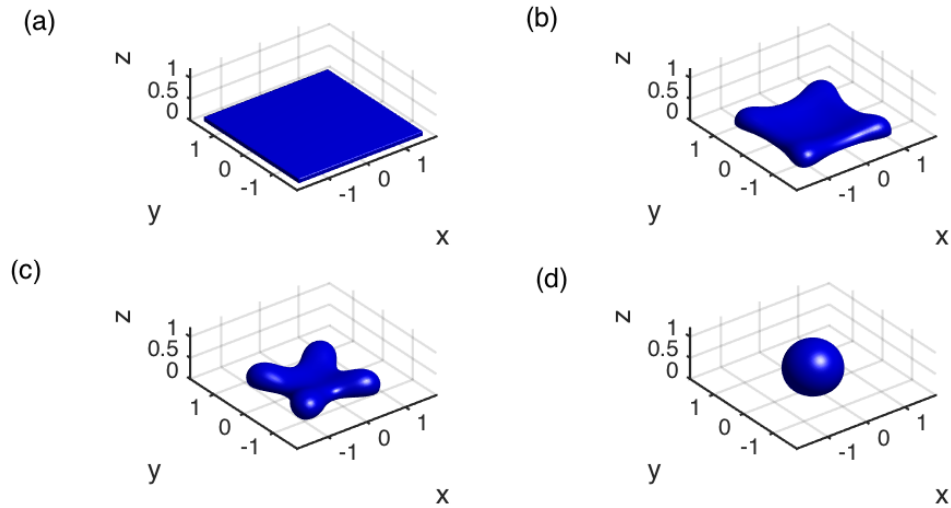
Figure 4.15: Several snapshots in the evolution of an initial cuboid with dimension $(3.2, 3.2, 0.1)$ towards its equilibrium. (a) $t = 0$; (b) $t = 0.0050$; (c) $t = 0.01$; (d) $t = 0.08$. The computational parameter is chosen as $\sigma = \cos(5\pi/6)$.
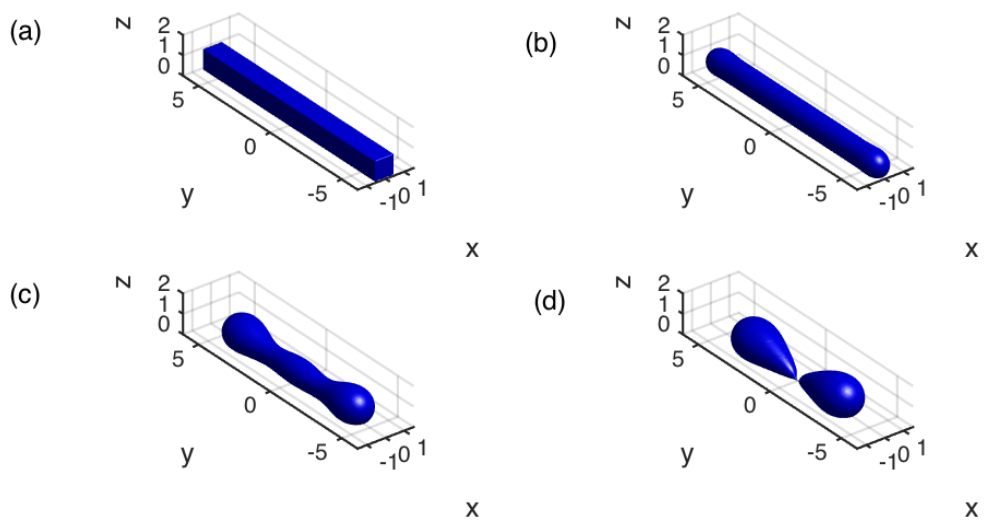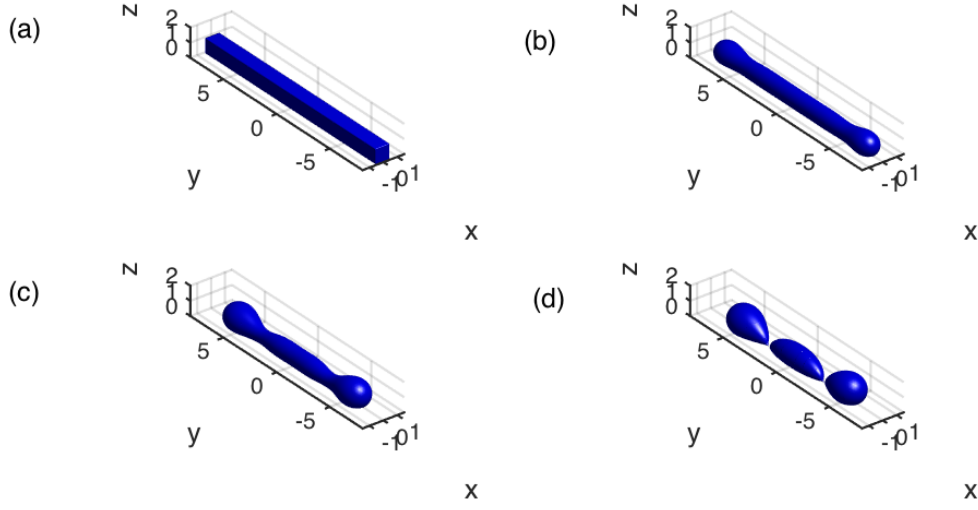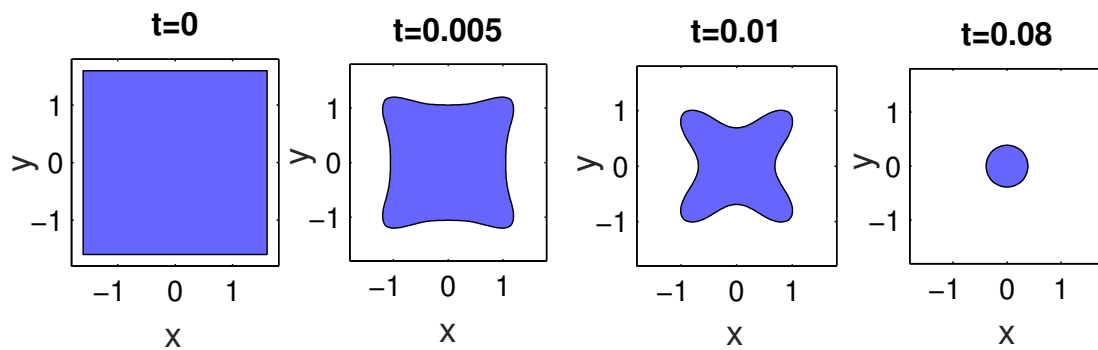

Figure 4.16: Several snapshots in the evolution of the interface between the thin film and substrate towards the thin film's equilibrium., and the initial cuboid is chosen with dimension $(3.2, 3.2, 0.1)$. The computational parameter is chosen as $\sigma = \cos(5\pi/6)$.
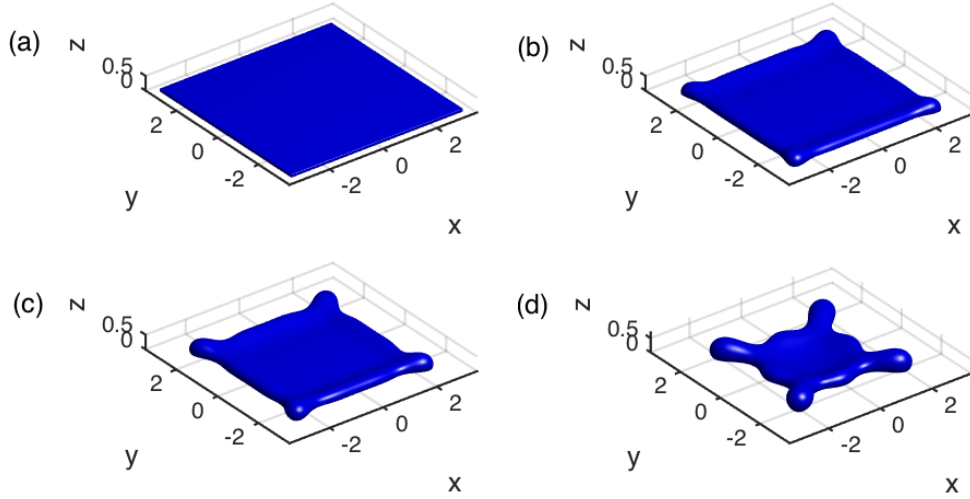
Figure 4.17: Several snapshots in the evolution of an initial cuboid with dimension $(6.4, 6.4, 0.1)$ until its pinch off. (a) $t = 0$; (b) $t = 0.005$; (c) $t = 0.010$; (d) $t = 0.031$. The computational parameter is chosen as $\sigma = \cos(5\pi/6)$.
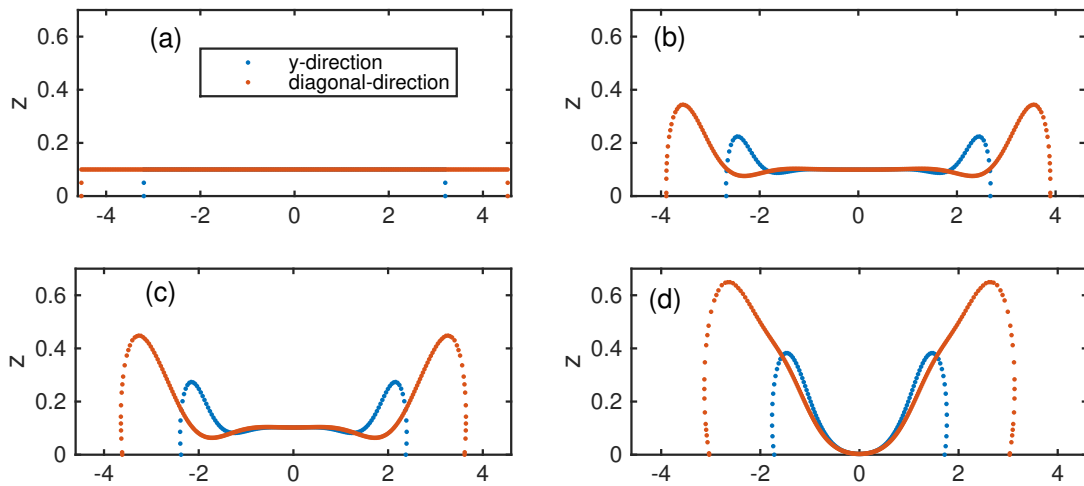
Figure 4.18: Several snapshots in the evolution of the cross section profile of the thin film along y-direction or diagonal direction until its pinch off, where the initial cuboid is chosen with dimension $(6.4, 6.4, 0.1)$. (a) $t = 0$; (b) $t = 0.005$; (c) $t = 0.010$; (d) $t = 0.031$. The computational parameter is chosen as $\sigma = \cos(5\pi/6)$.

4.3.5   Some special geometries

We investigate the morphology evolutions for islands initially given with some special geometries, such as the cross shape and square ring. Without special mention, the height of the initial thin film is always chosen to be 1, and the computational material constant is chosen as $\sigma = \cos\frac{3\pi}{4}$.

As illustrated in Fig. 4.19, it demonstrates several stages of the geometry evolution of an initial cross-shaped island. The island is chosen with a cube attached with four equal limbs, and the four limbs are given by cuboids with dimension $(1, 4, 1)$. From the figure, we can observe that thin film eventually evolves into a single island with spherical geometry. However, if the four limbs are replaced with longer cuboids, the evolution could be quite different, see Fig. 4.20. As depicted in the figure, the four limbs are chosen with $(1, 6, 1)$ cuboid. Instead of forming a single island, the cross-shaped film undergoes pinch off at the joint and breaks up into five small islands. Fig. 4.21 and Fig. 4.22 are illustrations of the dynamic interface between the film and the substrate for the case of Fig. 4.19 and Fig. 4.20 respectively. It clearly demonstrates the migrations of the contact line during the evolution. When the thin film forms a single island, the contact line evolves into a circular shape. On the contrary, when pinch-off event happens, the contact line, which is a closed curve, breaks up into five closed curves simultaneously.

We next consider the case when the initial thin film is given as a square ring with wall thickness equaling 1 but different dimensions for the outer edges. We start by considering the evolution of a small square ring with the length of outer edges chosen as 2.5, see Fig. 4.23. As depicted in the figure, it clearly demonstrates the geometry evolution of the island as well as the cross-section profiles. The square ring firstly evolves into a ringlike shape but with different heights in different cross-section directions. However, as time evolves, the ring becomes a toroidal shape with same height in all cross-section orientations, see Fig. 4.23(c). At the same time, the toroidal film is also migrating towards its centre. If we enlarge the length of the outer edges for the initial thin film, the thin film will undergo pinch-off, see Fig. 4.24
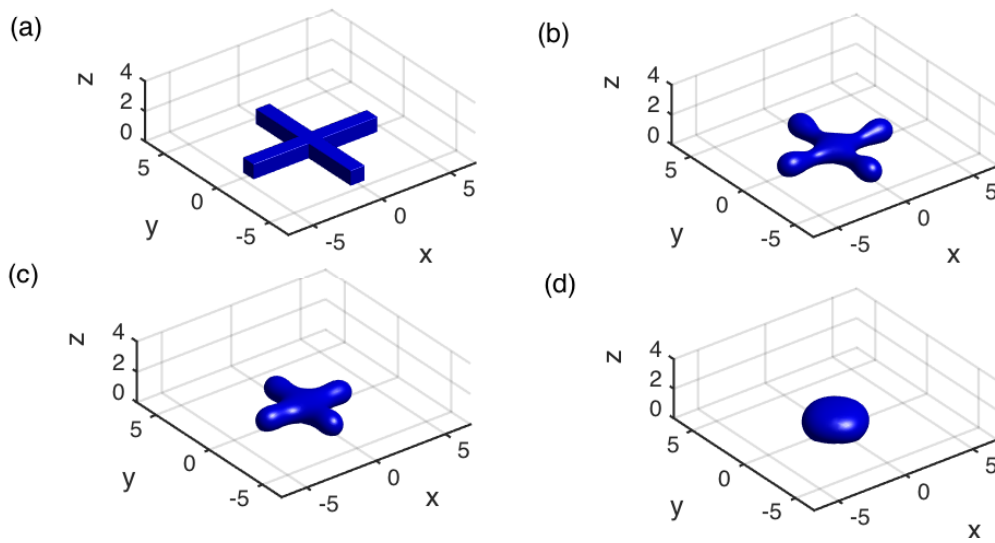
Figure 4.19: Several snapshots in the evolution of an initially cross-shaped island towards its equilibrium shape. Here the island consists of four (1,4,1) cuboids forming the limbs and one (1,1,1) cube in the centre, (a) $t = 0$; (b) $t = 0.15$; (c) $t = 0.5$; (d) $t = 0.9$; $\sigma = \cos(3\pi/4)$.
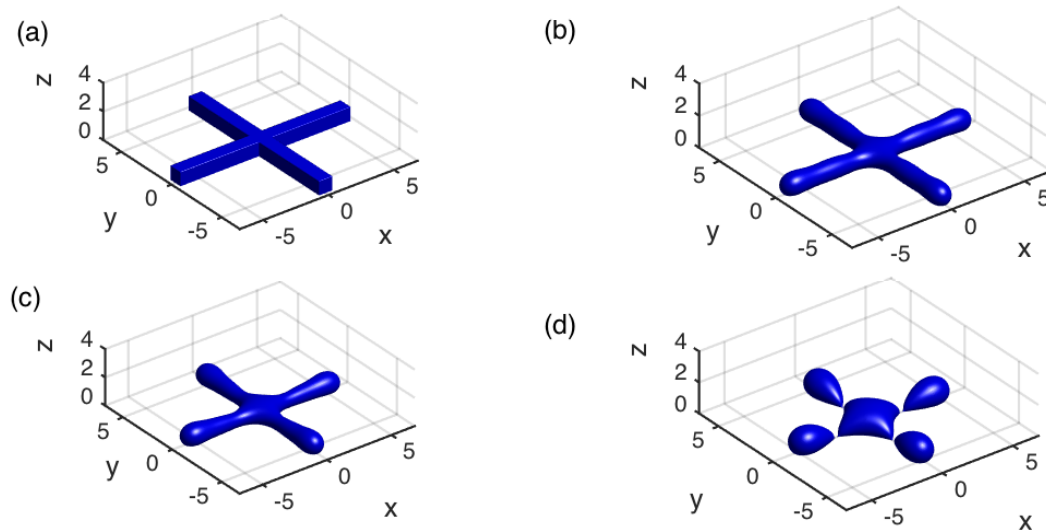
Figure 4.20: Several snapshots in the evolution of an initially cross-shaped island before its pinch-off. Here the island consist of four (1,6,1) cuboids forming the limbs and one (1,1,1) cube in the centre, (a) $t = 0$; (b) $t = 0.05$; (c) $t = 0.15$; (d) $t = 0.386$, $\sigma = \cos(3\pi/4)$.
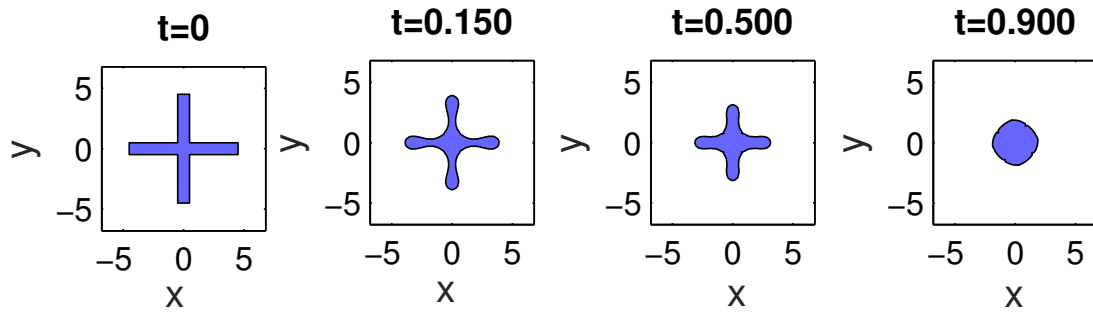
Figure 4.21: Several illustrations of the dynamic interface between the substrate and the island film (shaded in blue) for an initially cross-shaped island. The computational set up is as same as Fig. 4.19.
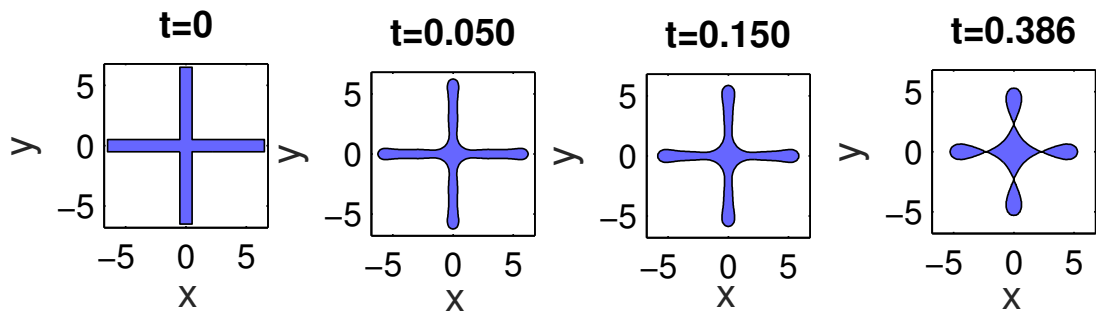
Figure 4.22: Several illustrations of the dynamic interface between the substrate and the island film (shaded in blue) for an initially cross-shaped island. The computational set up is as same as Fig. 4.20.
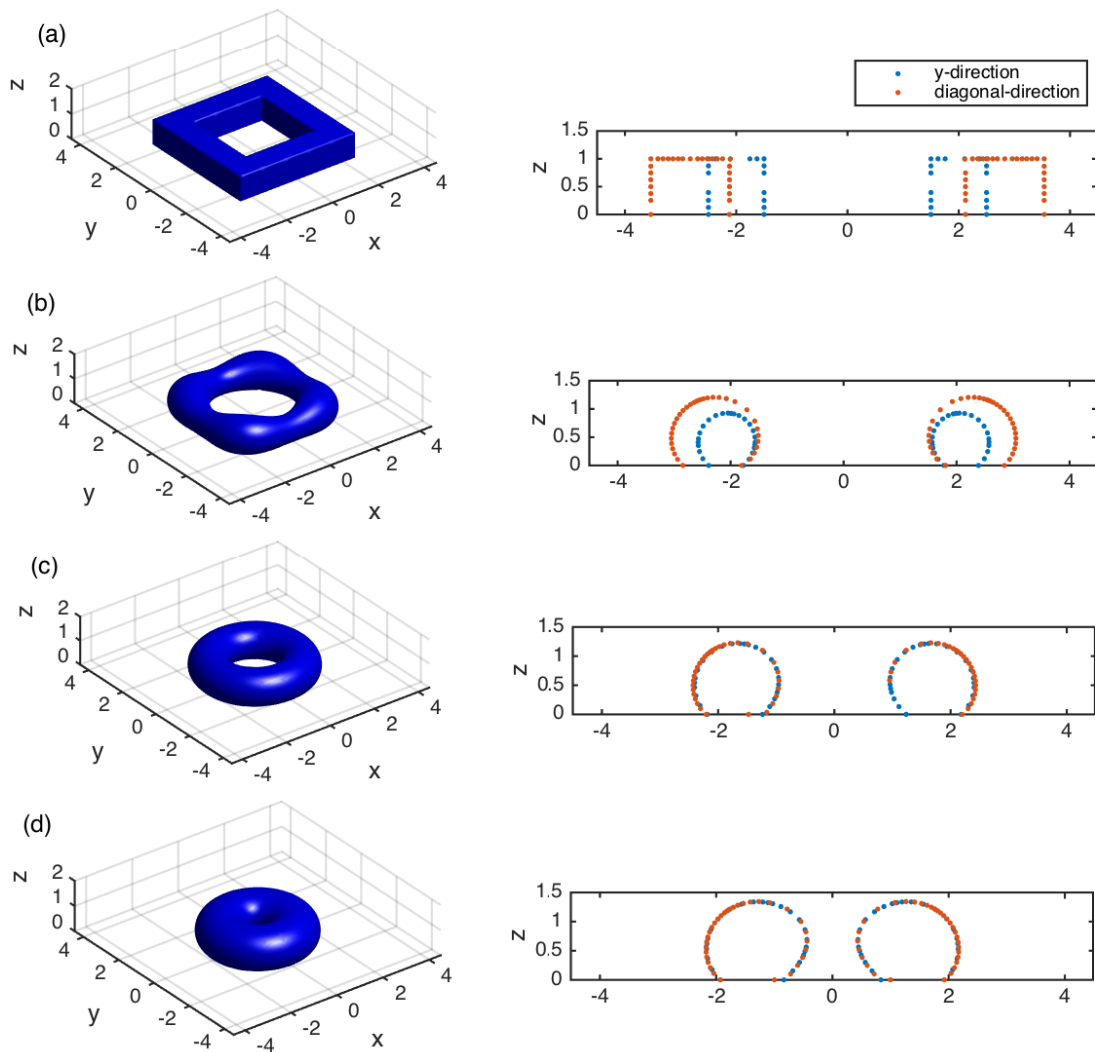
Figure 4.23: Several snapshots in the evolution of an initial island of square ring obtained from $(2.5, 2.5, 1)$ cuboid by cutting out a $(1.5, 1.5, 1)$ cuboid. (a) $t = 0$; (b) $t = 0.15$; (c) $t = 1.0$; (d) $t = 1.5$. The material constant is chosen as $\sigma = \cos(3\pi/4)$.
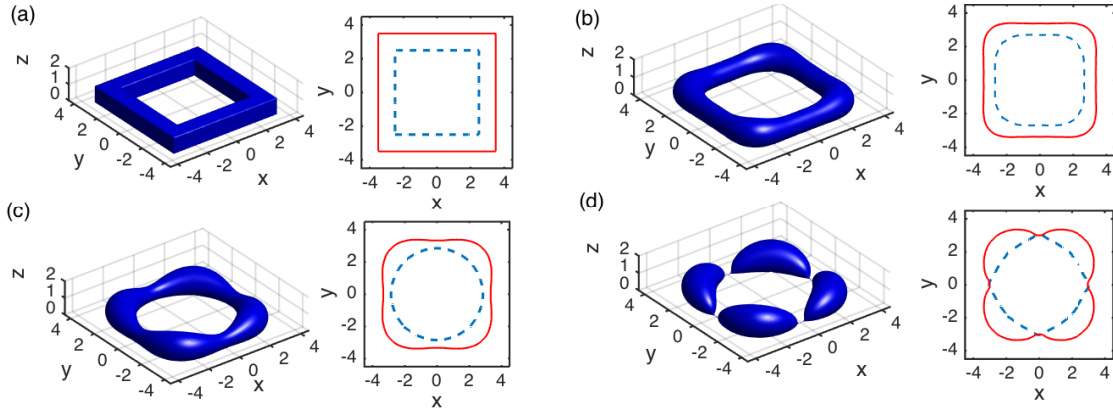
Figure 4.24: Several snapshots in the evolution of an initial island of square ring obtained from a $(3.5, 3.5, 1)$ cube by cutting out a $(2.5, 2.5, 1)$ cube. (a) $t = 0$; (b) $t = 0.15$; (c) $t = 0.4$; (d) $t = 0.614$. The material constant is chosen as $\sigma = \cos(3\pi/4)$.
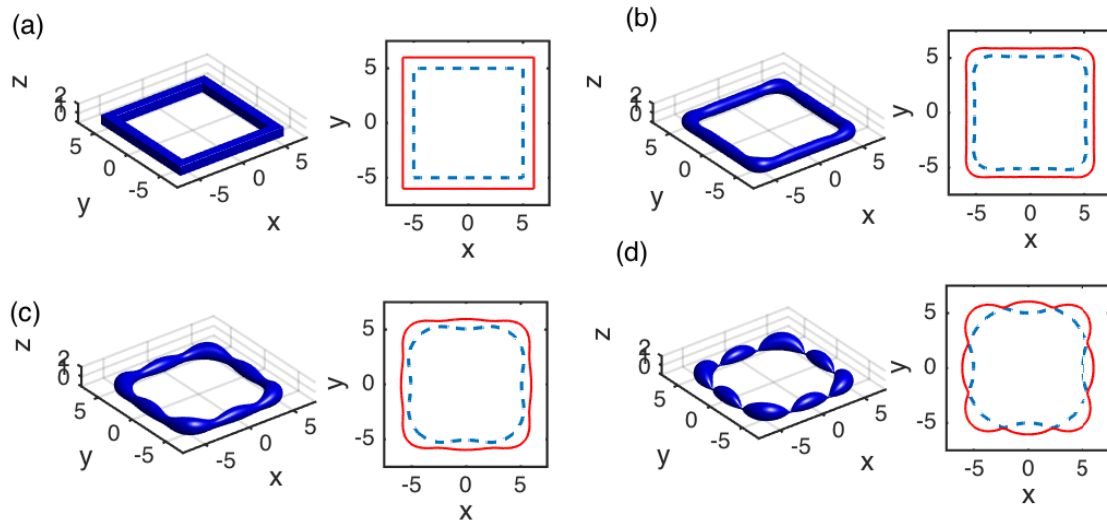
Figure 4.25: Several snapshots in the evolution an initial island of square ring obtained from a $(5, 5, 1)$ cube by cutting out a $(6, 6, 1)$ cube. (a) $t = 0$; (b) $t = 0.15$; (c) $t = 0.7$; (d) $t = 1.004$. The material constant is chosen as $\sigma = \cos(3\pi/4)$.

and Fig. 4.25. The length of the outer edges could control the number of the islands the thin film breaks up into. As depicted in Fig. 4.24, it reveals the geometry evolution and the migrations of the two contact lines of the thin film for a square ring with the length of outer edges chosen as 3. As times evolves, the thickness of the film becomes various in different cross-section directions. The thick becomes even thicker and the thin becomes even thiner, thus making the thin film breaking up into 4 pieces finally. If the length of the outer edges for the initial square ring is further increased, then thin film is possible to break up into more small islands, see Fig. 4.25. This could be explained by Rayleigh instability [99]. For the cylinder, a small volume-preserving perturbation with wavelength exceeding the circumference of the cylinder could grow exponentially in order to reduce the surface area of the cylinder, thus the cylinder will break up into a series of small spherical islands. This breakup has been verified by our previous numerical examples, see Fig. 4.11 and Fig. 4.12. In addition to geometry of cylinder, the Rayleigh instability for more complex geometries such as torus has received great attention and has been studied theoretically and experimentally recently [85,88]. Analogous to the cylinder, a wavelength perturbation of torus in the azimuthal direction could also force the torus to break up into small particles. However, the existence of the radial curvature plus the periodicity in the azimuthal direction make the study much complicated. In the axial direction, the torus is unstable and will always migrate towards the centre to form spherical shape by decreasing the major radius and increasing minor radius. Experiments by E. Pairam [88] show that toroidal droplets can break up into a precise number of droplets or only shrink towards its centre to from a single spherical droplet, depending on the initial aspect ratio of the torus. This demonstrates that the Rayleigh instability in the azimuthal direction and shrinking instability in the axial direction are competing with each other to determine the dynamics geometries of the torus. Here for solid-thin film on a substrate, our numerical examples for square ring has clearly verified this theory.

4.4   Extension to weakly anisotropic case

In the previous section, we have proposed a variational formulation for the sharp interface model of solid-state dewetting with isotropic surface energy. Here we want to extend this variational form to the case when the surface energy is anisotropic. In isotropic case, the variation formulation for the chemical potential is given as

$$\iint_S \mu \mathbf{n} \cdot \mathbf{g} \, dS - \iint_S \nabla_s \mathbf{X} \cdot \nabla_s \mathbf{g} \, dS = 0, \quad \forall \mathbf{g} \in (H_0^1(S))^3. \tag{4.4.1}$$

Given the chemical potential $\mu = \nabla_s \cdot \boldsymbol{\xi}$, for $\mathbf{g} \in (H_0^1(S))^3$, a similar equation has been derived for anisotropic case [34, 94, 115], which reads as

$$\iint_S \mu \mathbf{n} \cdot \mathbf{g} \, dS - \iint_S \gamma(\mathbf{n}) \nabla_s \mathbf{X} \cdot \nabla_s \mathbf{g} \, dS = -\sum_{k,l=1}^3 \iint_S \xi_k n_l \nabla_s x_k \cdot \nabla_s g_l \, dS. \tag{4.4.2}$$

4.4.1   Variational formulation

Based on Eq. (4.4.2), the variational formulation for the sharp interface model Eqs. (3.4.5),(3.4.6) with boundary conditions (3.4.8)-(3.4.10) can be stated as follows: given the initial surface $S(0) = \mathbf{X}(U,0)$ with its boundary $\Gamma(0) = \mathbf{X}_\Gamma(\partial U, 0)$, we want to find $\mathbf{X} \in H_\alpha^1(U) \times H_\beta^1(U) \times H_0^1(U), \mu \in H^1(S(t))$ such that

$$\langle \partial_t \mathbf{X} \cdot \mathbf{n}, \, \phi \rangle_S + \langle \nabla_s \mu, \, \nabla_s \phi \rangle_S = 0, \quad \forall \phi \in H^1(S), \tag{4.4.3a}$$

$$\langle \mu, \, \mathbf{n} \cdot \mathbf{g} \rangle_S - \langle \gamma(\mathbf{n}) \nabla_s \mathbf{X}, \, \nabla_s \mathbf{g} \rangle_S = -\sum_{l,k=1}^3 \langle \xi_k \nabla_s X_k, \, n_l \nabla_s g_l \rangle_S, \quad \forall \mathbf{g} \in (H_0^1(S))^3, \tag{4.4.3b}$$

with $S = S(t)$, and $\alpha, \; \beta$ represents the $x, \; y$-coordinates of the moving contact line $\Gamma = \Gamma(t)$, which is determined via the following variational formulation: find $\Gamma = \mathbf{X}_\Gamma(\partial U, t), \kappa \in H^1(\Gamma)$ such that

$$\langle \partial_t \mathbf{X}_\Gamma \cdot \mathbf{n}_\Gamma, \, \varphi \rangle_\Gamma + \varepsilon^2 \langle M_\Gamma \partial_s \kappa, \, \partial_s \varphi \rangle_\Gamma = -\eta \langle \mathbf{c}_\Gamma^\gamma \cdot \mathbf{n}_\Gamma - \sigma, \, \varphi \rangle_\Gamma, \; \forall \varphi \in H^1(\Gamma), \tag{4.4.4a}$$

$$\langle \kappa, \, \mathbf{n}_\Gamma \cdot \boldsymbol{\omega} \rangle_\Gamma - \langle \partial_s \mathbf{X}_\Gamma, \, \partial_s \boldsymbol{\omega} \rangle_\Gamma = 0, \quad \forall \boldsymbol{\omega} \in (H^1(\Gamma))^3. \tag{4.4.4b}$$

Here the smooth regularization for the contact line migration is given as

$$\partial_t \mathbf{X}_\Gamma = \varepsilon^2 \partial_s (M_\Gamma \partial_s \kappa) \mathbf{n}_\Gamma - \eta[\mathbf{c}_\Gamma^\gamma \cdot \mathbf{n}_\Gamma - \sigma] \mathbf{n}_\Gamma, \tag{4.4.5}$$

where $M_\Gamma = (\mathbf{c}_\Gamma^\gamma \cdot \mathbf{n}_\Gamma - \sigma)^2$. As the contact line for the equilibrium shape is no longer a circle, we add this mobility M_Γ to ensure that when the numerical solution approaches the steady state, the contact line satisfies anisotropic Young equation

$$\mathbf{c}_\Gamma^\gamma \cdot \mathbf{n}_\Gamma - \sigma = 0. \tag{4.4.6}$$

4.4.2 Full-discretization scheme

Given the spatial discretization and temporal discretization, the fully discrete parametric finite element method for solid-state dewetting with weakly anisotropic surfac energy can be stated as follows: assume $S^0 = \bigcup_{j=1}^{N} \bar{D}_j^0$ is a discretization of the initial surface $S(0)$ with good mesh quality, and $\Gamma^0 = \bigcup_{j=1}^{N_c} \bar{h}_j^0$, for $1 \le m \le M - 1$, we want to find $S^{m+1} := \mathbf{X}^{m+1} \in \mathcal{W}_{\Gamma^{m+1}}^h(S^m), \mu^{m+1} \in \mathcal{V}^h$, such that

$$\left\langle \frac{\mathbf{X}^{m+1} - \mathbf{X}^m}{\tau_m} \cdot \mathbf{n}^m, \ \phi_h \right\rangle_{S^m} + \left\langle \nabla_s \mu^{m+1}, \ \nabla_s \phi_h \right\rangle_{S^m} = 0, \quad \forall \phi_h \in \mathcal{V}^h(S^m), \tag{4.4.7a}$$

$$\left\langle \mu^{m+1}, \ \mathbf{n}^m \cdot \mathbf{g}_h \right\rangle_{S^m} - \left\langle \gamma(\mathbf{n}^m) \nabla_s \mathbf{X}^{m+1}, \ \nabla_s \mathbf{g}_h \right\rangle_{S^m} = - \sum_{l,k=1}^{3} \left\langle \xi_k^m \nabla_s x_k^m, \ n_l^m \nabla_s g_{h,l} \right\rangle_{S^m},$$

$$\forall \mathbf{g}_h \in (\mathcal{V}_0^h(S^m))^3, \tag{4.4.7b}$$

where Γ^{m+1} is determined as follows: find $\Gamma^{m+1} := \mathbf{X}_{\Gamma^{m+1}} \in (\mathcal{V}^h(\Gamma^m))^3, \kappa^{m+1} \in \mathcal{V}^h(\Gamma^m)$, such that

$$\left\langle \frac{\mathbf{X}_{\Gamma^{m+1}} - \mathbf{X}_{\Gamma^m}}{\tau_m} \cdot \mathbf{n}_{\Gamma^m}, \ \varphi_h \right\rangle_{\Gamma^m} + \varepsilon^2 \left\langle M_{\Gamma^m} \partial_s \kappa^{m+1}, \ \partial_s \varphi_h \right\rangle_{\Gamma^m}$$

$$+ \eta \left\langle \mathbf{c}_{\Gamma^m}^\gamma \cdot \mathbf{n}_{\Gamma^m} - \sigma, \ \varphi_h \right\rangle_{\Gamma^m} = 0, \quad \forall \varphi_h \in \mathcal{V}^h(\Gamma^m), \tag{4.4.8a}$$

$$\left\langle \kappa^{m+1}, \ \mathbf{n}_{\Gamma^m} \cdot \boldsymbol{\omega_h} \right\rangle_{\Gamma^m} - \left\langle \partial_s \mathbf{X}_{\Gamma^{m+1}}, \ \partial_s \boldsymbol{\omega_h} \right\rangle_{\Gamma^m} = 0, \quad \forall \boldsymbol{\omega_h} \in (\mathcal{V}^h(\Gamma^m))^3. \tag{4.4.8b}$$

Here $M_{\Gamma^m} = (\mathbf{c}_{\Gamma^m}^\gamma \cdot \mathbf{n}_{\Gamma^m} - \sigma)^2$, $\boldsymbol{\xi}^m = (\xi_1^m, \xi_2^m, \xi_3^m))$, $\mathbf{g}_h = (g_{h,1}, g_{h,2}, g_{h,3})$, $\mathbf{X}^m = (x_1^m, x_2^m, x_3^m)$. For the scheme, we have the following theorem,

Theorem 4.4.1 (Well-posedness of the PFEM scheme). *The discrete variational problem, Eqs. (4.4.7a), (4.4.7b), (4.4.8a) and (4.4.8b) is well-posed.*

Proof. The proof of this theorem is the same as proof of Theorem. 4.2.1 by noting that $\gamma(\mathbf{n}^m)$ is always positive. □

In view of the definition of $\boldsymbol{\xi}$ vector, one can defined: $\boldsymbol{\xi}^m$ as

$$\boldsymbol{\xi}_j^m = \boldsymbol{\xi}^m \Big|_{D_j^m} = \nabla \hat{\gamma}(\mathbf{n}_j^m). \tag{4.4.9}$$

In addition, $\mathbf{c}_{\Gamma^m}^\gamma$ is defined as

$$\mathbf{c}_{\Gamma^m,j}^\gamma = \mathbf{c}_{\Gamma^m}^\gamma \Big|_{h_j^m} = (\boldsymbol{\xi}_{j_k}^m \cdot \mathbf{n}_{j_k}^m)\mathbf{c}_{\Gamma^m,j} - ((\boldsymbol{\xi}_{j_k}^m \cdot \mathbf{c}_{\Gamma^m,j})\mathbf{n}_{j_k}^m), \tag{4.4.10}$$

with $D_{j_k}^m$ contains the line segment h_j^m.

For the weakly anisotropic surface energy, if $\gamma(\mathbf{n})$ is chosen as the cubic surface energy defined in Eq. (1.1.6) with a smaller enough, the mesh equality can be well preserved like the isotropic case. However, when the surface energy is chosen as the cusps or facet surface energies defined in Eq. (2.5.2), the mesh quality will deteriorate along the time evolution, thus mesh regularization is necessary in order to make the scheme stable. We refer to [6] for the volume-preserving mesh regularization method.

4.4.3   Numerical results

In this section, we report some numerical simulation results under the anisotropic surface energies. We will mainly consider the following cubic anisotropy

$$\gamma_c(\mathbf{n}) = 1 + a[n_1^4 + n_2^4 + n_3^4], \qquad 0 \le a < \frac{1}{3}. \tag{4.4.11}$$

Fig. 4.26 shows the convergence results of the equilibrium shapes with $\sigma = \cos(\frac{15\pi}{36}), a = 0.25$. We compute the equilibrium shapes for an initial $(1, 2, 1)$ cuboid with different meshes, which are given with a set of small isosceles right triangles. If we define the mesh size indicator h as the length of the hypotenuse of the right triangle, then Mesh1 represents the initial mesh with $h = h_0 = 0.125$, and the time step is chosen as $\tau = \tau_0 = 0.00125$ for computation. Meanwhile, the time step for Mesh2 and Mesh3 are chosen as $\tau = \frac{\tau_0}{4}$ and $\tau = \frac{\tau_0}{16}$ respectively. For easy comparison, we have depicted the x-directional cross-section profiles both for the numerical equilibrium shapes and the theoretical equilibrium shape. We can clearly observe that as the mesh size decrease, the numerical cross-section profiles

are convergent to the cross-section profiles of the theoretical equilibrium shapes. This prove that our PFEM scheme for the weakly anisotropic surface energy is convergent.
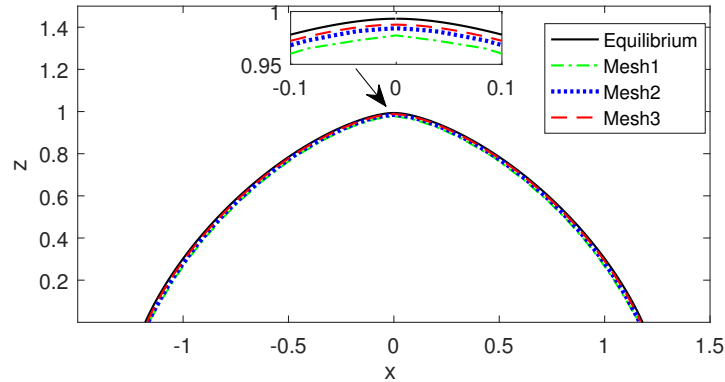
Figure 4.26: Comparison of the cross section profiles of the numerical equilibrium with the theoretical equilibrium shape obtained from Winterbottom construction. The material constant is given as $\sigma = \cos \frac{15\pi}{36}$.
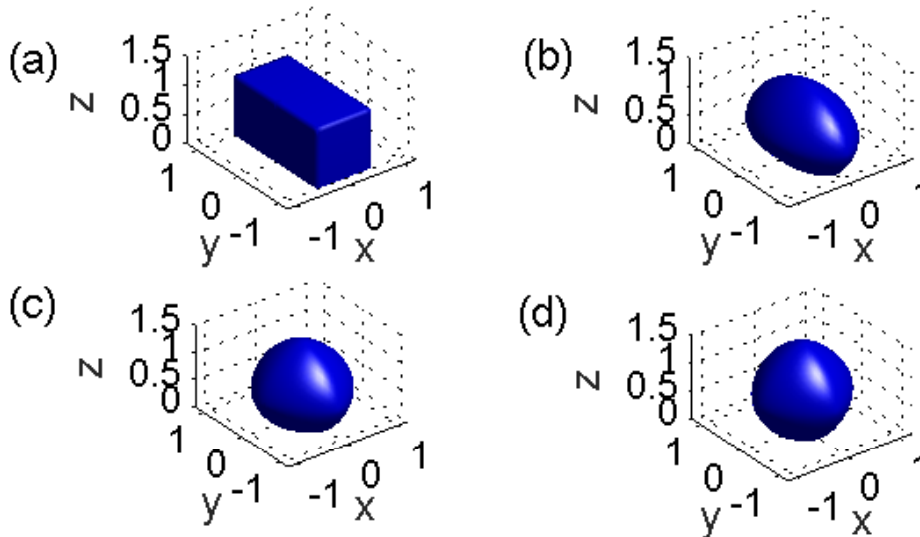
Figure 4.27: Several snapshots in the evolution of an initial $(1, 2, 1)$ cuboid towards its equilibrium under the cubic anisotropy with $a = 0.25$. The material constant is chosen as $\sigma = \cos \frac{5\pi}{6}$.

Fig. 4.27 shows the geometry evolution of an island film under the cubic anisotropy with $a = 0.25$. The initial island is a cuboid with dimension $(1, 2, 1)$, and the material constant is chosen as $\sigma = \cos(\frac{5\pi}{6})$. The island film evolves towards a shape with corners. In order to investigate the effect of the degree of anisotropy on the equilibrium shape, we have shown the equilibrium shapes under different a with same $\sigma = \cos\frac{5\pi}{6}$. As clearly observed from Fig. 4.28(a)-(c), the corners of the equilibrium shapes become sharper as a becomes bigger, which is consistent with the theoretical predications. On the other hand, we compute the equilibrium shape by fixing the degree of the anisotropy $a = 0.25$, and changing the material constant σ. The equilibrium shapes for $\sigma = 0.5, 0, -0.5$ are given in Fig. 4.29(a),(b) and (c) respectively. In addition, the corresponding cross-section profiles and contact lines of the equilibrium shapes are also shown in Fig. 4.30. From these figures, we can clearly see that σ determines the contact angles of the equilibrium shape.
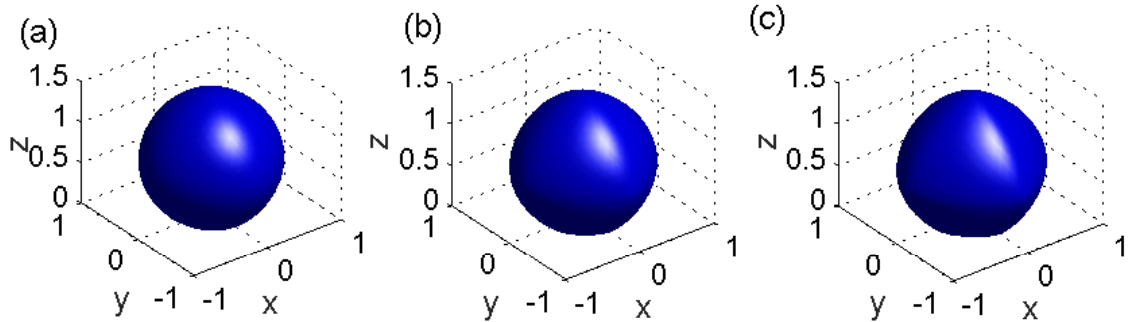
Figure 4.28: The equilibrium shapes of an initial $(1, 2, 1)$ cuboid under the cubic anisotropy with different degrees of anisotropy. (a) $a = 0.1$; (b) $a = 0.2$; (c) $a = 0.3$. The material constant is chosen as $\sigma = \cos\frac{5\pi}{6}$.

Unlike the isotropic case, a rotation of the surface energy density is equivalent to a rotation of the corresponding equilibrium shape. Assume $M_x(\theta)$ is a rotation matrix, which represents an anti-clockwise rotation about the x-axis in three dimensions under the right-hand rule. To observe the rotation effects, we compute the equilibrium shapes under the anisotropies $\gamma = \gamma_c(M_x(\frac{\pi}{6}\mathbf{n}))$ and $\gamma = \gamma_c(M_x(-\frac{\pi}{6}\mathbf{n}))$. As shown in Fig. 4.31, the equilibrium shapes exhibit the corresponding rotation effects
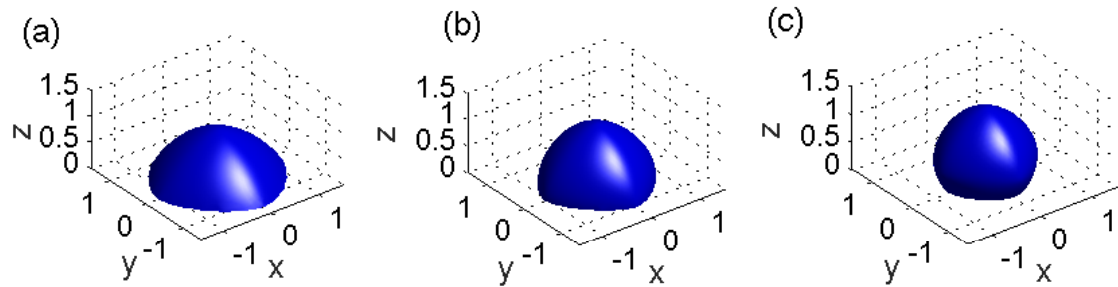
Figure 4.29: The equilibrium shapes of an initial $(1, 2, 1)$ cuboid under cubic anisotropy with $a = 0.25$. (a) $\sigma = 0.5$; (b) $\sigma = 0$; (c) $\sigma = -0.5$.
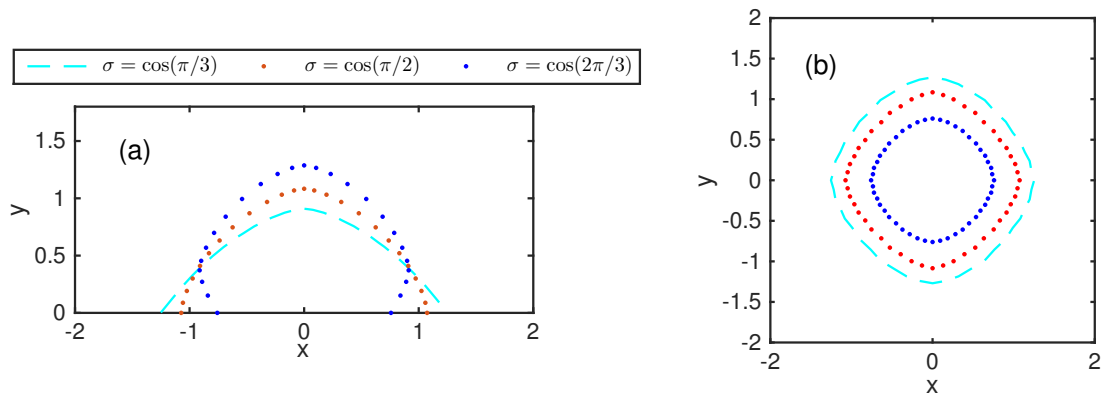
Figure 4.30: (a) The cross-section profiles of the equilibrium shapes. (b) The contact lines of the equilibrium shapes.

along x-axis. In addition to the cubic anisotropy, we have also performed numeri-
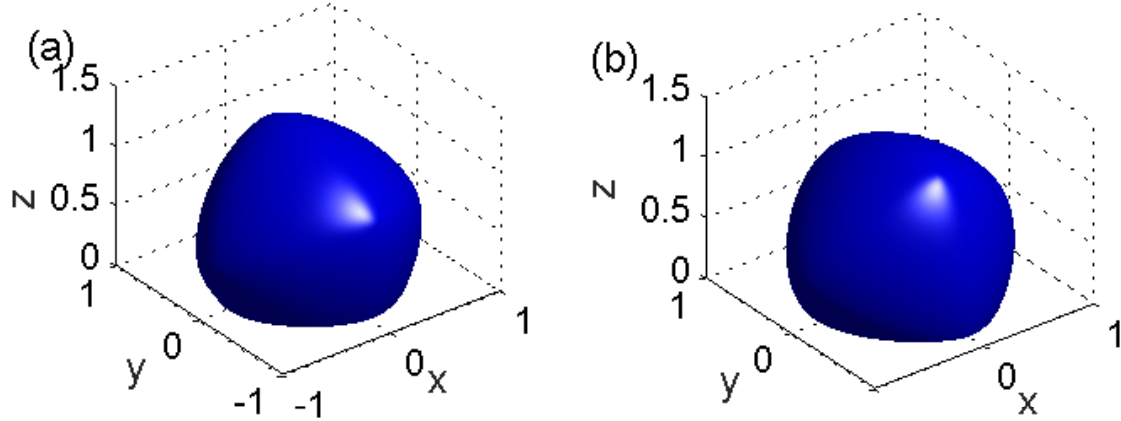
Figure 4.31: The equilibrium shapes of an initial $(1, 2, 1)$ cuboid, and the material constant is chosen as $\sigma = \cos \frac{3\pi}{4}$. (a) $\gamma = \gamma_c(M_x(\frac{\pi}{6})\mathbf{n})$; (b) $\gamma = \gamma_c(M_x(-\frac{\pi}{6})\mathbf{n})$.

.
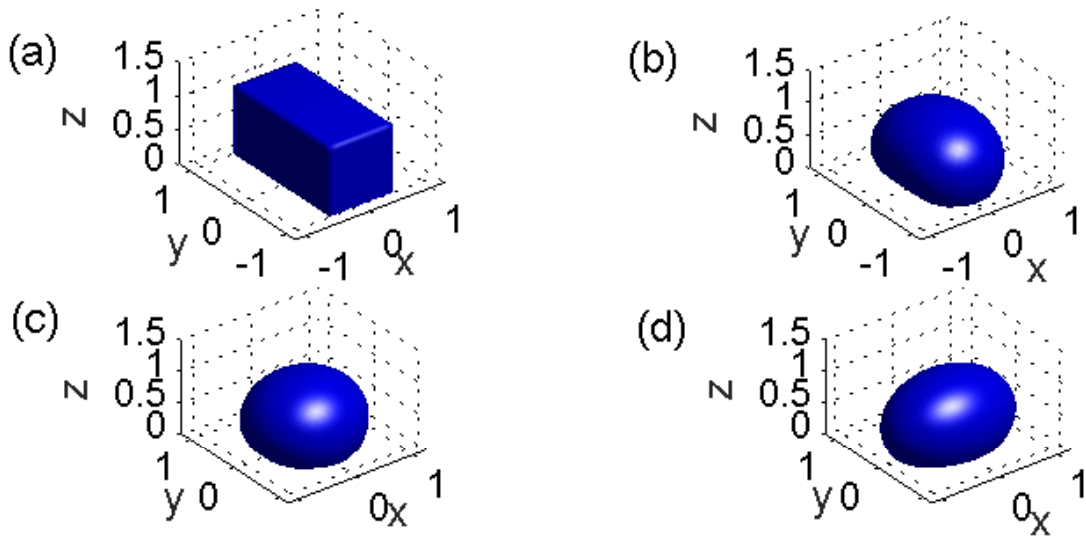
Figure 4.32: Several snapshots in the evolution of an initial $(1, 2, 1)$ cuboid towards its equilibrium under the ellipsoidal anisotropy with $a_1 = 2, a_2 = 1, a_3 = 1$. The material constant is chosen as $\sigma = \cos \frac{3\pi}{4}$. (a) $t = 0$; (b) $t = 0.02$; (c) $t = 0.04$; (d) $t = 1.0$.

cal simulations for the ellipsoidal anisotropy defined in Eq. (1.1.7). Fig. 4.32 shows

the geometry evolution of an initially cuboid island towards its equilibrium shape with $\sigma = \cos\frac{3\pi}{4}$. The surface energy density is chosen as $\gamma(\mathbf{n}) = \sqrt{2n_1^2 + n_2^2 + n_3^2}$. From the figure, we can see that thin film eventually obtains the equilibrium with ellipsoidal geometry. This is consistent with our predictions since the corresponding Wulff shape for the anisotropy $\gamma(\mathbf{n}) = \sqrt{2n_1^2 + n_2^2 + n_3^2}$ is given by an ellipsoid with implicit equation $\frac{x^2}{2} + y^2 + z^2 = 1$.

Chapter 5

Extensions

In this chapter, we mainly focus on some extensions of the sharp interface model. We will extend the model to the strongly anisotropic case and curved substrate. Moreover, the migration of the toroidal thin film on the flat substrate will be investigated under the assumption of axis-symmetry.

5.1 For strongly anisotropic surface energy

In 2D, some orientations are missing in the equilibrium shape (see Fig. 5.1(a)) when the surface stiffness $\gamma(\theta) + \gamma''(\theta)$ is negative for some orientations [67, 105]. In this strongly anisotropic case, the anisotropic surface diffusion flow becomes backward and ill-posed. In order to avoid this ill-posedness, the Willmore energy regularization is generally utilized [30, 58]. In 3D, a similar regularization is necessary when missing orientations appear in the equilibrium shape (see Fig. 5.1(b)). Therefore in this section, we perform the extension in 3D and derive the model for strongly anisotropic case.
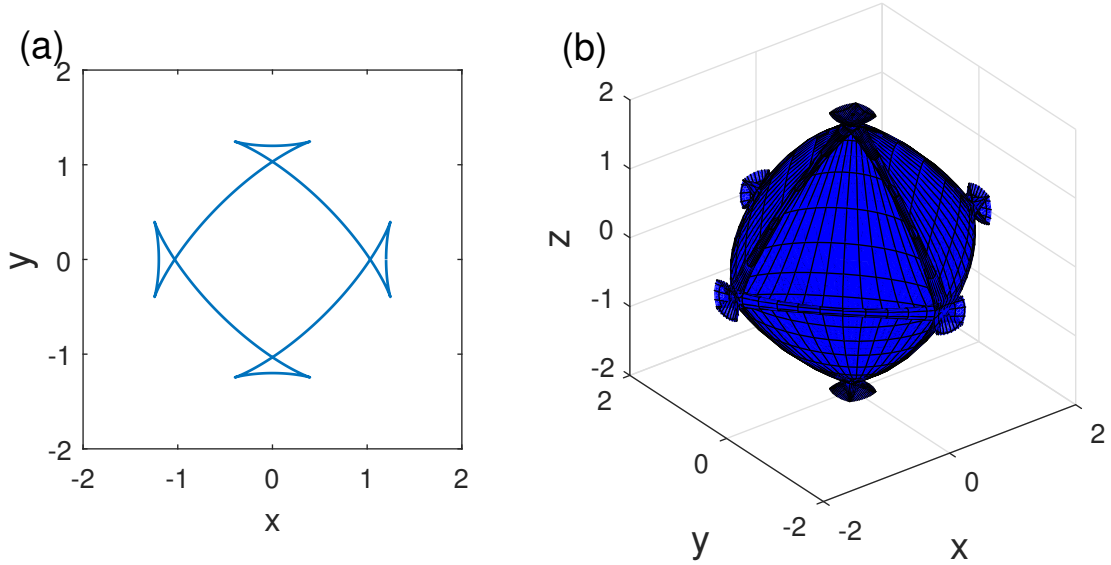
Figure 5.1: Ears appear in $\boldsymbol{\xi}$-plot for strongly anisotropic surface energy. (a) $\gamma(\theta) = 1 + 0.2\cos(4\theta)$ in 2D; (b) $\gamma(\mathbf{n}) = 1 + (n_1^4 + n_2^4 + n_3^4)$ in 3D.

5.1.1 The regularized energy and first variation

The Willmore energy can be written as

$$W_r = \iint_S \mathcal{H}^2 \, dS. \tag{5.1.1}$$

We have the following lemmas which is helpful for calculating the first variation of the Willmore energy functional.

Lemma 5.1.1. *Asuume $S \in \mathbb{R}^3$ is a C^k-hypersurface, with $k \geq 3$. $\mathcal{H}$ is the mean curvature of S, then the normal derivative of $\mathcal{H}$ is given by*

$$\partial_\mathbf{n}\mathcal{H} = -(\kappa_1^2 + \kappa_2^2) = -(\mathcal{H}^2 - 2\mathcal{K}), \tag{5.1.2}$$

where κ_1, κ_2 are the two principle curvatures of the surface, $\mathcal{K}$ is the Gauss curvature.

Proof. We omit the proof as this is a simple application of the signed distance function defined in Eq. (3.1.42) and the proof can be found in [58, 64] $\qquad\square$

Lemma 5.1.2. *Let $S \in \mathbb{R}^3$ be C^k-hypersurface with smooth boundary, and $k \geq 4$. If $W_r(S) = \iint_S \mathcal{H}^2 \, dS$, then we have the first variation of $J(S)$ in the direction of $\mathbf{V}$ is given by*

$$
\begin{aligned}
dW_r(S; \mathbf{V}) &= 2 \int_\Gamma [(\nabla_s \mathcal{H} \cdot \mathbf{c}_\Gamma)(\mathbf{n} \cdot \mathbf{V}_0) - \mathcal{H} \mathbf{c}_\Gamma \cdot \nabla_s(\mathbf{n} \cdot \mathbf{V}_0) + \mathcal{H}^2 \, \mathbf{V}_0 \cdot \mathbf{c}_\Gamma] \, d\Gamma \\
&\quad - 2 \iint_S [\Delta_S \mathcal{H} + \frac{\mathcal{H}^3}{2} - 2\mathcal{H}\mathcal{K}] \, \mathbf{n} \cdot \mathbf{V}_0 \, dS.
\end{aligned}
\tag{5.1.3}
$$

Here $\mathcal{K}$ is the Gaussian curvature.

Proof. To calculate the variation, using Eqs. (3.1.41) and (3.1.44), we have

$$
\begin{aligned}
dW_r(S; \mathbf{V}) &= \iint_S 2\mathcal{H}(-\Delta_s(\mathbf{n} \cdot \mathbf{V}_0)) \, dS + \iint_S [\partial_\mathbf{n} \mathcal{H}^2 + \mathcal{H}^3] \, \mathbf{n} \cdot \mathbf{V}_0 \, dS \\
&\quad + \int_\Gamma \mathcal{H}^2 \mathbf{V}_0 \cdot \mathbf{c}_\Gamma \, d\Gamma.
\end{aligned}
\tag{5.1.4}
$$

Not that $\partial_\mathbf{n} \mathcal{H} = -(\mathcal{H}^2 - 2\mathcal{K})$ by lemma. 5.1.1, integration by parts based on Eq. (3.1.10), we get

$$
\begin{aligned}
&dW_r(S; \mathbf{V}) \\
&= 2 \iint_S \nabla_s \mathcal{H} \cdot \nabla_s(\mathbf{n} \cdot \mathbf{V}_0) \, dS - 2 \int_\Gamma \mathcal{H} \mathbf{c}_\Gamma \cdot \nabla_s(\mathbf{n} \cdot \mathbf{V}_0) \, dS \\
&\quad - \iint_S [\mathcal{H}(\mathcal{H}^2 - 4\mathcal{K})] \, \mathbf{n} \cdot \mathbf{V}_0 \, dS + \int_\Gamma \mathcal{H}^2 \, \mathbf{c}_\Gamma \cdot \mathbf{V}_0 \, dS \\
&= -2 \iint_S \Delta_s \mathcal{H} \, \mathbf{n} \cdot \mathbf{V}_0 \, dS + 2 \int_\Gamma (\nabla_s \mathcal{H} \cdot \mathbf{c}_\Gamma)(\mathbf{n} \cdot \mathbf{V}_0) \, d\Gamma \\
&\quad - 2 \int_\Gamma \mathcal{H} \, \mathbf{c}_\Gamma \cdot \nabla_s(\mathbf{n} \cdot \mathbf{V}_0) \, dS - \iint_S [\mathcal{H}(\mathcal{H}^2 - 4\mathcal{K})] \, \mathbf{n} \cdot \mathbf{V}_0 \, dS + \int_\Gamma \mathcal{H}^2 \, \mathbf{c}_\Gamma \cdot \mathbf{V}_0 \, d\Gamma \\
&= 2 \int_\Gamma [(\nabla_s \mathcal{H} \cdot \mathbf{c}_\Gamma)(\mathbf{n} \cdot \mathbf{V}_0) - \mathcal{H} \mathbf{c}_\Gamma \cdot \nabla_s(\mathbf{n} \cdot \mathbf{V}_0) + \mathcal{H}^2 \, \mathbf{V}_0 \cdot \mathbf{c}_\Gamma] \, d\Gamma \\
&\quad - 2 \iint_S [\Delta_S \mathcal{H} + \frac{\mathcal{H}^3}{2} - 2\mathcal{H}\mathcal{K}] \, \mathbf{n} \cdot \mathbf{V}_0 \, dS.
\end{aligned}
\tag{5.1.5}
$$

$\square$

The total dimensionless surface energy after regularization becomes

$$
W_{reg}^\delta = W + \frac{\delta^2}{2} W_r = \iint_S \gamma(\mathbf{n}) \, dS - \sigma A(\Gamma) + \frac{\delta^2}{2} \iint_S \mathcal{H}^2 \, dS,
\tag{5.1.6}
$$

From the lemma. 5.1.2 and the variation of W, also noting that on the boundary,

$$
\mathbf{n} \cdot \mathbf{V}_0 = (P_{sub}\mathbf{n}) \cdot \mathbf{V}_0 = (\mathbf{n} \cdot \mathbf{n}_\Gamma)(\mathbf{n}_\Gamma \cdot \mathbf{V}_0),
\tag{5.1.7}
$$

we can easily obtain that

$$
\begin{aligned}
dW_{reg}^{\delta}(S; \mathbf{V}) &= \iint_S [\nabla_s \cdot \boldsymbol{\xi} - \delta^2(\Delta_s \mathcal{H} + \frac{\mathcal{H}^3}{2} - 2\mathcal{H}\mathcal{K})]\mathbf{V}_0 \cdot \mathbf{n} \, dS \\
&+ \int_\Gamma [\mathbf{c}_\Gamma^\gamma \cdot \mathbf{n}_\Gamma - \sigma + \delta^2(\nabla_s \mathcal{H} \cdot \mathbf{c}_\Gamma)(\mathbf{n} \cdot \mathbf{n}_\Gamma)]\mathbf{V}_0 \cdot \mathbf{n}_\Gamma \, d\Gamma \\
&+ \delta^2 \int_\Gamma [\mathcal{H}^2 \mathbf{c}_\Gamma \cdot \mathbf{V}_0 - \mathcal{H}\mathbf{c}_\Gamma \cdot \nabla_s(\mathbf{n} \cdot \mathbf{V}_0)] \, dS.
\end{aligned}
\tag{5.1.8}
$$

The variation of the total energy with respect to the surface S is immediately given by

$$
\frac{\delta W_{reg}^{\delta}}{\delta S} = \nabla_s \cdot \boldsymbol{\xi} - \delta^2(\Delta_s \mathcal{H} + \frac{\mathcal{H}^3}{2} - 2\mathcal{H}\mathcal{K}).
\tag{5.1.9}
$$

Since a higher order energy is added to the surface energy for regularization, the governing equations will result in a sixth order geometric PDE, thus an additional boundary condition should be included for them. In consideration of the undesirable term in the variation $\mathcal{H}\,\mathbf{c}_\Gamma \cdot \nabla_s(\mathbf{n} \cdot \mathbf{V}_0)$, if we want to obtain the variation of W_{reg}^{δ} with respect to the boundary Γ, we need to impose the following zero curvature boundary condition

$$
\mathcal{H}\big|_\Gamma = 0.
\tag{5.1.10}
$$

Such boundary condition is also imposed in two dimensions, which serves as the condition to make sure the system is dissipative. Therefore the variation of W_{reg}^{δ} with respect to the Γ is

$$
\frac{\delta W_{reg}^{\delta}}{\delta \Gamma} = \mathbf{c}_\Gamma^\gamma \cdot \mathbf{n}_\Gamma - \sigma + \delta^2(\nabla_s \mathcal{H} \cdot \mathbf{c}_\Gamma)(\mathbf{n} \cdot \mathbf{n}_\Gamma).
\tag{5.1.11}
$$

5.1.2 The regularized model

Similar to the weakly anisotropic case, the variation of the total energy with respect to the surface S and Γ give the chemical potential and contact line migration velocity, respectively. Now we assume S is a C^k-hypersurface with smooth boundary, where $k \geq 6$. Let $\mathbf{X}$ and $\mathbf{X}_\Gamma$ denote a local parametrization of S and Γ respectively.

The sharp interface model for solid-state dewetting with strongly anisotropic surface energy is given by

$$\partial_t \mathbf{X} = \Delta_s \mu \, \mathbf{n}, \qquad t > 0, \tag{5.1.12}$$

$$\mu = \nabla_s \cdot \boldsymbol{\xi} - \delta^2 (\Delta_s \mathcal{H} + \frac{\mathcal{H}^3}{2} - 2\mathcal{H}\mathcal{K}), \tag{5.1.13}$$

$$\mathcal{H} = -\Delta_s \mathbf{X} \cdot \mathbf{n}, \qquad \mathcal{K} = \frac{\mathcal{H}^2 + \Delta_s \mathbf{n} \cdot \mathbf{n}}{2}, \tag{5.1.14}$$

together with the following boundary conditions

(1) contact line condition

$$\Gamma \subset S_{sub}, \qquad t \geq 0, \tag{5.1.15}$$

(2) relaxed contact angle condition

$$\partial_t \mathbf{X}_\Gamma = -\eta \Big[\mathbf{c}_\Gamma^\gamma \cdot \mathbf{n}_\Gamma - \sigma + \delta^2 (\nabla_s \mathcal{H} \cdot \mathbf{c}_\Gamma)(\mathbf{n} \cdot \mathbf{n}_\Gamma) \Big] \mathbf{n}_\Gamma, \qquad t \geq 0; \tag{5.1.16}$$

where $\mathbf{c}_\Gamma^\gamma = (\boldsymbol{\xi} \cdot \mathbf{n})\mathbf{c}_\Gamma - (\boldsymbol{\xi} \cdot \mathbf{c}_\Gamma)\mathbf{n}$, $\mathbf{n}_\Gamma = \frac{1}{\sqrt{n_1^2 + n_2^2}}(n_1, n_2, 0)$, $\sigma = \frac{\gamma_{VS} - \gamma_{FS}}{\gamma_0}$.

(3) zero-mass flux condition

$$\mathbf{c}_\Gamma \cdot \nabla_s \mu \Big|_\Gamma = 0, \qquad t \geq 0; \tag{5.1.17}$$

(4) zero-curvature condition

$$\mathcal{H} \Big|_\Gamma = 0, \qquad t \geq 0. \tag{5.1.18}$$

The mass conservation and energy dissipation can also be proved easily. Here we omit the proof as it is similar to that for weakly anisotropic case.

5.2 For curved substrate

Previously we always assume that the rigid substrate is flat and represented by the xOy plane, however, experiments have shown that the topologies of the substrate

could have great influence on dewetting of the thin films. For example, templated dewetting shows that substrate in order pattern could produce thin films of ordered structure. Thus it is necessary to extend our sharp interface model to the curved substrate case. See Fig. 5.2, S is the open surface representing the interface between
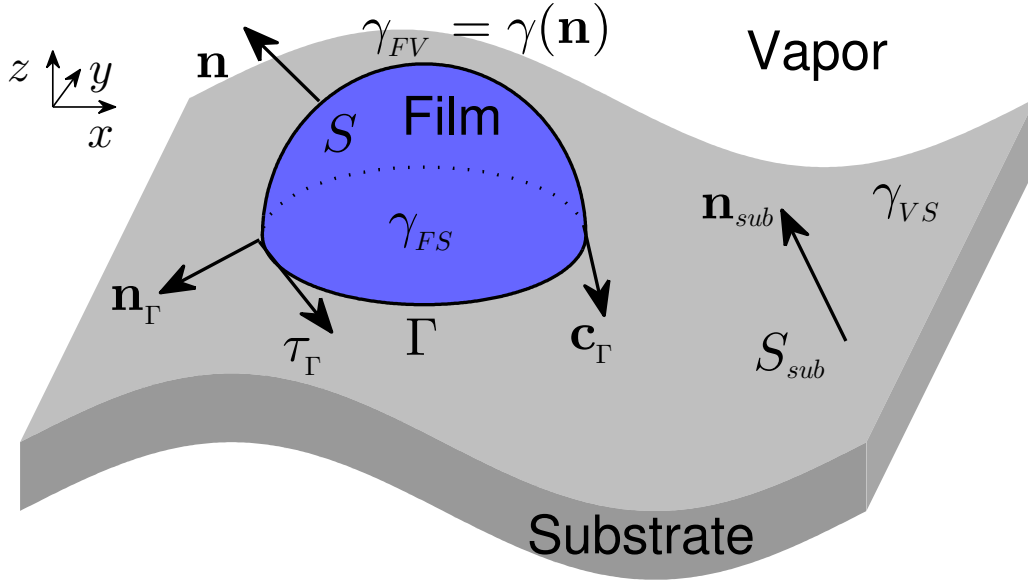
Figure 5.2: A schematic illustration of solid-state dewetting on a curved substrate.

the vapor and film while S_{sub} is the surface representing the substrate. $\Gamma \subset Su$ is a space curve in three dimensions, which represents on the contact line of the substrate and the film. $\mathbf{n}$ is the outer unit normal vector of S and $\mathbf{n}_{sub}$ is the outer unit normal vector of the substrate S_{sub}. $\mathbf{n}_\Gamma$ is the outer unit normal vector of the contact line Γ in S_{sub}. From the above defintion, we can clearly see the following equations hold

$$\mathbf{n}_\Gamma(\mathbf{x}) \perp \boldsymbol{\tau}_\Gamma(\mathbf{x}), \quad \mathbf{n}_\Gamma(\mathbf{x}) \perp \mathbf{n}_{sub}(\mathbf{x}), \quad \forall \mathbf{x} \in \Gamma, \tag{5.2.1a}$$

$$\mathbf{c}_\Gamma(\mathbf{x}) \perp \boldsymbol{\tau}_\Gamma(\mathbf{x}), \quad \mathbf{c}_\Gamma \perp \mathbf{n}(\mathbf{x}), \quad \forall \mathbf{x} \in \Gamma. \tag{5.2.1b}$$

If we assume that the γ_{FS}, γ_{VS} are constants and $\gamma_{FV} = \gamma(\mathbf{n})$, then we the total dimensionless surface energy can be written as

$$W = W_{int} + W_{sub} = \iint_S \gamma(\mathbf{n}) \, dS - \sigma A(\Gamma, S_{sub}), \tag{5.2.2}$$

where $\sigma = \frac{\gamma_{VS} - \gamma_{FS}}{\gamma_0}$, $A(\Gamma; S_{sub})$ is the area enclosed by the space curve Γ on the surface S_{sub}.

Here we assume the substrate is not deformable, thus surface S_{sub} is a fixed surface. Give the surface S as the initial surface with boundary $\Gamma \subset S_{sub}$, consider a transformation T_ε of S. Under this transformation, we always assume that the boundary of S is attached on the surface S_{sub}, that is

$$T_\varepsilon \Gamma \subset S_{sub}. \tag{5.2.3}$$

The first variation of W_{int} in the direction of $\mathbf{V}$ is given by Eq. (3.2.10),

$$dW_{int}(S; \mathbf{V}) = \iint_S \nabla_s \cdot \boldsymbol{\xi} \, dS + \int_\Gamma \mathbf{c}_\Gamma^\gamma \cdot \mathbf{V}_0 \, d\Gamma. \tag{5.2.4}$$

For the second part, if we assume that the surface of S_{sub} enclosed by Γ is given by S_Γ. Consider the transformation on S_Γ, such that

$$T_\varepsilon S_\Gamma = S_\Gamma^\varepsilon, \qquad T_\varepsilon \Gamma = \Gamma^\varepsilon \subset S_{sub}. \tag{5.2.5}$$

This indicates that the transformation T_ε satisfies the following on the boundary of S_Γ^ε

$$\mathbf{V} \parallel \mathcal{T}_\mathbf{x} S_{sub}, \qquad \mathbf{V} \perp \mathbf{n}_{sub}. \tag{5.2.6}$$

For $W_{sub}(\Gamma) = \iint_{S_\Gamma} dS_\Gamma$, by using Eq. (3.2.1) again, we obtain

$$dW_{sub}(\Gamma; \mathbf{V}) = -\sigma \int_\Gamma \mathbf{n}_\Gamma \cdot \mathbf{V}_0 \, dS. \tag{5.2.7}$$

Similarly, we know that $\mathbf{V}_0\big|_\Gamma \perp \mathbf{n}_{sub}$, thus we can project $\mathbf{c}_\Gamma^\gamma$ on the tangential space of S_{sub}, we obtain

$$dW_{int}(S; \mathbf{V}) = \iint_S \nabla_s \cdot \boldsymbol{\xi} \, dS + \int_\Gamma (\mathbf{c}_\Gamma^\gamma \cdot \mathbf{n}_\Gamma)(\mathbf{n}_\Gamma \cdot \mathbf{V}_0) \, d\Gamma. \tag{5.2.8}$$

Thus combine the variation of W_{int} and W_{sub}, we can get the variation is exactly the same as Eq. (3.2.1). This indicates that the the sharp interface model for solid-stat dewettting on a curved substrate is consistent to the the models for solid-state

dewetting on a flat substrate. For curved substrate, the contact line migrates along the substrate in the directions $\mathbf{n}_\Gamma$. Thus if we denote the $\mathbf{X}$ and $\mathbf{X}_\Gamma$ as the local parameterization of S and Γ respectively. Then the dimensionless sharp interface model for solid-state dewetting on a curved substrate is given by

$$\partial_t \mathbf{X} = \Delta_s \mu \, \mathbf{n}, \qquad t > 0, \tag{5.2.9}$$

$$\mu = \nabla_s \cdot \boldsymbol{\xi}, \qquad \boldsymbol{\xi} = \nabla \hat{\gamma}(\mathbf{n}), \tag{5.2.10}$$

together with the following boundary conditions

(1) contact line condition

$$\Gamma \subset S_{sub}, \qquad t \geq 0, \tag{5.2.11}$$

(2) relaxed contact angle condition

$$\partial_t \mathbf{X}_\Gamma = -\eta \left[\mathbf{c}_\Gamma^\gamma \cdot \mathbf{n}_\Gamma - \sigma \right] \mathbf{n}_\Gamma, \qquad t \geq 0, \tag{5.2.12}$$

where $\mathbf{c}_\Gamma^\gamma = (\boldsymbol{\xi} \cdot \mathbf{n}) \mathbf{c}_\Gamma - (\boldsymbol{\xi} \cdot \mathbf{c}_\Gamma) \mathbf{n}$, $\mathbf{n}_\Gamma = \frac{\boldsymbol{\tau}_\Gamma \times \mathbf{n}_{sub}}{|\boldsymbol{\tau}_\Gamma \times \mathbf{n}_{sub}|}$, $\sigma = \frac{\gamma_{VS} - \gamma_{FS}}{\gamma_0}$,

(3) zero-mass flux condition

$$\left. (\mathbf{c}_\Gamma \cdot \nabla_s \mu) \right|_\Gamma = 0, \qquad t \geq 0. \tag{5.2.13}$$

5.3 For axis-symmetric case

Capillary instabilities (e.g., occur in solid-state dewetting) are especially well-known in liquid systems. They have shown that a small volume-preserving sinusoidal perturbation with wavelength exceeding the circumference of the cylinder can grow exponentially in order to reduce the surface energy, and consequently, the cylinder will break up into a series of small spherical islands. Recently, the Rayleigh instability for more complex geometries (such as liquid toroids on a substrate) have attracted considerable interest in the physics and materials science community. In

analogy to the cylinder, a toroid can also exhibit a Rayleigh instability in the azimuthal direction. On the other hand, its radial curvature also produces a variation of the mean curvature, forcing the toroid to shrink towards its own center, leading to its collapse into a compact object and eventually to a section of a sphere. This demonstrates that the Rayleigh instability in the azimuthal direction and the shrinking instability in the radial direction are competing with each other to determine the dynamics of the toroid. This is a competition between the two time scales: one for toroid shrinkage towards its center and the other for neck pinch-off along the azimuthal direction. A toroid behaves like a cylinder when the aspect ratio (i.e., the ratio between the overall radius R and the tube radius a) is large; this Rayleigh instability has been widely investigated. The shrinking instability, induced by the radial curvature, is a signature of the non-compact topology of the toroid and has not been well studied in literature, especially for solid-state dewetting.

In this section, we apply the Onsager's variational principle to derive a reduced-order model for analyzing the shrinking of a solid toroidal island on a solid substrate via surface diffusion. This application provides a concrete demonstration of the efficacy and simplicity of the Onsager's variational principle for describing the surface diffusion-controlled morphology evolution problems, and applicability for analyzing even complex solid-state dewetting phenomena (e.g., a simultaneous consideration of the shrinking instability and Rayleigh instability).

5.3.1 The full sharp-interface model

In this section, we consider the shrinking dynamics of a solid toroidal island (in blue region) bonded to a flat rigid substrate towards its center via a surface diffusion-controlled solid-state dewetting process, as illustrated in Fig. 5.3(a). We assume that the island maintains its axisymmetric shape during the evolution (i.e., we do not consider a Rayleigh instability along the azimuthal direction), and therefore, the film/vapor interface surface S can be parameterized in cylindrical coordinate as (see
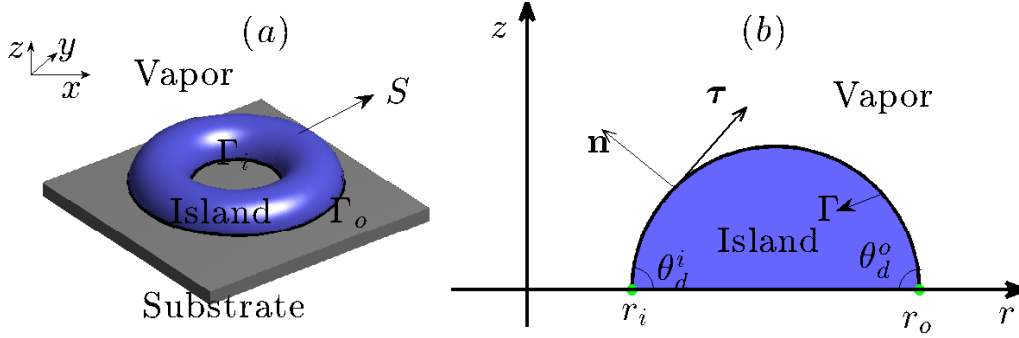
Figure 5.3: (a) A schematic illustration of the solid-state dewetting of an initially, toroidal island on a flat, rigid substrate; (b) the cross-section profile (i.e., denoted as Γ) of the island is represented in a cylindrical coordinate system (r, z), where r_i, r_o representing the inner and outer contact points, respectively. Note that Γ is not necessarily a circular arc during the evolution.

Fig. 5.3(b))

$$S = (r(s,t)\cos\varphi, \ r(s,t)\sin\varphi, \ z(s,t)), \tag{5.3.1}$$

where $r(s,t)$ is the radial distance, $z(s,t)$ is the local height with s representing the arc length of the cross-section profile $\Gamma = (r(s,t), z(s,t))$ of the surface S, and $\varphi \in [0, 2\pi]$ is the azimuthal angle.

The total interfacial free energy of the system can be described as (up to a constant) [?, 136]

$$W = \iint_S \gamma_{FV} \, dS + \underbrace{(\gamma_{FS} - \gamma_{VS})\pi(r_o^2 - r_i^2)}_{\text{Substrate Energy}}, \tag{5.3.2}$$

where the constants γ_{FV} (i.e., γ_0), γ_{FS} and γ_{VS} represent the film/vapor, film/substrate and vapor/substrate surface energy densities, respectively, and r_o and r_i are the radii of the outer and inner contact lines, respectively (shown in Fig. 5.3(b)).

Because we assume that the surface is axisymmetric, the island morphology evolution can be described in terms of the evolution of the cross-section curve Γ. For brevity, we denote $\Gamma(t) = \mathbf{X}(s,t) = (r(s,t), z(s,t))$ as the cross-section profile of the

surface S with $0 \le s \le L(t)$ and $r(0,t) = r_i, r(L,t) = r_o$. Based on a thermodynamic variational analysis, we previously proposed a sharp-interface model for simulating solid-state dewetting in three dimensions for axisymmetric geometries [136]. By choosing a length scale and surface energy density scale for normalization as L_0 and γ_0 respectively, the time normalized by $L_0^4/B\gamma_0$, and the contact line mobility by B/L_0^3, this leads to the following dimensionless sharp-interface evolution model (for isotropic surface energy) [136]:

$$\partial_t \mathbf{X} = \frac{1}{r}\partial_s(r\partial_s\mu)\,\mathbf{n}, \quad 0 < s < L(t), \ t > 0, \tag{5.3.3}$$

$$\mu = \mathcal{H} = \kappa - \frac{\partial_s z}{r}, \quad \kappa = -(\partial_{ss}\mathbf{X})\cdot\mathbf{n}; \tag{5.3.4}$$

where μ is the dimensionless chemical potential, $\mathcal{H}$ is the mean curvature of the surface S, and κ is the curvature of the curve Γ, $\mathbf{n} = (-\partial_s z, \partial_s r)$ is the outer unit normal vector of the curve Γ.

The above equations are subject to the following dimensionless boundary conditions:

(i) Contact line condition

$$z(0,t) = 0, \quad z(L,t) = 0; \tag{5.3.5}$$

(ii) Relaxed contact angle condition

$$\frac{dr_i}{dt} = \eta(\cos\theta_d^i - \cos\theta_i), \qquad fracdr_odt = -\eta(\cos\theta_d^o - \cos\theta_i); \tag{5.3.6}$$

(iii) Zero-mass flux condition

$$\partial_s\mu(0,t) = 0, \quad \partial_s\mu(L,t) = 0. \tag{5.3.7}$$

Here θ_d^i, θ_d^o are the (dynamic) contact angles for the inner and outer contact lines, respectively, $0 < \eta < +\infty$ denotes the dimensionless contact line mobility, and θ_i is the isotropic equilibrium (Young) contact angle, i.e., $\cos\theta_i = (\gamma_{VS} - \gamma_{FS})/\gamma_0$. Boundary condition (i) ensures that contact lines always move along the substrate,

(ii) describes the dynamic relaxation of the contact angle, and (iii) ensures that the total volume/mass of the island is conserved (i.e., no mass flux into/from the island at the contact lines).

Note that when the contact line mobility η goes to infinity, $\theta_d^i = \theta_d^o = \theta_i$ (since the velocity of moving contact lines is finite). In this limit, boundary condition (ii) reduces to a fixed contact angle condition and contact line motion will not dissipate any free energy. We use the relaxed contact angle boundary condition (ii) in our numerical computations because it can improve numerical stability and, in the fast contact line motion limit, it is also physically important. The accurate, efficient parametric finite element method for numerically solving the above sharp-interface model is described in [8, 136].

In general, it would be impossible to directly obtain analytical solutions for the above full sharp-interface model. In the following sections, we develop an Onsager's variational principle approach to derive a reduced-order model for describing the dynamics of a toroidal island shrinking via surface diffusion. We validate the resultant analytical approach by comparison with the numerical results from solving the above full sharp-interface model.

5.3.2   A reduced model via Onsager's principle

In the reduced-order variational model, we assume that (i) during the island evolution (see Fig. 5.4), the cross-section profile of the island is a circular arc which meets the substrate at the isotropic Young contact angle $\theta_i \in [0, \pi]$ and (ii) the contact line does not dissipate any free energy when it moves along the substrate. As noted above, we do not consider the instability along the azimuthal direction (i.e., Rayleigh instability) here.
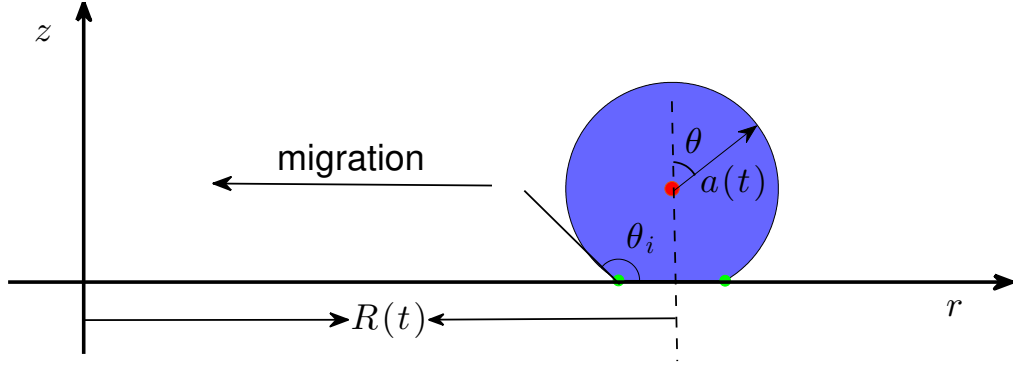
Figure 5.4: A cross-section profile of solid-state dewetting of an initially, toroidal island on a flat, rigid substrate in cylindrical coordinates, where $a := a(t)$ is the radius of the circle (or toroid), $R := R(t)$ is the overall radius (i.e., the distance between the origin of the circle and the z-axis). We assume that the ratio $a(t)/R(t)$ is not large.

We express the cross-section profile of the island $\Gamma(t) := (r(\theta, t), z(\theta, t))$ in cylindrical coordinates (r, z) as

$$\begin{cases} r(\theta, t) = R(t) + a(t) \sin \theta, \\ \\ z(\theta, t) = a(t)(\cos \theta - \cos \theta_i), \end{cases} \quad \theta \in [-\theta_i, \theta_i], \tag{5.3.8}$$

where θ is a parametrization of the cross-section curve Γ. The three-dimensional surface profile of the island is obtained by rotating Γ around the z-axis, i.e., $S(t) = (r(\theta, t) \cos \varphi, \ r(\theta, t) \sin \varphi, \ z(\theta, t))$, where $\varphi \in [0, 2\pi]$ is the azimuthal angle. Since the total volume of the solid island is conserved during the evolution, the initial volume of the island V_0, i.e.,

$$V_0 = \pi R a^2 (2\theta_i - \sin 2\theta_i), \tag{5.3.9}$$

constrains the state variables $a := a(t)$ and $R := R(t)$. Use of this constraint implies that there is only one independent parameter, i.e., R or a. Without loss of generality, we consider the evolution of the island in terms of the parameter R and define the Rayleighian of the system $\mathcal{R}$ as

$$\mathcal{R} = \dot{W}(R, \dot{R}) + \Phi(\dot{R}, \dot{R}). \tag{5.3.10}$$

Minimizing the Rayleighian with respect to the rate $\dot{R}$ yields the time evolution equation of R. We now determine the total free energy function W and the dissipation function Φ of the system, respectively.

We write the total interfacial free energy of the system in terms of the state variable R, using Eq. (5.3.2), as

$$W = \gamma_0 \Big[2\pi R\, a \big(2\theta_i - \sin 2\theta_i \big) \Big]. \tag{5.3.11}$$

By using Eq. (5.3.9), we obtain $a = \sqrt{V_0/\pi R(2\theta_i - \sin 2\theta_i)}$. Substituting this relation into Eq. (5.3.11), and taking the time derivative, we obtain

$$\dot{W} = \gamma_0 \sqrt{\pi V_0 (2\theta_i - \sin 2\theta_i)}\, R^{-\frac{1}{2}} \dot{R}. \tag{5.3.12}$$

The island morphology evolution is driven by the interfacial free energy minimization and its mass transport occurs through surface-diffusion. The resulting dissipation function can be written as

$$\Phi = \frac{1}{2} \iint_S \frac{k_B T}{D_s} |\mathbf{V}|^2 \nu \, dS = \frac{1}{2} \frac{k_B T}{D_s \nu} \iint_S |\mathbf{J}|^2 \, dS, \tag{5.3.13}$$

where $\mathbf{J}$ is the surface current (or mass flux) of atoms along the interface [?],

$$\mathbf{J} = \nu \mathbf{V} = -\frac{D_s \nu}{k_B T} \nabla_s \mu, \tag{5.3.14}$$

and ∇_s is the surface gradient operator. By multiplying by the atomic volume Ω_0, the mass flux can be converted to the normal velocity v_n of the surface element,

$$v_n = -\Omega_0 \left(\nabla_s \cdot \mathbf{J} \right). \tag{5.3.15}$$

Because the island shape is assumed to be axisymmetric, the normal velocity v_n of the island can be calculated by restricting the problem to the cross-section profile Γ (shown in Fig. 5.4). By taking the time derivative of the surface profile Γ, i.e., Eq. (5.3.8) and multiplying by the surface unit normal vector $\mathbf{n} = (\sin\theta, \cos\theta)$, we obtain the normal velocity v_n of the surface element along the cross-section curve Γ:

$$v_n(\theta) = \dot{R}\sin\theta + \dot{a}(1 - \cos\theta_i \cos\theta), \quad \theta \in [-\theta_i, \theta_i]. \tag{5.3.16}$$

The mass flux vector $\mathbf{J}$ is only parallel to the tangential to Γ; hence, $\mathbf{J} = J\boldsymbol{\tau}$ where $\boldsymbol{\tau}$ representing the unit tangential vector, where J is the magnitude of the mass flux vector. The surface divergence of the flux is related to the surface velocity by

$$-\Omega_0\big[\nabla_s \cdot (J\boldsymbol{\tau})\big] = -\Omega_0\frac{\partial_s(rJ)}{r} = v_n(\theta), \tag{5.3.17}$$

where ∂_s represents the first-order derivative with respect to the arc length of Γ. By integrating both sides and applying the zero-mass flux boundary condition $J(-\theta_i) = 0$, the magnitude of the mass-flux is

$$J(\theta) = -\frac{1}{r\Omega_0} \int_{-\theta_i}^{\theta} r\, v_n(\theta)\, a\, d\theta. \tag{5.3.18}$$

Inserting the expression v_n from Eq. (5.3.16) and the expression $r = R + a\sin\theta$ into the above Eq.(5.3.18), the mass flux magnitude can be reformulated as:

$$\begin{aligned}
J(\theta) = -\frac{a}{\Omega_0(R + a\sin\theta)}\Big[R\dot{R} \int_{-\theta_i}^{\theta} \sin\theta d\theta \\
+ a\dot{R} \int_{-\theta_i}^{\theta} \sin^2\theta\, d\theta + R\dot{a} \int_{-\theta_i}^{\theta} (1 - \cos\theta_i \cos\theta)d\theta \\
+ a\dot{a} \int_{-\theta_i}^{\theta} \sin\theta(1 - \cos\theta_i \cos\theta)\, d\theta\Big].
\end{aligned} \tag{5.3.19}$$

Taking the time derivative of Eq. (5.3.9) yields

$$a\dot{R} = -2R\dot{a}. \tag{5.3.20}$$

Since $\delta = \frac{a}{R} \ll 1$, and making use of Eq. (5.3.20), we can reformulate the mass flux magnitude $J(\theta)$ in terms of δ as the following form,

$$J(\theta) = \frac{\cos\theta - \cos\theta_i}{\Omega_0}\Big[1 - \frac{1}{2}\delta\sin\theta + \mathcal{O}(\delta^2)\Big]a\dot{R}. \tag{5.3.21}$$

Substituting this expression for $J(\theta)$ into Eq. (5.3.13), we obtain the dissipation function to leading-order as

$$\begin{aligned}
\Phi &= \frac{1}{2}\frac{k_B T}{D_s \nu} \iint_S |\mathbf{J}|^2\, dS = \frac{1}{2}\frac{k_B T}{D_s \nu} \int_0^{2\pi} r\, d\varphi \int_{-\theta_i}^{\theta_i} J^2(\theta)\, a\, d\theta \\
&= \frac{k_B T}{D_s \nu}\pi a \int_{-\theta_i}^{\theta_i} (R + a\sin\theta)J^2(\theta)\, d\theta = \frac{k_B T}{D_s \nu}\pi Ra \int_{-\theta_i}^{\theta_i} (1 + \delta\sin\theta)J^2(\theta)\, d\theta, \\
&= \frac{k_B T}{D_s \nu\Omega_0^2}\pi Ra^3\dot{R}^2\Big[g(\theta_i) + \mathcal{O}(\delta^2)\Big],
\end{aligned} \tag{5.3.22}$$

where

$$g(\theta_i) = \theta_i(2 + \cos 2\theta_i) - \frac{3}{2}\sin 2\theta_i. \tag{5.3.23}$$

With the time derivative of the total free energy function $\dot{W}$ (Eq. (5.3.12)) and the dissipation function Φ (Eq. (5.3.22)) in terms of R and $\dot{R}$, we apply the Onsager's variational principle by minimizing the Rayleighian function $\mathcal{R}$ (Eq. (5.3.10)) with respect to $\dot{R}$. The resultant kinetic equation for the shrinking rate v is found, to leading order, to be

$$v = -\dot{R}(t) \approx C(\theta_i)\frac{B\gamma_0}{V_0}, \tag{5.3.24}$$

where

$$C(\theta_i) = \frac{\pi(2\theta_i - \sin 2\theta_i)^2}{2\,g(\theta_i)}. \tag{5.3.25}$$

The torus shrinking rate is (to leading order) proportional to the material constants B and γ_0, and inversely proportional to the volume of the toroid V_0, and the coefficient $C(\theta_i)$ only depends on the isotropic Young angle θ_i. Given the initial toroidal island location R_0, we find that the toroidal island evolves as

$$R(t) = R_0 - C(\theta_i)\frac{B\gamma_0}{V_0}t, \qquad 0 \le t < t_\delta(\theta_i), \tag{5.3.26}$$

where $t_\delta(\theta_i)$ represents a time where the leading-order approximation breaks down (i.e., where the assumption that $\delta = a/R \ll 1$ is no longer valid); this time depends on θ_i.

In order to validate the variational model, we compare our predictions with the results of numerical simulations based on the full sharp-interface model. In the following numerical simulations, we choose a large contact line mobility (e.g., $\eta = 100$) to ensure that the contact angle is always near its equilibrium value and the dissipation associated with contact line motion is negligible small as possible, and the initial shape of the toroidal island is chosen as half of a torus (i.e., the initial contact angle is $\pi/2$).

Our numerical simulations under the conditions represented in Fig. 5.5 demonstrate that assumption (i), that the cross-section profile $\Gamma(t)$ is always a circular arc, is valid. Taking $\theta_i = \pi/2$ as an example, we find that this assumption is valid for about $\delta \leq 1/3$. We also found that this assumption is valid up to the time when $R(t)$ begins to deviate from the predicted trajectory by the analytical formula in Eq. (5.3.26) (see Fig. 5.5).
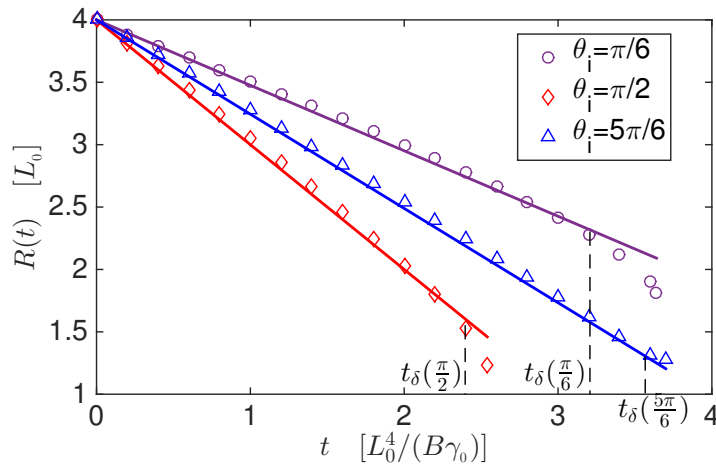
Figure 5.5: Comparisons between the numerical results of $R(t)$ by solving the full sharp-interface model as described in Section 2 and the variational prediction (Eq. (5.3.26)). The "circles", "rhombi" and "triangles" are numerical results obtained from solving the full model and the solid lines are the predicted formula for different isotropic Young angles. The initial parameters are chosen as $R_0 = 4.0$, $a_0 = 0.5$, and L_0 is the length scale.

Figure 5.5 shows a comparison of $R(t)$ from the numerical simulation results based upon the full sharp-interface model as well as the analytical results from the variational model Eq. (5.3.26) for three different isotropic Young angles θ_i. As shown in the figure, the numerical results (symbols) for $R(t)$ are in very good agreement with the analytical predictions (solid lines) for all contact angles from the beginning to the late time $t_\delta(\theta_i)$. Our numerical simulation also indicate that when $\delta =$

$a(t)/R(t)$ is small (not shown), the toroid shrinks towards its center in a quasi-static manner, i.e., its cross-section profile remains nearly a circular arc, consistent with our assumption in the analysis. However, as time evolves, δ increases to a value at which the cross-section profile begins to show non-negligible deviations from the circular arc assumption and the simple analytical result Eq. (5.3.26) breaks down.
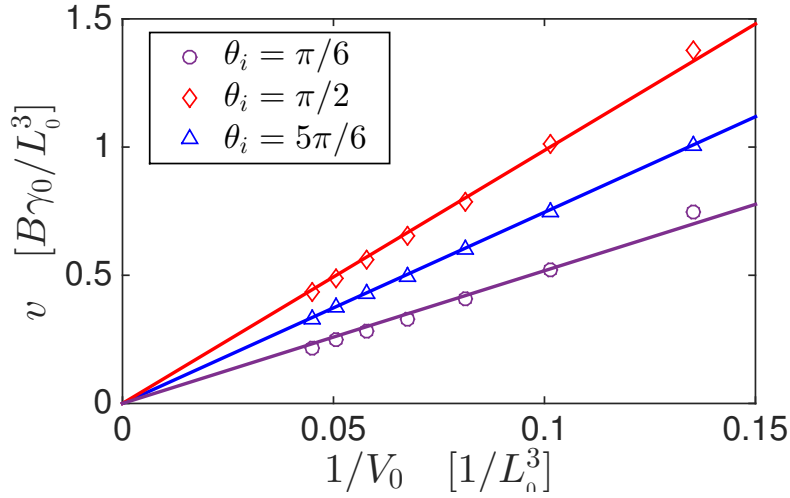
Figure 5.6: Comparisons between the rate at which the toroidal island shrinks v obtained from solving the full sharp-interface model (symbols) and the theoretical shrinking speed, by Eq. (5.3.24) (solid lines) as a function of the island volume V_0 for different isotropic Young angles θ_i.

We performed a least-square linear fitting to numerical data of $R(t)$ obtained from solving the full sharp-interface model for $0 \leq t \leq t_\delta(\theta_i)$ in order to determine the variation of toroidal island shrinking speeds for several isotropic Young angles θ_i and initial volumes V_0. Figure 5.6 shows the comparisons between the rate of island shrinking from the numerical simulations and analytical predictions, where the values of $C(\theta_i)$ were estimated from the numerical results. This figure shows that the numerical results suggest that v is inversely proportional to the toroidal island volume V_0 as predicted analytically by Eq. (5.3.24).

Figure 5.7 shows some comparisons between $C(\theta_i)$ obtained from numerical results (shown in "circles") and the analytical expression in Eq. (5.3.25). Again, we

see that the numerical results based upon the full model are accurately predicted by the analytical results based upon the variational model. These results show that the function $C(\theta_i)$ reaches the maximum value when $\theta_i = \pi/2$; i.e., the toroidal island shrinks fastest when $\theta_i = \pi/2$.
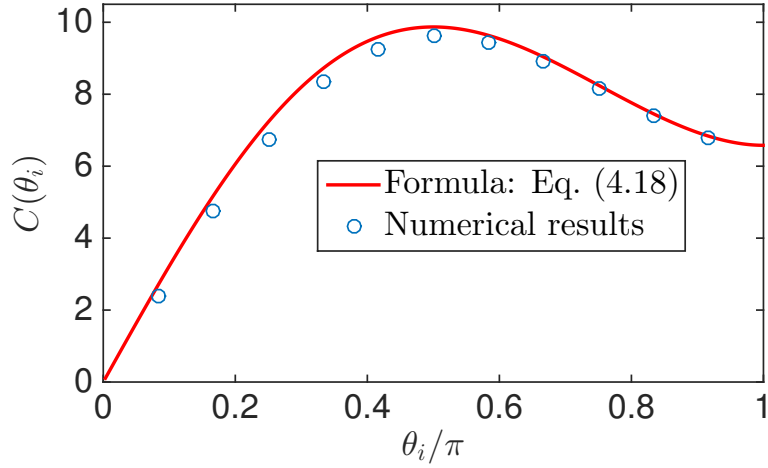
Figure 5.7: Comparisons between the fitting values of $C(\theta_i)$ (shown in "circles") obtained by numerically solving the full sharp-interface model and the analytical values given by Eq. (5.3.25) (shown in red solid line).

We considered the evolution of a solid toroidal island on a flat substrate, evolving by capillarity-driven surface diffusion. This problem is an example of the evolution of the complex local geometric features often observed in dewetting of a solid film on a substrate. Our general approach to such problems as that described here, is based upon Onsager's variational principle. Using this approach, we derived a reduced-order variational model for describing and analyzing the shrinking of a toroidal island. We obtained an analytical formula for the rate at which the island shrinks; the shrinking rate is proportional to the material constants $B = \frac{D_s \nu \Omega_0^2}{k_B T}$ and γ_0, and inversely proportional to the island volume V_0. The analytical predictions are validated by detailed comparisons with accurate numerical simulations based upon a full sharp-interface model; and the agreement is excellent.

Chapter 6

Conclusion and Future Works

This thesis focuses on the derivation of sharp interface models for solid-state dewetting problem and development of efficient numerical approximations for solving the governing geometric partial differential equations. The problem has been studied both in two dimensions and three dimensions in the form of Cahn-Hoffman $\boldsymbol{\xi}$-vector.

In chapter 2, the two-dimensional problem was studied via the energy variational approach. The equations for the equilibrium shape and its stability conditions were derived by calculating the first and second variation of the energy functional. We have presented the sharp interface model for solid-state dewetting in the form of Cahn-Hoffman $\boldsymbol{\xi}$-vector. Moreover, a semi-implicit parametric finite element method was proposed for solving the sharp interface models. The mass conservation and energy dissipation were proved to be satisfied for the variational formulation and semi-discrete scheme. The strongly anisotropic case was also included via Willmore energy regularzation. A similar parametric finite element method was presented. Numerical simulations for the evolution of small islands, large islands have demonstrates the accuracy of the model, efficiency of the numerical schemes and anisotropic effect on the island evolution. The power law for the edge retraction of semi-infinite thin film was investigated under the cusp surface energy.

In chapter 3, based on thermodynamic variation, we derived a sharp interface model for solid-state dewetting with anisotropic surface energy in three dimensions.

Unlike two dimensions, we calculate the energy variation by using the shape derivatives and speed method. The mass conservation and energy dissipation for the model were presented afterwards. In chapter 4, based on the model we presented a parametric finite element method for solving the sharp interface model with isotropic surface energy. The surface diffusion flow for the open surface can be approximated by a simple extension of variational formulation in two dimensions. The contact line migration for the plane curve was formulated with a small surface diffusion regularization. The parametric finite element scheme has also been extended to the weakly anisotropic case. Moreover, extensive numerical simulation results have validated the convergence of the discrete schemes, shown consistent morphological evolutions observed in physical experiments, and proven the accuracy of the models.

In Chapter 5, based on thermodynamic variation, the sharp interface model has been generalized to the case when the surface energy is strongly anisotropic and when the substrate is curved. Moreover, we studied the migration of toroidal thin film for solid-state dewetting under the cylindrical symmetry. We obtained a reduced model via Onsager's Principle for describing the migration rate. This reduced model was then validated by numerical results.

Some future works can be summarised as follows.

- The parametric finite element method will be extended to the cases when the surface energy is strongly anisotropic and when the substrate is curved. However, this extension is not straight forward for the two cases. The introduction of the Gauss curvature in the governing equations for the strongly anisotropic case may require some techniques for a good variational formulation. In addition, when the substrate is curved, the contact line where the thin film, vapor and substrate meet becomes a space curve in three dimensions. The variational formulation as well as the smooth regularization for the plane curve will be extended for space curve.

- Although our parametric finite element scheme has some good properties with respect to the mesh distribution. However, this is only true for isotropic case.

For strongly anisotropic case, the polygonal mesh has high possibility to deteriorate. Therefore, a good mesh regularization is required to ensure the stability of the discrete scheme. Moreover, our mesh generation procedure is only applicable to an initially cuboid island, and efficient mesh generation algorithms for complex geometries need to be developed.

- Although there are some numerical convergence tests for parametric finite element method in solving surface diffusion flow [20], however, to our knowledge, the rigorous mathematical analysis for the convergence rate of PFEM scheme is still unclear. For solid-state dewetting problem. the complicated boundary conditions could further make the mathematical analysis more difficult.

- Our simulation examples will be set up more realistically in the further. This includes the simulations of hole growth, the power law for edge retraction. As a consequence, the computational cost as well as the storage could be very large. If possible, the parallel computation will be considered.

- The phase field approach to solid-state dewetting will be considered in the future as a comparison with the sharp interface approach. The sharp interface limit will be analysed. The numerical simulation results for the phase field approach and sharp interface approach could provide a benchmark for solid-state dewetting.

- The solid-state dewetting problem will be studied by including the elasticity of the materials, considering a demforable substrate and so on.

Taylor expansions for linear perturbation

Under the perturbation

$$\mathbf{X}(\rho, \varepsilon) = \mathbf{X}(\rho, 0) + \varepsilon \mathbf{X}^1(\rho), \tag{A.1}$$

we have

$$\mathbf{V}_0 = \partial_\varepsilon \mathbf{X}(\rho, \varepsilon) = \partial_\varepsilon \mathbf{X}(\rho, \varepsilon)\Big|_{\varepsilon=0} = \mathbf{X}^1(\rho), \qquad \partial_\varepsilon^2 \mathbf{X}(\rho, \varepsilon) = 0. \tag{A.2}$$

We show the expansions of $|\partial_\rho \mathbf{X}(\rho, \varepsilon)|$ and $\mathbf{n}^\varepsilon$ at $\varepsilon = 0$.

For $|\partial_\rho \mathbf{X}(\rho, \varepsilon)|$, we have

$$\partial_\varepsilon |\partial_\rho \mathbf{X}(\rho, \varepsilon)| = \frac{\partial_\varepsilon \partial_\rho \mathbf{X}(\rho, \varepsilon) \cdot \partial_\rho \mathbf{X}(\rho, \varepsilon)}{|\partial_\rho \mathbf{X}(\rho, \varepsilon)|}. \tag{A.3}$$

$$\begin{aligned}
\partial_\varepsilon^2 |\partial_\rho \mathbf{X}(\rho, \varepsilon)| &= \partial_\varepsilon \left[\frac{\partial_\varepsilon \partial_\rho \mathbf{X}(\rho, \varepsilon) \cdot \partial_\rho \mathbf{X}(\rho, \varepsilon)}{|\partial_\rho \mathbf{X}(\rho, \varepsilon)|} \right] \\
&= \frac{\partial_\varepsilon \partial_\rho \mathbf{X}(\rho, \varepsilon) \cdot \partial_\varepsilon \partial_\rho \mathbf{X}(\rho, \varepsilon)}{|\partial_\rho \mathbf{X}(\rho, \varepsilon)|} - \frac{\partial_\varepsilon \partial_\rho \mathbf{X}(\rho, \varepsilon) \cdot \partial_\rho \mathbf{X}(\rho, \varepsilon) \partial_\varepsilon |\partial_\rho \mathbf{X}(\rho, \varepsilon)|}{|\partial_\rho \mathbf{X}(\rho, \varepsilon)|^2} \\
&= \frac{|\partial_\rho \mathbf{V}_0|^2}{|\partial_\rho \mathbf{X}(\rho, \varepsilon)|} - \frac{(\partial_\rho \mathbf{V}_0 \cdot \partial_\rho \mathbf{X}(\rho, \varepsilon))^2}{|\partial_\rho \mathbf{X}(\rho, \varepsilon)|^3}. \tag{A.4}
\end{aligned}$$

Denote $\mathbf{X} = \mathbf{X}(\rho, 0)$, take the value at $\varepsilon = 0$, and also note that $\partial_\rho s(\rho, \varepsilon) = |\partial_\rho \mathbf{X}(\rho, \varepsilon)|$, we obtain

$$\partial_\varepsilon |\partial_\rho \mathbf{X}(\rho, \varepsilon)|\Big|_{\varepsilon=0} = |\partial_\rho \mathbf{X}| \partial_s \mathbf{V}_0 \cdot \boldsymbol{\tau}. \tag{A.5}$$

$$\partial_\varepsilon^2 |\partial_\rho \mathbf{X}(\rho, \varepsilon)|\Big|_{\varepsilon=0} = |\partial_\rho \mathbf{X}| (|\partial_s \mathbf{V}_0|^2 - (\boldsymbol{\tau} \cdot \partial_s \mathbf{V}_0)^2). \tag{A.6}$$

Thus we obtain the expansion of $|\partial_\rho \mathbf{X}(\rho, \varepsilon)|$ at $\varepsilon = 0$

$$|\partial_\rho \mathbf{X}(\rho, \varepsilon)| = |\partial_\rho \mathbf{X}|\Big[1 + (\boldsymbol{\tau} \cdot \partial_s \mathbf{V}_0)\varepsilon + \frac{1}{2}\big(\partial_s \mathbf{V}_0 \cdot \partial_s \mathbf{V}_0 - (\boldsymbol{\tau} \cdot \partial_s \mathbf{V}_0)^2\big)\varepsilon^2\Big] + O(\varepsilon^3). \quad \text{(A.7)}$$

For $\mathbf{n}^\varepsilon = \mathbf{n}(\rho, \varepsilon)$, note that we can express

$$\mathbf{n}^\varepsilon = -\frac{[\partial_\rho \mathbf{X}(\rho, \varepsilon)]^\perp}{|\partial_\rho \mathbf{X}(\rho, \varepsilon|}. \quad \text{(A.8)}$$

So we have

$$\begin{aligned}
\partial_\varepsilon \mathbf{n}^\varepsilon &= -\frac{[\partial_\varepsilon \partial_\rho \mathbf{X}(\rho, \varepsilon)]^\perp}{|\partial_\rho \mathbf{X}(\rho, \varepsilon)|} + \frac{[\partial_\rho \mathbf{X}(\rho, \varepsilon)]^\perp \partial_\varepsilon |\partial_\rho \mathbf{X}(\rho, \varepsilon)|}{|\partial_\rho \mathbf{X}(\rho, \varepsilon)|^2} \\
&= -\frac{[\partial_\varepsilon \partial_\rho \mathbf{X}(\rho, \varepsilon)]^\perp}{|\partial_\rho \mathbf{X}(\rho, \varepsilon)|} + \frac{[\partial_\rho \mathbf{X}(\rho, \varepsilon)]^\perp [\partial_\varepsilon \partial_\rho \mathbf{X}(\rho, \varepsilon) \cdot \partial_\rho \mathbf{X}(\rho, \varepsilon)]}{|\partial_\rho \mathbf{X}(\rho, \varepsilon)|^3}. \quad \text{(A.9)}
\end{aligned}$$

$$\begin{aligned}
\partial_\varepsilon^2 \mathbf{n}^\varepsilon &= \frac{[\partial_\varepsilon \partial_\rho \mathbf{X}(\rho, \varepsilon)]^\perp \partial_\varepsilon \partial_\rho \mathbf{X}(\rho, \varepsilon) \cdot \partial_\rho \mathbf{X}(\rho, \varepsilon)}{|\partial_\rho \mathbf{X}(\rho, \varepsilon)|^3} + \frac{[\partial_\varepsilon \partial_\rho \mathbf{X}(\rho, \varepsilon)]^\perp [\partial_\varepsilon \partial_\rho \mathbf{X}(\rho, \varepsilon) \cdot \partial_\rho \mathbf{X}(\rho, \varepsilon)]}{|\partial_\rho \mathbf{X}(\rho, \varepsilon)|^3} \\
&\quad + \frac{[\partial_\rho \mathbf{X}(\rho, \varepsilon)]^\perp [\partial_\varepsilon \partial_\rho \mathbf{X}(\rho, \varepsilon) \cdot \partial_\varepsilon \partial_\rho \mathbf{X}(\rho, \varepsilon)]}{|\partial_\rho \mathbf{X}(\rho, \varepsilon)|^3} \\
&\quad - \frac{3[\partial_\rho \mathbf{X}(\rho, \varepsilon)]^\perp |\partial_\varepsilon \partial_\rho \mathbf{X}(\rho, \varepsilon) \cdot \partial_\rho \mathbf{X}(\rho, \varepsilon)|^2}{|\partial_\rho \mathbf{X}(\rho, \varepsilon)|^5}. \quad \text{(A.10)}
\end{aligned}$$

Taking value at $\varepsilon = 0$, we obtain

$$\begin{aligned}
\partial_\varepsilon \mathbf{n}^\varepsilon\Big|_{\varepsilon=0} &= -[\partial_s \mathbf{V}_0]^\perp - \mathbf{n}\,(\partial_s \mathbf{V}_0 \cdot \boldsymbol{\tau}). \quad \text{(A.11)} \\
\partial_\varepsilon^2 \mathbf{n}^\varepsilon\Big|_{\varepsilon=0} &= [\partial_s \mathbf{V}_0]^\perp(\partial_s \mathbf{V}_0 \cdot \boldsymbol{\tau}) + (\partial_s \mathbf{V}_0)^\perp(\partial_s \mathbf{V}_0 \cdot \boldsymbol{\tau}) - \mathbf{n}\,(\partial_s \mathbf{V}_0)^2 + 3\mathbf{n}\,(\partial_s \mathbf{V}_0 \cdot \boldsymbol{\tau}). \quad \text{(A.12)}
\end{aligned}$$

Note that the expansion of $\gamma(\mathbf{n}^\varepsilon)$ at $\varepsilon = 0$ is given as

$$\begin{aligned}
\gamma(\mathbf{n}^\varepsilon) &= \gamma(\mathbf{n}) + \nabla\hat\gamma(\mathbf{n})\partial_\varepsilon \mathbf{n}^\varepsilon\Big|_{\varepsilon=0}\varepsilon \\
&\quad + \frac{1}{2}\Big(\nabla\hat\gamma(\mathbf{n})\partial_\varepsilon^2 \mathbf{n}^\varepsilon\Big|_{\varepsilon=0} + \mathrm{H}_\gamma(\mathbf{n})\partial_s \mathbf{n}^\varepsilon \cdot \partial_\varepsilon \mathbf{n}^\varepsilon\Big|_{\varepsilon=0}\Big)\varepsilon^2 + \mathrm{O}(\varepsilon^3). \quad \text{(A.13)}
\end{aligned}$$

Thus we immediately obtain the expansion of $\gamma(\mathbf{n}^\varepsilon)$ at $\varepsilon = 0$

$$\begin{aligned}
\gamma(\mathbf{n}^\varepsilon) &= \gamma(\mathbf{n}) + \Big[-\gamma(\mathbf{n})(\boldsymbol{\tau} \cdot \partial_s \mathbf{V}_0) - \nabla\hat\gamma(\mathbf{n}) \cdot (\partial_s \mathbf{V}_0)^\perp\Big]\varepsilon \\
&\quad + \frac{1}{2}\Big[2\nabla\hat\gamma(\mathbf{n}) \cdot (\partial_s \mathbf{V}_0 \cdot \boldsymbol{\tau})(\partial_s \mathbf{V}_0)^\perp - \gamma(\mathbf{n})(\partial_s \mathbf{V}_0 \cdot \partial_s \mathbf{V}_0) \\
&\quad + 3\gamma(\mathbf{n})(\boldsymbol{\tau} \cdot \partial_s \mathbf{V}_0)^2 + \mathrm{H}_\gamma(\mathbf{n})(\partial_s \mathbf{V}_0)^\perp \cdot (\partial_s \mathbf{V}_0)^\perp\Big]\varepsilon^2 + \mathrm{O}(\varepsilon^3). \quad \text{(A.14)}
\end{aligned}$$

Bibliography

[1] M. Altomare, N.T. Nguyena and P. Schmuki, Templated dewetting: designing entirely self-organized platforms for photocatalysis, Chem. Sci., 7 (2016), 6865-6886.

[2] D. Amram, L. Klinger and E. Rabkin, Anisotropic hole growth during solid-state dewtting of singale-crystal Au-Fe thin film, Acta Mater., 60 (2012), 3047-3056.

[3] S. Angenet and M.E. Gurtin, Multiphase thermomechanics with interfacial structure. 2. Evolution of an isothermal interface, Arch. Rational Mech. Anal., 108 (1989), 323-391.

[4] R.W. Balluffi, S.M. Allen, and W.C. Careter, Kinetics of Materials, Wiley-Interscience, John Wiley, 2005.

[5] E. Bansch, P. Morin and R.H. Nochetto, Surface diffusion of graphs: Variational formulation, error analysis and simulation, SIAM J. Numer. Anal., 42 (2004), 773-799.

[6] E, Bansch, P. Morin and R.H. Nochetto, A parametric finite element method for surface diffusion, the parametric case, J. Comput. Phys., 203 (2005), 321-343.

[7] K. Bao, Y. Shi, S. Sun and X.P. Wang, A finite element method for the numerical solution of the coupled Cahn-Hilliard and Navier-Stokes system for moving contact line problems, J. Comput. Phys., 231 (2012), 8083-8099.

[8] W. Bao, W. Jiang, Y. Wang and Q. Zhao, A parametric finite element method for solid-state dewetting problems with anisotropic surface energies, J. Comput. Phys., 330 (2017), 380-400.

[9] W. Bao, W. Jiang, D. J. Srolovitz and Y. Wang, Stable equilibria of anisotropic particles on substrates: a generalized Winterbottom construction, SIAM J. Appl. Math., to appear.

[10] W. Bao, W. Jiang and Q. Zhao, A sharp interface model for solid-state dewetting in three dimensions, in preparation.

[11] W. Bao, W. Jiang and Q. Zhao, A parametric finite element method for solid-state dewetting problem in three dimensions, in preparation.

[12] T.L. Barbosa and M. do Carmo, Stability of hypersurfaces of constant mean curvature , Math. Zeit., 185 (1984), 339-353.

[13] J.W. Barrett, J.F. Blowey and H. Garcke, Finite element approximation of the Cahn-Hilliard equation with degenerate mobility, SIAM J. Numer. Anal., 37 (1999), 286-318.

[14] J.W. Barrett and J.F. Blowey, Finite element approximation of the Cahn-Hilliard equation with concentration dependent mobility, Math. Comp., 68 (1999), 487-517.

[15] J.W. Barrett and J.F. Blowey, Finite element approximation of a degenerate Allen-Cahn/Cahn-Hilliard system, SIAM J. Numer. Anal., 39 (2001), 1598-1624.

[16] J.W. Barrett, H. Garcke, and R. Nürnberg, A parametric finite element method for fourth order geometric evolution equations, J. Comput. Phys., 222 (2007), 441-467.

[17] J.W. Barrett, H. Garcke, and R. Nürnberg, On the variational approximation of combined second and fourth order geometric evolution equations, SIAM J. Sci. Comp., 29 (2007), 1006–1041.

[18] J.W. Barrett, H. Garcke, and R. Nürnberg, A varaiational formulation of anisotropic geometric evolution equations in higher dimensions, Numer. Math., 109 (2008), 1–44.

[19] J.W. Barrett, H. Garcke and R. Nürnberg, Numerical approximation of anisotropic geometric evolution equations in the plane, SIMA J. Numer. Anal., 28 (2008), 292-330.

[20] J.W. Barrett, H. Garcke, and R. Nürnberg, On the parametric finite element approximation of evolving hypersurfaces in $\mathbb{R}^3$, J. Comput. Phys., 227 (2008), 4281-4307.

[21] J.W. Barrett, H. Garcke, and R. Nürnberg, Parametric approximation of Willmore flow and related geometric evolution equations, SIAM J. Sci. Comp., 31 (2008), 225-253.

[22] J.W. Barrett, H. Garcke and R. Nürnberg, Numerical approximation of gradient flows for closed curves in R^d, SIMA J. Numer. Anal., 30 (2010), 4-60.

[23] J.W. Barrett, H. Garcke and R. Nürnberg, Parametric approximation of surface clusters driven by isotropic and anisotropic surface energies, Interfaces Free Bound., 12 (2010), 187–234.

[24] J.W. Barrett, H. Garcke and R. Nürnberg, Finite element approximation of coupled surface and grain boundary motion with applications to thermal grooving and sintering, European J. Appl. Math., 21 (2010), 519-556.

[25] J.W. Barrett, H. Garcke, and R. Nürnberg, On the stable discretization of strongly anisotropic phase field models with applications to crystal growth, ZAMM Z. Angew. Math. Mech., 93 (2013), 719-732.

[26] W.K. Burton, N. Cabrera and F.C. Frank, The growth of crystals and the equilibrium structure of their surfaces, Phil. Trans. R. Soc. Lond. A., 243 (1951), 299-358.

[27] J.W. Cahn and D.W. Hoffman, A vector thermodynamics for anisotropic surfaces. II. Curved and faceted surfaces, Acta Metall. Mater., 22 (1974), 1205-1214.

[28] J.W. Cahn and C.A handwerker, Equilibrium geometries of anisotropy surfaces and interfaces, Mater. Sci. Eng. A., 162 (1993) 83-95.

[29] J.W. Cahn and J. Taylor, Surface motion by surface diffusion, Acta Metall. Mater., 42 (1994), 107-123.

[30] A.D. Carlo, M.E. Gurtin and P. Podio-guidugli, A regularized equation for anisotropic motion by curvature, SIAM J. APPL. MATH., 52 (1992), 1111-1119.

[31] D.L. Chopp and J.A. Sethian, Motion by intrinsic Laplacian of curvature, Interfaces Free Bound., 1 (1999), 107-123.

[32] U. Czubayko, V.G. Sursaeva, G. Gottstein and L.S. Shvindlerman, Influence of triple junctions on grain boundary motion, Acta Mater., 46 (1998), 5863-5871.

[33] D.T. Danielson, D.K. Sparacin, J. Michel and L.C. Kimerling, Surface-energy-driven dewetting theory of silicon-on-insulator agglomeration, J. Appl. Phys., 100 (2006), article 083057.

[34] K. Deckelnick, G. Dziuk and C. M. Elliott, Computation of geometric partial differential equations and mean curvature flow, Acta Numerica., (2005),139-232

[35] K. Deckelnick and G. Dziuk , A fully discrete numerical scheme for weighted mean curvature flow, Numer. Math., 91 (2002), 423-452.

[36] K. Deckelnick, G. Dziuk and C. M. Elliott, Fully discrete finite element approximation for anisotropic surface diffusion of graphs, SIAM. J. Numer. Anal., 43 (2005), 1112-1138.

[37] P.G. de Gennes, Wetting: statics and dynamics, Rev. Mod. Phys., 57 (1985), 827-863.

[38] A. Dinghas, Uber einen geometrischen Satz von Wulff für die gleichgewichtsform von Kristallen, Z. Krystallogr., 105 (1944), 304-314.

[39] G. Dogan, and R.H. Nochetto, First variation of the general curvature-dependent surface energies, ESAIM Math Model. Numer.Anal., 46 (2012), 59-79.

[40] E. Dornel, J.C. Barbe, F. Crecy, G. Lacolle and J. Eymery, Surface diffusion dewetting of thin solid films: Numerical method and application to Si/SiO_2, Phys. Rev. B, 73 (2006), article 115427.

[41] P. Du, and H. Wong, An analytic solution for three-dimensional axisymmetric equilibrium crystal shapes, Script. Mater., 60 (2009), 631-634.

[42] P. Du, M. Khenner and H. Wong, A tangent-plane marker-particle method for the computation of three-dimensional solid surface evolving by surface on a substrate, J. Comput. Phys., 229 (2010), 813-827.

[43] M. Dufay and O. Pierre-Louis, Anisotropy and coarsening in the instability of solid dewetting fronts, Phys. Rev. Lett., 106 (2011), article 105506.

[44] G. Dziuk, An algorithm for evolutionary surfaces, Numer. Math., 58 (1991), 603-611.

[45] G. Dziuk and C.M. Elliot, Finite elements for surface PDEs, Acta. Numerica., (2013) 289-396.

[46] M. Dziwnik, A. Munch and B. Wagner, A phase-field model for solid-state dewetting and its sharp interface limit, preprint.

[47] C.M. Elliott and H. Garcke, Existence results for diffusive surface motion laws, Adv. Math. Sci. Appl., 7 (1997), 465-488.

[48] J. Escher, U.F. Mayer and G. Simonett, The surface diffusion flow for immersed hypersurfaces, SIAM J. Math. Anal., 29 (1998), 1419-1433.

[49] E.C. Frank, Metal Surfaces, American Society for Metals, Metals Park, OH, (1963), 1-15.

[50] Y. Fan, R. Nuryadi, Z.A. Burhanudin, and M. Tabe, Thermal Agglomeration of Ultrathin Silicon-on-Insulator Layers: Crystalline Orientation Dependence. Japanese Journal of Applied Physics., 47 (2008), 14611464.

[51] M. Gao and X.P. Wang, A gradient stable scheme for a phase field model for the moving contact line problem, J. Comput. Phys., 231 (2012), 1372-1386.

[52] M. Gao and X.P. Wang, An efficient scheme for a phase field model for the moving contact line problem with variable density and viscosity, J.comput. Phys., 272 (2014), 704-718.

[53] A.L. Giermann and C.V. Thompson, Solid-state dewetting for ordered arrays of crystallographically oriented metal particles, Appl. Phys. Lett., 86 (2005), article 121903.

[54] Y. Giga and K. Ito, On pinching of curves moved by surface diffusion., Comm. Appl. Anal., 2 (1998), 393405.

[55] G. Gottstein and L.S. Shvindlerman, Triple junction dragging and von Neu-mannMullins relation, Script. Mater., 38 (1998), 1541-1547.

[56] G. Gottstein, V. Sursaeva and L.S. Shvindlerman, The effect of triple junctions on grain boundary motion and grain microstructure evolution, Interf. Sci., 7 (1999), 273-283.

[57] M.E. Gurtin and M.E. Jabbour, Interface evolution in three dimensions with curvature-dependent energy and surface diffusion: interface-controlled evolution, phase transitions, epitaxial growth of elastic films, Arch. Rat. Mech. Anal., 163 (2002), 171-208.

[58] F. Hausser and A. Voigt, A discrete scheme for regularized anisotropic surface diffusion: a 6th order geometric evolution equation, Interfaces Free Bound., 7 (2005), 353-369.

[59] C. Herring, Effect of change of scale on sintering phenomena, J. Appl. Phys., 21 (1950), 301-303.

[60] C. Herring, Physics of Powder Metallurgy, ed. W.E. Kingston, McGraw-Hill, 1951.

[61] C. Herring, Some theorems on the free energies of crystal surfaces, Phys. Rev., 82 (1951), 87-93.

[62] H. Hilton, Mathematical crystallography, Oxford, 1903.

[63] S.Y. Hon, S. Leung and H.K. Zhao, A cell based particle method for modeling dynamic interfaces, J. Comput. Phys., 272 (2014), 279-306.

[64] M. Hintermuller and W. Ring, A second order shape optimization approach for image segmentation, SIAM J.Appl.Math, 64 (2003), 442-467.

[65] D.W. Hoffman and J.W. Cahn, A vector thermodynamics for anisotropic surfaces. I. Fundamentals and application to plane surface junctions, Surf. Sci., 31 (1972), 368-388.

[66] W. Jiang, W. Bao, C.V. Thompson and D.J. Srolovitz, Phase field approach for simulating solid-state dewetting problems, Acta Mater., 60 (2012), 5578-5592.

[67] W. Jiang, Y. Wang, Q. Zhao, D.J. Srolovitz and W. Bao, Solid-state dewetting and island morphologies in strongly anisotropic materials, Script. Mater., 115 (2016), 123-127.

[68] E. Jiran and C.V. Thompson, Capillarity instabilities in thin films, J. Elect.Mater., 19 (1990), 1153-1160.

[69] E. Jiran and C.V. Thompson, Capillary instabilities in thin, continuous films, Thin Solid Films, 208 (1992), 23-28.

[70] G.H. Kim, R.V. Zucker, W. C. Carter, and C. V. Thompson, Quantitative analysis of anisotropic edge retraction by solid-state dewetting of thin single crystal films, J. Appl. Phys., 113 (2013), article 043512.

[71] L. Klinger and E. Rabkin, Effect of strong surface anisotropy on morphology of periodic surface profiles, Acta Mater., 50 (2002), 343-352.

[72] L. Klinger and E. Rabkin, Shape evolution by surface and interface diffusion with rigid body rotations, Acta Mater., 59 (2011), 6691-6699.

[73] L. Klinger and E. Rabkin, Capillary-driven motion of nanoparticles attached to curved rigid substrates, Acta Mater., 60 (2012), 6065-6075.

[74] E.M. Kolahdouz and D. Salac, A semi-implicit gradient augmented level set method, SIAM J. Sci. Comput., 35 (2013), 231-254.

[75] M.V. Laue, Der Wulffsche Satz für die gleichgewichtsform von kristallen, Z. Krystallogr, 105 (1943), 124-133

[76] A.A. Lee, A. Munch and E. Suli, Degenerate mobilities in phase field models are insufficient to capture surface diffusion, Appl. Phys. Lett., 107 (2015), article 081603.

[77] F. Leroy, F. Cheynis, T. Passanante and P. Muller, Dynamics, anisotropy, and stability of silicon-on-insulator dewetting fronts, Phys. Rev. B, 85 (2012), article 195414.

[78] S. Leung, H.K. Zhao, A grid based particle method for moving interface problems, J. Comput. Phys., 228 (2009), 7706-7728.

[79] S. Leung, J. Lowengrub and H.K. Zhao, A grid based particle method for solving partial differential equations on evolving surfaces and modeling high order geometrical motion, J. Comput. Phys., 230 (2011), 2540-2561.

[80] B. Li, J. Lowengrub, A. Ratz and A. Voigt, Geometric evolution laws for thin crystalline films: modeling and numerics, Commun. Comput. Phys., 6 (2009), 433-482.

[81] H. Liebmann, Der Curie-Wulffsche Satz über combinationsformen von krystallen, Z. Kristallogr., 53 (1914), 171-177.

[82] D. Mattissen, D.A. Molodov, L.S. Shvindlerman and G. Gottstein, Drag effect of triple junctions on grain boundary and grain growth kinetics in aluminium, Acta Mater., 53 (2005), 2049-2057.

[83] W.L. Ling, T. Giessel, K. Thurmer, R.Q. Hwang, N. C. Bartelt and K .F. McCarty, Crucial role of substrate steps in de-wetting of crystalline thin films, Surf. Sci., 570 (2004) 297-303.

[84] M.S. Mccallum, P.W. Voorhees, M.J. Miksis, H.D. Stephen and H. Wong, Capillary instabilities in solid thin films: Lines, J. Appl. Phys.,79 (1996), 7604-7611.

[85] H. Mehrabian and J.J. Feng, Capillary break up of liquid torus, J.Fluid Mech., 717 (2013), 281-292.

[86] W.W. Mullins, Theory of thermal grooving, J. Appl. Phys., 28 (1957), 333-339.

[87] B. Palmer, Stability of the Wulff shape. Proc. Amer. Math. Soc., 126 (1998), 3661-3667.

[88] E. Pairam and A. Fernandez-Nieves, Generation and stability of toroidal droplets in a viscous liquid. Phys. Rev. Lett., 102 (2009), article 234501.

[89] D.P. Peng, S. Osher, B. Merriman and H.K. Zhao, The geometry of Wulff crystal shapes and its relations with Riemann problems, Contemp. Math., 238 (1999), 251-303.

[90] J. Petersen and S.G. Mayr, Dewetting of Ni and NiAg solid thin films and formation of nanowires on ripple patterned substrates, J. Appl. Phys., 103 (2008) article 023520.

[91] O. Pierre-Louis and Y. Saito, Wetting of solid adsorbate islands on nanogroove surfaces, Europhys. Lett., 86 (2009), article 46004.

[92] O. Pierre-Louis, A. Chame and Y. Saito, Dewetting of ultrathin solid films, Phys. Rev. Lett., 103 (2009), article 195501.

[93] A. Polden, Curves and surfaces of least total curvature and forth-order flows, Ph.D. dissertation, Universität Tübingen, Germany, (1996).

[94] P. Pozzi, Anisotropic mean curvature flow for two dimensional surfaces in higher codimension: a numerical scheme, Interfaces Free Bound, 10 (2008), 539-576.

[95] S.G. Protasova, G. Gottstein, D.A. Molodov, V.G. Sursaeva, and L.S. Shvindlerman, Triple junction motion in aluminum tricrystals, Acta Mater. 49 (2001), 2519-2525.

[96] T. Qian, X.P. Wang and P. Sheng, Generalized Navier boundary condition for the moving contact line, Comm. Math. Sci., 1 (2003), 333-341.

[97] T. Qian, X.P. Wang and P. Sheng, Molecular hydrodynamics of the moving contact line in two phase immiscible flows, Commun. Comput. Phys., 1 (2006), 1-52.

[98] T. Qian, X.P. Wang, and P. Sheng, A variational approach to moving contact line hydrodynamics, J. Fluid Mech., 564 (2006), 333-360.

[99] L. Rayleigh, On the instability of jest, Proc.Lond.Math.Soc., 10 (1878), 4-13.

[100] W. Ren and W. E, Boundary conditions for the moving contact line problem, Phys. Fluid, 19 (2007), article 022101.

[101] W. Ren, D. Hu, and W. E, Continuum models for the contact line problem, Phys. Fluid, 22 (2010), article 102103.

[102] W. Ren and W. E, Contact line dynamics on heterogeneous surfaces, Phys. Fluid, 23 (2011), article 072103.

[103] W. Ren, P. Trih and W. E, on the distinguished limit of Navier slip model of the moving contact line problem, J.Fluid Mech., 772 (2015), 107-126.

[104] T.V. Savina, A.A. Golovin, S.H. Davis, A.A. Nepomnyashchy and P.W. Voorhees, On faceting of a growing crystal surface by surface diffusion, Phys. Rev. E, 67 (2003), article 02160.

[105] R.F. Sekerka, Analytical criteria for missing orientations on three-dimensional equilibrium shapes, J. Cryst. Growth., 275 (2005) 77-82.

[106] M. Siegel, M.J. Miksis and P.W. Voorhees, Evolution of material voids for highly anisotropic surface energy, J. Mech. Phys. Solids., 52 (2004), 1319-1353.

[107] P. Smereka, Semi-implicit level set methods for curvature and surface diffusion motion, J. Sci. Comp., 19 (2003), 439-456.

[108] C.S. Smith, Introduction to grains, phases, and interfaces: an interpretation of microstructure, Trans. AIME., 175 (1948), 15-51.

[109] J. Sokolowski and J.-P. Zolesio, Introudction to shape optimization: shape sensitivity analysis, Springer Verlag Berlin, 1992.

[110] D.J. Srolovitz and S. A. Safran, Capillarity instabilities in thin films. I, Energetics, J. Appl. Phys., 60 (1986), 247-254.

[111] D.J. Srolovitz and S. A. Safran, Capillarity instabilities in thin films. II. Kinetics, J. Appl. Phys., 60 (1986), 255-260.

[112] A. Sundar, C.J. Decker, R.A. Hughes and S. Neretina, The templated assembly of highly faceted three-dimensional gold microstructures into periodic arrays, Mater. Lett., 76 (2012) 155-158.

[113] A.P. Sutton and R.W. Balluffi, Interfaces in Crystalline Materials, Clarendon, Oxford University, 1996.

[114] J.E. Taylor, Crystalline variational problems, Bull. Amer. Math. Soc., 84 (1978), 568-588.

[115] J.E. Taylor, Mean curvature and weighted mean curvatue, Acta Metall. Mater., 40 (1992), 1475-1485.

[116] J.E. Taylor, Crystalline variational methods, Proc, Natl. Acad. Sci., USA, 99 (2002), 15277-15280.

[117] C.V. Thompson, Solid-state dewetting of thin films, Annu. Rev. Mater. Res., 42 (2012), 399-434.

[118] M. Upmanyu, D.J. Srolovitz, L.S. Shvindlerman and G. Gottstein, Triple junction mobility: a molecular dynamics study, Interf. Sci., 7 (1999), 307-309.

[119] X.P. Wang, T. Qian and P. Sheng, Moving contact line on chemically patterned surfaces, J. Fluid Mech., 605 (2008), 59-78.

[120] Y. Wang, W. Jiang, W. Bao, D.J. Srolovitz, Sharp interface model for solid-state dewetting problem with weakly anisotropic surface energies, Phys. Rev. B, 91 (2015), article 045303.

[121] H. Wente, A note on the stability theorem of J.L. Barbosa and M. do Carmo for closed surfaces of constant mean curvature. Pacific J. Math., 147 (1991), 375-379.

[122] S. Winklmannm, A note on the stability of the Wulff shape, Arch. Math., 87 (2006), 272-279.

[123] W. L. Winterbottom, Equilibrium shape of a small particle in contact with a foreign substrate, Acta Metall., 15 (1967), 303-310.

[124] S. Wise, J. Kim and J. Lowengrub, Solving the regularized, strongly anisotropic Cahn-Hilliard equation by an adaptive nonlinear multigrid method, J. Comput. Phys., 226 (2007), 414-446.

[125] H. Wong, P. W. Voorhees, M.J. Miksis, S. H. Davis, Periodic mass shedding of a retracting solid film step, Acta Mater., 48 (2000), 1719-1728.

[126] G. Wulff, Zur frage der geschwindigkeit des wachstums und der auflosung der krystallflachen, Z. Kristallogr., 34 (1901), 449-530.

[127] J. Ye and C. V. Thompson, Mechanisms of complex morphological evolution during solid-state dewetting of single-crystal nickel thin films, Appl. Phys. Lett., 97 (2010), article 071904.

[128] J. Ye and C. V. Thompson, Regular pattern formation through the retraction and pinch-off of edges during solid-state dewetting of patterned single crystal films, Phys. Rev. B, 8 (2010), article 193408.

[129] J. Ye and C.V. Thompson, Templated solid-state dewetting to controllably produce complex Patterns, Adv. Mater., 23 (2011), 1567-1571.

[130] J. Ye and C.V. Thompson, Anisotropic edge retraction and hole growth during solid-state dewetting of single crystal nickel thin films, Acta Mater., 59 (2011), 582-589.

[131] T. Young, An essay on the cohesion of fluids, Philos. Trans. R. Soc., London, 95 (1805), 65-87.

[132] W. Zhang and I. Gladwell, Evolution of two-dimensional crystal morphologies by surface diffusion with anisotropic surface free energies, Comput. Mater. Sci., 27 (2003), 461-470.

[133] W. Zhang, Evolution of crystal morphologies to equilibrium by surface diffusion with anisotropic surface free energy in three dimensions, J. Cryst. Growth., 297 (2006), 169-179.

[134] Q. Zhao, W. Jiang, D.J. Srolovitz and W. Bao, Triple junction drag effects during topological changes in evolution of polycrystalline microstructures, Acta Mater., 128 (2017), 345-350.

[135] Q. Zhao, W. Jiang, T.Z. Qian, D.J. Srolovitz and W. Bao, Migrations of Tinny toroidal thin film in solid-state dewetting, preprint.

[136] Q. Zhao and W. Jiang, A sharp interface approach for solid-state dewetting in two dimensions via Cahn-Hoffman vector, preprint.

[137] R. V. Zucker, D. Chatain, U. Dahmen, S. Hagege and W. C. Craig, New software tools for the calculation and display of isolated and attached interfacial-energy minimizing particle shapes, J. Mater. Sci., 47 (2012), 8290-8302.

[138] R.V. Zucker, G.H. Kim, W.C. Carter and C.V. Thompson, A model for solid-state dewetting of a fully-faceted thin film, C. R. Physique., 14 (2013), 564-577.

[139] R.V. Zucker, G.H. Kim, J. Ye, W.C. Carter and C.V. Thompson, The mechanism of corner instabilities in single-crystal thin films during dewetting, J. Appl. Phys., 119 (2016), article 125306.

List of Publications

[1] *Solid-state dewetting and island morphologies in strongly anisotropic materials* (with W. Jiang, Y. Wang, W.Z. Bao and D. J. Srolovitz), Scripta Materialia, Vol. 115 (2016), pp. 123-127.

[2] *A parametric finite element method for solid-state dewetting problems with anisotropic Surface energies* (with W.Z. Bao, W. Jiang and Y. Wang), J. Comput. Phys., Vol. 330 (2017), pp. 380-400 (arXiv: 1601.05877).

[3] *Triple junction drag effects during topological changes in the evolution of polycrystalline microstructures* (with W. Jiang, D.J. Srolovitz and W.Z. Bao), Acta Mater., Vol. 128 (2017), pp. 345-350 (arXiv: 1611.09449).

[4] *A sharp interface approach for solid-state dewetting in two dimensions via Cahn-Hoffman vector* (with W. Jiang), preprint.

[5] *Migration of toroidal thin films in solid-state dewetting* (with W. Jiang, T.Z. Qian, D.J. Srolovitz and W.Z. Bao), preprint.

[6] *A sharp interface model for solid-state dewetting in three dimensions* (with W.Z. Bao, W. Jiang), in preparation.

[7] *A parametric finite element method for solid-state dewetting problems in three dimensions* (with W.Z. Bao, W. Jiang), in preparation.